THE EUROPEAN LIGHT SOURCE

HIGHLIGHTS 2007

ESRF

European Synchrotron Radiation Facility

HIGHLIGHTS 2007

CONTENTS

ESRF

European Synchrotron Radiation Facility

Introduction

The European Synchrotron Radiation Facility is more productive than ever, progressing on many different fronts. This volume of the *Highlights* bears witness to the great diversity of subjects studied by our users and staff. The performance of the X-ray source and beamlines, of the technical, data-handling and user support, all contributed to the quality and volume of the science produced on the 43 (public and CRG) beamlines. The ESRF's combination of scientific and technical performance, and support to the users, is the acknowledged reference world-wide, despite the twenty years that have passed since the beginning of the ESRF's design and construction phase.

Preparations for the future moved to the front of the stage in 2007, which will be remembered as the year when the ESRF Upgrade Programme changed from a set of concepts and ideas to become a well-defined project. The major milestone in this process was the publication in October 2007 of the "Purple Book"[1], two volumes totalling 360 pages, which summarise two years of teamwork by over one hundred staff, users and outside experts. We gratefully acknowledge their selfless work and the excellent achievement that is the Purple Book.

[1] ESRF Science and Technology Programme 2008-2017, available in print or electronic format from www.esrf.eu/Upgrade.

The science case for the future development of the ESRF has been convincingly presented and the technical and managerial feasibility of our aspirations firmly established. Just as today's performance of the ESRF is the result of many different factors, the Upgrade Programme will improve all aspects of the ESRF, enabling the ESRF to continue to play a leading role in science for Europe and the world. The very long beamlines and their state-of-the-art instrumentation, the next-generation data-handling and storage facilities, the new-technology detectors and the research partnerships will all inspire further developments at national light sources by making available world-class expertise and knowledge. Sharing expertise and technology is high on the agenda for many ESRF staff who are regularly called upon to exchange ideas with colleagues at other light sources, both existing laboratories and facilities under construction.

This volume of the scientific *Highlights* provides a glimpse, today, of the future. The rebuilt and extended beamlines ID11 and ID13 with their nanofocusing capabilities are now in routine operation, highly-automated beamlines for macromolecular crystallography handle very large numbers of precious single-crystal samples, and many terabytes of information are analysed and stored by the ESRF's advanced computers.

In 2007 there were more than 6000 user visits to the ESRF including several hundred new ("first-time") users. So far the ESRF library has registered more than 1400 refereed papers based on work at the ESRF or by an ESRF staff member. To some extent this impressive figure reflects the increase in the number of accepted proposals, made possible thanks to improved automation and efficiency on the beamlines. With the help of our hard-working beamtime allocation panels, the ESRF does not compromise on the scientific quality of experiments accepted for beamtime. However, the fact that in some fields two thirds or even three quarters of the proposals deemed acceptable are refused due to lack of beamtime is a concern that must be considered in the future.

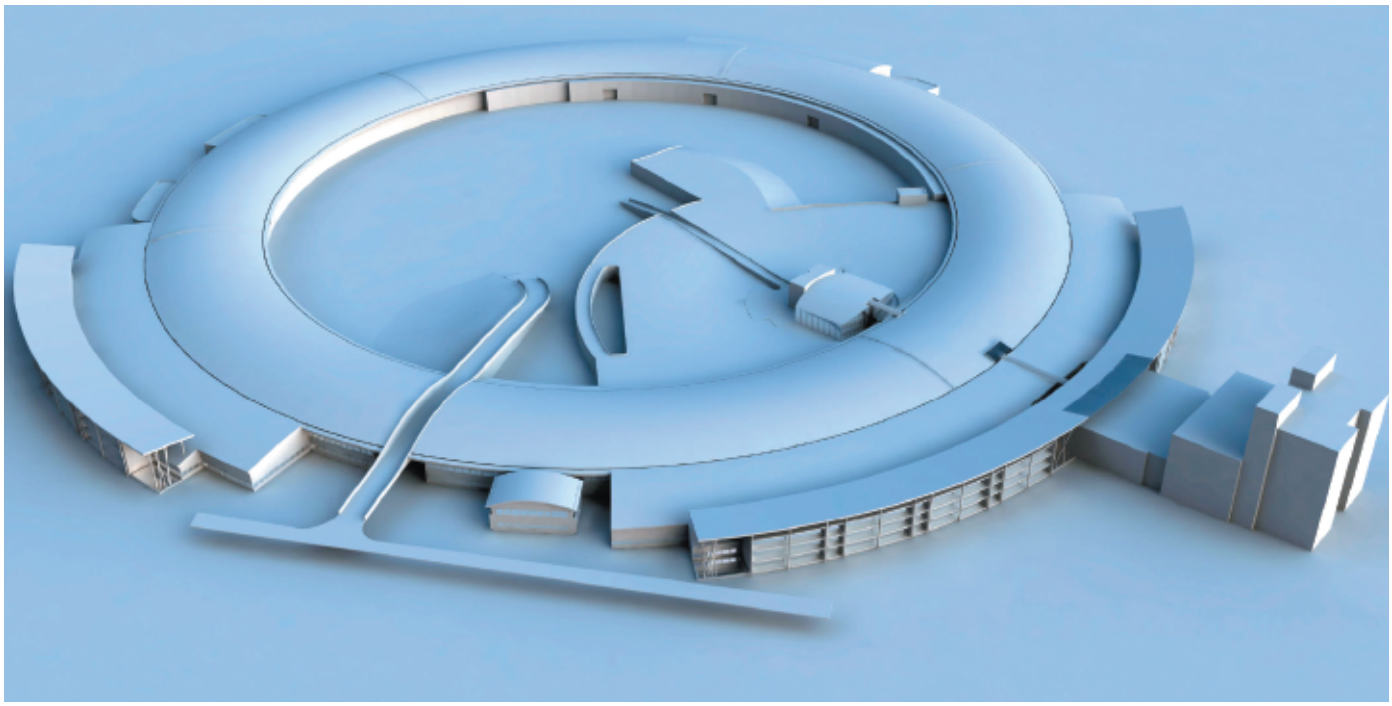

Artist's impression of the Upgraded ESRF showing experimental hall and extensions.

All Divisions at the ESRF again combined their efforts to prepare for the future while continuing with day-to-day operations for the users. Of particular note was the removal of the High Quality Power Supply (HQPS), a large installation protecting the storage ring and beamlines from interruptions and "spikes" on the public electricity power grid. The existing system, installed in 1995 had reached the end of its useful life, with many faults and failures, and consequently was dismantled to make place for a new system to be installed during 2008. During 2007, the storage-ring lattice was further optimised, achieving performance (emittance, lifetime, stability,...) equal to or higher than that of the lattice used for the previous 10 years, but with the capability of increasing all insertion device (ID) lengths from 5 to 6 m, and in addition the future possibility of installing some 7 m long IDs. Also in 2007, the prototype cryogenic in-vacuum undulator was calibrated and installed in the ID06 straight section, with detailed tests with beam continuing during 2008. Devices of this type will very likely be the high energy undulators of the future at the ESRF. On the buildings and infrastructure side, considerable efforts were expended in preparing the construction of extensions to the Experimental Hall featuring more than 20,000 square metres of additional floor space, foreseen by the Upgrade Programme to house new and refurbished beamlines and improved support facilities.

In November 2007, we presented the two volumes of the Purple Book to the ESRF Council where it received strong support despite a difficult funding context in many Member States. In 2006, the Upgrade Programme had been included on the list of 35 priority projects for European research infrastructures known as the "ESFRI roadmap". This enabled the ESRF to submit an application to the European Commission (EC) in June 2007, which, after international evaluation, resulted in a 5 million euro grant to support a wide range of activities during the preparatory phase of the Upgrade. For example, there is a work-package to define Europe's need for a very high magnetic field capability at ESRF and ILL. Also, much of the extensive (and expensive) preparatory work for the experimental hall extension will be covered by the grant from the EC. However, funding the Upgrade is not an easy task for our Member States as our programme is competing with many other national research infrastructure projects. A decision on the funding of the Upgrade Programme is needed in 2008 to avoid damaging delays and to maintain the long-term competitivity of the laboratory.

The steady growth of the number of users, coupled with continuous expansion into

new fields of science, has made the ESRF a true European success story that started more than twenty years ago, when scientists across Europe convinced their politicians that a world-leading European light source was needed. Included with this volume is a poster that we invite our readers to display prominently in their offices or laboratories to demonstrate their support for the ESRF and its Upgrade Programme 2008-2017. A special Web page www.esrf.eu/Upgrade includes more information on how users can help today to repeat the success of their peers some twenty years ago in persuading European governments to join forces to maintain the ESRF as a first-class laboratory and a shared European facility.

The ESRF *Highlights 2007* feature a selection of the best results from the ESRF over the last twelve months. We hope that regular and new *Highlights* readers alike enjoy hearing about the science and the remarkable range of scientific disciplines studied at the ESRF.

W.G. Stirling, M. Rodriguez Castellano, P. Elleaume, R. Dimper, H. Krech, S. Larsen, F. Sette, P. Thiry and C. Habfast.

High Resolution and Resonance Scattering

Introduction

This year was devoted to a greater extent to the preparation and discussion on the ESRF Upgrade Programme. Our group gave major input to the "Purple Book" on *Dynamical properties and Electronic Structure in Matter* (chapter 1.4). We also contributed to other chapters for subjects such as *Single objects at surfaces and interfaces*, *Fundamental chemical reaction processes*, *Matter at extreme pressure and temperature*, *Soft and fragile matter*, and *Time-resolved X-ray absorption and emission spectroscopy using pump-and-probe*. These topics are the main fields studied at the group's beamlines. The scientific cases were accompanied by five *Conceptual Design Reports* which elaborate on the technical and methodological challenges and possible solutions (see The ESRF Science and Technology Programme 2008-2017 Vol.2).

Beyond this, the beamline operation continued with exciting experiments and results. A selection is presented in these Highlights. Investigations on glasses and liquids already have a tradition in our group and are well represented here in the contribution on *Structural and collisional relaxations in liquids and supercritical fluids*. In 2005 we reported on *Iron oxidation state in impact glasses*. In continuation of that work, new and partly unexpected results are presented here on the *iron oxidation state in micro tektites*. The development of new techniques also continued and is highlighted in the contributions of *Complementary bulk-sensitive spectroscopies of Yb-based valence fluctuators* and *High-energy Mössbauer transitions in Ni using NFS*.

The already well-established applications studied at the high resolution and resonance scattering beamlines follow in the second and third parts of this chapter. They are introduced and summarised by G. Kotliar, *At the Interface between Experiment and Theory*, and by F.M.F. de Groot, *Spins probed with X-rays*.

Finally, the Inelastic X-ray Scattering beamline, ID28, has passed its regular review process with great success. New ideas and developments have been proposed, which have now to be discussed in the general ESRF context in order to be implemented.

The FP6 collaboration DYNASYNC came to an end with more exceptional results than ever anticipated. One example is outlined in the contribution by T. Ślęzak on *Phonons at the Fe (110) surface*. The advances permitted by this collaboration has stimulated the community to search for means of ensuring the continunity of the project, and thus to harvest even greater gains in the future.

R. Rüffer

Principal publication and authors
F. Bencivenga (a,b), A. Cunsolo (c), M. Krisch (a), G. Monaco (a), L. Orsingher (d), G. Ruocco (e), F. Sette (a), and A. Vispa (f), *Physical Review Letters*, **98,** 085501 (2007).
(a) ESRF
(b) Now at Sincrotrone Trieste S.C.p.A., Trieste (Italy)
(c) OGG c/o ILL, INFM-CNR, Grenoble (France)
(d) Università di Trento (Italy)
(e) Università di Roma 'La Sapienza' (Italy)
(f) Università di Perugia (Italy)

Structural and collisional relaxations in liquids and supercritical fluids

Relaxation processes in fluids have fascinated scientists for many years and remain, to date, a matter of debate. Despite intense efforts, the microscopic origin of these processes still eludes a comprehensive understanding. Among the various relaxations, the structural relaxation is the one related to cooperative rearrangements of the local structure. It is characterised by a relaxation time, τ, with a strong (typically Arrhenius) temperature dependence resembling that of viscosity. Recent studies performed on hydrogen bonded (HB) systems suggest that the microscopic mechanism responsible for the structural relaxation is the making and breaking of the hydrogen bonded network, which occurs on the picosecond timescale [1]. The aim of the work presented here was to investigate how this relaxation is affected by the transition from the liquid to the supercritical state. In order to evidence any possible common phenomenology, four systems (neon, nitrogen, ammonia and water), characterised by different intermolecular interactions and intramolecular structures, were studied. The relaxation time was experimentally determined by analysing inelastic X-ray scattering spectra taken at beamlines **ID16** and **ID28** (further details on the data analysis are reported in [2]). The values obtained for τ are reported in

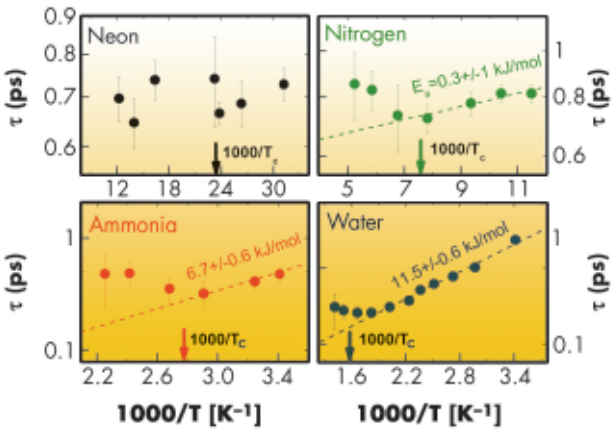

Fig. 1: Structural relaxation time, τ, as a function of the inverse temperature for neon (black), nitrogen (green), ammonia (red) and water (blue). The dashed lines highlight the activation behaviour observed in the liquid phase. The respective activation energies are reported in the figure.

Figure 1. Data belonging to the liquid phase (*i.e.* for $T<T_c$, with T_c being the critical temperature) can be empirically described by an Arrhenius law: $\tau = \tau_0 \exp(E_a/k_B T)$. This allowed the activation energy (E_a) of the relaxation to be derived, which was found similar to the energy of the respective intermolecular bonds. In the case of neon the data above T_c are too sparse and dispersed to draw any conclusions.

From **Figure 1**, one can also appreciate that, above T_c, the Arrhenius behaviour is lost. This suggests that, on approaching the supercritical state, the role of intermolecular bonds as the leading microscopic mechanism responsible for the relaxation is progressively reduced. In order to quantitatively compare data from different systems, the mean free time between intermolecular collisions, $\langle\tau\rangle$, was utilised as a scaling parameter.

Figure 2 reports the dimensionless quantity $\tau/\langle\tau\rangle$ as a function of T_c/T. It can be readily observed that, close and above T_c, $\tau/\langle\tau\rangle$ is constant and similar for all systems. This suggests that the dynamics of the system above T_c is dominated by collisions. On the other hand, below T_c, data for hydrogen bonded and non-hydrogen bonded systems split into two different curves. This can be explained considering that (i) on lowering the temperature a larger number of bonds can be established, and (ii) a stronger attractive potential (as the one of hydrogen bonded systems) increases their lifetime. This difference disappears above T_c, where the role of attractive interactions is strongly reduced.

In conclusion, the comparative study of these four prototype fluids across the liquid-to-supercritical transition reveals major changes in the microscopic mechanism responsible for the observed relaxation process. More specifically, in the liquid phase the leading mechanism is the making and breaking of intermolecular bonds. However, as soon

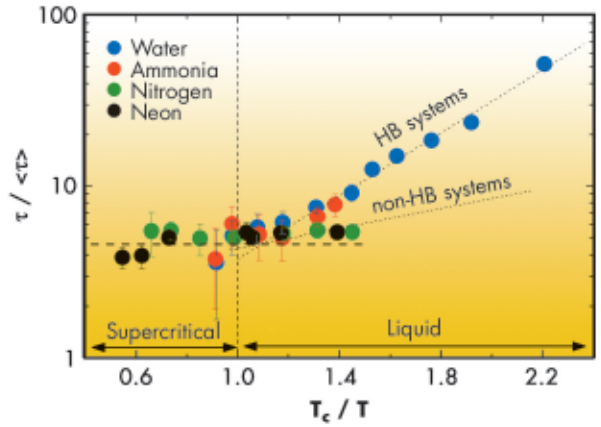

Fig. 2: Values of $\tau/\langle\tau\rangle$ vs. T_c/T for the investigated samples (legend as in Figure 1). The horizontal line describes the temperature dependence of $\tau/\langle\tau\rangle$ above T_c.

References
[1] See, *e.g.*, G. Monaco, A. Cunsolo, G. Ruocco and F. Sette, *Physical Review E*, **60**, 5505 (1999).
[2] F. Bencivenga, A. Cunsolo, M. Krisch, G. Monaco, G. Ruocco and F. Sette, *Physical Review E*, **75**, 051202, (2007).

as supercritical conditions are reached, binary collisions rule the microscopic dynamics of the system, as witnessed by the scaling of the data according to the mean free time between intermolecular collisions. These results provide an intuitive picture of the liquid-to-supercritical transition from a microscopic point of view since it was found that, with increasing the temperature, the lifetime of intermolecular bonds decreases to become, close to T_c, shorter than the average time between intermolecular collisions. As a consequence, the time needed for a molecule to get close to another one and eventually to form a new intermolecular bond becomes shorter than the average lifetime of the bond itself, thus preventing the fluid system from developing an extended bond network, typical of the liquid phase.

Impact cratering effects on the target rock: iron oxidation state in microtektites

Principal publication and authors
G. Giuli (a), S.G. Eeckhout (b), C. Koeberl (c), M.R. Cicconi (a), E. Paris (a), *Meteoritics and Planetary Sciences* **42**, A56 (2007); G. Giuli *et al.*, *Meteoritics and Planetary Sciences, in press* (2008).
(a) Dip. Scienze della Terra, Università di Camerino (Italy)
(b) ESRF
(c) Dept. of Geological Sciences, University of Vienna (Austria)

Impact cratering is a geological process that has affected the surface of the Earth crust since its formation. High-energy impacts volatilise and melt the target rocks; in some cases, large volumes of melt are generated. The oxidation state of the transition elements in these melts is important in determining the crystallisation history and trace element distribution of such impact melt rocks. Accurate studies on the oxidation state of Fe (the most common transition element in the Earth's crust) in glasses resulting from the fast cooling of these melts can provide information on the effect of impact cratering on the oxidation state of the molten target rock.

Tektites and microtektites are unaltered impact glasses produced during impact events from the Cenozoic era (beginning 65 My ago). Despite the availability of geochemical studies on tektites and microtektites, very few studies exist on the Fe oxidation state in such materials [1]. As microtektites constitute a large fraction of the mass of the glass produced by a tektite-generating impact event, such studies are of great importance for a more complete study of impact-generated glasses and, in particular, the effects of impacts on oxygen fugacity of melts produced during these events.

XAS spectroscopy is an excellent technique to study the oxidation state of Fe in such materials. In particular, XAS is the only technique allowing the study of impact glass samples regardless of Fe concentration (down to very low Fe contents) and sample size. We examined the iron oxidation state in a number of microtektites (submillimetre-sized glassy spherules that are distal ejecta of

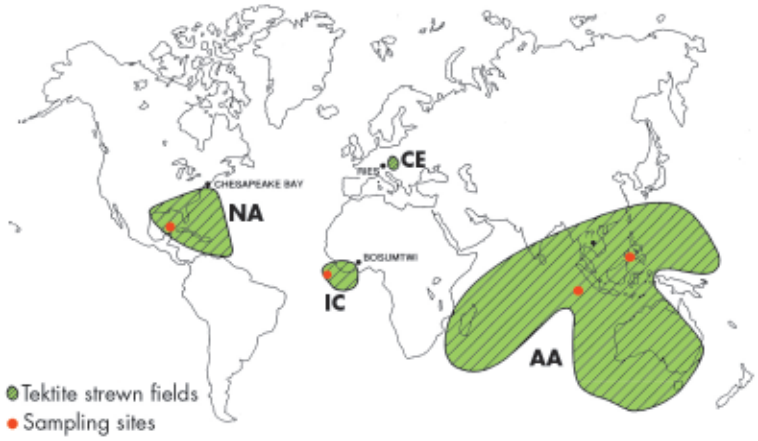

Fig. 3: Location of the ocean floor sampling sites (red dots) and source crater (black dots) within the tektites Strewn Fields (green): AA = Australasian, CE = Central European, IC = Ivory Coast and NA = North American strewn field. Modified from [3].

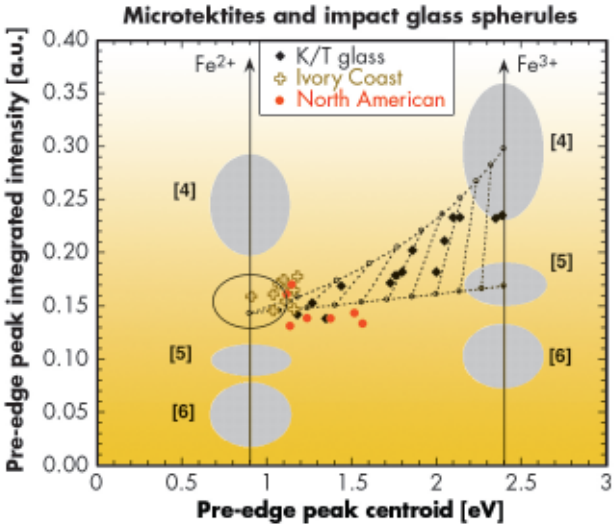

Fig. 4: Plot of the XANES pre-edge peak integrated intensity versus centroid energy (zero corresponds to the edge energy of metallic iron). The shaded ellipses indicate the field of data occupied by Fe model compounds of known oxidation state and coordination number, whereas the open ellipse shows the range for all tektites studied so far [1]. Also shown are the mixing lines (dashed lines + circles) between $^{[4]}Fe^{3+}$ or $^{[5]}Fe^{3+}$ and Fe^{2+} in a mixture of 4- and 5-fold coordinated sites. K/T glass = Cretaceous/Tertiary boundary impact glass.

meteorite impact events) from all three known strewn fields of microtektites. namely, the North American, Ivory Coast and Australasian fields. The samples were collected during the Deep Sea Drilling Project (**Figure 3**). The samples were studied by Fe K-edge X-ray absorption near-edge structure (XANES) spectroscopy, and Kα- or Kβ-detected XANES spectroscopy. The latter techniques offer the advantage of providing spectra of even higher resolution than XAS, thus allowing the detection of minor variations of Fe oxidation state. Experimental data were collected at beamline **ID26** using a Si (311) monochromator and with a beam size at the sample of 55 x 300 µm.

The pre-edge peaks of our XANES spectra display discernible variations in intensity and energy (**Figure 4**), which are indicative of significant changes in the Fe oxidation state. In the Australasian and Ivory Coast microtektites all Fe is divalent. Small components in the pre-edge peak are detected as relating to Fe^{3+} at well below 10 mole% level. North American microtektites display a varying $Fe^{3+}/(Fe^{2+} + Fe^{3+})$ ratio ranging from 0 to 0.5 (±0.1). All data fall within the same area of the graph, between two mixing lines joining a point calculated as the mean of the group of tektites studied so far (consisting of 4- and 5- coordinated Fe^{2+}) to $^{[4]}Fe^{3+}$ and $^{[5]}Fe^{3+}$, respectively. Thus, the XANES spectra show a mixture of $^{[4]}Fe^{2+}$, $^{[5]}Fe^{2+}$, $^{[4]}Fe^{3+}$ and $^{[5]}Fe^{3+}$. There is no evidence for six-fold coordinated Fe; however, its presence in small amounts cannot be excluded from XANES data alone.

The relatively high $Fe^{3+}/(Fe^{2+} + Fe^{3+})$ ratio in North American microtektites is a completely new and unexpected result, and poses a problem regarding the mechanism of impact melt reduction. No obvious relationship is evident between Fe oxidation state and glass composition. Possibly several parameters affect the Fe oxidation state, including target rock type, marine versus continental target, amount of energy released, and mass of produced glass.

The North American microtektites data and those of the globally distributed impact glasses from the Cretaceous/Tertiary boundary [2] are compatible with a strong interaction between impact glass microspherules and a CO_2-rich plume in the Earth's atmosphere generated by impact volatilisation of the target rock. Of all the impact glasses studied so far, only those produced during large impact events in marine targets (*i.e.*, with a cover of carbonate rocks) produced such a wide spread of the Fe oxidation state.

References
[1] G. Giuli, G. Pratesi, E. Paris, C. Cipriani, *Geochimica et Cosmochimica Acta* **66**, 4347-4353 (2002).
[2] G. Giuli, S.G. Eeckhout, E. Paris, C. Koeberl, G. Pratesi, *Meteoritics and Planetary Sciences* **40**, 1575-1580 (2005).
[3] A. Montanari and C. Koeberl, *Impact stratigraphy. The Italian record*. Springer-Verlag, Berlin-Heidelberg, 364 pp, (2000).

Complementary bulk-sensitive spectroscopies of Yb-based valence fluctuators

Authors
L. Moreschini (a), C. Dallera (b), J.J. Joyce (c), J.L. Sarrao (c), E.D. Bauer (c), V. Fritsch (c), S. Bobev (c), E. Carpene (b), S. Huotari (d), G. Vankó (d), G. Monaco (d), P. Lacovig (e), G. Panaccione (e), A. Fondacaro (f), G. Paolicelli (e), P. Torelli (g) and M. Grioni (a).
(a) IPN, Ecole Polytechnique Fédérale (EPFL), Lausanne (Switzerland)
(b) CNR-INFM, Dipartimento di Fisica, Politecnico di Milano (Italy)
(c) Los Alamos National Laboratory, Los Alamos, New Mexico (USA)
(d) ESRF
(e) Laboratorio TASC, INFM, Basovizza (Italy)
(f) INFM and Dipartimento di Fisica, Università di Roma III (Italy)
(g) LURE, Université de Paris-Sud, Orsay (France)

Novel synchrotron-based techniques provide an opportunity to look again at the classic problem of intermediate valence (IV) in lanthanide materials. Traditional electronic probes such as photoemission (PES) and X-ray absorption spectroscopy (XAS), although quite powerful, suffer from specific drawbacks: the energy resolution of XAS is often limited by the short lifetime of deep core holes, and the small probing depth of PES makes it very sensitive to surface conditions. Consequently, comparison of the experimental results with theory, *e.g.* the Anderson Impurity Model or its lattice extension, is not free from ambiguities. On the other hand, photon in-photon out spectroscopies like "high-resolution" partial fluorescence yield XAS (PFY-XAS) or resonant inelastic X-ray scattering (RIXS) [1], and hard X-ray photoemission (HAXPES) [2], have recently demonstrated the ability to probe changes in the bulk *4f* configuration occurring at the characteristic low-energy "Kondo" scale k_BT_K. Our experiment performed at beamline **ID16** on selected Yb compounds was an attempt to compare the information available from these complementary techniques [3].

Figure 5a shows PFY-XAS data for the IV compound $YbInCu_4$, measured at the Yb L_3 ($2p_{3/2}$) edge by recording the intensity of the Yb Lα ($3d_{5/2} \rightarrow 2p_{3/2}$) fluorescence. The spectra reveal distinct Yb^{2+} and Yb^{3+} features, split in the final state by the Coulomb interaction with the core hole. Their intensities are proportional to the weights of the Yb^{2+} and Yb^{3+} configurations in the hybrid ground state. The spectral weight transfer observed between 300 K and 20 K in $YbInCu_4$, but not in the Yb^{2+} reference material, demonstrates the Yb valence change predicted by the Kondo scenario [4]. The temperature changes are even more visible in the RIXS data of **Figure 5b**, which illustrate the energy distribution of the photons emitted in the $3d_{5/2} \rightarrow 2p_{3/2}$ radiative recombination. The excitation energy was set at the maximum of the 2+ XAS feature, which led to a selective resonant enhancement of the Yb^{2+} contribution.

A temperature-dependent intensity transfer between the Yb^{2+} and Yb^{3+} spectral features is also observed in the HAXPES data of **Figure 6a**, measured at **ID16** with the VolPE spectrometer [5]. The experimental *4f* spectrum of **Figure 6b** was obtained by subtracting the data for

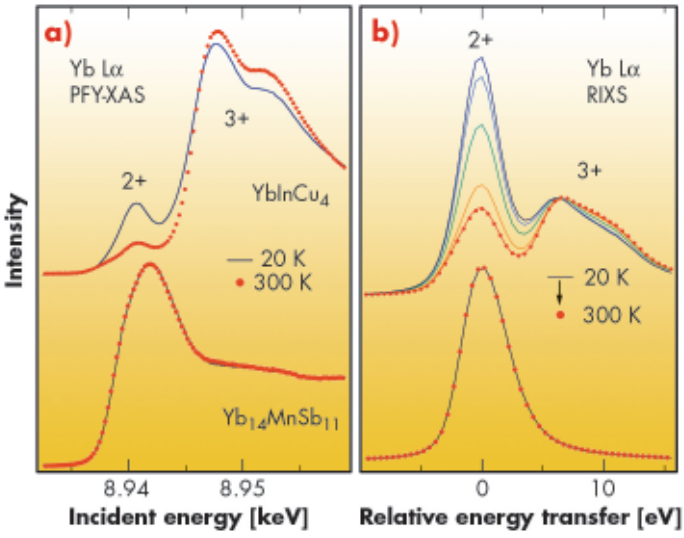

Fig. 5: a) PFY-XAS spectra of $YbInCu_4$ and of an Yb^{2+} reference compound at 300 K and 20 K. b) Lα RIXS spectra measured at the maximum of the Yb^{2+} resonance.

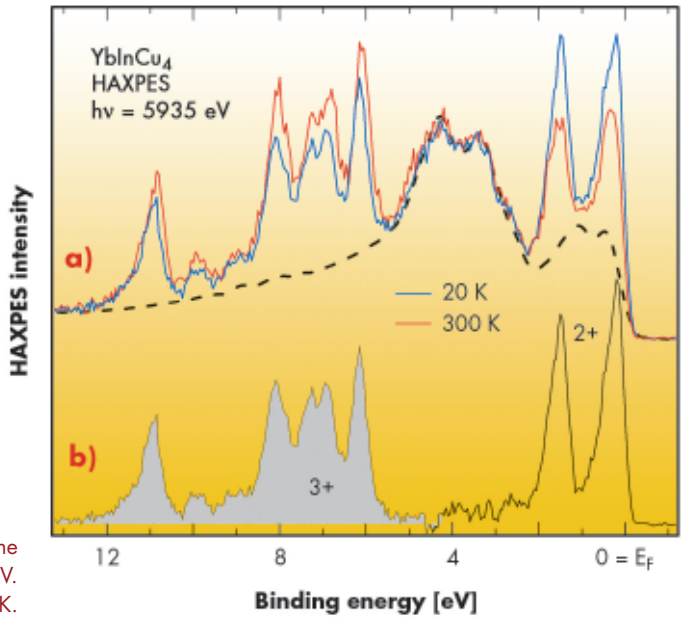

Fig. 6: Valence band HAXPES spectra of $YbInCu_4$. The dashed line is the spectrum of $LuInCu_4$ after removal of the atomic-like *4f* doublet at ~8 eV. The difference spectrum is shown in (b) for T=20 K.

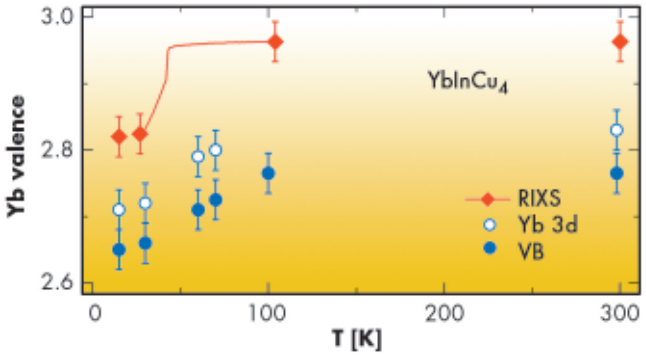

Fig. 7: Yb valence of $YbInCu_4$ determined from RIXS and HAXPES (valence band (VB) and Yb $3d_{5/2}$ core level).

the sister compound $LuInCu_4$, after removal of the core-like Lu 4*f* doublet. The Kondo resonance located at k_BT_K below the Fermi level E_F and its spin-orbit satellite are remarkably free from the broad "surface satellites" that are typically observed in conventional PES data. The contribution from the first surface layer is estimated to be less than 5%. We have observed a similar spectral weight transfer in the Yb $3d_{5/2}$ core levels (at E_B=1528 eV; not shown).

Figure 7 summarises the RIXS and HAXPES results. The temperature dependence could be measured continuously by RIXS, thanks to high detection efficiency. The RIXS data are in good agreement with thermodynamic and magnetic measurements, and capture the sudden valence drop at 42 K, in correspondence of a first-order electronic phase transition. They confirm that RIXS is a reliable bulk probe of the 4*f* configuration. HAXPES is directly sensitive to the 4*f* spectrum, and the data confirm a lower valence at low temperature. Nevertheless there is a quantitative discrepancy, especially for the valence band data. We have observed similar discrepancies for the other Yb compounds we have investigated. This suggests that the HAXPES data are still influenced by a perturbed surface layer extending over a range of a few tens of angstroms below the scraped surface. Its influence is likely to be reduced on cleaved single crystal surfaces, and especially by further increasing the photon energy, and therefore the probing depth, in HAXPES. Experiments at energies as high as ~10 keV are now possible by VolPE, and will be performed in the future.

References
[1] C. Dallera *et al.*, *Phys. Rev. Lett.* **88**, 196403 (2002).
[2] H. Sato *et al.*, *Phys. Rev. Lett.* **93**, 246404 (2004).
[3] L. Moreschini *et al.*, *Phys. Rev. B* **75**, 35113 (2007).
[4] N.E. Bickers *et al.*, *Phys. Rev. B* **36**, 2036 (1987).
[5] P. Torelli *et al.*, *Rev. Sci. Instrum.* **76**, 020939 (2005).

High-energy Mössbauer transition in Ni using NFS

Principal publication and authors
I. Sergueev (a), A. I. Chumakov (a), T.H. Deschaux Beaume-Dang (a), R. Rüffer (a), C. Strohm (a,b) and U. van Bürck (b), *Phys. Rev. Lett*, **99**, 097601 (2007).
(a) ESRF
(b) Physik-Department E13, Technische Universität München, Garching (Germany)

Nuclear forward scattering of synchrotron radiation has become an important technique to study magnetic and electronic properties of solids. Observation of the nuclear forward scattering relies on the finite lifetime of an excited nuclear state and a pulse structure of synchrotron radiation. Nuclear resonant scattering, delayed in time, is differentiated from the prompt pulse of incident radiation by a fast detector. The huge intensity of the prompt pulse leads, however, to an overload of the detector which has to be avoided by decreasing the energy bandwidth of synchrotron radiation using appropriate monochromators. For low-energy nuclear resonances, this is routinely achieved using a special monochromator with high-order reflections of perfect silicon crystals, which provide a narrow band pass (~meV) and high angular acceptance matching the angular divergence of synchrotron radiation. However, for nuclear resonances beyond 30 keV this approach is no longer applicable, because the angular widths of high-order reflections become very small.

In this work we show that nuclear forward scattering applied to high-energies can be performed with X-ray optics based on silicon crystals. This was done using low-order reflections with a moderate energy resolution but sufficiently high angular acceptance. With this, in combination with a multi-element detector, the overload problem is circumvented. The method was applied to study the 67.41 keV Mössbauer transition in ^{61}Ni, which is an element of particular industrial and biological importance.

The experiment was performed at **ID18**, the Nuclear Resonance beamline. The nickel foil enriched in ^{61}Ni to 85% was irradiated by the beam from the high-heat-load Si(111) double-crystal monochromator

with a band pass of 15 eV. The radiation after the sample was monochromatised further by two crystals. The first Si crystal with the highly asymmetrical (444) reflection worked as a dispersive element. The second Si(844) crystal was an energy analyser. The observed energy band pass of this monochromator was 120 meV. The time evolution of scattered radiation was measured using a novel 16-element array of Si avalanche photodiodes. The elements of the array were adjusted to the incident radiation at small glancing angle and displaced laterally relative to each other. Each element covered only a part of the beam in order to distribute the load over the photodiodes.

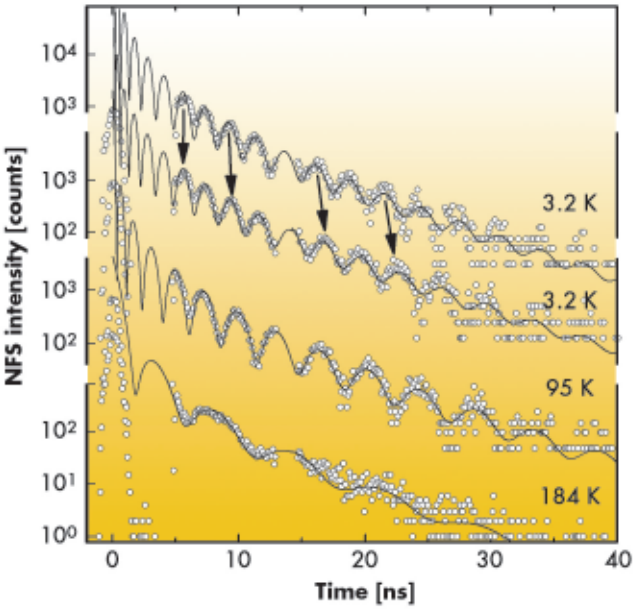

Fig. 8: Time evolution of the nuclear forward scattering for metal Ni foil. All measurements except for the upper curve were performed with external magnetic field B=4T. The solid lines show the fit. The arrows emphasise stretching of the dynamical beat structure by the applied magnetic field.

Time evolution of the nuclear forward scattering from the metal nickel foil is shown in **Figure 8** for various temperatures and with or without applied external magnetic field. The thickness of the sample, chosen to optimise the count rate, was extremely large. This brought us into a so far unknown regime of nuclear forward scattering, characterised by large effective thicknesses. In this regime the beats in the measured time spectra are determined mainly by multiple scattering. On the other hand, the role of hyperfine magnetic splitting is manifested as a scaling of the time axis which is seen by comparison of the two top curves in the **Figure 8**. The application of the magnetic field of 4T, which decreases the hyperfine magnetic splitting by about a factor of 2, leads to the stretching of the beat structure. The fit to the data allows us to obtain values of the magnetic field at the nuclear site, which is 7.4(2) T without magnetic field and 3.7(2) T with applied magnetic field. These results are consistent with that obtained by NMR. The pronounced beat structure of multiple scattering allows the precise determination of the effective thickness and, therefore, the Lamb-Mössbauer factor, which equals 0.167(3) for 3.2 K.

In this work we have studied nuclear forward scattering of the 67.41 keV radiation by ^{61}Ni. The method can be applied to a series of other isotopes. Among them, ^{73}Ge(68.75 keV) is a classical elementary semiconductor, ^{157}Gd(64.0 keV), ^{145}Nd(67.25 keV), ^{175}Yb(76.46 keV) and ^{170}Er (79.31 keV) are important compounds for the magnetism in strongly-correlated systems and ^{99}Ru (89.36 keV) is interesting in catalysis and material science. Thus, routine hyperfine spectroscopy of high-energy Mössbauer isotopes will become available, especially under extreme conditions.

At the interface between experiment and theory

Exciting research opportunities lie in the interfaces between disciplines. Even within a single field of research, the combination of complementary techniques brings new insights into complex problems. that cannot be obtained by either of the methods alone. There is a long tradition of constant interplay between experiment and theory in condensed matter physics and materials science research. In this interdisciplinary area, Rrecent advances in experimental techniques, promise to bring the interplay of experimental and theoretical research to new levels of quantitative detail.

On the experimental front, recent advances in instrumentation and techniques are taking place using advanced X-ray sources

such as the ESRF. In the field of computational material theory, novel algorithms and faster computers are opening up uncharted territories in materials research. The combination of these two approaches is illustrated in the following articles, highlighted in this note below.

The first paper, by Weissker *et al.* [1], studies the frequency and momentum dependence of silicon's dielectric function in a broad region of frequency and momentum transfer. Silicon, a textbook material, is an excellent model system for testing the accuracy of different theoretical approaches. The measurements use high-resolution, non-resonant, inelastic X-ray scattering. The theoretical methods used include non-self-consistent many-body perturbation theory in the GW approximation as well as the time dependent density functional theory in the LDA (local density approximation). The latter approach turns out to be remarkably successful in accounting for all the main features of the data, provided that an energy dependent lifetime broadening is added, as suggested in ref. [2]. The calculations relate the different features of the experimental data to the quasiparticle bands and the plasmon mode of the material. Theory is required to make this connection since off diagonal elements of the microscopic dielectric function (which are generally known as local field effects) give rise to non trivial features in the frequency and wavevector dependence of the macroscopic dielectric constant.

The second paper, by Ślęzak *et al.* [3], determined the in-plane phonon density of states of monolayers at and near a clean Fe (100) surface in ultra-high high-vacuum conditions. Phonon spectroscopy is made This break-through became possible by the combination of nuclear inelastic scattering, availability at third-generation synchrotron radiation sources, and detectors advaavailable at the ESRF. Grazing-incidence nuclear scattering allows the determination of the surface phonon density of states.nced surface science techniques. Modern implementations of density functional theory, together with the direct method [4], allow the evaluation of the phonon spectra in materials with large unit cells. The studies of ref. [3] use a thick slab containing 29 iron layers.

The combined experimental/theoretical study establishes that, while the second layer of the surface vibrates at almost the same frequencies as the bulk, the first layer is markedly different. The surface vibrational amplitudes are clearly enhanced relative to the bulk, while the surface phonon frequencies are substantially softened (of the order of 30%) relative to the bulk values. The power of the experimental setup to select the contribution from the first layer and of different phonon polarisation states is bolstered by the theoretical capabilities allowing the identification of each phonon branch and its weight in the phonon density of states.

The third paper, by Raymond *et al.* [5], studies $PuCoGa_5$, a remarkable material which undergoes a direct transition from a very incoherent metallic state, characterised by Curie-like susceptibility, to an unconventional superconducting state at low temperatures. To determine the degree of correlation in this material, i.e. to which extent the f electrons in Pu are localised, Raymond *et al.* present a combined experimental and theoretical study of the phonon spectra.

The effects of correlation on the phonon spectra are modelled by varying the Hubbard parameter U of the LDA+U method. The experimental determination of phonon properties in small crystals containing actinide elements is made possible by inelastic X-ray scattering. Comparing theory and experiment, a value of U=3 is was determined for ^{242}Pu. This type of calculation had only been previously carried out on much simpler materials such as NiO and MnO [6]. The results of Raymond *et al.* support the idea that strong correlations are indeed present in such Pu materials. The combined experimental and theoretical study of Raymond *et al.* supports the idea that strong correlations are indeed present in ^{242}Pu materials.

In summary, advances in computational physics and in experimental

References
[1] H. Weissker *et al. PRL* **97**, 237602 (2006).
[2] S. Rahman and G. Vignale, *PRB* **30**, 6951 (1984).
[3] T. Ślęzak *et al., PRL* **99**, 66103 (2007).
[4] K. Parlinski *et al.*, PRL **78**, 4063 (1997).
[5] S. Raymond *et al., PRL*, **96**, 237003 (2006).
[6] S. Savrasov and G. Kotliar, *PRL* **90**, 056401 (2003).

instrumentation are enabling a much closer interaction between theory and experiment. This interplay of theory and experiment holds promise for reaching a deeper and more quantitative understanding of the physical properties of complex materials.

***G. Kotliar**, Center for Materials Theory, Rutgers University (USA)*

Dielectric function of silicon for finite momentum transfer

Principal publication and authors

H.-Ch. Weissker (a,d), J. Serrano (b), F. Bruneval (a,d), F. Sottile (a,d), S. Huotari (b), G. Monaco (b), M. Krisch (b), V. Olevano (c,d), and L. Reining (a,d); Phys. Rev. Lett. **97**, 237602 (2006).

(a) LSI UMR 7642, CNRS-CEA/DSM, Ecole Polytechnique, Palaiseau (France)
(b) ESRF
(c) Institut NEEL, CNRS, Grenoble (France)
(d) European Theoretical Spectroscopy Facility (ETSF)

Modern theoretical solid state physics often aims to understand the properties of materials by means of numerical calculations which do not use parameters taken from experiment. The starting point of these *ab initio* calculations for many-electron systems is mostly the well-established *static* density-functional theory (DFT). For many spectroscopic quantities (which are always connected to the response of the system to a time-dependent perturbation), the *time-dependent* density-functional theory (TDDFT) [1] can be employed. One of its important ingredients is the so-called exchange-correlation kernel f_{xc} that represents the electron-electron interactions in the response beyond a simple Hartree picture (where only the classical Coulomb potential is varied). It is a complicated quantity, the exact expression of which is unknown, and which has to be approximated. To this end, close interaction of theory and experiment is essential.

The design of good approximations is closely linked to the identification of the relevant physical effects. One of the most widely used approximations, in particular for finite systems like molecules, is the adiabatic local-density approximation (ALDA, also called TDLDA), although it fails for the optical absorption spectra of bulk materials, *i.e.*, in the long-wavelength limit in extended systems. We, by contrast, investigate the situation of finite momentum transfers.

We performed inelastic X-ray scattering (IXS) measurements on beamline **ID16**. Using monochromatic X-rays of 7.909 keV and a Si wafer with the normal parallel to the [110] direction, the dynamic structure factor, proportional to the loss function, was measured for momentum transfers between 0.27 and 2.40 a.u. along the [111] and [100] directions. The energy resolution was 1.1 eV; no additional features were observed in the spectra upon increase in resolution to 0.2 eV.

We find that the TDLDA improves greatly upon the result in the random-phase approximation (RPA, where f_{xc} is neglected altogether and only the induced Hartree potential is considered). Comparison between theory and experiment led to the conclusion that the TDLDA describes the valence excitations very well provided that lifetime effects are added. The latter is done under the assumption that the lifetimes of the electrons and holes created in the system, calculated on a one-quasi-particle level, are essentially independent. The excellent agreement between experiment and theory shows that lifetime effects are not contained in the TDLDA but can be added separately.

Moreover, we have extracted the dielectric function from the measured structure factor by means of the Kramers-Kronig relations, which connect the real and the imaginary part of the dielectric function. In **Figure 9** we show its imaginary part. The good result of the TDLDA stands in contrast to its

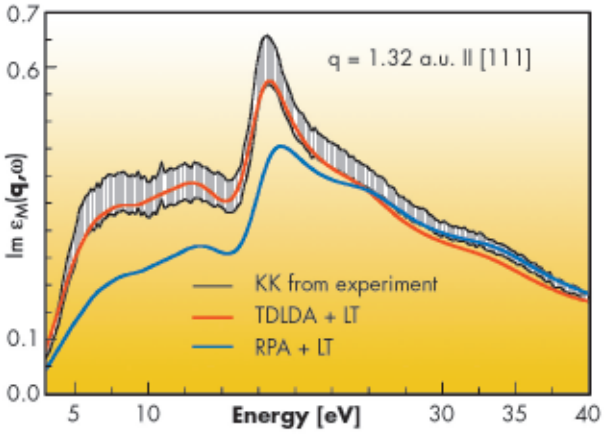

Fig. 9: Imaginary part of the dielectric function extracted from the measured dynamic structure factor using the Kramers-Kronig (KK) relations and compared to the TDLDA and the RPA calculations, both with added lifetime (LT) effects. The shaded area shows the error bar of the extraction.

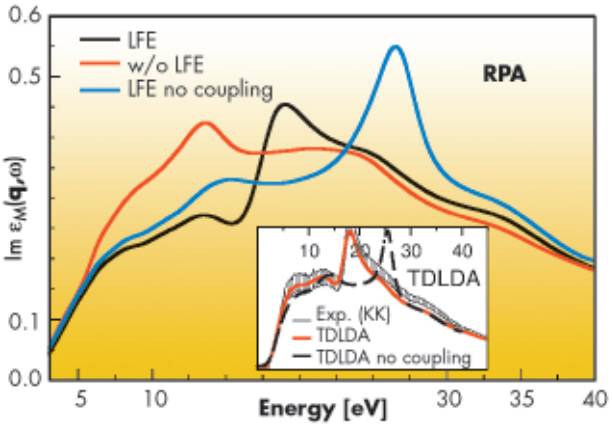

Fig. 10: Influence of local-field effects (LFE) for the RPA spectra of Figure 9, and influence of the coupling with the transitions of negative energy. The inset shows the influence of the coupling for the TDLDA.

performance in the optical limit (vanishing momentum transfer) where the dielectric function calculated in TDLDA is far from experiment.

The excellent agreement between experiment and theory allowed for the identification of important effects. We could elucidate the role of an important mixing between single interband transitions, that is, transitions between states calculated within the simple independent-particle picture. This mixing is due to induced Hartree and exchange-correlation potentials, with components of the wavelength of the perturbation and other components. These other components give rise to the so-called local-field effects (LFE) which are mediated by the microscopic inhomogeneity of the material and shown in **Figure 10**. Unlike in the optical spectra of bulk silicon, their influence is strong. Moreover, we compare with a calculation that neglects the coupling of the transitions of positive energy with transitions of negative energy. Our results show that this coupling is very important, although often neglected (Tamm-Dancoff approximation), and this in contrast to optical spectra.

In conclusion, thanks to the close interaction of theory and experiment we have been able to determine the approximation adequate for the description of valence excitations in semiconductors for finite momentum transfer. The combination of TDLDA and electron and hole lifetime effects yields spectra of predictive quality. Moreover, we could elucidate the role of the microscopic inhomogeneity of the material for the coupling of otherwise independent transitions. The connection of state-of-the-art experiment with theoretical investigations has thus greatly improved our understanding of electronic excitations in semiconductors.

References
[1] S. Botti, A. Schindlmayr, R. Del Sole, and L. Reining, *Rep. Prog. Phys.* **70**, 357-407 (2007).

Phonons at the Fe (110) surface

Authors
T. Ślęzak (a), J. Łażewski (b), S. Stankov (c), K. Parlinski (b), R. Reitinger (d), M. Rennhofer (d), R. Rüffer (c), B. Sepiol (d), M. Ślęzak (a), N. Spiridis (b), M. Zając (a), A. I. Chumakov (c), and J. Korecki(a, b).
(a) AGH University of Science and Technology, Kraków (Poland)
(b) Polish Academy of Science (Poland)
(c) ESRF
(d) University of Vienna (Austria)

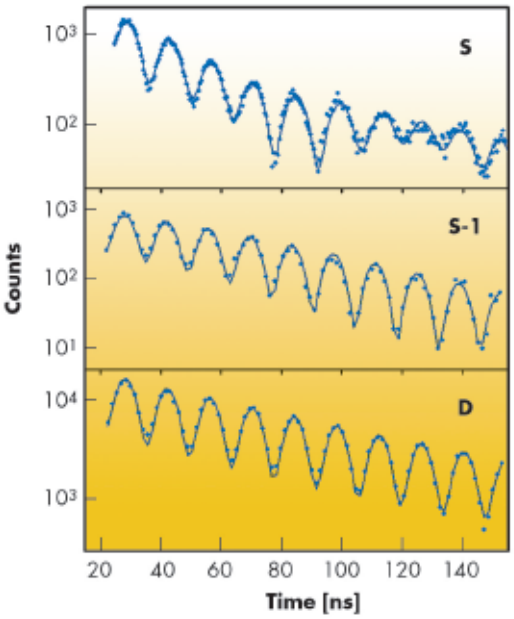

Fig. 11: Fitted NRS time spectra for the Fe(110) surface (S), subsurface (S-1), and deep (D) layers measured with the X-ray beam along the [110] direction.

The fascinating development of nanoscale science requires a precise understanding of dynamical and thermodynamical properties of surfaces and nano-objects. What are the surface modifications of the phonon dynamics with respect to the bulk? How "thick" from the thermodynamical point of view is a surface? These key-questions have been addressed theoretically [1] but experimental verification using surface sensitive methods [2] did not allow direct measurements of the phonon density of states (DOS) on a clean surface. Recent developments at beamline **ID18** have enabled the phonon spectroscopy of monolayer films and nanostructures using *in situ* nuclear inelastic scattering (NIS) [3]. The method gives phonon DOS which is (i) partial -only atoms of the resonant isotope contribute-

and (ii) projected onto the direction of the incident photons. The contributions of various branches are weighted by the squared projection of the phonon polarisation vector to the incident photon's direction [3].

We measured phonon DOS for single atomic monolayers at and near a clean Fe(110) surface. The samples were single-crystalline Fe(110) films epitaxially grown on W(110) crystal, where the chosen atomic monolayers were filled with the resonant ^{57}Fe isotope, while the rest of the film was composed of the non-resonant ^{56}Fe atoms. Using a special preparation protocol, the ^{57}Fe monolayers could be precisely located at the surface (referred as "S"), one atomic layer below the surface (referred as "S-1") and deeper ("D"). Due to the ideal isotope selectivity of nuclear resonant scattering, this approach gives the resolution of a single atomic layer in a chemically homogeneous crystal. Moreover, a combination of the grazing-incidence coherent nuclear scattering (NRS) and incoherent NIS provided the direct correlation between electronic (including magnetic) and phononic properties. The measurements were performed at room temperature with the X-ray beam along both high-symmetry directions of the 2-dimensional rectangular unit cell of the Fe(110) surface, *i.e.* along [001] and [1$\bar{1}$0].

Figure 11 shows the time spectra of coherent grazing-incidence nuclear scattering measured with the X-ray beam along the [1$\bar{1}$0] direction. The spectra of (S-1) and (D) show a single frequency quantum beat pattern described by a well-defined hyperfine magnetic field B_{hf} oriented parallel to the beam, *i.e.* along the [1$\bar{1}$0] direction, in contrast to the [001] easy magnetisation axis in bulk Fe. The surface (S) spectrum is clearly different by an additional intensity modulation, which results from a finite electric field gradient caused by the termination of ionic and electronic charges at the surface. Along with the electronic properties, the vibrational ones are also subjected to a strong modification. **Figure 12** shows the DOS extracted from the measured energy dependencies of incoherent NIS. The DOS of the first surface monolayer (panel S) is

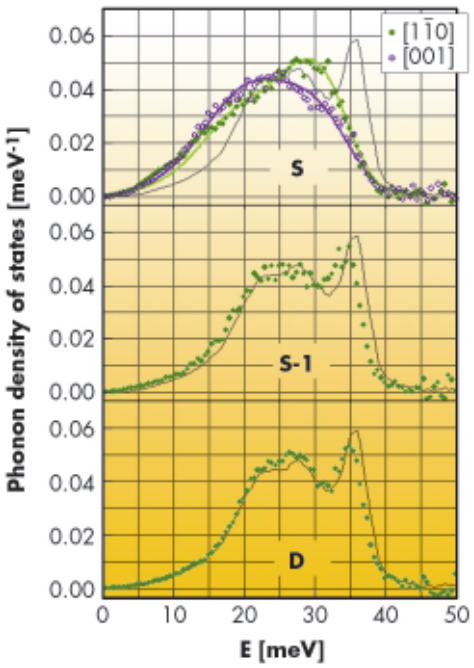

Fig. 12: Measured phonon DOS for the surface (S), subsurface (S-1), and deep (D) layers near the Fe(110) surface projected onto the [1$\bar{1}$0] (solid symbols) and [001] (open symbols) directions. The solid lines in (S) depict results of DFT calculations. The phonon DOS of an ^{57}Fe foil is shown for comparison in each panel as a continuous line.

very different from those of two other samples, as well as from the DOS of the bulk iron. The most striking anomalies are the suppression of the phonon peak at 35 meV and a considerable enhancement of vibrational states below 15 meV. In addition, the DOS projected onto the [1$\bar{1}$0] and [001] directions are clearly different, which is unusual for the cubic lattice. The observed anomalies of atomic dynamics are strongly localised within the first atomic monolayer. Already in the second atomic layer (panel S-1) most of the bulk DOS features are restored and the deeper layers (panel D) display truly bulk behaviour. This striking observation that the surface is only one monolayer thick was convincingly confirmed by first principle phonon calculations [4] using density functional theory, which perfectly reproduced surface DOS and its anisotropy as depicted in **Figure 12**, panel S. Also dynamic and thermodynamic parameters (*e.g.* mean force constants, thermodynamic functions, mean square displacement) derived from the measured DOS are in good agreement with the theory.

Besides the new insight in the field of surface dynamics, the present work opens new perspectives for nuclear inelastic scattering experiments in systems for even lower dimensionality, such as nano-wires and nano-dots.

The work was performed in the framework of the 6 FP STRP project DYNASYNC.

References

[1] R. Heid and K.-P. Bohnen, *Phys. Rep.* **387**, 151 (2003).

[2] J. P. Toennies, in *Surface Phonons*, edited by W. Kress and F.W. deWette, Springer Series in Surface Sciences Vol. **21** (Springer, Berlin, 1991), p. 111.

[3] R. Röhlsberger, *Nuclear Condensed Matter Physics with Synchrotron Radiation*, Springer Tracts in Modern Physics Vol. **208** (Springer-Verlag, Berlin, 2004).

[4] K. Parlinski, *Phys. Rev. B* **74**, 184309 (2006).

Probing the Coulomb interaction of the unconventional superconductor $PuCoGa_5$

Principal publications and authors
S. Raymond (a), P. Piekarz (b), J.P. Sanchez (a), J. Serrano (c), M. Krisch (c), B. Detlefs (d), J. Rebizant (d), N. Metoki (e), K. Kaneko (e), P.T. Jochym (b), A.M. Oleś (b,f), and K. Parlinski (b), *Phys. Rev. Lett.* **96,** 237003 (2006); and *J. Alloys Comp.* **444-445**, **104** (2007).
(a) CEA-Grenoble, DRFMC / SPSMS, Grenoble (France)
(b) Institute of Nuclear Physics, Polish Academy of Sciences, Krakow (Poland)
(c) ESRF
(d) European Commission, Institute for Transuranium Elements, Karlsruhe (Germany)
(e) Japan Atomic Energy Agency, Tokai (Japan)
(f) Max Planck Institut für Festkörperforschung, Stuttgart (Germany)

The discovery of superconductivity in the plutonium based intermetallic compound $PuCoGa_5$ in 2002 came as a surprise with regard to the high transition temperature T_c=18.5 K for an actinide material [1]. This lead to a renewed interest in actinide research and launched an intensive search for new *5f* electron-based superconductors resulting in the discovery of the heavy fermion superconductor $NpPd_5Al_2$ (T_c=4.9 K) in 2007 [2]. Beyond the specific field of actinide research, it turns out that, given its characteristic energy scales, the unconventional superconductor $PuCoGa_5$ is playing the central role of a missing link between the canonical heavy fermion superconductors and the high-T_c cuprates [3]. The understanding of its physical properties will thus allow advances in the global understanding of unconventional superconductivity. The analogy to the isostructural heavy fermion superconductor compound $CeCoIn_5$ (T_c=2.3 K) strongly suggests a magnetic mechanism for the electron pairing. Despite this, the study of the phonon spectrum is nonetheless of interest. This is partly due to tremendous recent progress in band structure calculations that allow an accurate computation of phonon spectrum of strongly-correlated electron systems [4].

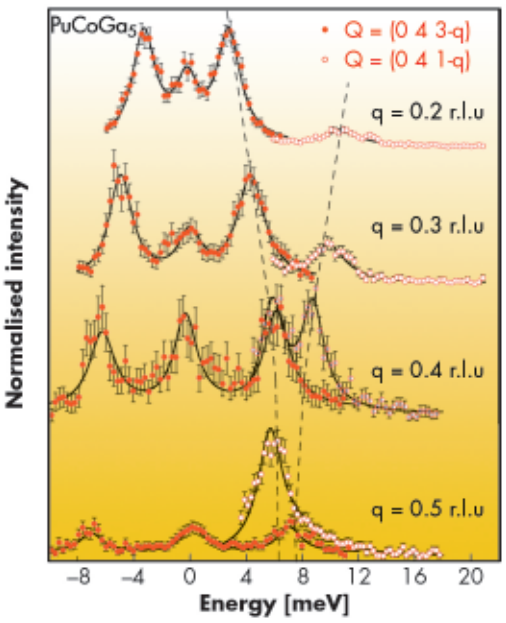

Fig. 13: IXS phonon spectra of $PuCoGa_5$ measured at T = 297 K. The full and open symbols correspond to modes measured at Q = (0, 4, 3-q) and Q = (0, 4, 1-q), respectively. The dashed lines indicate the dispersion of the corresponding TA and TO modes.

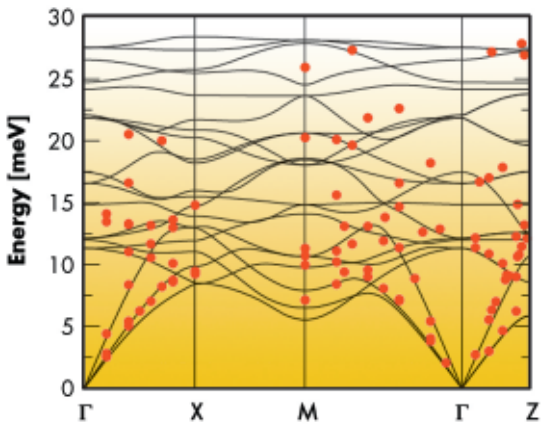

Fig. 14: Measured (circles) and calculated (lines) phonon dispersion relations of $PuCoGa_5$.

We determined the phonon dispersion curves of single crystalline $PuCoGa_5$ samples along the [100], [110] and [001] directions by inelastic X-ray scattering (IXS) at beamline **ID28** at room temperature. Representative spectra are shown in **Figure 13** for transverse acoustic (TA) and transverse optic (TO) modes propagating along [001]. The IXS data are compared with a density functional theory (DFT) *ab initio* calculation using the generalised gradient approximation with finite *U* (GGA+U) method [4]. We conclude that the inclusion in the calculation of a finite on-site repulsion between *f* electrons, *U*, of approximately 3 eV is essential to describe quantitatively the lattice dynamics of $PuCoGa_5$. This conclusion is primarily drawn from the sensitivity of the lowest energy TO modes to the Coulomb repulsion that undergo up to 30% change in energy between the calculations with U = 0 and U = 3 eV. This makes apparent the strong influence of the *5f* charge distribution on the force constants. The measured and calculated phonon dispersion is shown in **Figure 14**; an overall good agreement with the calculation with U = 3 eV is obtained for all the investigated branches. In contrast, an inelastic neutron scattering study performed on the parent compound $UCoGa_5$ indicated that the phonon

spectrum of this later system is better described with U = 0 eV in agreement with its itinerant paramagnet ground state [5].

Our study gives new evidence for localised degrees of freedom of f electrons in $PuCoGa_5$ in agreement with photoemission results. We show that phonon spectroscopy is an alternative way of probing electronic properties of strongly-correlated electron systems. The localised versus itinerant nature of the f electrons, whose duality is at the strongest in actinides, is an essential information for any theory aiming to describe superconductivity in such strongly-correlated electron system.

References
[1] J.L. Sarrao *et al.*, *Nature* **420**, 297 (2002).
[2] D. Aoki *et al.*, *J. Phys. Soc. Japan* **76**, 063701 (2007).
[3] N.J. Curro *et al.*, *Nature* **434**, 622 (2005).
[4] P. Piekarz *et al.*, *Phys. Rev. B* **72**, 014521 (2005).
[5] N. Metoki *et al.*, *Physica* B **378-380**, 1003 (2006).

Spins probed with X-rays

Transition metals, rare earths and actinides share the occurrence of local spin and orbital moments, due to strong intra-atomic electrostatic interactions. In the 3d transition metal ions these local interactions are similar in magnitude to the interatomic interactions, which gives rise to a range of ground states with different spin and orbital moments and affected by spin-orbit coupling and charge transfer. In transition metal oxide systems, these states act as the local components of the band structure and the resulting orbital and magnetic ordering. The determination of the spin moment implies (in most cases) the determination of the ground state symmetry. Recent experiments on mixed valent Mn, Fe and Co oxides show that their basic understanding is still far from clear. Because these systems play a crucial role in, for example, devices, sensors, catalysts and batteries, a more unified knowledge of their fundamental properties would be helpful.

The spin moment of transition metals can be determined from various synchrotron X-ray methods. Vanko *et al.* (page 18) use Kβ X-ray emission to probe the high-spin and low-spin state of Fe^{II}. They study switchable spin-crossover complexes that can be trapped in a long-lived metastable state that has a different spin moment than the ground state. The interesting finding was that the X-rays themselves can be used to bring the Fe^{II} ions into their excited state. It is proposed that irradiation with hard X-rays can be exploited to populate metastable states when optical excitation is limited by the characteristics of the sample or by its environment, such as for nontransparent samples or under extreme conditions.

Sikora *et al.* (page 20) use the Kβ X-ray emission spectra to study the spin state evolution of the transition metals in the $LaMn_{1-x}Co_xO_3$ perovskite series. They show that the spin moment can be derived from Kβ X-ray emission spectra by calculations and with reference systems. The average spin states of Mn and Co can be quantified using the integrals of the absolute values of the difference spectra (IAD), as developed by Vanko. The Kβ X-ray emission spectra reveal that the spin state of Mn changes from S=2 Mn^{III} in $LaMnO_3$ to S=3/2 Mn^{IV} in $LaCo_{0.98}Mn_{0.02}O_3$. Concurrently, the spin state of Co at room temperature changes from S=3/2 Co^{II} in $LaCo_{0.02}Mn_{0.98}O_3$ to S=1/2 Co^{III} in $LaCoO_3$, with a further decrease to S=0 Co^{III} at 10K. A Co^{III} ion is highly covalent and has a charge transfer energy close to zero. This suggests that the S=0 low-spin state with a $t_{2g}^6e_g^0$ configuration mixes with an S=1 intermediate state $t_{2g}^5e_g^1$ configuration via the charge transfer state with a $t_{2g}^6e_g^1\underline{L}$ configuration. This S=1/2 Co^{III} state can be seen as a mixed spin state between the low-spin and intermediate-spin state. Sikora *et al.* also use K edge X-ray absorption to determine the spin state, using the determination of the average valence from the edge position and also the assumption that the average valence can be transferred to the average spin state. This method works fine for manganese but yields results

different from Kβ X-ray emission in the case of cobalt. This indicates that the room temperature spin configuration of the Co^{III} is altered upon doping.

An alternative to probing the spin state is to use nuclear resonance scattering. McCammon *et al.* (page 21) show the use of Mössbauer and nuclear forward scattering (NFS) at high temperature and pressure to study materials that exist in the lower mantle, *i.e.* $Mg_{0.88}Fe_{0.12}SiO_3$ and $Mg_{0.86}Fe_{0.14}Si_{0.98}Al_{0.02}O_3$ oxides. The main valence of iron in these 8-fold (distorted) cubic systems is Fe^{II} and a transition is visible from S=2 high-spin Fe^{II} with an $e_g^3\ t_{2g}^3$ configuration to a S=1 intermediate spin Fe^{II} with an $e_g^4\ t_{2g}^2$ configuration between 40 and 80 GPa. Because of charge transfer both Fe^{II} states mix with a $e_g^4\ t_{2g}^3\ \underline{L}$ configuration and can generate a mixed spin state, where the mixing of the components depends on pressure. The experimental NFS data show that elevated temperatures stabilise the intermediate-spin state, implying that Fe^{II} in silicate perovskite is predominantly in this state throughout most of the lower mantle.

***F.M.F. de Groot**, Department of Inorganic Chemistry and Catalysis, Utrecht University, The Netherlands.*

Principal publication and authors
G. Vankó (a,b), F. Renz (c), G. Molnár (d), T. Neisius (e), S. Kárpáti (f), *Angew. Chem. Int. Ed.* **46,** 5306 (2007).
(a) ESRF
(b) KFKI Research Institute for Particle and Nuclear Physics, Budapest (Hungary)
(c) Johannes Gutenberg University, Mainz (Germany)
(d) LCC-CNRS Toulouse (France)
(e) Univ. Paul Cézanne, CP2M Marseille (France)
(f) Eötvös Loránd University, Budapest (Hungary)

Hard X-ray induced excited spin state trapping (HAXIESST)

Molecular compounds with switchable electronic states have great potential for information technology in very high-density devices. Systems with the necessary electronic bistability can be found among coordination compounds of transition metal ions. For instance, temperature variation can trigger a redistribution of 3d electrons between t_{2g} and e_g orbitals in compounds with medium ligand-field strength, leading to thermal spin state transition between the low-spin (LS) ground state and the close-lying high-spin (HS) state. A number of these spin-crossover complexes were also found to exhibit light-induced spin-state switching phenomena at temperatures far below their transition temperature. The photo-induced excited HS state often displays a very long lifetime at low temperatures (vide infra). The phenomenon of populating this metastable low-temperature HS state by irradiation with visible light was called light-induced excited spin-state trapping (LIESST) [1]. The switching of such compounds proceeds through excited

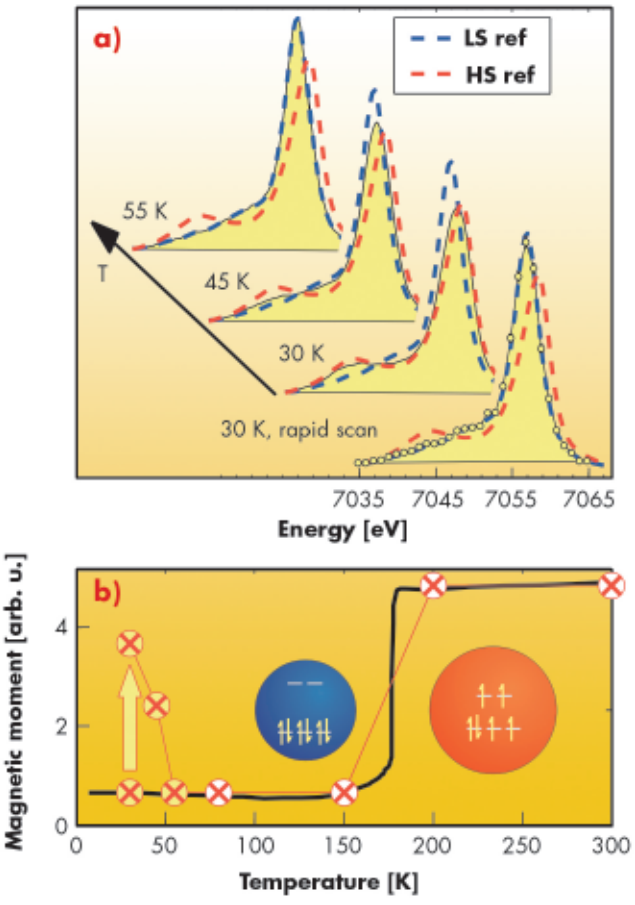

Fig. 15: a) Low-temperature Kβ spectra of $[Fe(phen)_2(NCS)_2]$. Reference HS/LS spectra, taken at 80 and 295 K, respectively, are shown as red/blue dashed curves for each spectrum. b) X-ray data (circles with symbol X) compared to conventional magnetisation measurements (solid line). The distribution of the six 3d electrons on the t_{2g} and e_g levels in the different spin states is depicted in blue (LS) and red (HS) circles.

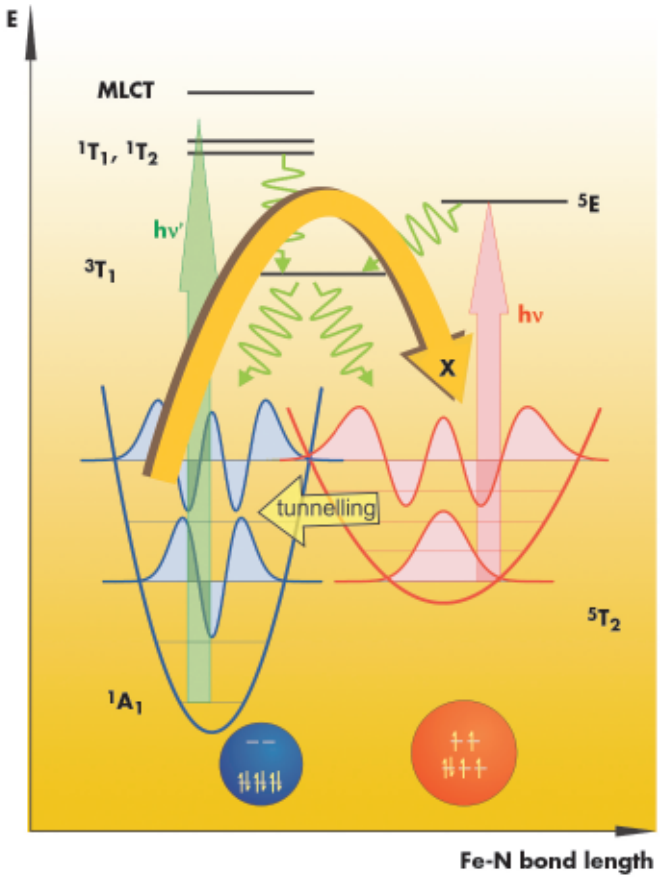

Fig. 16: Schematical electronic structure of $[Fe(phen)_2(NCS)_2]$. Vertical arrows indicate optical transitions (ligand field or metal to ligand charge transfer exitations (MCLT)), green curly arrows show rapid intersystem crossings. (Back-switching with red light, not discussed in the text, is also indicated.) The curved golden arrow symbolises the observed X-ray switching. Relaxation (tunnelling) is determined by the overlap of the vibrational wavefunctions.

states; the excitation and relaxation mechanisms are determined by the strongly-coupled electron, magnetic, and structural dynamics. Light excitation has proven extremely valuable in the study of such processes. However, investigation of alternative switching mechanisms can offer further insight into the related electron structure and dynamics.

Recently, we reported studies on different molecular compounds of transition metals, and showed that X-ray emission spectroscopy (XES) can probe the 3d spin momentum quantitatively [2]. The investigated systems included the spin-crossover complex $[Fe(phen)_2(NCS)_2]$, which has a $3d^6$ central ion. This compound shows a $^1A_{1g}$ ($t_{2g}^6e_g^0$, LS) to $^5T_{2g}$ ($t_{2g}^4e_g^2$, HS) transition around 180 K, which we monitored with Kβ XES. However, further measurements carried out at **ID26** revealed an anomalous behaviour below 55 K, as shown in **Figure 15**. While a rapid scan at 30 K still reflects the LS ground state, a second, longer scan shows that the majority of the sample (72%) has transformed to the metastable HS state in the beam after several minutes of exposure. Systematically, upon increasing the temperature, a lower X-ray induced metastable HS fraction is observed: 42% is measured at 45 K, and it completely disappears at 55 K. The observed temperature dependence is fully reversible and reproducible, which excludes artefacts due to a local heating or decomposition caused by the X-ray beam.

Observations of an anomalous metastable HS state in $[Fe(phen)_2(NCS)_2]$ upon irradiation with green light and below 50 K were interpreted as LIESST [1]. Excited spin-state trapping emerges because the decay of the excited HS state is impeded at low temperatures. The non-adiabatic multiphonon relaxation, which could bring the system back to the LS ground state, is hindered below 50 K as the relevant vibrational modes are inactive; this leads to a very small tunnelling rate (typically 10^{-6} s^{-1}) [1]. At higher temperatures, where the higher vibrational states of the HS molecules are populated, the relaxation becomes fast due to the larger overlap of the higher vibrational wave functions of the two spin states, as indicated in **Figure 16**. The remarkably similar temperature dependence of the metastable HS population created with light and X-ray irradiation suggest identical underlying relaxation mechanisms. Consequently, we can conclude that we observed hard X-ray induced excited spin state trapping (HAXIESST).

While the low-*T* HS state and its decay conditions are the same in LIESST and HAXIESST, the excitation is obviously very different: visible light can make the necessary ligand-field excitations; however, the energy of hard X-rays is far too high for this. We propose that the spin-state trapping occurs in the relaxation processes that follow electronic excitations caused mostly by secondary electrons. Thus the majority of the complexes experiences only a valence excitation before the probing quantum arrives as the excitation here is made by secondary electrons originating from a remote ionisation.

References
[1] A. Hauser, *Top. Curr. Chem.* **234,** 155 (2004), and references therein.
[2] G. Vankó, T. Neisius, G. Molnár, F. Renz, S. Kárpáti, A. Shukla, F.M.F. de Groot, *J. Phys. Chem. B* **110,** 11647 (2006).

This result is of the utmost importance for the community, which has to be aware of the non-innocent nature of low-temperature hard X-ray investigations, where spectroscopy or diffraction experiments might lead to excitations similar to visible light-induced ones. The HAXIESST effect can be exploited as an alternative excitation source of high efficiency and large penetrating power for dark-coloured samples or non-transparent sample environments.

Principal publication and authors
M. Sikora (a,b), K. Knížek (c), Cz. Kapusta (b), P. Glatzel (a), *J. Appl. Phys* (2008) - *in press.*
(a) ESRF
(b) Faculty of Physics and Applied Computer Science, AGH University of Science and Technology, Cracow (Poland)
(c) Institute of Physics, Czech Academy of Science, Prague (Czech Republic)

Evolution of charge and spin state of transition metals in the $LaMn_{1-x}Co_xO_3$ perovskite series

Transition metal oxides reveal a variety of unusual phenomena, among which the magneto-electronic properties are of great interest because of the potential applications of these materials in spin electronics devices. In particular, the solid solution of $LaMn_{1-x}Co_xO_3$ has attracted a considerable interest due to the occurrence of a ferromagnetic ground state at intermediate *x*, which is in contrast to the behaviour of the end members of the series which are the antiferromagnetic $LaMnO_3$ and the diamagnetic $LaCoO_3$. The effect was originally attributed to the superexchange interaction between Mn^{III} ions, without any magnetic contribution of a low-spin Co^{III} ($t_{2g}^6e_g^0$, S=0). More recently, the strong tendency towards formation of Mn^{IV}+Co^{II} clusters coupled via positive superexchange interaction was suggested and later observed in $LaMn_{0.5}Co_{0.5}O_3$ [1]. For other intermediate compositions both scenarios of charge segregation were discussed: the solution of Co^{III}/Mn^{III} and/or the stable pairs of Mn^{IV}+Co^{II} coexisting with a surplus of Mn^{III} and Co^{III}, generating the magnetic moment from a complex set of oxygen mediated interactions. Among them, the ferromagnetic Mn^{III}-O-Mn^{IV}, Mn^{III}-O-Mn^{III}, Co^{II}-O-Mn^{IV} and antiferromagnetic Mn^{IV}-O-Mn^{IV}, Co^{II}-O-Co^{II}, Mn^{III}-O-Co^{II} are the most likely.

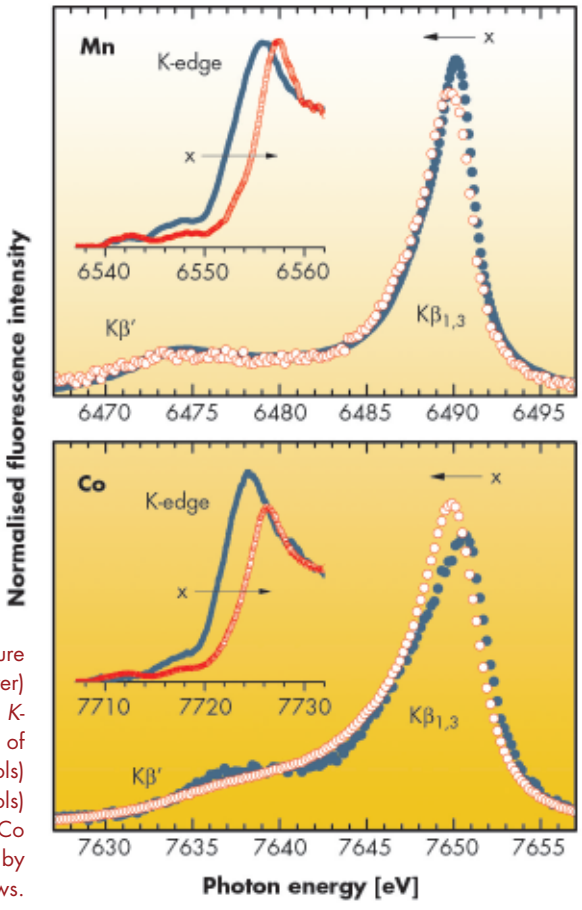

Fig. 17: Room temperature Mn (upper) and Co (lower) high resolution *Kβ* XES and *K*-edge XAS (insets) spectra of $x = 0.02$ (blue, solid symbols) and 0.98 (red, open symbols) compounds. Increasing Co content, *x*, is indicated by arrows.

To determine which of the proposed scenarios dominates the properties of the series, a study of the effective charge and spin state of manganese and cobalt has been carried out at room temperature by means of *K*β emission (XES) and high resolution *K*-edge absorption (XAS) spectroscopy at the **ID26** beamline. *K*-edge XAS probes the density of p-like unoccupied electronic states and exhibits a strong dependence on the effective charge and symmetry of the probed site in transition metal oxides. *K*β emission spectra (3p → 1s decay) probe the localised spin moment of transition metals revealed in a multiplet structure due to

exchange interaction between the 3p hole and the 3d orbitals.

Figure 17 shows examples of the measured spectra for the extreme Mn and Co concentrations. Absorption spectra (insets) reveal a gradual shift of the edge position to higher energy with increasing Co content at both edges, indicating the electron transfer from the Mn to the Co site. The Mn emission spectra reveal the distinct exchange feature (*K*β′) over the entire series indicating a high spin state for Mn irrespective of the average Mn valence state. The Co *K*β spectra also show a gradual shift of the $K\beta_{1,3}$ line to lower energy with increasing Co content while the Kβ′ feature diminishes for the highest Co doping indicating a lowering of spin configuration. This unequivocally proves that the Co spin state changes substantially upon doping.

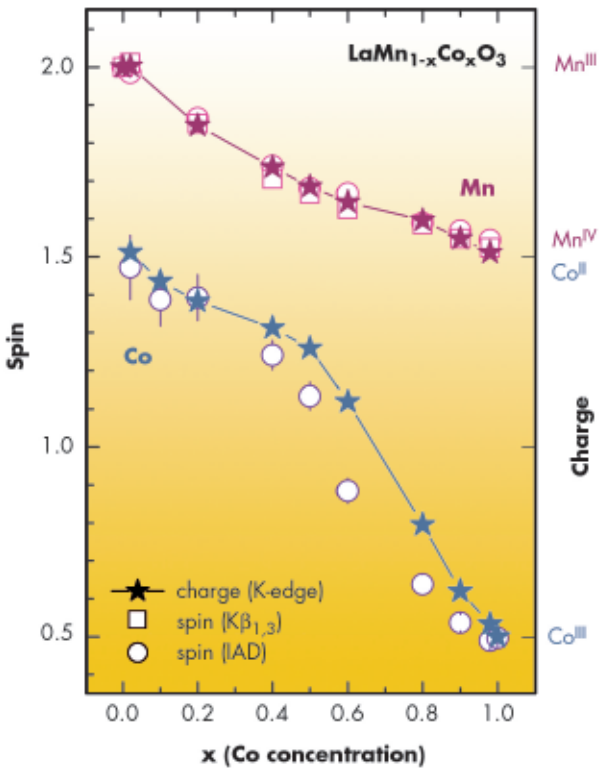

Fig. 18: The evolution of the average spin of Mn and Co ions as determined from XAS (stars and lines) and XES (circles for IAD and squares for first moment).

Assuming a linear dependence between edge position and effective charge, the average spin states were obtained from XAS spectra. The Mn spin was derived within the high-spin only model, while in the case of Co, a gradual variation between the end member configurations was assumed, *i.e.* the change from high spin S=3/2 Co^{II} to mixed spin S=1/2 Co^{III} [2]. These indirect predictions are compared to the values derived from the K*β* XES spectra by means of two techniques: integrals of the absolute values of the difference spectra (IAD) method [2,3] and shift of the first moment of the Mn $K\beta_{1,3}$ line (**Figure 18**).
A perfect correlation of the Mn spin predictions confirms consistency of the methods employed. In the case of Co these two dependences do not agree revealing a considerable difference in the $0.4 < x < 0.9$ region. The effect is attributed to the average Co^{III} spin state lower than the assumed S=1/2 due to a larger admixture of the low spin configuration. A variation of the Co^{III} spin state can plausibly explain anomalies observed in bulk magnetic measurements of the system in the Co rich region. The experimental method presented can be applied to other mixed transition metal systems allowing exploration of the spin and magnetic properties irrespective of the magnetic ordering.

References
[1] J.B. Goodenough *et al.*, *Phys. Rev.* **124**, 373 (1961); G.H. Jonker, *J. Appl. Phys.* **37**, 1424 (1966); R.I. Dass and J.B. Goodenough, *Phys. Rev. B* **67**, 014401 (2003).
[2] G. Vankó *et al.*, *Phys. Rev. B* **73**, 024424 (2006).
[3] J.P. Rueff *et al.*, *Phys. Rev. B* **63**, 132409 (2001).

Intermediate-spin iron in lower mantle silicate perovskite

Spin-pairing transitions of iron were predicted to occur within the Earth's interior nearly 50 years ago, but only in the past few years has direct experimental evidence for such transitions at lower mantle conditions been reported. A high-spin to low-spin transition of Fe^{2+} in (Mg,Fe)O is now well established by both experimental and computational data to occur near 50 GPa at room temperature for lower mantle compositions. However in the Earth's most abundant phase, $(Mg,Fe)(Si,Al)O_3$ perovskite, the picture is not so clear. X-ray emission (XES) and nuclear forward scattering (NFS) data present conflicting results on the location, number and sharpness of the transition(s), and whether

Principal publication and authors
C. McCammon (a), I. Kantor (a), O. Narygina (a), J. Rouquette (a,b), U. Ponkratz (c), I. Sergueev (c), M. Mezouar (c), V. Prakapenka (d), L. Dubrovinsky (a), *Nature*, submitted.
(a) Bayerisches Geoinstitut, Universität Bayreuth (Germany)
(b) now at: Université de Montpellier II, LPMC, Montpellier (France)
(c) ESRF
(d) Center for Advanced Radiation Sources, University of Chicago (USA)

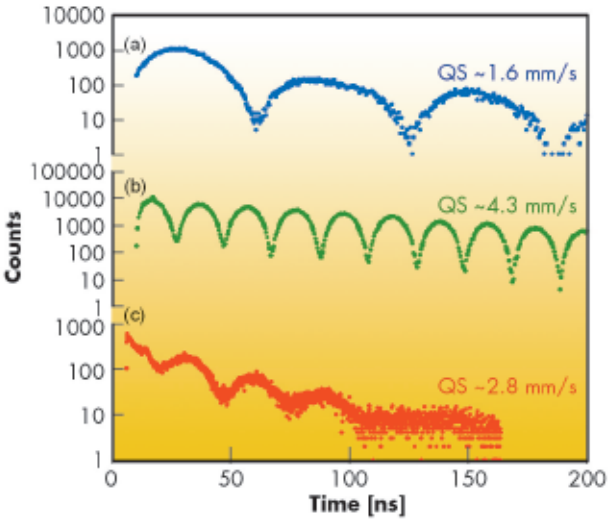

Fig. 19: NFS data of $Mg_{0.88}Fe_{0.12}SiO_3$ perovskite at a) 7 GPa, 290 K; b) 110 GPa, 290 K; c) 62 GPa, ~ 1000 K. At low pressure only high-spin Fe^{2+} is present, characterised by low QS, while intermediate-spin Fe^{2+} is stabilised by high pressure (b,c) and high temperature (c), recognised by high QS. In c) QS is reduced due to the temperature effect, but is still significantly higher than it would be for high-spin Fe^{2+}.

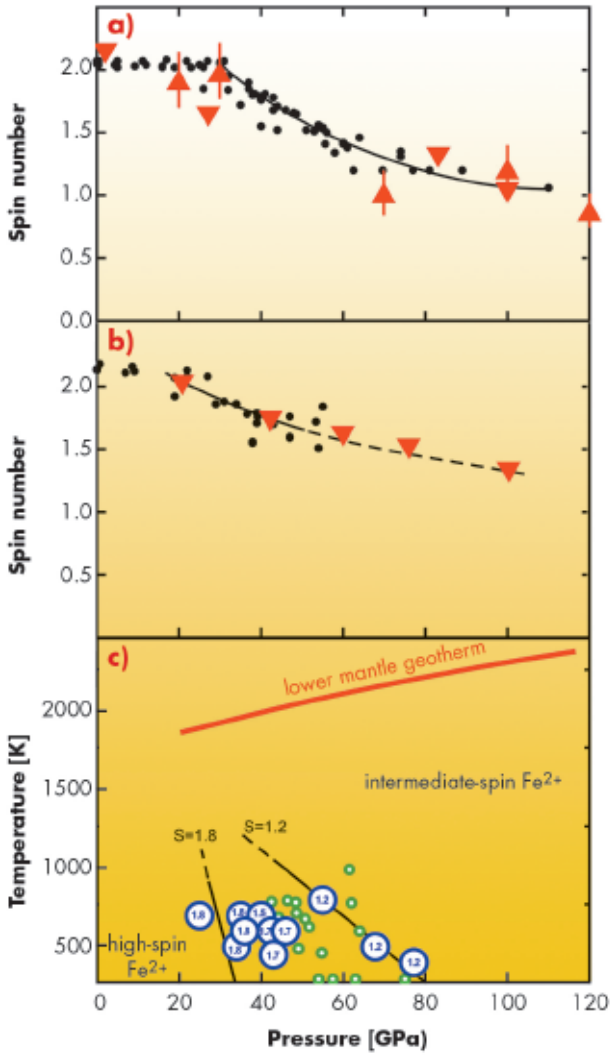

Fig. 20: Effect of pressure on the average spin number of a) $Mg_{0.88}Fe_{0.12}SiO_3$ perovskite and b) $Mg_{0.86}Fe_{0.14}Si_{0.98}Al_{0.02}O_3$ perovskite calculated from room temperature Mössbauer spectra (circles) assuming assignment of the new component to intermediate-spin Fe^{2+}. Previous XES data [1,2] are shown as triangles and inverted triangles, respectively. c) Effect of pressure and temperature on the average spin number of $Mg_{0.88}Fe_{0.12}SiO_3$ perovskite. Blue circles (spin number indicated within) indicate Mössbauer data, while green circles correspond to NFS data, and all spin numbers show a consistent decrease with increasing pressure and temperature. Lines of equal spin number have negative slope, hence along the lower mantle geotherm Fe^{2+} is predicted to be predominantly in the intermediate-spin state.

Fe^{2+} or Fe^{3+} or both are involved [1-4]. To reconcile these observations, we undertook the first high-pressure high-temperature study of iron-containing silicate perovskite using combined Mössbauer, NFS and X-ray diffraction techniques to determine the spin state of iron in the dominant lower mantle phase.

We collected 119 ^{57}Fe Mössbauer and 32 NFS data sets of $Mg_{0.88}Fe_{0.12}SiO_3$ and $Mg_{0.86}Fe_{0.14}Si_{0.98}Al_{0.02}O_3$ perovskite at beamline **ID18**. Experimental conditions included using a resistively-heated diamond-anvil cell at pressures up to 110 GPa and temperatures up to ~ 1000 K, combined with high-resolution X-ray diffraction of several of the same sample loadings. All data show the appearance of a new component above 30 GPa with high quadrupole splitting (QS) whose stability is enhanced with increasing pressure, and *in situ* high-temperature data show that this component is also stabilised by higher temperatures (**Figure 19**). The transition involved in the sudden change of QS is purely electronic, since high-resolution X-ray diffraction data show no change in crystal structure up to 110 GPa. The most likely possibility is a spin transition, and a decrease in spin number with pressure in silicate perovskite was already found using XES [1,2]. Using the relative abundance of components derived from our Mössbauer data to

calculate the spin number as a function of pressure and temperature, we find that a high-spin to intermediate-spin transition of Fe^{2+} agrees well with all XES data (**Figure 20 a** and **20b**). Intermediate-spin Fe^{2+} is also consistent with the high quadrupole splitting and large centre shift of the new component, which was observed in previous NFS data [3,4]. From the observed trend of spin number with temperature, we predict that Fe^{2+} in $(Mg,Fe)(Si,Al)O_3$ perovskite will be predominantly in the intermediate-spin state throughout most of the lower mantle (**Figure 20c**).

Spin transitions affect the electronic structure of Fe^{2+}, which in turn influences lower mantle properties such as radiative and electrical conductivity, rheology and iron partitioning. Much of our knowledge of lower mantle behaviour is based on experiments on quenched samples, yet spin transitions are reversible with respect to both pressure and temperature. The stability of intermediate spin-state Fe^{2+} in lower mantle perovskite is not the first surprising revelation for the Earth's most abundant phase, and based on the implications of spin transitions for lower mantle properties, is probably also not the last.

References

[1] J. Badro *et al.*, *Science* **305**, 383 (2004).

[2] J. Li *et al.*, *Proc. Nat. Acad. Sci.* **101**, 14027 (2004).

[3] J.M. Jackson *et al.*, *Am. Miner.* **90**, 199 (2005).

[4] J. Li *et al.*, *Phys. Chem. Miner.* **33**, 575 (2006).

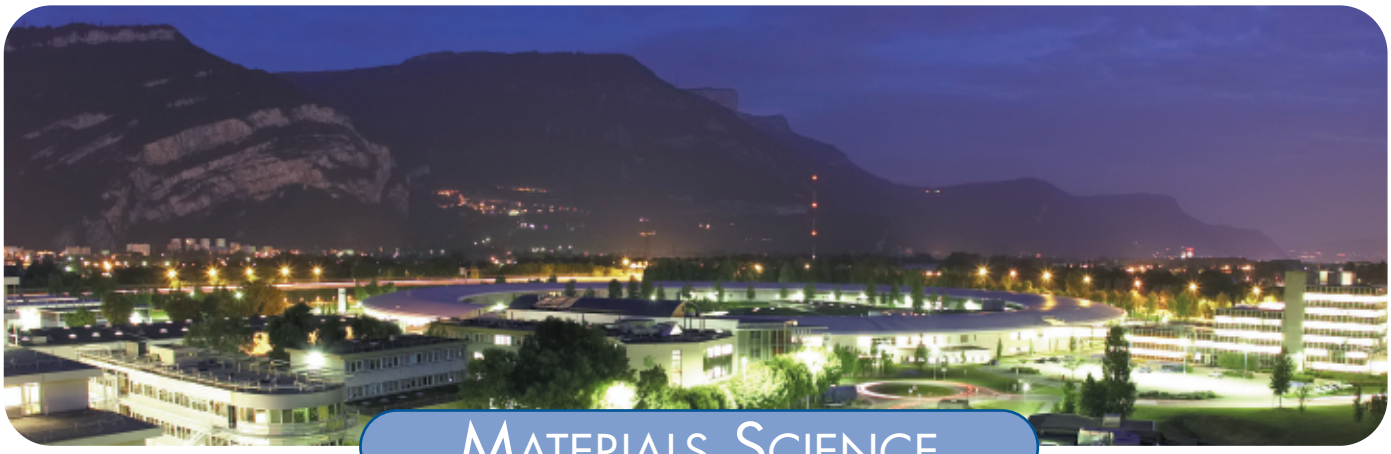

Materials Science

Introduction

Materials science research investigates the fundamental relationships between the structure of materials and their properties. An understanding of how behaviour is linked to structure is a vital consideration in the development of materials with new attributes or improved performance. The examples described in this chapter are drawn from work conducted at both ESRF and CRG beamlines. The predominant technique exploited is diffraction, from which information about a material's atomic structure and its microstructure can be derived. The former describes the arrangement of the atoms that form the basic building blocks of the substance, while the latter portrays the size, shape and aggregation of the grains that make up the bulk. Both are relevant since structural characteristics on all length scales are important in defining materials' properties.

The samples investigated cover a very wide range and include: biological and biosynthesised systems; novel chemical materials with known or potential catalytic properties; pure chemical elements; ceramics; superconductors; metals and alloys. Crystalline and glassy solids, liquids, thin films and a quasicrystalline intermetallic alloy are represented. The hard-energy X-ray beams of ESRF beamlines are particularly well suited to such studies for they provide a combination of penetration through absorbing materials, high flux for fast measurements and high statistical quality, and excellent spatial and angular resolution. These ensure high quality data for the most complex of samples under demanding experimental conditions. Moreover, the newly extended and refurbished ID11 beamline will allow focussing of the X-ray beam to sub-micrometre dimensions for even greater spatial resolution. Other important techniques used to study materials at the ESRF include imaging, *e.g.* of voids, cracks or dislocations, reflectivity from thin films and interfaces, small-angle scattering from samples with structural features on the nanometre scale, absorption spectroscopy, etc.

Studies can be performed under a wide range of conditions, such as high and low temperature, at high pressures, or under extreme conditions when diamond anvil cells are coupled with laser heating. A recently-developed approach involves laser heating and aerodynamic levitation of the sample, thus eliminating any possible chemical reaction between the sample and its container or parasitic scatter from the sample environment. *In situ* measurements allow the detailed evolution of a material's structure to be followed as it is processed or transforms from one form to another, *e.g.* solid to liquid, liquid to glass, etc. With fast multichannel detectors, high time resolution (*e.g.* 50 ms) can be used to follow transformations during rapid changes in temperature or other conditions.

Understanding these processes can be of great practical importance, for example quenching is a fundamental step in the production of glasses. For the fastest time resolution, needed to follow the steps of fundamental chemical processes such as photo-induced cleavage of a chemical

bond, the pulsed nature of the synchrotron source must be exploited by means of the pump-probe approach, which gives time resolution down to 100 ps.

Of academic and practical relevance, the examples chosen are but a small subset of the numerous studies of complex materials performed in the past year. The accounts speak for themselves and illustrate the rich diversity of materials problems investigated at ESRF.

A. Fitch

High-throughput screening of combinatorial materials libraries by high-energy diffraction

Principal publication and authors

D.A. Kukuruznyak (a), H. Reichert (a), J. Okasisnski (a), H. Dosch (a), T. Chikyow (b), J. Daniels (c), V. Honkimäki (c), *Appl. Phys. Lett.* **91**, 071916 (2007).
(a) Max Planck Institute for Metals Research, Stuttgart (Germany)
(b) National Institute for Materials Science, Tsukuba (Japan)
(c) ESRF

Inorganic materials can acquire functional properties such as superconductivity in complex combinations of the components. Discovering useful compositions is difficult and time consuming. Fortunately, recent technological advances help speed up this gold-mining process. Several research groups have begun fabricating complex materials libraries in the form of continuous composition-spread thin films [1]. In order to reach the ultimate goal of producing structure-property maps, the materials science community demands fast high-throughput structural characterisation of the composition spreads [2].

Here we describe scanning transmission high-energy X-ray diffraction (HEXRD) and apply it to a high-throughput structural analysis of the ternary CeO_2–Al_2O_3–HfO_2 composition-spread thin-film materials library, deposited on a single-crystal Si(100) substrate. These oxide insulators exhibit high dielectric constant (high-*k*) and are presently being investigated as prospective gate compounds for MOSFET transistors. A schematic of the spread is shown in the inset of **Figure 21**. The sample consists of three interpenetrating and intermixed stripes of elemental oxides rotated with respect to each other by 120°.

The high-energy X-ray diffraction experiments were performed at beamline **ID15B**. We used transmission geometry instead of conventional reflection geometry. Transmission is achieved by employing a high-energy X-ray beam, E = 89 keV, which penetrates thick samples without substantial absorption and reduction of intensity.

High-energy X-rays produce Ewald spheres with large and almost flat sections in the forward direction in reciprocal space. This allows one to set up diffraction conditions similar to high-resolution transmission electron microscopy, where all the information on the in-plane structure of the film can be retrieved with a single illumination. Unambiguous identification of epitaxial phases then becomes possible. This is accomplished by a 3-dimensional reconstruction of reciprocal space around the origin: the thin-film sample is tilted in the incident beam at fixed X,Y-position,

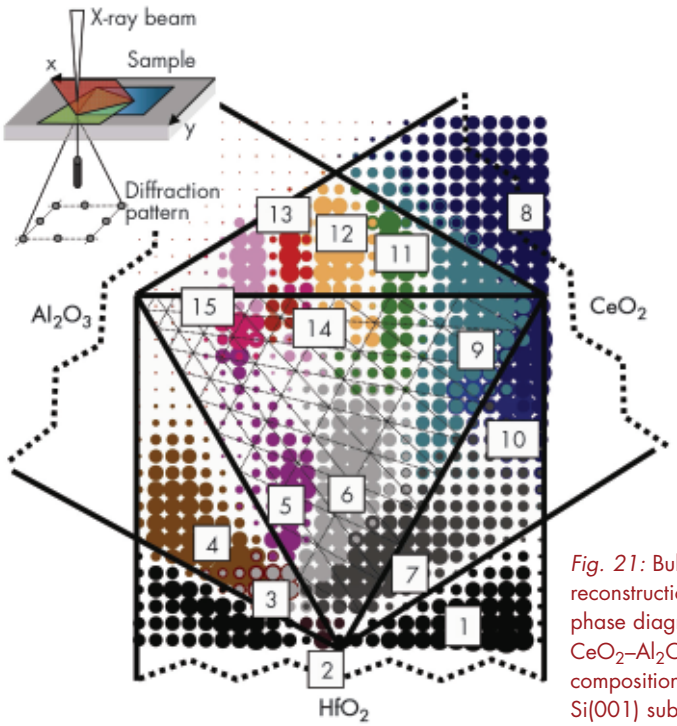

Fig. 21: Bubble plot reconstruction of the crystal phase diagram for the CeO_2–Al_2O_3–HfO_2 composition-spread thin film on Si(001) substrate. Polycrystalline phases: (1) monoclinic HfO_2; (2) cubic $Hf_{0.97}Al_{0.03}O_2$; (3) tetragonal $Al_{0.1}Hf_{0.9}O_{1.95}$; (4) rhombohedral $Hf_3Al_2O_9$; (5) $Hf_7Al_2CeO_{19}$ fluorite; (6) $Hf_6Ce_3AlO_{19}$ distorted fluorite; (7) $Hf_4CeO_{5.5}$ cubic fluorite; (8) cubic CeO_2; (9) tetragonal $Ce_{0.85}Hf_{0.1}Al_{0.05}O_{1.975}$; (10) cubic Ce_3HfO_8; (11) $Ce_8Al_2O_{19}$. Epitaxial phases: (12) $Ce_{1.12}Al_{0.88}O_3$ apatite; (13) hexagonal $Ce_{1.06}Al_{0.94}O_3$; (14) tetragonal $Ce_{0.95}Al_{0.95}Hf_{0.1}O_{3.05}$; (15) cubic $CeAlO_3$ perovskite.

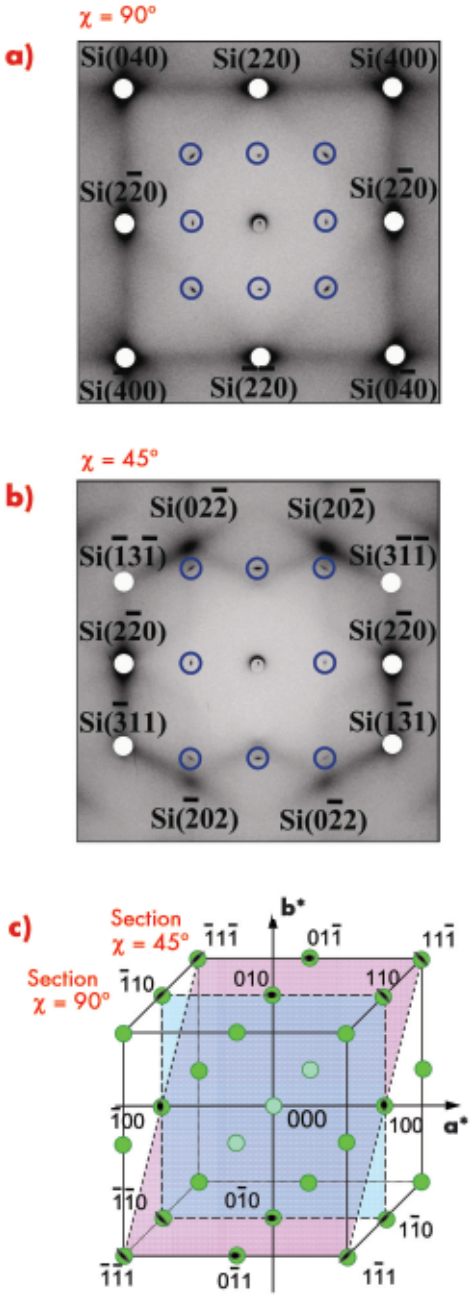

Fig. 22: Diffraction patterns from the epitaxial perovskite phase (a) for normal incidence, and (b) for an incident angle of 45°. The additional signals originate from unsubtracted thermal diffuse X-ray scattering around Si Bragg peaks. (c) Reconstruction of reciprocal space for the epitaxial perovskite.

and additional diffraction images are recorded at every angle.

For combinatorial exploration, the ternary composition spread was scanned in the X and Y directions with the X-ray beam at normal incidence. By analysing the 2-dimensional Laue diffraction patterns the ternary crystal phase diagram was reconstructed as a colour 'bubble plot'. In this plot the size of the solid bubble corresponds to the amount of a particular crystal phase calculated from the integrated diffraction intensity. The reconstruction of the ternary crystal phase diagram for the CeO_2–Al_2O_3–HfO_2 spread is shown in **Figure 21**. Part of the spread around the Al_2O_3 corner contained amorphous compounds hard to discern with X-rays. Corresponding pixels in the phase diagram are shown as empty spaces. In the crystalline part of the spread, we found eleven polycrystalline and four previously unknown epitaxial phases.

By way of example, **Figure 22** shows the diffraction pattern for the compound $CeAlO_3$ at incident angles of 0° and 45°. For this particular phase, other tilt angles contained no diffraction signals from the epitaxial thin film. The figure also illustrates the reconstruction of reciprocal space indicating an epitaxial phase with a cubic perovskite crystal structure and lattice parameter a = 3.87 Å.

In summary, we have demonstrated that focused synchrotron radiation with high-energy X-rays is the most adequate probe for producing structural maps for multicomponent materials libraries. It provides fast characterisation in a single measurement, high compositional/spatial resolution, and high throughput. In addition, it has unique advantages that substantially facilitate positive identification of epitaxial phases. Complete phase maps can be constructed after initial screening at a fixed X-ray beam incident angle. After the identification of epitaxial areas on the composition-spread thin film, a small number of additional measurements with the sample tilted in the incident beam allow a full crystallographic characterisation of the epitaxial structure by entirely reconstructing reciprocal space.

References
[1] H. Koinuma, I. Takeuchi, *Nature Materials* **3**, 429 (2004).
[2] Ji-Cheng Zhao, *Prog. Mat. Sci.* **51**, 557 (2006).

Void formation in Nb_3Sn superconductors

Principal publication and authors
C. Scheuerlein (a), M. Di Michiel (b), A. Haibel (c), *Appl. Phys. Lett.* **90**, 132510 (2007).
(a) European Organization for Nuclear Research (CERN), Geneva (Switzerland)
(b) ESRF
(c) Hahn-Meitner Institut Berlin (HMI) (Germany)

The formation of voids during the reaction heat treatment of Nb_3Sn superconductors degrades their microstructural homogeneity and increases the strain sensitivity of the critical superconducting properties. The void formation mechanisms and possible remedies to limit void growth remain subjects of debate.

Previous studies of void growth in Nb_3Sn strands have used destructive metallographic techniques. Since the void shape and distribution within Nb_3Sn strands are strongly irregular, metallographic results about void formation are erratic and can be misleading. In contrast, by using synchrotron microtomography, a quantitative description of void volume, shape and distribution can be obtained. Owing to the short acquisition time of less than a minute per tomogram, tomography experiments during *in situ* heat treatments are routinely performed at beamline **ID15A** [1].

Here we report combined synchrotron microtomography and diffraction measurements during *in situ* heating cycles that have been performed at ID15A in order to reveal the void growth mechanisms in Nb_3Sn strands of the internal tin (IT) design. Synchrotron microtomography was performed using a high intensity filtered white X-ray beam. For the diffraction measurements in transmission geometry, an 88.005 keV monochromatic X-ray beam with a bandwidth of 0.1 keV was used. Debye-Scherrer diffraction patterns were acquired with a MAR 345 image-plate detector. *In situ* heating was performed using a dedicated furnace built by ID15 that enables accurate sample temperature control during the tomographic and diffraction experiments.

In **Figure 23** the voids that are formed at different temperatures in the diffusion centres of the Nb_3Sn strand are shown. The tomograms were acquired during an *in situ* heat treatment with a ramp rate of 60°C h^{-1}, with three isothermal holding steps for 2 h at 200°C, 5 h at 340°C and 2 h at 540°C. Above 160°C the growth of globular voids is observed and the average shape factor (calculated from the ratio of void volume to void surface area) increases with increasing temperature. At 390°C the maximum total void volume is obtained (7.5×10^{-3} mm^3, corresponding to 1.1% of the analysed strand volume). A strong reduction of total void volume from 5.7×10^6 to 2.5×10^6 μm^3 occurs in the temperature interval 510 to 530°C. During the isothermal 540°C heating, the number of the relatively small interfilament voids increases strongly.

After the acquisition of each tomogram a diffraction pattern was acquired for phase analysis. The 110 diffraction patterns obtained during the heat treatment are summarised in **Figure 24a**.

During the first stage of the heat treatment up to 540°C five phase transformations

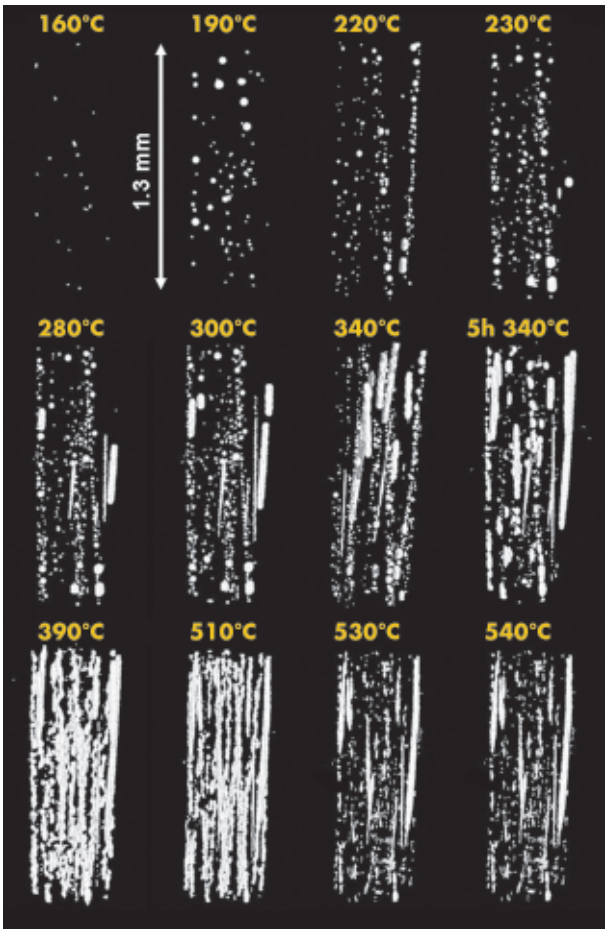

Fig. 23: Voids inside the IT Nb_3Sn strand acquired at different temperatures during the *in situ* heat treatment.

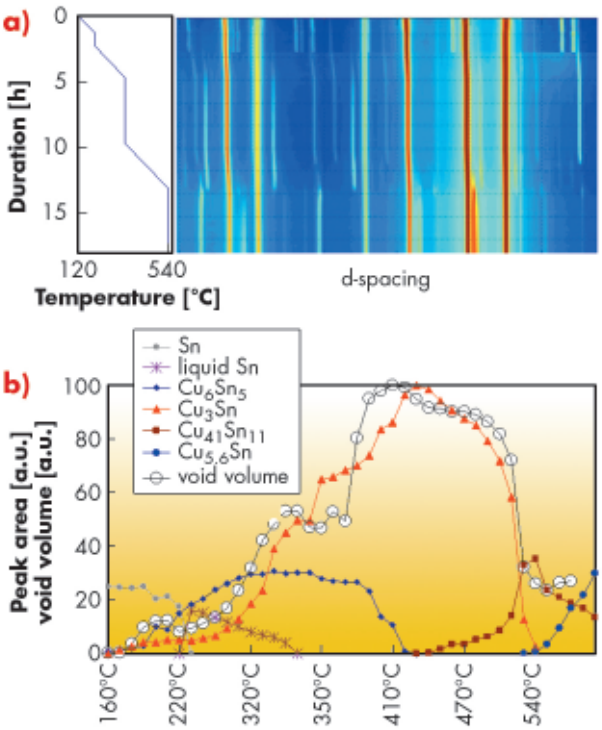

Fig. 24: a) Variation of the diffraction patterns of the Nb_3Sn strand during the heat treatment cycle between 120°C and 540°C. b) Diffraction peak areas of all Sn-containing phases, apart from α-bronze, that exist in the IT Nb_3Sn strand during the reaction heat treatment up to 540°C. For comparison the total void volume is also plotted. Void volume is clearly correlated with the Cu_3Sn content in the strand.

References
[1] M. Di Michiel, J.M. Merino, D. Fernandez-Carreiras, T. Buslaps, V. Honkimäki, P. Falus, T. Martins, O. Svensson, *Rev. Sci. Instrum.* **76**, 043702 (2005).

are detected. At first pure Sn and Cu are transformed into Cu_6Sn_5 and Cu_3Sn by solid state diffusion. At around 230°C the remaining Sn melts. Liquid Sn is present in the strand until 340°C and at 430°C nearly all Sn in the strand is transformed into Cu_3Sn. The Cu_3Sn reflections vanish in the temperature region 500 to 540°C and simultaneously a strong reduction in void volume occurs. $Cu_{41}Sn_{11}$ starts to form above 430°C. During the isothermal 540°C heat treatment, $Cu_{5.6}Sn$ peaks grow until the formation of Nb_3Sn starts at about 580°C (Nb_3Sn growth results are not shown in **Figure 24**).

Combining the microtomography and the diffraction results, three different void-growth mechanisms in IT Nb_3Sn superconductors can be deduced. The growth of the globular voids up to a temperature of about 200°C is driven by a gain in free energy through a reduction of the total void surface area when smaller voids agglomerate to larger globular voids. The main void volume increase is caused by density changes during the formation of Cu_3Sn (the Cu_3Sn density exceeds the density of stoichiometric Sn and Cu by 4%). Therefore, the maximum void volume is obtained when Sn is almost entirely transformed into Cu_3Sn. The void growth caused by density changes is partly reversible when Cu-Sn intermetallics are transformed into the lower density α-bronze. The relatively small interfilament voids that grow at the Cu-Sn intermetallic/α-bronze interface during the isothermal 540°C heat treatment and at higher temperatures are Kirkendall voids.

Principal publication and authors
H. Reichert (a), M. Denk (a), J. Okasinski (a), V. Honkimäki (b), H. Dosch (a,c), *Phys. Rev. Lett.* **98**, 116101 (2007).
(a) Max Planck Institute for Metals Research, Stuttgart (Germany)
(b) ESRF
(c) Institut für Theoretische und Angewandte Physik, Universität Stuttgart (Germany)

Giant metal compression at liquid-solid (Pb-Si, In-Si) Schottky junctions

Metal-semiconductor junctions -known as Schottky contacts- form the basis of the earliest man-made hybrid interface structures. The electronic structure across the Schottky contact exhibits a characteristic band deformation at the semiconductor side of the interface. It is generally accepted that no specific change in the electronic structure should be induced on the metal side of the interface, since the high-density Fermi liquid limits all electronic screening effects within the metal to a rather small interfacial layer given by the screening length in the metal, which is of the order of 1Å.

The effect of a solid wall onto the structure of the adjacent liquid has been investigated by theory in great detail, predicting a liquid density oscillation normal to the wall with a period and decay length which are governed by the bulk nearest neighbour distance d and the bulk liquid correlation length ξ, respectively. The experimental observation of this packing phenomenon for simple liquids is challenging and has been successful only for a very small number of systems. Here we consider liquid metals in contact with a single crystalline semiconductor surface, where we

investigated the electron density profile across the interface by X-ray reflectivity.

High energy X-ray reflectivity measurements from a variety of solid-liquid Schottky interfaces have been taken at the high energy beamline **ID15A** using the HEMD instrument for surface and interface diffraction. The energy of the microfocused X-ray beam was typically 71 keV allowing the beam to penetrate the 20 mm long sample from the Si side of the interface at almost normal incidence. In this way only the metal-semiconductor interface is illuminated, where the incoming X-ray beam is then internally reflected. All samples have been prepared and kept in a specially designed UHV chamber during the experiments.

In a first experiment the X-ray reflectivity at the interface Pb(liq.)-Si(100) was measured (see **Figure 25**). The reflectivity exhibits pronounced oscillations pointing to the existence of density anomalies at this interface, which were found to be temperature-independent. The X-ray reflectivity could be reproduced assuming a giant densification of the liquid Pb adjacent to the interface. In order to check the conjecture that the giant densification of liquid metallic Pb in contact with Si(100) is a generic phenomenon, several control experiments were carried out, measuring X-ray reflectivity profiles from the liquid indium in contact with Si(100), liquid Pb in contact with Si(111), and liquid indium in contact with insulating Al_2O_3 (see **Figure 25**).

A simple two-layer model for the electron density profile across the interface was sufficient to reproduce the generic features of the reflectivity curves (lines in **Figure 25**). The corresponding electron density profiles are summarised in **Figure 26**. All metal-semiconductor interfaces are characterised by a large density increase at the interface followed by a layer with depleted density before reaching the bulk density of the liquid metal. The observation that all metal-semiconductor interfaces display similar features while the metal-insulator interface In-Al_2O_3(001) does not display any anomalies, suggests that charge transfer might be the origin for the interfacial density anomalies.

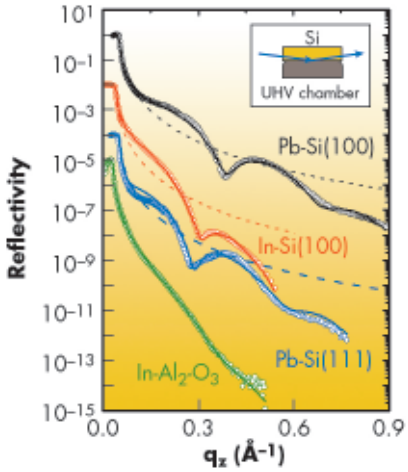

Fig. 25: High energy X-ray reflectivities of different metal-semiconductor interfaces. For comparison, the reflectivity of a metal-insulator interface, In-Al_2O_3(001), is shown. The lines are fits using a simple two-layer model for the electron density profile across the interface. The data are shifted vertically for clarity.

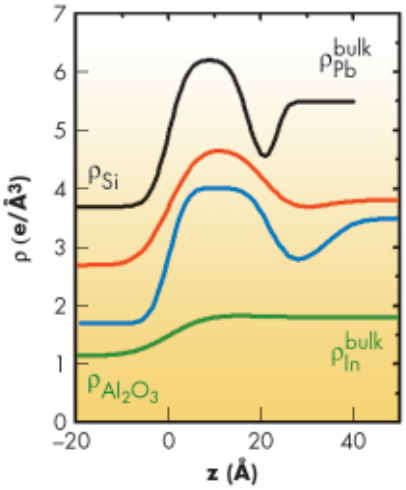

Fig. 26: Electron density profiles for the interfaces Pb-Si(100), In-Si(100), Pb Si(111), and In-Al_2O_3(001). Oscillatory density anomalies are found only at the metal-semiconductor interfaces. The profiles are shifted by a constant offset for clarity.

Our experiments present a new interfacial phenomenon which emerges at liquid Pb/Si and liquid In/Si interfaces. Rather straightforward high energy X-ray reflectivity measurements exhibit very unusual intensity oscillations which can only be understood assuming a giant densification of the liquid metal adjacent to the semiconductor. The densification of more than 30% points to a charge transfer phenomenon between the metal and the semiconductor leading to a shrinkage of the ionic radius of the metal ions. The thickness of this densified layer is around 1.5-2 nm and thus beyond the screening length in metals.

Principal publication and authors
E. Jimenez-Melero (a), N.H. van Dijk (a), L. Zhao (a), J. Sietsma (a), S.E. Offerman (a), J.P. Wright (b), S. van der Zwaag (a), *Scripta Mater.*, **56**, 421-424 (2007).
(a) Delft University of Technology (The Netherlands)
(b) ESRF

Monitoring metastable grains in steel

Novel metallic materials of increasing complexity are being developed in order to meet current demanding mechanical requirements. An intelligent combination of multiple phases with different mechanical characteristics can lead to a significant improvement of the mechanical response of the material [1]. Furthermore, the presence of a soft metastable phase in these complex multiphase microstructures, which can transform into a hard stable phase, opens the door to advanced materials with an extraordinary combination of strength and formability. Despite the beneficial effects of metastable phases for the macroscopic mechanical properties, limited knowledge is available on the conditions leading to their transformation. Previous experimental studies have aimed to link the phase fraction, average chemical composition and average grain size of the metastable phases to their stability. However, this average information has proved to be insufficient to tailor the stability for improved mechanical properties.

Our study investigates the stability of the metastable austenite phase present in the complex ferritic microstructure of low-alloy TRIP (Transformation Induced Plasticity) steels. In these high-strength materials, the outstanding elongation-strength combination stems mainly from the transformation of the soft metastable austenite phase into a hard martensite phase under applied stress [2]. Rather than studying the transformation as a function of stress, the equivalent transformation of the individual micrometre-sized austenite grains as a function of temperature was studied *in situ* by making use of the high-energy (80 keV) X-ray microbeam available at beamline **ID11**. **Figure 27a** displays the two-dimensional diffraction pattern of TRIP steel at room temperature. Each diffraction spot contains information on an individual grain within the material. The metastable austenite grains become unstable while cooling the sample from room temperature down to 100 K, owing to an increase in the chemical driving force for the transformation. The transformation behaviour of the individual austenite grains is assessed *in situ* by following the corresponding diffraction spot on the detector. In **Figure 27b** a single austenite diffraction spot is considered in detail. As shown in **Figure 27c**, this spot has vanished after cooling the sample to 100 K, indicating that the corresponding grain has transformed into martensite during cooling.

We have studied seventy individual austenite grains during the cooling of the TRIP-steel sample. The intensity of each diffraction spot is directly proportional to the volume of the grain from which it originates. Moreover, the lattice parameter of each individual grain, and hence the carbon content of that specific grain, is derived from the position of the corresponding diffraction spot. We have observed three forms of transformation behaviour for the austenite grains (**Figure 28**). Most grains transform

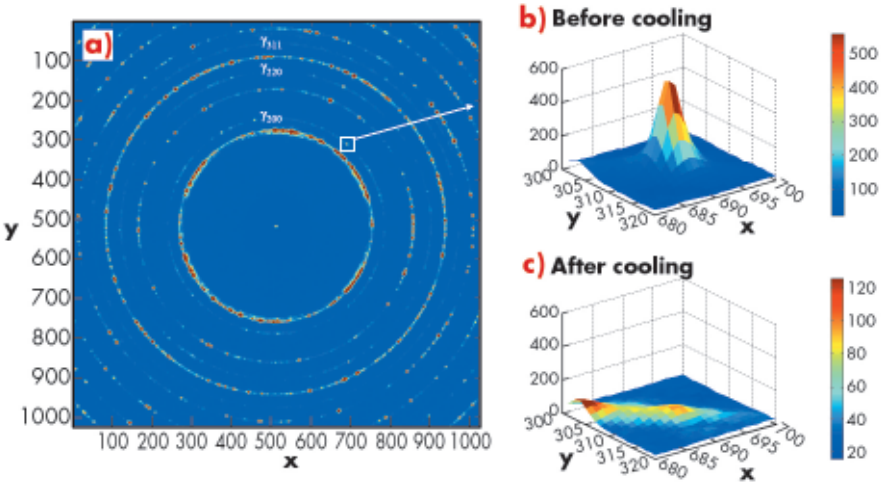

Fig. 27: X-ray diffraction pattern of TRIP steel. (a) The pattern at room temperature shows both ferrite and austenite reflections on separate diffraction rings. Single spots originating from individual grains appear within the austenite diffraction rings denoted in the figure as γ_{200}, γ_{220} and γ_{311}, respectively. (b) A single austenite diffraction peak at room temperature before cooling. (c) The same region as in (b) after cooling the sample to 100 K and heating back to room temperature.

completely into martensite in a single temperature step. However, a few grains show an incomplete or two-step transformation. Finally, a significant number of grains do not show any transformation down to 100 K. The occurrence of the martensitic transformation of the austenite grains at different temperatures reveals a stability distribution within the austenite phase. It is therefore clear that previously performed research on average characteristics is insufficient for optimal control of the material. The carbon content is found to be the dominant parameter that governs the stability of the large austenite grains. However, our results show that the stability of the austenite grains increases for decreasing grain volumes below 20 μm³.

These experiments provide the first *in situ* information about the phase transformation of individual metastable grains present in modern metallic materials of great complexity. The results reveal that the grain volume plays a key role in the stability of the grains when approaching the boundary between the micrometre and submicrometre scales.

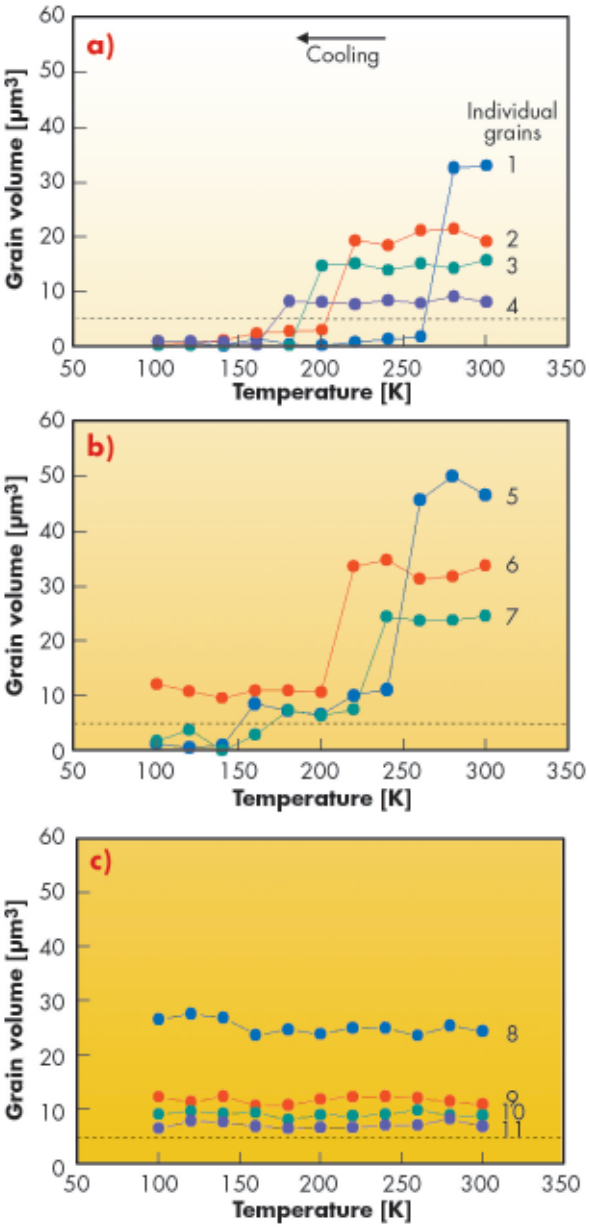

Fig. 28: Observed transformation behaviour of individual austenite grains. (a) Grains that completely transform into martensite in a single temperature step. (b) Grains that partly transform into martensite. For some of these grains, a second transformation is observed at lower temperatures. (c) Grains that remain stable during cooling to 100 K.

References
[1] G.B. Olson, *Science*, **277**, 1237-1242 (1997).
[2] P. Jacques, Q. Furnémont, A. Mertens, F. Delannay, *Phil. Mag. A*, **81**, 1789-1812 (2001).

Time-resolved structural study of the glass transition in glass forming liquids

Authors and principal publication
A. Bytchkov (a), L. Hennet (b), I. Pozdnyakova (b), D. Zanghi (b), D.L. Price (b), F. Kargl (c), N. Greaves (c), S. Jahn (d).
(a) ESRF
(b) CRMHT, Orléans (France)
(c) University of Wales, Aberystwyth (UK)
(d) GFZ, Telegrafenberg, Potsdam (Germany)

Although the phenomena of supercooling and glass transition have been the subject of considerable study over the past ten years, understanding glass formation is still a challenge in condensed matter physics. It is therefore important to develop experimental techniques capable of probing the evolution of glass structure during the cooling from the liquid state to room temperature.

Aerodynamic levitation combined with laser heating has proved to be a powerful and versatile technique for studying the structure and dynamics of refractory oxide liquids [1,2]. In particular, this method eliminates the problems of sample-container interactions and contamination and it makes it possible to obtain the rapid quench necessary for glass formation.

Time-resolved structural studies during the glass transition require fast X-ray diffraction (XRD) measurements since the process occurs within a few seconds. Therefore, an aerodynamic levitation setup has been designed and installed at

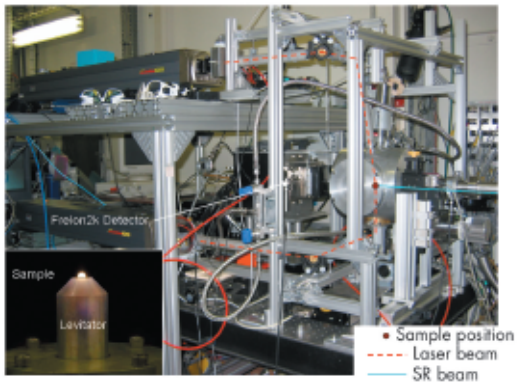

Fig. 29: Aerodynamic levitation experimental setup at ID11.

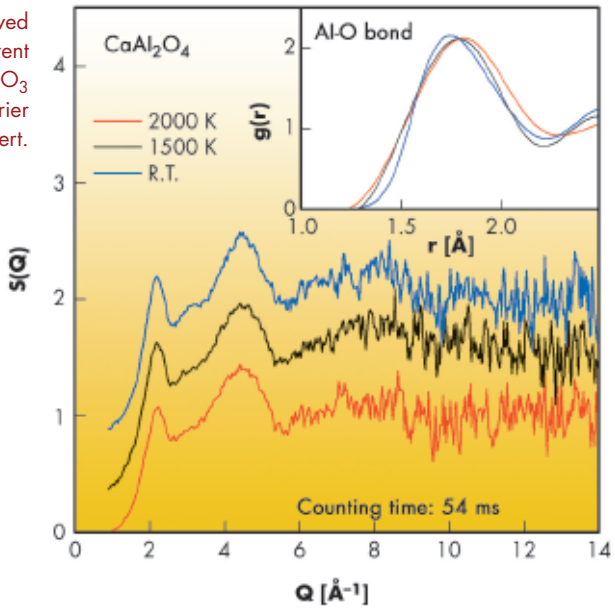

Fig. 30: Time-resolved measurements at different temperatures for $CaO\text{-}Al_2O_3$ with their respective Fourier transforms in the insert.

the **ID11** beamline where time-resolved diffraction measurements were performed using the ESRF Frelon detector.

The experimental setup is shown in **Figure 29**. Spherical samples with diameters between 2.5 and 3 mm were aerodynamically levitated using an argon/oxygen gas jet and melted with two CO_2 lasers heating the sample from the top and from the bottom in order to have a homogeneous temperature. The laser beams are focused onto the sample using several spherical copper mirrors. The temperature is measured using an optical pyrometer. A 10 x 10 cm^2 high-resolution fast CCD detector was placed close to the levitation chamber. Time-resolved X-ray measurements require short counting times with good statistics over a wide range of scattering vector *Q*. For the experiment we used high energy monochromatic X-rays (80 keV), giving a maximal *Q* value of about 19 Å^{-1}. The high-temperature setup is controlled remotely with a computer and synchronised with diffraction measurements.

We studied the structural evolution of the liquid glass former $CaAl_2O_4$ as it cooled from the stable liquid phase well above the melting point Tm (1878 K) to the cold glass below Tg (1173 K). Fast diffraction measurements were carried out with counting times of 54 ms. **Figure 30** shows the structure factors measured at three temperatures: in the stable liquid, in the supercooled state, and in the glass at room temperature. The inset presents the corresponding pair distribution functions *g(r)* calculated using the Fourier transform of S(Q).

The evolution is characterised by a sharpening of the first sharp diffraction peak and a shortening of the average nearest-neighbour bond length at about 1467 K, indicating an increase in the degree of both intermediate-range and short-range order. This transformation occurs close to the crossover temperature (~1.2 T_g).

This work shows that the combination of aerodynamic levitation and laser heating with fast XRD is a powerful technique for obtaining reliable structural information during glass formation.

References
[1] L. Hennet, D. Thiaudière, M. Gailhanou, C. Landron, J.P. Coutures, D.L. Price, *Rev. Sci. Instrum.* **73**, 124 (2002).
[2] I. Pozdnyakova, L. Hennet, J.-F. Brun, D. Zanghi, S. Brassamin, V. Cristiglio, D.L. Price, F. Albergamo, A. Bytchkov, S. Jahn, M.-L.Saboungi, *J. Chem. Phys.* **126**, 114505 (2007).

Studying a catalyst while it grows

Principal publication and authors
A.M. Beale (a), A.M.J. van der Eerden (a), S.D.M. Jacques (b), O. Leynaud (b), M.G. O'Brien (b), F. Meneau (c), S. Nikitenko (c), W. Bras (c) and B.M. Weckhuysen (a)
(a) Inorganic Chemistry and Catalysis, University of Utrecht (The Netherlands)
(b) UCL London (UK)
(c) DUBBLE Beamline, ESRF

Zeolites are a family of tectosilicates that contain porous channels up to about 2 nm in size. These channels confer on zeolites properties such as molecular sieving and shape-selective catalysis, which have been widely exploited by the chemical industry. Controlling the outcome of the chemical synthesis, through an understanding of the formation and growth mechanisms, has therefore become one of the primary goals of the zeolite synthesis scientific community over the past 50 years. The rational design of such materials aims to improve their catalytic performance, amongst other things. A very powerful but

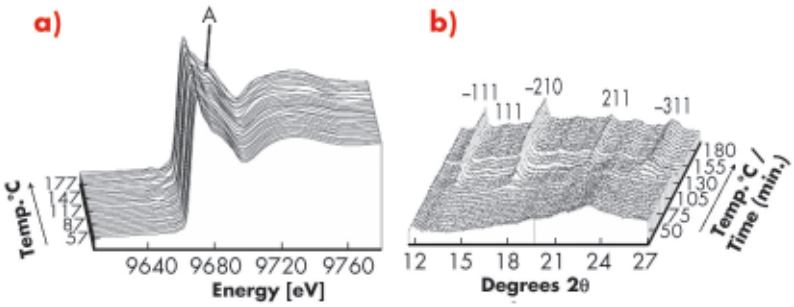

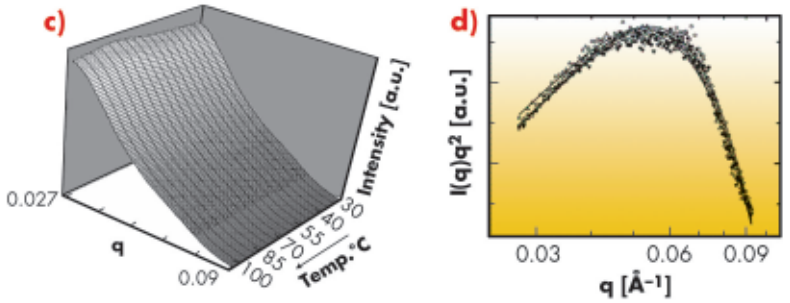

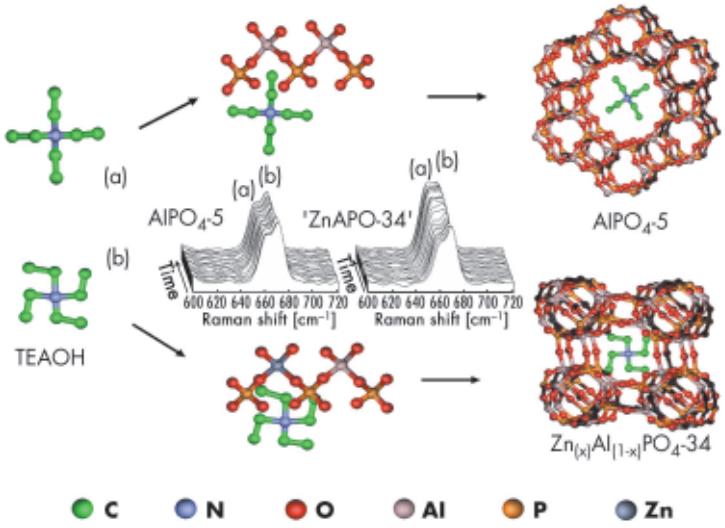

Fig. 31: (a) *In situ* Zn K-edge XANES with arrow marking the multiple scattering feature at ~ 9.685 keV; (b) WAXS with reflections indexed to ZnAlPO-34; (c) raw SAXS data; (d) $I(q)*q^2$-log(q) plots (Kratky type plot) from the SAXS data collected during crystallisation.

relatively unexplored way of probing the processes involved in zeolite synthesis is to perform *in situ* studies during crystallisation. This is particularly powerful when complementary *in situ* measurements are performed using either a variety of techniques or when multiple techniques are combined into one setup.

Recently we have developed a setup that combines small-angle X-ray scattering (SAXS), wide-angle X-ray scattering (WAXS) and X-ray absorption spectroscopy (XAS) and have used it to study the crystallisation processes leading to the formation of a zinc aluminophosphate zeotype (ZnAlPO-34) at **BM26**, the DUBBLE beamline. This combination of techniques allowed us to follow the changes that occur with time at the molecular, nanoscopic and crystalline level, with a time resolution in the order of a few minutes and represents, to the best of our knowledge, the first data of its kind acquired in such a manner, **Figure 31**.

Growth of the zeolite occurred via a two-step aggregation/crystallisation process. The similarity of the average aggregate size measured by SAXS (*ca.* 12.3 nm) and WAXS (also *ca.* 12 nm) suggested that size retention occurs during crystallisation, implying that either critically-sized aggregates form in the gel structure or else a sort of amorphous-to-crystalline transition leads to the formation of a ZnAlPO-34 material. The growth of this crystalline phase began in preference to the AlPO-5 (AFI) structure despite the synthesis gel and conditions being typical to those used previously for AFI formation. Further measurements using *in situ* Raman spectroscopy demonstrated that an important interaction between the Zn^{2+} ions present and the tetraethylammonium hydroxide (TEAOH) template occurred. Changes in the Raman spectra were accompanied by the formation of a –34 type framework over the commonly occurring –5 type and hinted that such an interaction is critical for the formation of the –34 type structure, **Figure 32**. Zn^{2+} ions therefore appear to act as both nucleating agents and exert some structure-directing effect for the formation of the ZnAlPO-34 (CHA) phase. Clearly this setup is capable of providing a lot of congruent, simultaneous information in one experiment making it a new and powerful tool for studying crystallisation processes of molecular sieves. Futhermore, its application need not be restricted to this field alone since it could also provide information on the assembly processes of other crystalline and nano-structured materials.

Fig. 32: Schematic diagram detailing the formation of microporous aluminophosphate types –5 and –34. The stacked Raman data in the middle suggest that TEAOH forms an intermediate complex with the aluminophosphate units and, depending on the nature of the TEAOH conformer (a or b), leads to either $AlPO_4$-5 or ZnAPO-34 formation.

References

[1] A.M. Beale, A.M.J. van der Eerden, S.D.M. Jacques, O. Leynaud, M.G. O'Brien, F. Meneau, S. Nikitenko, W. Bras, B.M. Weckhuysen, *J. Am. Chem. Soc.* **128**, 12386 (2006).

[2] M.G. O'Brien, A.M. Beale, C.R.A. Catlow, B.M. Weckhuysen, *J. Am. Chem. Soc.* **128**, 11744 (2006).

Principal publication and authors
A. Dewaele (a), M. Mezouar (b), N. Guignot (b,c) and P. Loubeyre (a), *Phys. Rev. B* **73**, 144106 (2007).
(a) CEA, Bruyères le Châtel (France)
(b) ESRF
(c) Synchrotron Soleil (France)

Melting of lead under high pressure using second-scale time-resolved X-ray diffraction

The phase diagram of an element reflects the evolution of its chemical bonds, through the phases adopted under different pressure and temperature conditions. The high pressure and high temperature phase diagrams of the elements are only partially known, despite their importance for fundamental condensed matter physics and their implication for planetary physics [1]. For example, knowing the melting point of iron at 329 GPa would lead to prediction of the temperature at the Earth's inner core boundary, which would help to establish a reliable thermal model of the deep Earth [2].

For most of the elements, the sequence of phase changes by ambient temperature compression has been observed up to at least 100 GPa. First-order phase changes have also been inferred from the analysis of shock compression data, but only along the Hugoniot curve of each element. Although the laser-heated diamond-anvil cell technique allows extreme conditions (~ 200 GPa and 5000 K [2]) to be reached, *in situ* crystallographic measurements have only rarely been carried out under these conditions. For instance, the usual diagnostic for melting is based on the observation of changes in the optical properties of the laser-heated sample's surface [2,3]. Surprisingly, the melting curve measured using this method is lower than the melting points measured by shock compression for several elements, such as lead [4].

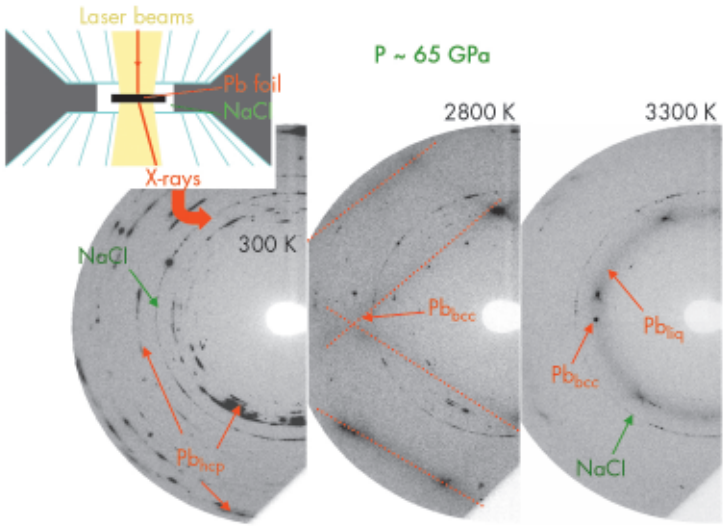

Fig. 33: Three monochromatic diffraction patterns recorded upon temperature increase at P ≈ 65 GPa. The signal from the lead foil can be clearly distinguished: it first transforms from a hexagonal closed packed (hcp) to a body centered cubid (bcc) solid phase and then melts at ~3300 K. The NaCl pressure-transmitting medium remains solid.

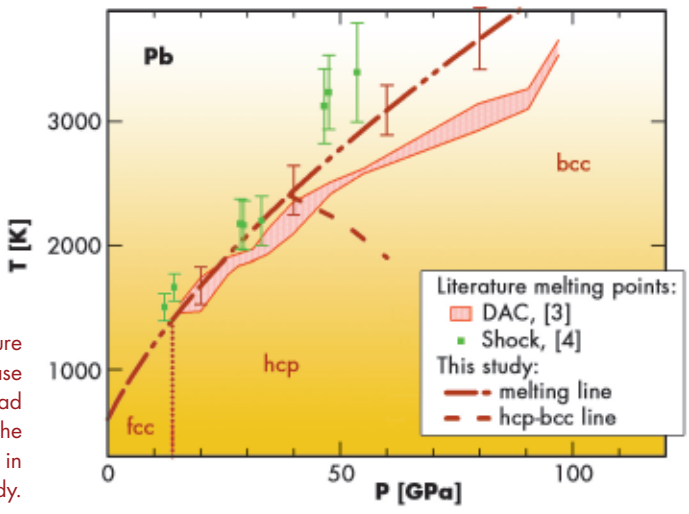

Fig. 34: High pressure high temperature phase diagram of lead established in the literature [3,4] and in the present study.

We have developed a technique for the determination of high pressure and high temperature phase diagrams, based on the coupling of laser-heated diamond-anvil cell and short timescale X-ray diffraction. Using this technique, we have unambiguously detected the melting of lead, up to 80 GPa and 3700 K, by recording the X-ray pattern characteristic of a liquid sample (**Figure 33**). We observed that melting has a lifetime that can be as low as 1 s, which corresponds to the timescale of the diffraction technique used here. This explains why numerous previous trials to detect melting by X-ray diffraction with a timescale of ~30 s have been unsuccessful. This melting criterion is objective, which is a large improvement over the "classical" diagnosis of melting.

The melting curve of lead obtained in this study lies significantly above the melting curve measured using "classical"

diagnostic measurements [3] (**Figure 34**). It is in agreement with the melting points obtained by shock-wave compression [4]. We have also been able to locate the hcp-bcc-liquid triple point and the hcp-bcc transition line for solid lead. Fast and reliable, the technique used in this work opens a new avenue in the study of high pressure and high temperature phase diagrams.

References
[1] E.Y. Tonkov and E.G. Ponyatovsky, *Phase transformations of elements under high pressure*, CRC Press, London, (2005).
[2] R. Boehler, *Nature*, **363**, 534 (1993).
[3] B.K. Godwal, C. Meade, R. Jeanloz, A. Garcia, A.Y. Liu, M.L. Cohen, *Science*, **248**, 462 (1990).
[4] D. Partouche-Sebban, J.L. Pélissier, F.G. Abeyta, W.W. Anderson, M.E. Byers, D. Dennis-Koller, J.S. Esparza, R.S. Hixson, D.B. Holtkamp, B.J. Jensen, J.C. King, P.A. Rigg, P. Rodriguez, D.L. Shampine, J.B. Stone, and D.T. Westley, S.D. Borror and C.A. Kruschwitz, *J. Appl. Phys.* **97**, 043521 (2005).

Phosphorous becomes six-fold-coordinated by oxygen under high pressure

Principal publication and authors
J. Pellicer-Porres (a), A.M. Saitta (b), A. Polian (b), J.P. Itié (c) and M. Hanfland (d), *Nature Materials* **6**, 698-702 (2007).
(a) ICMUV, Universidad de Valencia, Burjassot (Spain) + Malta Consolider Team.
(b) Physique des Milieux Denses, IMPMC, CNRS, Université Pierre et Marie Curie -Paris 6 (France)
(c) Synchrotron SOLEIL, Gif-sur-Yvette (France)
(d) ESRF

Aluminium phosphate is a quartz analogue that gives its name to a family of oxides called berlinites, which are characterised by spirals of tetrahedra like those of silica, but where Si is alternatively replaced by Al and P. The high-pressure behaviour of quartz-like materials has been the subject of many studies in the past because, apart from their intrinsic interest, their high-pressure behaviour can help towards understanding polymorphism in silica. Previous Raman and XRD measurements showed that the high-pressure phase of $AlPO_4$ might be a poorly crystallised solid with lattice parameters corresponding to the $InPO_4$ structure. The stability of this structure has been confirmed through *ab initio* calculations, although a discrepancy remained between the calculated and measured lattice parameters. In the $InPO_4$ structure, the aluminium atoms are octahedrally bonded, whereas the phosphorus atoms remain in their tetrahedral coordination scheme.

At higher pressure, a denser structure is expected for berlinite, where both cations would be in an octahedral environment, as happens in $GaAsO_4$ or $AlAsO_4$. However, to the best of our knowledge, a pressure-induced change in coordination from 4 to 6 for a compound containing phosphorus has never been reported before.

We have performed angle-dispersive X-ray diffraction experiments up to the 100 GPa range at beamline **ID09A**. The laser heating technique was used at some of the pressure points to increase the kinetics of the transformation and also to improve the quality of the spectra. The experimental findings are supported and complemented by *ab initio* calculations.

Figure 35 shows the experimental spectra. At 13.3 GPa new peaks not belonging to the berlinite phase appear, which become more evident at 15.6 GPa. At this point we annealed the sample with the laser heating system.

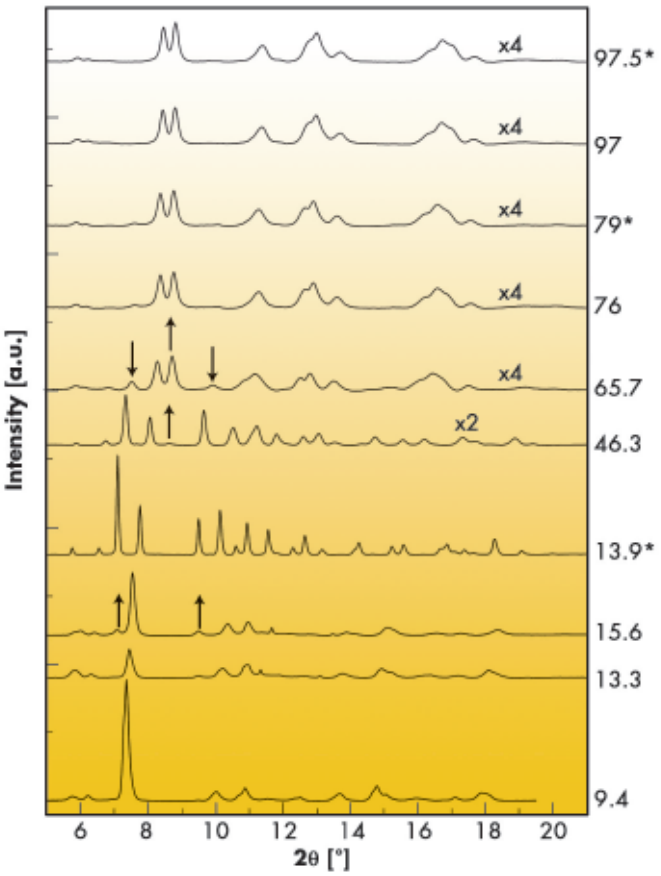

Fig. 35: X-ray diffraction spectra under high pressure.

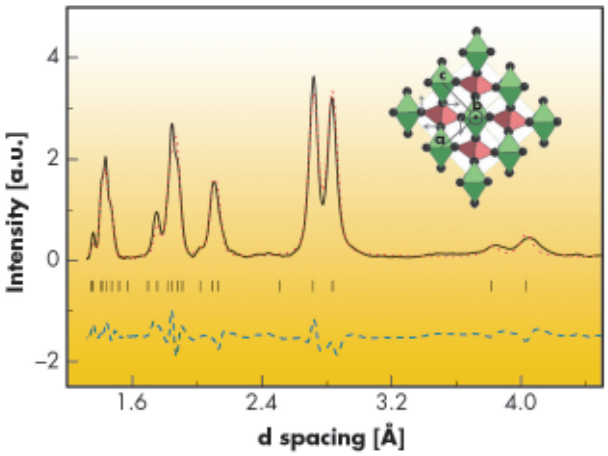

Fig. 36: Rietveld refinement of the spectrum acquired at 97.5 GPa with a m-$CaCl_2$ model. Inset: m-$CaCl_2$ sketch. Green and red polyhedra are centred around Al and P atoms, respectively.

As the spectrum shows, this produced a complete transition. The indexing supports an $InPO_4$ type phase, which is confirmed by the Rietveld refinement.

The $InPO_4$ phase is stable up to 46.3 GPa. Between 46 and 66 GPa, $AlPO_4$ transforms in a continuous way. At 76 GPa, most of the sample has adopted a new structure. Further pressure increase or laser heating has little impact on the spectra up to 97.5 GPa, the maximum pressure studied. At 97.5 GPa, the diffraction peaks can be indexed with a monoclinic cell. The indexing shows a striking similarity to that of orthorhombic $CaCl_2$ silica. This similitude is translated to the equation of state. The Rietveld refinement is presented in **Figure 36**. We conclude that after the second phase transition $AlPO_4$ adopts a monoclinic distorted $CaCl_2$ structure (m-$CaCl_2$), which is sketched in the inset of **Figure 36**. The *ab initio* computations support the experimental findings, as they show that the m-$CaCl_2$ phase is stable with respect to the $InPO_4$ phase from 31.5 GPa up, and also yield very close internal parameters and equations of state. The main structural novelty induced by the phase transition is the increment in phosphorus coordination from 4 to 6.

The observed phase-transition sequence can be discussed in the context of previous studies, which shed light on the complex phase diagram of SiO_2. According to these studies, high-pressure-induced densification is accompanied in a first step by the formation of a (distorted) hexagonal sublattice of oxygen atoms. In a second step, the smaller silicon cations redistribute in the interstices. In $AlPO_4$ we observe a similar pattern and add the possibility, as in other berlinites, of a pressure-delayed change in coordination of the two cations. The hexagonal compact array of oxygens (ABC, slightly distorted) is already present in the $InPO_4$ phase. Al occupies octahedral interstices but P is still in tetrahedral interstices. AlO_6 octahedra form edge-sharing rows connected by PO_4 tetrahedra. In the m-$CaCl_2$ phase the oxygen stacking changes to ABAB... and P atoms modify their site and attain the octahedral configuration. Both cations now define non-kinked edge-sharing octahedral rows, connected by vertices.

Finally, the finding of phosphorous octahedrally coordinated by oxygen may open new routes in high-pressure phosphorous chemistry. The existence of numerous crustal silicates where Si is six-fold coordinated is well known. In particular, the rutile, hollandite and calcium ferrite structures are formed from edge-sharing chains of silicon octahedra. The observation of the m-$CaCl_2$ structure in $AlPO_4$ and the close relationship of $AlPO_4$ with silica demonstrates the possibility of completely unexplored families of compounds analogous to those of the silicates but based on PO_6.

Molecular springs at the onset of life

How life emerged on Earth remains a mystery to us. Molecules with backbones forming stable double helices held together by Watson-Crick base pairings have an exceptional importance in this saga, in particular because they store genetic information. Many scenarios involve extreme conditions, thus we have undertaken a programme on the behaviour of this particular architecture under high pressure. Our first study was performed on crystals of the octanucleotide d(GGTATACC), where molecules are in the A-DNA form and

pack in infinite super-helices of duplexes down the six-fold axis of the $P6_1$ space group [1]. In addition to Bragg reflections of the A-form crystal, X-ray diffraction images exhibit a diffuse scattering pattern produced by molecules of the B-DNA forms trapped in the central channel of the super-helix [2]. Accordingly, these crystals gave us the opportunity to monitor the behaviour of both A- and B-forms up to 2.0 GPa (about 20000 atmosphere).

High-pressure macromolecular crystallography was pioneered two decades ago [3]. It has now become a fully-fledged method [4] with a broad range of applications. Crystals are hydrostatically compressed at room temperature in a cavity drilled in a metal gasket that is squeezed between the culets of two diamonds. Pressure is monitored using the wavelength shift of the fluorescence emitted by a ruby sphere deposited in the cavity. Diffraction data are collected using a parallel beam of high energy X-rays (33 keV) and a CCD detector. Special diamond-anvil cells were designed, providing a large useful aperture (82°) as well as a broad pressure range, up to about 2.5 GPa. High completeness diffraction data can be generally collected using few samples, even in cases of crystals with anisotropic habit (*e.g.* plate) and/or a low symmetry space group [4].

3D-structures of the A-form crystal at ambient pressure, 0.55, 1.09 and 1.39 GPa were refined at 1.6 Å resolution to R (R_{free})-factors of 15.2 (19.1), 16.9 (20.1), 19.3 (22.7) and 18.8 (22.6) %, respectively.

Figure 37 shows the large axial compression (11% at 1.39 GPa) of the molecule. The average base-pair step varies from 2.92 Å down to 2.73 Å. This spectacular plasticity associates with small changes only in phosphodiester backbone angles to accommodate the denser base stacking. The lengths of vectors C1′-C1′, which quantify the DNA cylinder transversal squeeze, are all identical within their standard deviations, whatever the applied pressure. The geometry of Watson-Crick base pairings remains essentially invariant in the pressure domain up to 1.39 GPa.

The broad meridional streaks produced by B-DNA octamers occluded within the channels of the crystalline A-form matrix were observed up to at least 2.0 GPa, as shown in **Figure 38**. The period of B-DNA stacking decreases from 3.40 to 3.10 Å in the range from ambient pressure to 2.0 GPa.

The remarkable adaptation of d(GGTATACC) to high pressure is clearly associated with the base-paired double-helix topology of the molecule, by which it behaves as a molecular spring.

Principal publication and authors

E. Girard (a,g), T. Prangé (b), A.-C. Dhaussy (c), E. Migianu-Griffoni (d), M. Lecouvey (d), J.-C. Chervin (e), M. Mezouar (f), R. Kahn (g), R. Fourme (a), *Nucl. Acids Res.*, **35**(14), 4800-4808 (2007).

(a) Synchrotron-SOLEIL, Saint-Aubin (France)
(b) UMR 8015 CNRS, Paris (France)
(c) CRISMAT, ENSICAEN, Caen (France)
(d) UMR CNRS 7033, Bobigny (France)
(e) IMPMC, Paris (France)
(f) ESRF
(g) IBS, UMR 5075 CEA-CNRS-UJF-PSB, Grenoble (France)

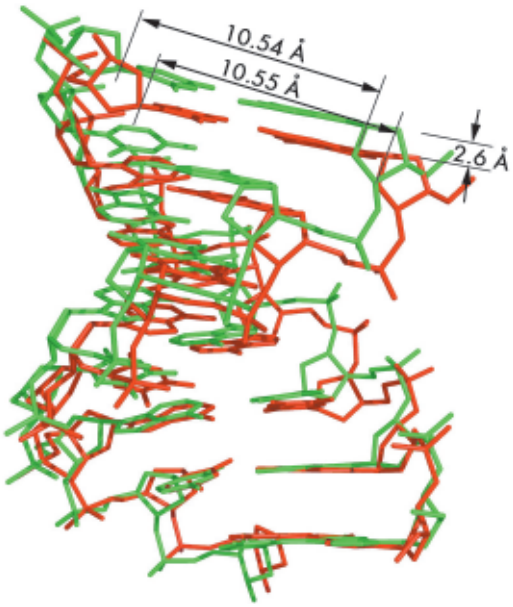

Fig. 37: Superimposition of the A-DNA duplex at ambient pressure (green) and 1.39 GPa (red). The full-duplex length reduces from 23.5 Å at ambient pressure to 20.9 Å at 1.39 GPa.

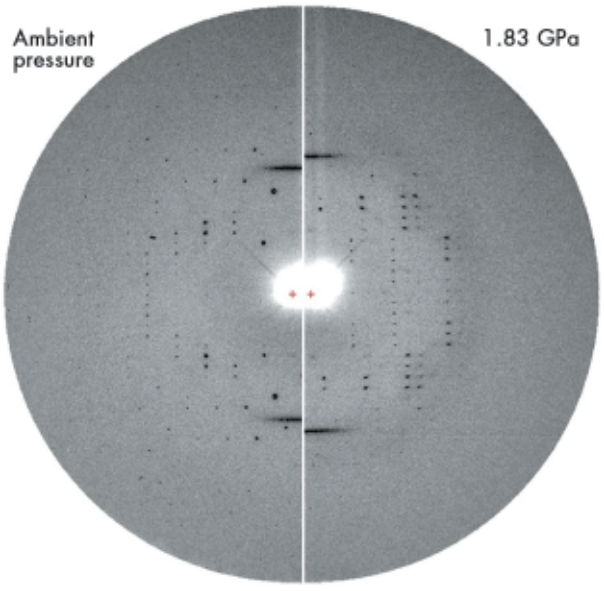

Fig. 38: Fibre diagram of B-DNA superimposed on the diffraction pattern of A-DNA crystal at ambient pressure (left) and 1.83 GPa (right). At 1.83 GPa, the two B-DNA meridian reflections still persist over the degrading A-DNA diffraction pattern. The fibre pattern is still observed at 2 GPa (Reproduced with permission from *Nucl. Acids Res.*, **35**(14), 4800-4808 (2007)).

References
[1] O. Kennard, W.B.T. Cruse, J. Nachman, T. Prangé, Z. Shakked, D. Rabinovitch, *J. Biol. Molec. Struct. and Dynamics*, **3**, 623-647 (1986).
[2] J. Doucet, J.P. Benoît, W.B.T. Cruse, T. Prangé, O. Kennard, *Nature*, **337**, 190-193 (1989).
[3] C.E. Kundrot, F.M. Richards, *J. Mol. Biol.*, **193**, 157-170 (1987).
[4] E. Girard, A.-C.Dhaussy, B. Couzinet, J.-C., Chervin, M. Mezouar, R. Kahn, I. Ascone, R. Fourme, *J. Appl. Cryst.*, **40**, 912-918 (2007).

These properties are probably shared by molecules featuring a similar topology, with sugar-phosphate or polypeptide backbones. Some of these molecules have catalytic properties and can store genetic information. Such architectures could withstand not only pressure in the deepest sea trenches but also much higher pressures found in Earth's interior or in the context of rare events such as the impact of a meteorite. We suggest that this remarkable adaptation to harsh conditions may have played a significant role in the selection process during the first steps of the emergence of life on Earth.

Principal publications and authors
Q.Y. Kong (a), M. Wulff (a), J.H. Lee (b), S. Bratos (c), H. Ihee (b), *J. Amer. Chem. Soc.* **129,** 13584 (2007).
(a) ESRF
(b) KAIST, Daejeon (Republic of Korea)
(c) Université Pierre et Marie Curie, Paris (France)

Ultrafast diffraction captures a complex photo-dissociation process for CBr_4 in solution

The photochemistry of bromine-containing molecules is important for the composition of the atmosphere. When exposed to UV light from the sun, they can decay into free Br atoms which may react with ozone (O_3) leading to a reduction in the ozone layer which protects living organisms from excessive solar UV exposure. Carbon tetrahalides such as CBr_4 are found in the atmosphere and they constitute an important source of reactive halogens. Their photochemistry in the gas and condensed phase has therefore become an area of active investigation [1].

Studies of the photodissociation of tetrabromomethane by time-resolved optical and X-ray absorption spectroscopy have led to contradictory results in the past. None gave a complete and satisfactory description. Therefore the photochemistry of CBr_4 in solution was investigated by time-resolved X-ray diffraction. This method offers the advantage that the scattered X-rays probe all interatomic distances in the sample, implying that all reaction intermediates are probed to within the experimental resolution. This is in stark contrast to optical spectroscopy where excited states might be optically silent, *i.e.* they would escape detection. Hence time-resolved X-ray diffraction offers an overall view of all intermediates. The laser pump X-ray

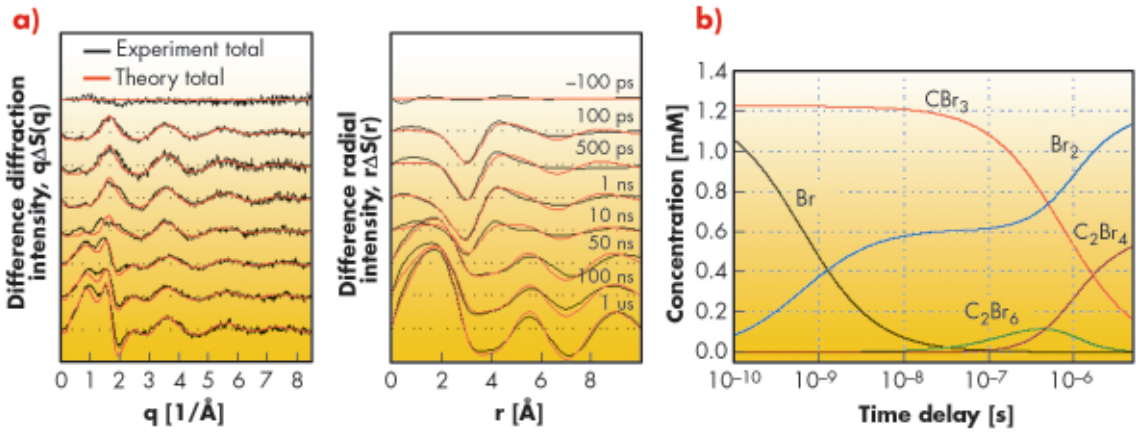

Fig. 39: Time-resolved difference diffraction signal of CBr_4 in methanol as a function of time delays. (a) Difference diffraction intensities, $q\Delta S(q)$ and difference radial distribution curves, $r\Delta S(r)$ at selected time delays. Least-squares fits to a theoretical model are also shown (red curves). (b) Population changes of various molecular species in the photodissociation reaction of CBr_4 in methanol: the CBr_3 (red) and Br (black) radicals, the intermediate C_2Br_6 (olive), and the final products Br_2 (blue) and C_2Br_4 (wine) as a function of time delay.

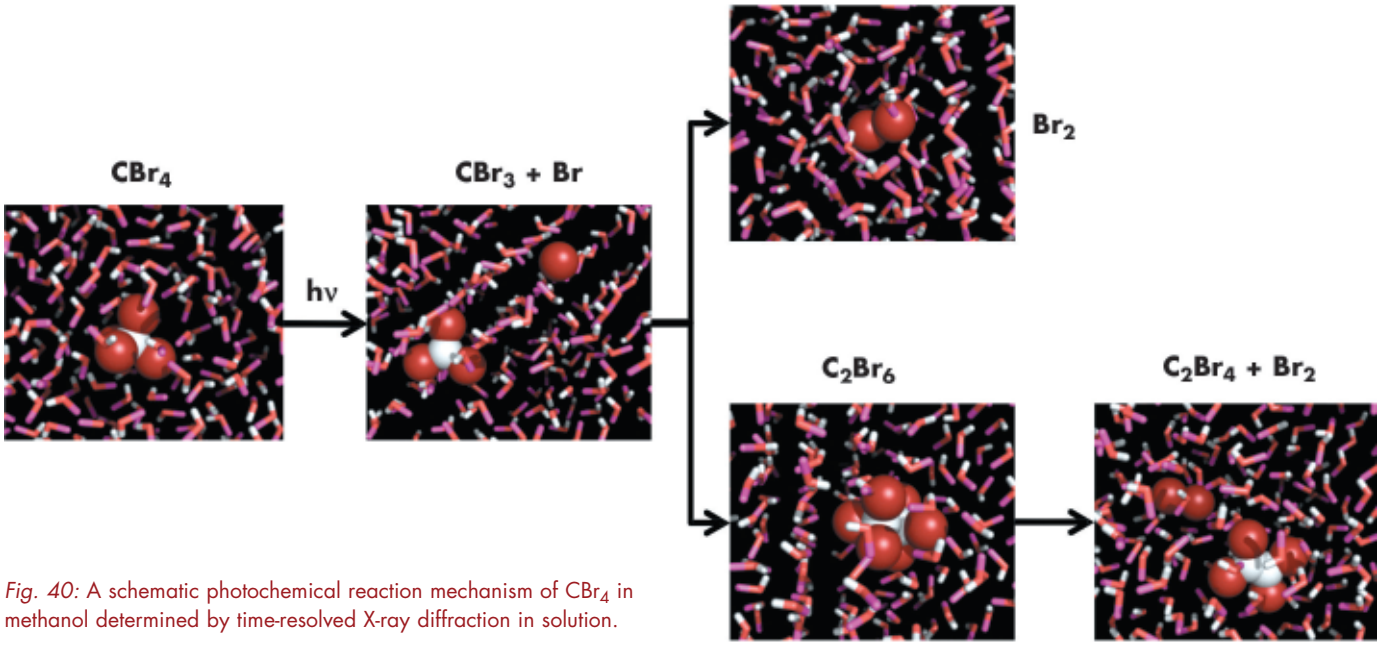

Fig. 40: A schematic photochemical reaction mechanism of CBr_4 in methanol determined by time-resolved X-ray diffraction in solution.

probe setup on **ID09TR** allowed us to follow the structure and composition of the photochemical pathway of the excited CBr_4 molecules in solution. The dissociation is triggered by the absorption of an ultraviolet 266 nm laser pulse (2 ps) which excites and breaks one of the four C-Br bonds and the ensuing structures are probed by a delayed 100 ps X-ray pulse. The experiment used a flowing sample and the pump-probe sequence was repeated at 986.3 Hz while the diffracted signal was accumulated on a MarCCD detector [2]. The difference diffraction signal of CBr_4 in methanol at various time delays (**Figure 39a**) contains the dynamics of the reaction intermediates as a function of time.

By modelling the measured diffraction intensities $\Delta S(q, t)$ with putative density functional theory (DFT) structures, modelled in solution by Molecular Dynamics(MD), the concentration of the actual reaction intermediates can be determined (**Figure 39b**). The results show that the CBr_3 and Br concentrations are dominant during the early stages, indicating the rupture of the C-Br bond in CBr_4 by the UV excitation. The Br radical decays rapidly into Br_2 by non-geminate recombination. The main reaction of CBr_3 is to leave the solvation cage and to pair up with another CBr_3 to form C_2Br_6. The C_2Br_6 intermediate is not stable and dissociates in microseconds to Br_2 and a new species, C_2Br_4, as the final products. At longer time delays, the stable bromine and C_2Br_4 molecules become the dominant species. Br_2 is formed through non-geminate recombination of Br at early time delays, whereas later, it is also formed from dissociation of C_2Br_6.

In conclusion, time-resolved X-ray diffraction has captured the complicated photodissociation pathways of tetrabromomethane in methanol over times ranging from 100 ps to 5 μs. X-ray diffraction offers the important advantage that the structure of short-lived and stable molecules are determined in one experiment: CBr_3, Br, C_2Br_6, C_2Br_4 and Br_2 and the associated rate constants connecting the complex reaction pathways were determined to ~ 1 pm spatial resolution and ~100 ps time resolution (**Figure 40**). Our experiment and analysis show that Br_2 can be released from the photolysis of tetrabromomethane in the liquid phase indicating that polybromomethanes are potentially important sources of active bromine that destroys ozone in the atmosphere.

References

[1] R. Vogt, P.J. Crutzen and R. Sander, *Nature* **383,** 327 (1996).
[2] H. Ihee, M. Lorenc, T.K. Kim, Q.Y. Kong, M. Cammarata, J.H. Lee, S. Bratos, M. Wulff, *Science* **309,** 1223 (2005).

Authors
B.Chazallon (a), C. Bourry (b), J.L. Charlou (b), J.P. Donval (b), M. Brunelli (c), C. Focsa (a)
(a) PhLAM, UMR CNRS 8523, FR-CNRS 2416, University Lille 1 (France).
(b) Géochimie et Métallogénie, Géosciences Marines, IFREMER Brest (France)
(c) ESRF

Acknowledgements
We thank the companies TOTAL and IFREMER for co-funding and gas hydrates collection during the joint projects ZAIANGO and NERIS II. Technical support from the ESRF is greatly appreciated.

Natural gas hydrates investigated by X-ray synchrotron diffraction

Gas-hydrates (clathrates) are crystalline inclusion compounds that occur naturally on Earth, where suitable conditions of high pressure and low temperature prevail. These conditions are encountered in marine sediments mainly offshore along continental margins, and to a lesser extent in polar regions (permafrost). Methane is present in huge amounts in these hydrates, estimated to 10000 Gt, which exceeds by far the other known fossil energy sources of coal, oil and gas. They will be of major economic interest in the future once techniques for their safe extraction are established. Consequently, natural gas hydrates continue to attract increasing attention from the gas industry because of their potential as an energy resource. In contrast to their potential benefits to mankind, their role has been repeatedly quoted in geological hazards, or global climate change. Different scenarios explain the possible role of hydrates in past and future global climate change because of the potentially enormous greenhouse feedback effect of released methane. Information about their occurrence in natural environments is of prime importance in order to establish relationships between climate change and gas hydrates, to elucidate the mechanism of gas hydrates' involvement in geo-hazards or to exploit the natural gas from hydrates profitably. This supposes a knowledge of how gas hydrates exists in the natural environment, their structural type, composition, their stability fields (p-T) etc.

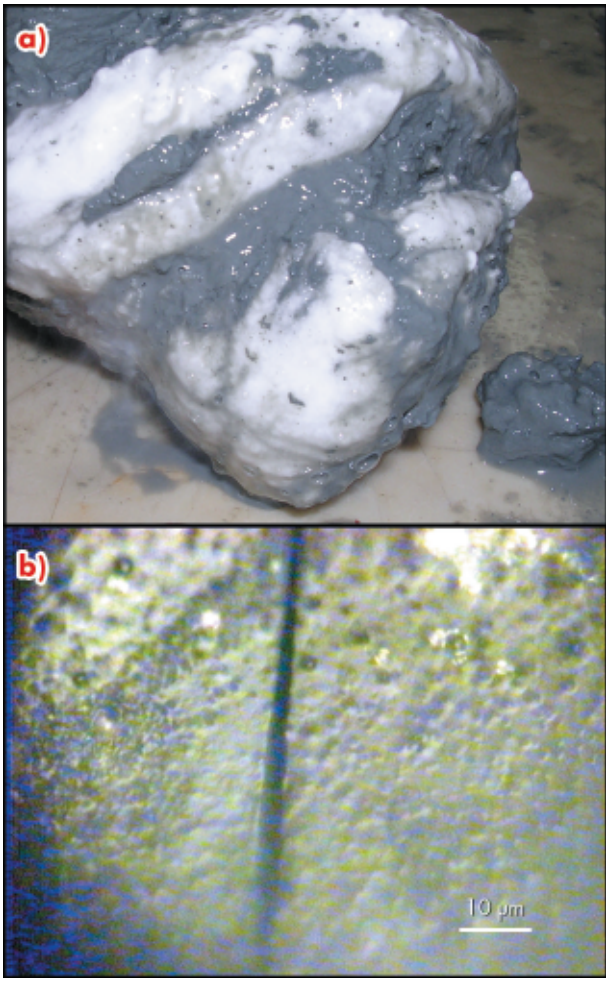

Fig. 41: a) Natural gas hydrate from the African margin decomposing at atmospheric conditions; b) Microscopic view of the gas hydrates from African margin preserved at 113 K.

We have used X-ray synchrotron diffraction to investigate the structure and thermal properties of natural samples. Gas hydrates have been recovered during the ZAIANGO cruise (ZAIROV-Leg 2 Dec. 2000, TOTAL - IFREMER) by gravity coring at 3160 m water depth in the Congo-Angola basin [1]. Other specimens were retrieved during the NERIS II campaign (Dec. 2004) at water depths between 1147 and 1203 m in the deep province of the Niger delta (Gulf of Guinea) (**Figure 41**). The powder data were recorded at beamline **ID31** which allowed high-quality powder-diffraction patterns to be obtained with a typical resolution of $\Delta d/d \sim 10^{-4}$. The physical (structure) and chemical properties of the gas hydrates can be preserved at low temperature (~ 90 K) and the thermal properties can be studied under controlled conditions.

The natural gas hydrates consist of mixed crystalline phases: ice Ih (hexagonal) and a cubic lattice structure I (sI), which is the most common structure adopted by natural specimens. Hydrocarbon gases in hydrates originate generally from two sources: biogenic and thermogenic. Our previous study using different laboratory techniques confirmed that the presence of sI is associated with methane (the major gas component) originating from microbial CO_2 reduction [1]. Hydrates of thermogenic origin (generally composed of higher hydrocarbons) are generated at high temperature in the deep sediment at

~ 1000 to 2000 m (or even deeper) below the sea floor. Their structure generally differs from sI. However, they can also form near the sea floor when associated with fluid and seepage.

Figure 42 displays the lattice constants of the Congo-Angola and Niger specimens (a = 11.8646 (39) Å and a = 11.8619 (23) Å, respectively) at ~ 90 K [2]. They are comparable but not identical to those obtained for sI natural hydrates from Cascadia margin in the Pacific, Okhotsk Sea and synthetic methane hydrates [3]. The differences in lattice constants between natural specimens collected at different geological sites may reflect the mixing of methane with components like H_2S, CO_2 and non-methane gases identified spectroscopically in the structure [4].

Another point investigated here is the thermal evolution of the lattice expansion. Gas hydrates are known to present unusual thermophysical properties when compared to ice. They appear to depend on the interactions of guests molecules with the water host lattice. We confirmed that the thermal expansivity is much larger than that of ice, especially below 200 K. Furthermore, it tends to become reduced as temperature increases up to the hydrate decomposition temperature [2]. Conversely, at lower temperature, the thermal expansivity is much larger than compared to ice. This is attributed to a perturbation of the vibrational motions of the water molecules that experience a large anharmonic potential due to strong interaction with the guests.

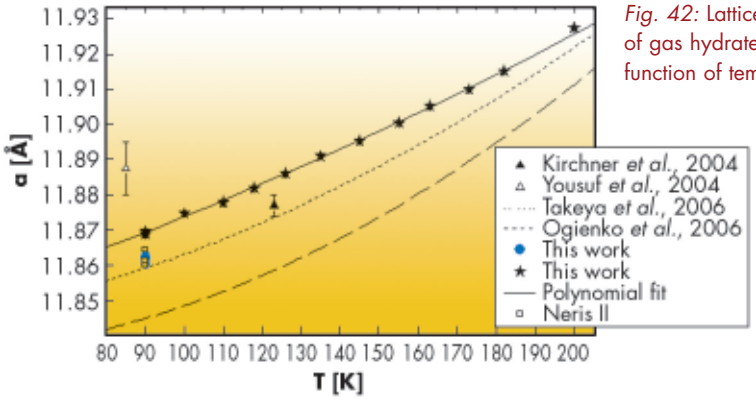

Fig. 42: Lattice expansion of gas hydrates as a function of temperature.

In conclusion, valuable structural information can be obtained on well-preserved natural hydrates. We suggest that non-methane gas components present in small proportions affect the lattice dimension of the sI structure to a small extent. Moreover, the derived thermal expansion coefficients show comparable values with those reported for synthetic methane hydrates at low temperature and tends to reach thermal expansion of ice at higher temperature.

References
[1] Charlou *et al.*, *Chem Geol.* **205**, 405 (2004).
[2] Bourry *et al.*, *Geophys. Res. Lett.* **34**, L22303 (2007).
[3] Yousuf *et al.*, *Appl. Phys. A* **78**, 925-939 (2004); Takeya *et al.*, *Chem. Eng. Sci.* **61**, 2670-2674 (2006); Ogienko *et al.*, *J. Phys. Chem. B.* **110**, 2840-2846 (2006).
[4] Chazallon *et al.*, *Chem. Geol.* **244**, 175 (2007).

Unusual microstructure modification in biogenic crystals under annealing

Biogenic crystals are crystals produced by living organisms. They attract a lot of attention because of their fascinating microstructures and superior properties [1]. The interrelation between a material's microstructure and its properties is of great interest for materials science and engineering. Impressive examples include our ability to control the strength of metals and alloys by annealing-mediated grain size, and band gap engineering in semiconductor thin films by lattice-mismatch-mediated interfacial strains. Unique methods of controlling microstructure and, hence, crystal properties also exist in nature. In fact, organisms can control the polymorphism, morphology, and orientation of crystalline blocks in biogenic crystals by means of organic macromolecules deeply involved in the biomineralisation process. Very recently it was shown that even the atomic structure of biogenic ceramics can be slightly different when compared to the structure of their geological counterparts [2]. In fact, the aragonite and calcite polymorphs of calcium carbonate extracted from various mollusc shells exhibited anisotropic distortions of the crystalline lattice of about 0.1–0.2% [3], which are rather high for ceramic materials. These distortions (lattice strains) are effectively relieved at surprisingly low annealing temperatures of about 150–200°C.

Principal publication and authors
B. Pokroy (a), A. Fitch (b), E. Zolotoyabko (a), *Advanced Materials* **18**, 2363 (2006); *Crystal Growth & Design* **7**, 1580 (2007).
(a) Department of Materials Engineering, Technion, Haifa (Israel)
(b) ESRF

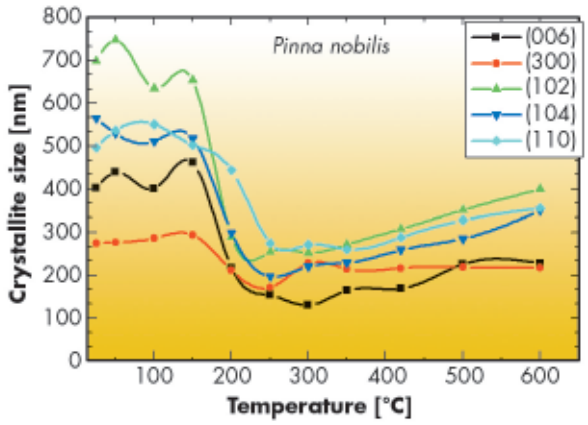

Fig. 43: Anisotropic crystallite sizes along different crystallographic directions in calcitic shells of *Pinna nobilis* measured as a function of annealing temperature. Prior to diffraction measurements at room temperature, the shell powders were annealed for 30 minutes at temperatures between 50 and 600°C.

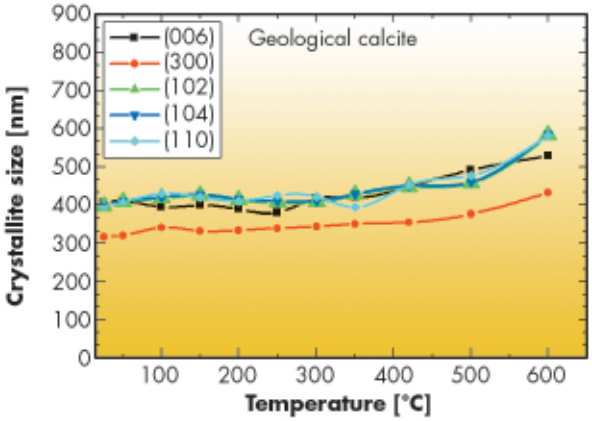

Fig. 44: Anisotropic crystallite sizes along different crystallographic directions in geological calcite (Creel, Chihuahua, Mexico) measured as a function of annealing temperature. Experimental condition and preparation were the same as for calcite shells (Figure 43).

In continuation of this work at the high-resolution powder diffraction beamline, **ID31**, we unexpectedly found that strain relaxation is accompanied by a remarkable broadening of the X-ray diffraction profiles, an effect easily visible by eye. By fitting the measured diffraction profiles to a Voigt function and separating the Lorentzian- and Gaussian-type contributions to the diffraction peak broadening, we were able to extract the crystallite size and averaged microstrain fluctuations as functions of annealing temperature.

The analysis revealed a considerable reduction in the crystallite size in biogenic calcite and aragonite annealed at temperatures above 150–200°C. Typical results are plotted in **Figure 43**. The crystallite size reduction correlates with a growth in the averaged microstrain fluctuations (not shown here) caused by the increased number of inter-crystallite boundaries, which are the sources of the inhomogeneous deformation fields [4]. The reduction of crystallite sizes (by a factor of three in some cases) with annealing temperature is very unusual for ceramic materials in which thermally-activated grain growth is regularly observed under annealing. The latter behaviour is thermodynamically justified since it reflects the tendency of the system to reduce free energy by diminishing the number of grain boundaries. In fact, we did observe a gentle grain growth in this type of sample with geological calcite, heat treated up to 600°C (see **Figure 44**). Geological aragonite did not reveal any changes in crystallite size under annealing at temperatures up to 400°C.

Based on these findings, we assumed that intra-crystalline organic macromolecules trapped within individual crystallites of calcium carbonate are responsible for the observed structural modifications. According to our model considerations, the network of organic macromolecules supplied by an organism assist in the nucleation of calcium carbonate at an early stage of biomineralisation. There is evidence that biogenic calcium carbonate initially grows as amorphous. Crystallisation of amorphous calcium carbonate within the confined space defined by the macromolecular network increases the forces imposed by organic macromolecules on the mineral lattice because of the difference in specific volumes per molecule in the amorphous and crystalline phases. These forces cause lattice distortions revealed in our high-resolution diffraction measurements.

Annealing at 150–200°C leads to degradation of the organic macromolecules, which initially support the strained mineral lattice. As a consequence, lattice strains are effectively relieved. Besides this, defragmentation of organic macromolecules modifies the topology of the connected crystalline units and, in particular, introduces angular misorientation between them, which is revealed as the reduction in the size of the coherence length of the crystalline blocks.

The high quality experimental data and the model developed provide new insight into the interactions between the organic and ceramic components in biogenic crystals. We believe that a deeper understanding of this interaction will facilitate future development of bio-inspired advanced materials.

References
[1] S. Weiner, L. Addadi, *J. Mater. Chem.* **7**, 689 (1997).
[2] B. Pokroy, J.P. Quintana, E.N. Caspi, A. Berner, E. Zolotoyabko, *Nature Mater.* **3**, 900 (2004).
[3] B. Pokroy, A. Fitch, P. Lee, J.P. Quintana, E.N. Caspi, E. Zolotoyabko, *J. Struct. Biol.* **153**, 145 (2006); B. Pokroy *et al.*, *J. Struct. Biol.* **155**, 96 (2006).
[4] E. Zolotoyabko, J.P. Quintana, *J. Appl. Cryst.* **35**, 594 (2002).

High-resolution powder diffraction and electron microscopy - a powerful combination

Principal publication and authors
Ch. Baerlocher (a), F. Gramm (a), L. Massüger (a), L.B. McCusker (a), Z. He (b), S. Hovmöller (b), X. Zou (b), *Science*, **315**, 1113-1116 (2007).
(a) Laboratory of Crystallography, ETH Zurich (Switzerland)
(b) Structural Chemistry, Stockholm University (Sweden)

Determination of a crystal structure from powder diffraction data is no longer a rarity thanks to impressive methodological advances in recent years. However, some problems have remained intractable. A case in point is that of the zeolite catalyst IM-5, whose structure eluded determination for almost ten years.

Over the years, high-resolution powder diffraction data had been collected on several different samples of IM-5 on **BM01B**, the SNBL beamline at the ESRF and on the materials science beamline at SLS. None of the samples were ideal: all contained impurities, none had particularly sharp peaks, and diffraction intensity decreased markedly with diffraction angle. Nonetheless, by comparing the different IM-5 patterns, the peaks corresponding to the IM-5 phase could be distinguished from those of the various impurities, and a tentative indexing of the patterns was achieved (*C*-centred orthorhombic with a = 14.299 Å, b = 57.413 Å and c = 20.143 Å). This was subsequently confirmed via electron diffraction.

This open-framework silicate has an unusually large unit cell, with a volume almost triple that of ZSM-5, which is one of the most complex zeolites known. There are also approximate relationships between the axes ($b \sim 4a$ and $c \sim \sqrt{2}a$), so symmetrically unrelated reflections have very similar *d*-spacings. These factors result in an enormous degree of reflection overlap, which is the key hindrance to structure solution from powder diffraction data. Of the 4120 reflections in the pattern, 3499 are within 0.2 FWHM of a neighbouring reflection with which it therefore overlaps. The pattern with the sharpest peaks, an identified impurity (analcime) and the largest range of *d*-spacings (SNBL, λ=0.99995Å, collected in 1998) was selected for further analysis.

The key to structure solution for another complex zeolite, (TNU-9), had proven to be the inclusion of crystallographic phases derived from high-resolution electron microscopy (HRTEM) images [1], so it was reasoned that a similar approach might also work for IM-5. In the case of TNU-9, the zeolite-specific program *Focus* had been used, but for IM-5 we decided to test the (material independent) powder charge-flipping (*pCF*) approach [2]. Both algorithms work in both real and reciprocal space, so information can be added easily in either realm. Phases for 95 reflections were derived from HRTEM images taken along three different directions and input to the program *Superflip*. Although there were some promising looking channel systems in some of the resulting electron density maps, detailed interpretation was not possible.

Meanwhile, a model had been derived from the HRTEM images, but its geometry was strained and its powder diffraction pattern did not match the experimental data very well, even after refinement. Speculating that this model was probably at least partially correct, it was used to calculate starting phase sets for *pCF* (instead of random phases). The phase of each reflection calculated from the structure was varied by up to 25% in a random fashion, thereby generating 1000 different starting points for 1000 distinct *pCF* runs. The best five electron density maps were then merged, and interpretation of the resulting map was almost trivial (**Figure 45**). Refinement of this structure converged with the *R*-values R_F = 0.075 and R_{wp} = 0.188 (R_{exp} = 0.142).

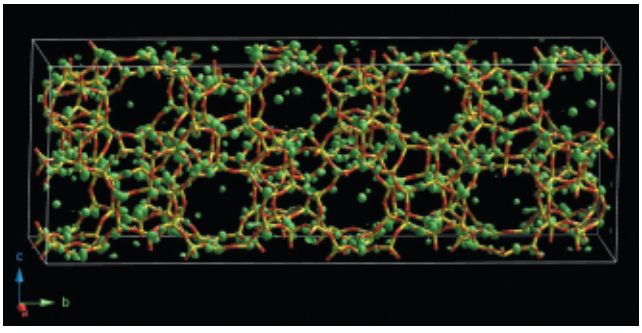

Fig. 45: Electron density map from *pCF* that was used to derive the structure of IM-5.

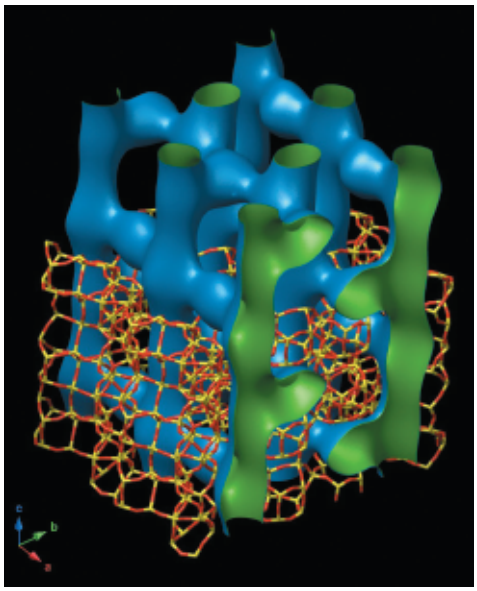

Fig. 46: The unusual 2-dimensional 10-ring channel system of IM-5.

References
[1] F. Gramm, Ch. Baerlocher, L.B. McCusker, S.J. Warrender, P.A. Wright, B. Han, S.B. Hong, Z. Liu, T. Ohsuna, O. Terasaki, *Nature*, **444**, 79-81 (2006).
[2] Ch. Baerlocher, L.B. McCusker, L. Palatinus, *Z. Kristallogr.* **222**, 47-53 (2007).

As suggested by catalytic tests, the IM-5 framework structure has a 2-dimensional 10-ring channel system with effective pore widths ranging from 4.8 to 5.5 Å. This channel system is unusual in that it also has a limited third dimension (**Figure 46**), giving it the character of a 3-dimensional one with complex channel intersections that can accommodate bulky intermediates in catalytic reactions, while retaining the overall effect of a 2-dimensional one with long-range diffusion restricted to just two dimensions.

There are 24 topologically distinct Si atoms in the asymmetric unit. This translates to 864 atoms (288 Si + 576 O) in the unit cell. Because no symmetry is assumed in charge flipping, the number of atoms per unit cell rather than the number per asymmetric unit is the prime limitation of the algorithm. This implies that the structures of other polycrystalline materials with similar numbers of atoms per unit cell, whatever their chemical composition, should also be accessible via this route, providing that high-resolution powder diffraction data and suitable HRTEM images can be obtained.

Principal publication and authors
H. Takakura (a), C.P. Gómez (b), A. Yamamoto (c), M. de Boissieu (d), A.P. Tsai (b), *Nature Materials* **6**, 58-63 (2007).
(a) Division of Applied Physics, Graduate School of Engineering, Hokkaido University, Sapporo (Japan)
(b) Institute of Multidisciplinary Research for Advanced Materials, Tohoku University, Sendai (Japan)
(c) Advanced Materials Laboratory, NIMS, Tsukuba (Japan)
(d) Laboratoire de Thermodynamique et de Physico-Chimie Métallurgique, UMR CNRS 5614, ENSEEG-INPG, Saint Martin d'Hères (France)

Solving the structure of the binary icosahedral Yb-Cd quasicrystal

Where are the atoms? This question has been puzzling scientists ever since the discovery of quasicrystals some 25 years ago by Shechtman and coworkers [1]. Quasicrystals are extremely well ordered structures whose atomic arrangement is non periodic. This shows up in their diffraction patterns which display sharp Bragg reflections (a signature of long-range order) but with a 5-fold rotational symmetry, incompatible with lattice translation. This prevents the application of standard crystallography techniques to solve the structure. A high dimensional crystallographic approach has been developed, in a way similar to that achieved for incommensurately modulated structures. In this approach, periodicity is recovered in a 6 dimensional space, allowing modelling and a comparison with experimental data.

The discovery of the icosahedral phase of $Cd_{5.7}Yb$ by Tsai and coworkers [2] has been a breakthrough. Indeed, all previously known stable quasicrystals were at least ternary compounds. The dicovery that the CdYb quasicrystal is binary makes the structural analysis much simpler. There is also good scattering contrast for X-rays between the Cd and Yb atoms. Finally, there are two so-called periodic approximants, which can be synthesised with chemical compositions very close to that of the quasicrystal. The structure of the approximant crystals could be solved using standard crystallographic techniques and is described by a periodic packing of a large structural unit with an icosahedral symmetry, whose external shell is a triacontahedron (**Figure 47**). Starting from the centre, there is a Cd tetrahedron, occurring with different orientations, enclosed in a Cd dodecahedron. Then comes an Yb icosahedron (blue colour atoms) enclosed in two following shells containing Cd atoms only. This large triacontahedral atomic cluster has a diameter of 1.57 nm and is extremely well ordered chemically. Clusters are densely packed and connected along

their 2-fold axes where they share a face and along 3-fold axes where they interpenetrate. The same cluster and connectivity rule has been used to model the quasicrystal, but on a quasiperiodic network.

The structure of the icosahedral CdYb quasicrystal has been solved using a set of Bragg intensities collected at **BM02**, the D2AM CRG beamline. A large number of independent reflections has been measured in a large Q range, and with special care for weak reflections which are crucial for detailed modelling. Using a 6-dimensional analysis including a phase reconstruction procedure and the information obtained from the approximant structure, a model could be proposed which has been refined against the experimental data. The 5000 measured Bragg intensities impose a severe constraint on the modelling, which results in a very good R factor equal to 0.11. We find that the CdYb quasicrystalline structure is described by a quasiperiodic packing of the triacontahedral cluster, with connections along 2- and 3- fold axes as observed in the approximant: 94% of the atoms belong to such clusters.

The model also leads to a hierarchical packing of the clusters, illustrated in **Figure 48** which shows the cluster centre distribution in a 5-fold plane. Blue colour dots stand for cluster centres in the plane, whereas other colours stand for cluster centres lying below or above the plane. The solid lines are the 2-fold connections with a length equal to 1.57 nm.
The clusters are packed together to form a 'cluster of clusters' whose trace is a 10-fold ring highlighted by a pale orange disk in **Figure 48**. In turn this 'cluster of clusters' which has an inner radius of about 2.5 nm also forms a larger cluster whose characteristic length is 10.7 nm, *i.e.* τ^3 larger, where $\tau = 1.6168$ is the golden mean (red arrows). This inflation property continues to infinity and might be used to explain some of the quasicrystal's physical properties.

Now that we have located the atoms in this icosahedral quasicrystal, detailed simulations can be performed to gain a deeper understanding of the physical properties and to tackle the still open and fascinating question of why the long range quasiperiodic order sets in.

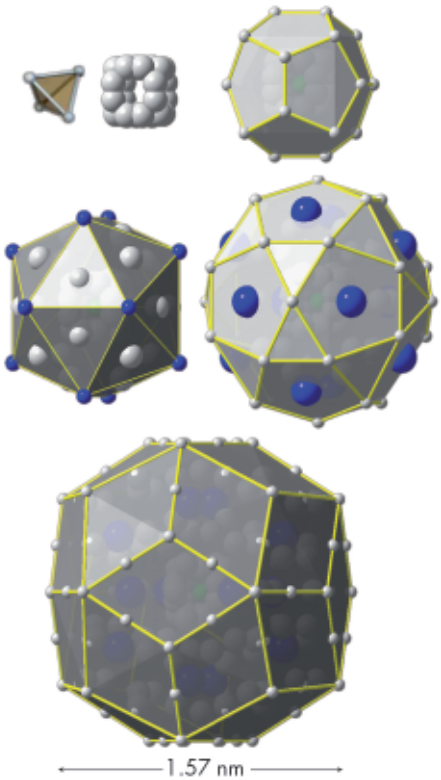

Fig. 47: Illustration of the shell structure of the cluster which appears in both the periodic approximant and the icosahedral quasicrystal. The external cluster has a diameter of 1.57 nm and contains 158 atoms.

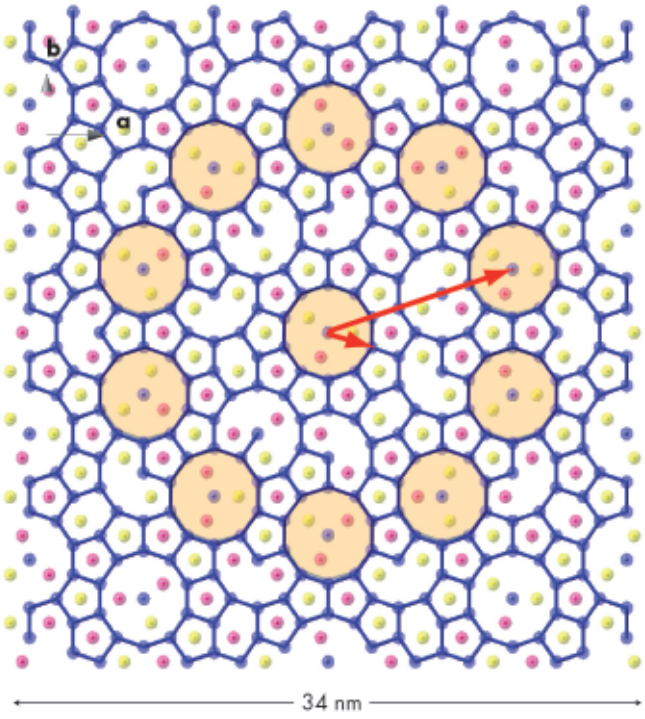

Fig. 48: Illustration of inflation properties in the quasicrystal. The distribution of cluster centres (blue dots) is shown in a 5-fold plane. The pale orange disk is a trace of a cluster of clusters forming a 10-fold ring. In turn this cluster of cluster forms a self similar larger unit as highlighted by the long red arrow.

References
[1] D. Shechtman, I. Blech, D. Gratias and J.W. Cahn, *Phys. Rev. Lett.* **53,** 1951 (1984).
[2] A.P. Tsai, J.Q. Guo, E. Abe, H. Takakura and T.J. Sato, *Nature* **408,** 537 (2000).

Soft Condensed Matter

Introduction

The 2007 scientific highlights from the Soft Condensed Matter Group beamlines cover a large range of scientific topics. This diversity is exemplified by the articles that will be mentioned within this introduction which reveal multiple links to neighbouring disciplines including surface science, structural biology and materials science. The ability to unite such a diverse range of scientific themes has become one of the Soft Condensed Matter Group's greatest strengths.

The importance of short range interactions at aqueous electrolyte solution interfaces has been deduced from grazing-incidence X-ray fluorescence at ID10B. New approaches to reach atomic resolution in surface diffraction on Langmuir films have also been explored at the same beamline. At first glance these two topics may seem unrelated, yet they are both contributing to similar goals which are to enhance our understanding of protein crystallisation and the structure of thin protein films.

A glimpse into the fascinating world of the microstructure and dynamics of ultrathin liquid films is provided by coherent X-ray scattering experiments performed at ID10A. The experiments, conducted in parallel at the APS beamline 8ID, contribute to our understanding of adsorption and wetting processes which are technologically important.

At ID02 and ID13, the very onset of structural developments during polymer and biopolymer processing have been explored using SAXS/WAXS techniques. Polypropylene crystallisation has been investigated with unprecedented sensitivity at ID02. This has allowed the elusive event of primary nucleation to be observed. At ID13, the very onset of cotton mercerisation by alkaline solution has been studied using a submicrometre beam. This demonstrates how industrial processes can be scaled down for study, in this case to the level of a single cotton fibre. This requires nanolitre reaction volumes generated by an inkjet system.

Microfluidic devices such as inkjet systems have enormous development potential for chemical and biological applications. The current challenge for the Soft Condensed Matter Group is to establish partnerships with external users and strengthen existing collaborations with other European synchrotron radiation beamlines. The SAXIER FP6 project serves as the catalyst to bring experts and users from the SAXS field together.

C. Riekel

Specific ion adsorption and short-range interactions at the air aqueous solution interface

Principal publication and authors
V. Padmanabhan (a), J. Daillant (a), L. Belloni (a), S. Mora (b), M. Alba (a), and O. Konovalov (c), *Phys. Rev. Lett.* **99**, 086105 (2007).
(a) CEA Saclay, Gif-sur-Yvette (France)
(b) UMR 5587 CNRS, Université Montpellier II (France)
(c) ESRF

The study of aqueous salt solutions continues to attract various research groups because of their fundamental importance in various physicochemical, biological and atmospheric processes. The air/water interface plays a crucial role in such processes and differs to a large extent when compared to bulk. To further understand the role of the interface, direct access to the surface excess or the knowledge of the concentration profiles of ions will not only improve our present understanding but also help to predict the properties associated with it. Ions, though of the same valency, tend to interact differently with proteins (salting in or salting out as predicted by Hofmeister) or differ in their degree of adsorption at the air-water interface. In recent times, there have been considerable efforts by various research groups using different sophisticated surface sensitive probes to understand the organisation of the ions and its impact on the solvent features and also through molecular dynamic simulation.

We have employed grazing incidence X-ray fluorescence to investigate an electrolyte solution under ambient conditions (**Figure 49**) at beamline **ID10B**. The X-ray fluorescence from the ions (chemical sensitive) is registered as a function of the angle of incidence (depth sensitive). Systematic investigations on acids, salts and their mixtures at different bulk concentrations yield quantitatively their surface excess. Theoretical analysis using a hyper-netted chain approximation to predict the concentration profile (**Figure 50**) invoke the necessity to include the short range surface-ion interaction potential in addition to the dispersion and the long range electrostatic interactions. Furthermore, the competition in ion adsorption for a mixture of 0.1 M KCl and 0.1 M KI reveal clearly the enhancement of iodide relative to chloride anion (Inset of **Figure 50**). We could apply this approach of analysis to 20 different experiments using 4 fit parameters. The strength of the effective potential deduced from such analysis were, -4.0 k_BT, -4.7 k_BT, -4.4 k_BT and -3.15 k_BT, for Cl^-, Br^-, I^- and H^+ (at contact), respectively. Our studies highlight the importance of the short range interactions at the interface of aqueous electrolyte solutions.

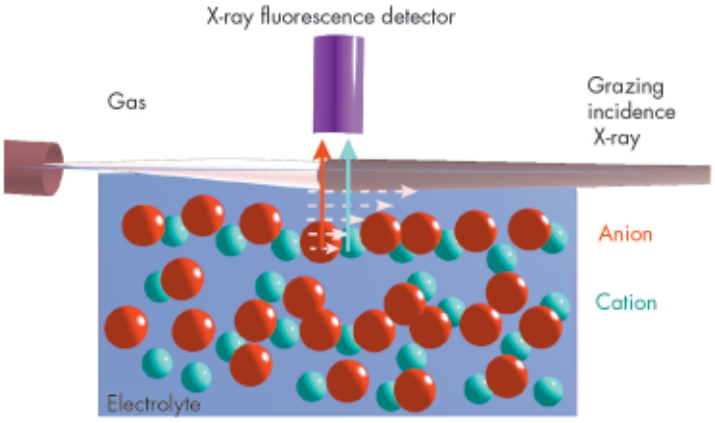

Fig. 49: Schematic sketch of the grazing-incidence X-ray fluorescence setup showing the evanescent X-ray excitation and subsequent fluorescence from the cation and the anion at the gas-electrolyte interface under ambient conditions.

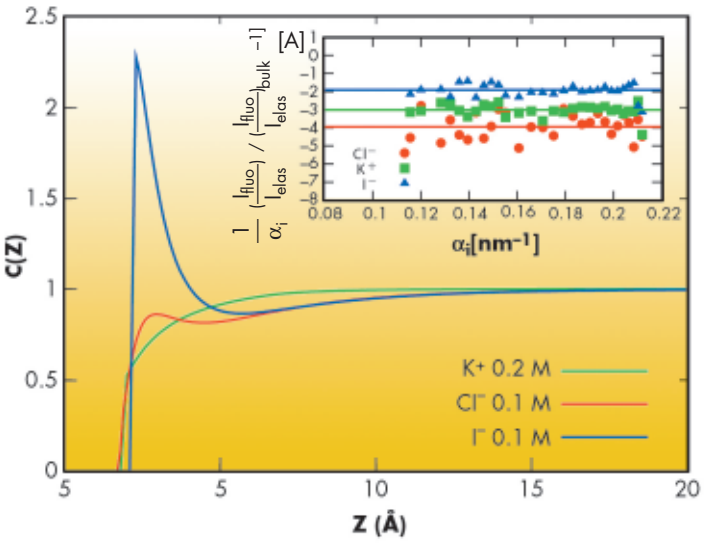

Fig. 50: Theoretically deduced concentration profiles, C(Z), for KCl (0.1 M) + KI (0.1 M) mixtures. The inset shows the experimentally measured surface excesses for K^+, Cl^- and I^- ions. Here, $\alpha_i = 2*\mathrm{Im}(k_z) + \mu_i$, where μ_i is the linear absorption coefficient at the fluorescence energy for the ion, i and Im k_z refers to the imaginary part of the wave vector, I_{fluo} and I_{elas} refer to the fluorescence and elastic peak intensities.

Thin liquid films in coherent X-ray light

Principal publications and authors
C. Gutt (a), M. Sprung (b), R. Fendt (c), A. Madsen (d), S.K. Sinha (e) and M. Tolan (c), *Phys. Rev. Lett.*, **99**, 096104 (2007).
(a) Hasylab/DESY, Hamburg (Germany)
(b) Argonne National Laboratory, Chicago (USA)
(c) Universität Dortmund (Germany)
(d) ESRF
(e) UCSD, San Diego (USA)

Adsorption and wetting of fluids on solid substrates are phenomena of long-standing interest in fundamental research. Since they determine the homogeneity of thin films and coatings, they also have a technological interest. Solid substrates exposed to a vapour atmosphere attract molecules from the gas phase leading to the formation of a thin liquid film with a thickness of a few nanometres. Such nanofilms are not only omnipresent in everyday life but they also provide a model system for studying properties of thin liquid films.

Thick films and bulk liquids display fluctuating surface contours driven by the thermal motion of molecules underneath the surface. However, the dynamical properties of thin films are strongly influenced by the interaction with the substrate and a rich variety of phenomena like correlated surface roughness and slowing down of surface fluctuations are expected. Moreover, in thin films, surface fluctuations are known to influence the early stages of dewetting processes.

Coherent X-rays are ideal for the investigation of thin liquid films as the corresponding speckle structure allows one to measure the exact arrangement of the surface contour as well as possible dynamical fluctuations. In experiments at ESRF beamline **ID10A** and APS beamline 8ID, silicon wafers were exposed to the gas phase of the highly volatile liquid n-hexane. The liquid molecules can be condensed on the substrate by lowering the substrate temperature slightly. In this way film thicknesses from monolayer coverage up to 80 nm have been prepared and investigated.

Figure 51a shows the static speckle structure of slowly-grown thin liquid films obtained by *in situ* rocking curves. The data represent scattering from the empty substrate, and films of thicknesses 3, 6, 10 and 14 nm. A comparison of the speckle structure yields direct information about the transfer of surface structures from the substrate to the liquid film. In the case of slow condensation the speckle structures of the liquid films are similar while not absolutely identical to that of the underlying substrate, implying that the surface structure of the liquid film is following the substrate. The degree of replication however depends on the deposition rate of the molecules on the substrate. **Figure 51b** displays the corresponding speckle structures for rapid condensation (*i.e.* 12 nm, within 1-2 minutes). Curve (i) represents the speckle structure from a 3 nm thick film. Curve (ii) is the repeated scan with a sudden decrease of the substrate temperature indicated by the position of the arrow. The resulting fast condensation of molecules immediately leads to a different surface structure as can be seen by the speckle structure. The surface structure of the final 15 nm thick film (curve (iii)) is completely different from the initial substrate surface.

Figure 52 shows an averaged CCD image of a 40 nm thick hexane film. Again a static speckle pattern is visible indicating that the film displays no surface dynamics. The inset shows the

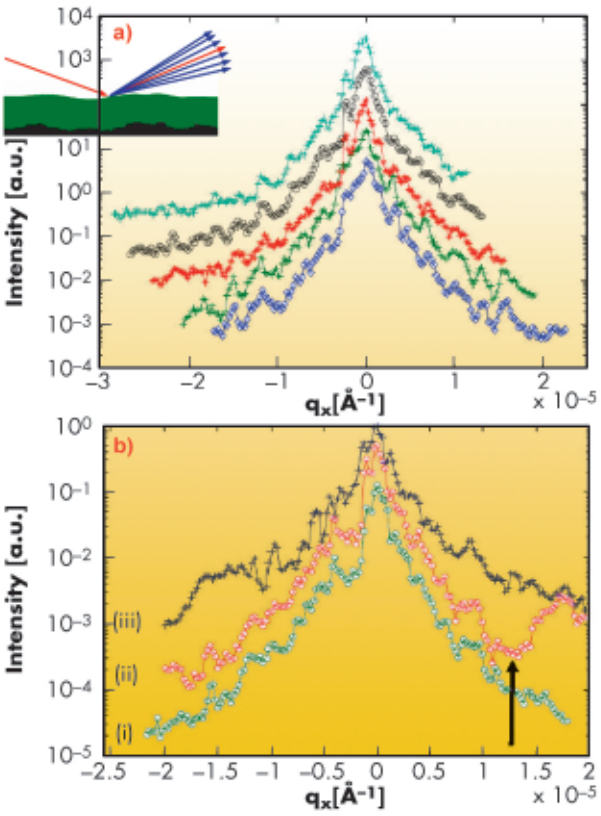

Fig. 51: Rocking scans of vapour deposited thin liquid hexane films on silicon substrates. a) Empty substrate and slowly grown films of thickness 3, 6, 10, and 14 nm – from bottom to top. b): Rapidly grown films (i) 3 nm thick film (ii) repeated scan, the arrow indicates rapid condensation (iii) 15 nm thick film.

ensemble averaged static structure factor S(q) of films of different thickness. For all but the thinnest film (6 nm) we observed the peculiar form S(q) ~ q^{-3} which suggest a self-affine fractal surface structure with a universal scaling exponent H=0.5 for the liquid films. This self-affine surface structure indicates a partial wetting situation.

The results reveal a more complex behaviour of thin liquid films than previously anticipated. Instead of a fluctuating surface contour induced by capillary waves, static surface structures were observed on length scales ranging from 10^6 Å to 10^3 Å. The experiments have been performed at temperatures far above the freezing point of bulk hexane; This suggests a different mechanism than solidification through freezing. Capillary waves are caused by long ranging, collective motion of molecules on length scales ranging from mm to nm. Partial wetting leads to a non-uniform film which causes classical hydrodynamics, as

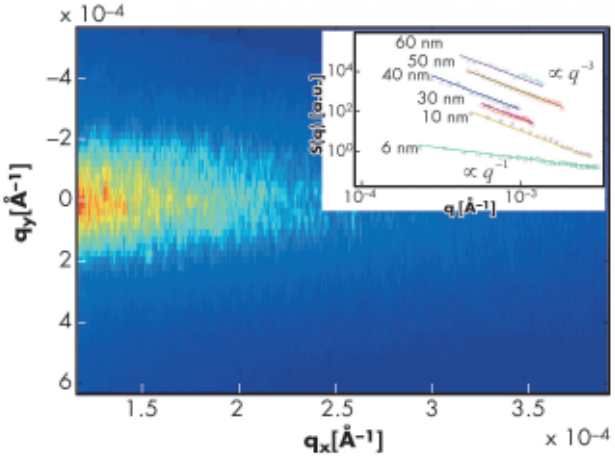

Fig. 52: Average CCD image from the scattering of a 40 nm thick hexane film on silicon. Inset: The ensemble averaged static structure factor S(q) for films of different thickness.

expressed by the Navier-Stokes equations, to be no longer valid on the probed length scales. The result is that the thin liquid films behave like solid matter on these length scales. This behaviour is visible in the diffuse scattering with a characteristic form of the power spectral density which is usually not seen on liquid surfaces and indicates a self-affine fractal surface structure with a correlation length larger than 3000 Å.

Slow dynamics and ageing in colloidal gels studied by XPCS

Principal publication and authors

A. Fluerasu (a), A. Moussaïd (a), A. Madsen (a), A. Schofield (b), *Phys. Rev. E* **76**, 010401(R) (2007).
(a) ESRF
(b) Dept. of Physics & Astronomy, University of Edinburgh (UK)

Aggregation and gelation are topics of fundamental interest in condensed matter physics [1] that also have many direct industrial applications. Delayed sedimentation is a non-equilibrium phenomenon encountered in a variety of soft-matter systems, including colloidal suspensions with sufficiently strong short-ranged attractive interactions. Due to the interactions, the colloidal particles can aggregate at relatively low concentrations (*e.g.* 20%) to form a space-filling structure often denoted as a gel. However, this non-equilibrium structure slowly evolves, until the spatial connectivity is lost and the gel suddenly collapses.

In this work we have used X-ray photon correlation spectroscopy (XPCS) to study the slow dynamics in a colloidal transient gel consisting of a mixture of polymethylmethacrylate (PMMA) nano-particles with a radius R = 1070 Å and non-adsorbing random-coil polystyrene (PS) dispersed in cis-decalin. The addition of polymers causes an effective attraction between the colloids via the so-called depletion mechanism [1] and leads to the formation of the gel. The XPCS experiments were performed using partially-coherent X-rays at beamline **ID10A** (Troïka). The scattering (speckle images) from the PMMA/PS gels were recorded by a direct illumination CCD with 22 µm pixels located 2.3 m downstream of the sample. Series of several thousand CCD frames were taken and the dynamic properties were investigated by calculation of two-time correlation functions,

$$C(Q,t_1,t_2) = \frac{\langle I(Q,t_1)\cdot I(Q,t_2)\rangle}{\langle I(Q,t_1)\rangle\cdot\langle I(Q,t_2)\rangle},$$

Where ‹› denotes an ensemble average performed over many pixels of the CCD

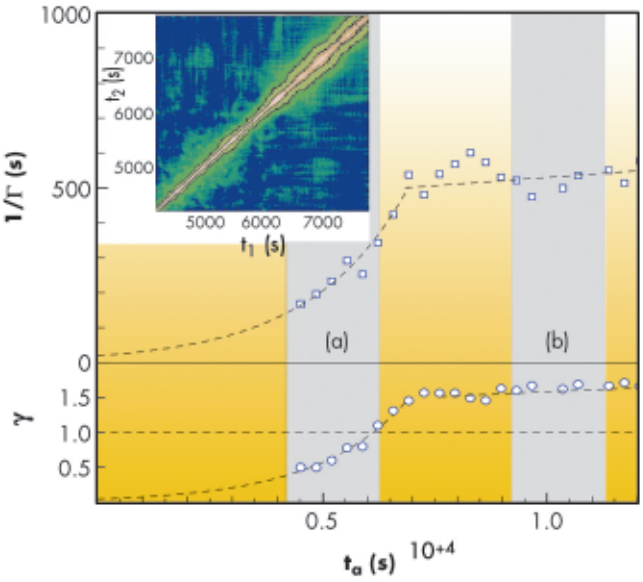

Fig. 53: Correlation times $1/\Gamma$ and γ exponents as a function of age obtained from equal-age slice fits of the two-time correlation functions calculated for QR=3. The grey areas highlight the time intervals defined as "early" (a) and "full" ageing (b) stages (dashed lines are guides for the eyes).

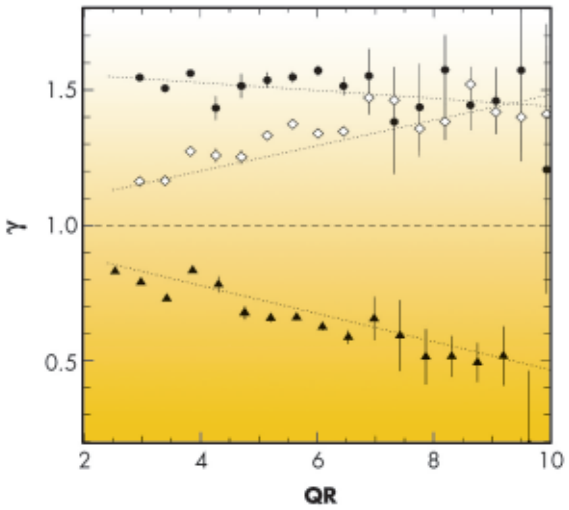

Fig. 54: γ exponents as a function of Q during the early stages (filled triangles), full ageing regime (filled circles), and late stages, just before the gel collapse (empty diamonds).

detector. The natural variables to describe the two-time correlation functions (see inset in **Figure 53**) are the average time or "age" $t_a=(t_1+t_2)/2$, measured by the distance along the $t_1=t_2$ diagonal and the time difference $t=|t_1-t_2|$ which is the distance from the $t_1=t_2$ diagonal in the perpendicular direction. The widening of the two-time correlation contour plots (**Figure 53**, inset) is indicative of an ageing process. The correlation times become increasingly longer with time (age). To quantify this phenomenon, the two time correlation functions were averaged over narrow, equal-age, slices. This leads to more common (albeit age dependant) "one-time" correlation functions. Unlike the case of simple Brownian motion where the correlation functions are well described by simple exponential decays, here a Kohlrausch (or "stretched exponential") form has to be used,

$$g(Q,t) \propto \exp[-2(\Gamma t)^{\gamma}]$$

The fitting parameters, the relaxation rate Γ and the exponent γ are both age (t_a) and Q-dependent. The age-dependence of Γ and γ, calculated for a single wave vector Q corresponding to a value of QR=3 are shown in **Figure 53**. After an initial stage (t_a < 7000s) during which the correlation times increase exponentially with age, a region with huge fluctuations is entered. We attribute these strong fluctuations to large scale rearrangements in the gel. Such behaviour has been observed previously in different systems and a universal model for ageing in soft matter was proposed [2]. A remarkable crossover from $\gamma<1$ to $\gamma>1$ can be observed during the early stages of the process. While relaxations with $\gamma \neq 1$ have been found before in several different systems, it is, to our knowledge, the first time that such an evolution with age is observed. Since compressed exponential relaxations ($\gamma>1$) have been found in putative jammed states, our measurements may indicate a jamming transition occurring during the initial stages of the delayed sedimentation process.

The age- and Q-dependent γ exponents can better be seen in **Figure 54**. While at the early stages they are sub-unitary on all length scales (filled triangles), the picture changes in the full-ageing regime, where the relaxations are better described by compressed exponentials ($\gamma \sim 1.5$). This indicates that the system is jammed on all the probed length scales. Interestingly, towards the final stages of the gel lifetime (diamonds), the situation changes again and the low-Q γ exponents start approaching unity. This is indicative of an "un-jamming" process on large length scales preceding the final gel collapse.

References
[1] K.N. Pham, A.M. Puertas, J. Bergenholtz, S.U. Egelhaaf, A. Moussaïd, P.N. Pusey, A.B. Schofield, M.E. Cates, M. Fuchs, W.C.K. Poon, *Science*, **296**, 104 (2002).
[2] L. Cipelletti, L. Ramos, S. Manley, E. Pitard, D.A. Weitz, E.E. Pashkovski and M. Johansson, *Faraday Disc.*, **123**, 237 (2003).

Grazing-incidence X-ray diffraction on Langmuir films: towards atomic resolution

Principal publication and authors
J. Pignat (a,b), J. Daillant (a), S. Cantin (b), F. Perrot (b), O. Konovalov (c), *Thin Solid Films* **515**, 5691-5695 (2007).
(a) LIONS/Service de Chimie Moléculaire, CEA-Saclay, Gif-sur-Yvette (France)
(b) LPPI, université de Cergy-Pontoise (France)
(c) ESRF

Langmuir films of long chain amphiphiles at the air-water interface present different phases depending on temperature and surface pressure (the difference between the surface tension of pure water and the actual surface tension in presence of the film $\Pi = \gamma_{H2O} - \gamma$). Their phase transitions were first identified by isotherm measurements (surface pressure as a function of molecular area for a fixed temperature). The first grazing-incidence X-ray diffraction (GIXD) experiments carried out directly on monolayers at the air-water interface were reported in 1987 [1]. GIXD has now become the primary technique used to determine the structure of amphiphilic monolayers on water, allowing the determination of unit cell parameters, molecular tilt angle and azimuth of tilt direction. It is however generally considered that going beyond this simple unit cell characterisation is impossible.

We have recently developed a different method, consisting of a careful extraction of the structure factors from the diffraction data followed by fitting of molecular parameters, which allowed us to obtain sub-molecular information [2]. The structure factor calculations are performed using the SHELX-97 program developed by George Scheldrick. We use the known chemical structure of fatty acid molecules by imposing atomic coordinate in a molecular model which allows us to fit relevant parameters such as hydrocarbon backbone plane azimuth, head-group rotation, or gauche defects in the hydrocarbon chain. Sterically impossible configurations are automatically rejected by SHELX.

Molecular parameters have a marked influence on the calculated structure factors and can be determined by model fitting. For example, the intensity ratio between reflections is very sensitive to the orientation of the backbone planes whereas the Bragg rod profiles along the vertical are sensitive to the conformation defects. Untilted phases of fatty acids have been investigated using a systematic exploration of all relevant parameters [2]. We were able to determine the orientation of the chain backbone planes and of the carboxylic head-groups directly, measurements that were previously inferred from 3d measurements. Our method allowed us to evidence a new phase of symmetry p2gm at high pressure, corresponding to a minimum in lattice energy, which had never been observed before.

The use of a simulated annealing technique allows a large reduction in computation time which enables the determination of conformational defects. Simulated annealing is a Monte-Carlo method where the "temperature" is progressively decreased in order to avoid local $\chi 2$ minima. With a proper temperature decrease scheme, the results obtained using the simulated annealing algorithm do not differ from those obtained by systematic variation of all parameters. The statistics of conformation defects were estimated by considering large super-cells composed of at least 18 unit cells.

An example is given in **Figures 55** and **56** for the so-called L2" phase of behenic acid (the fatty acid with a 21 carbon

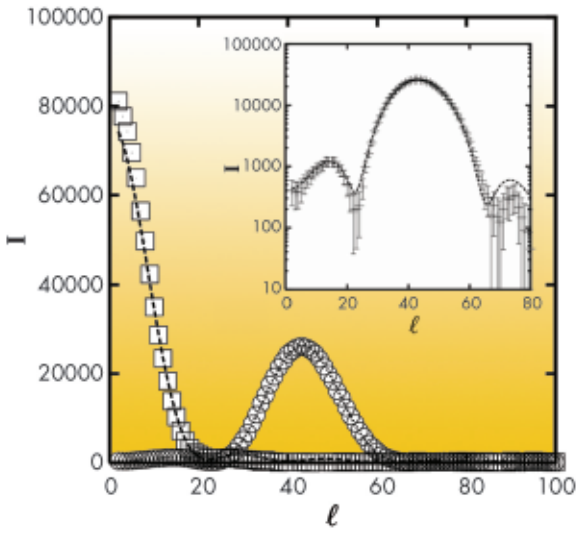

Fig. 55: Experimental Bragg rods corresponding to the (02) (squares) and (11) (circles) reflections for behenic acid in the L2" phase of behenic acid at 0.2 mN/m and T = –2.5°C. The dashed lines represent best fits. The same curves are shown in log scale in the insert in order to emphasise low intensity details.

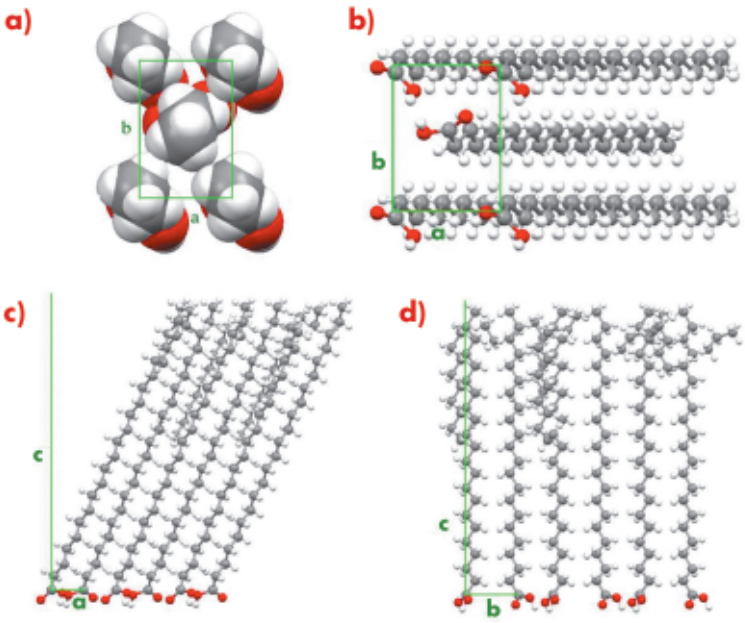

Fig. 56: L2″ phase of behenic acid at 0.2 mN/m and T = -2.5°C. (a) Transverse cell seen from the methyl groups. (b) Bottom view of the unit cell showing the headgroup organisation. Projection of the super-cell with 18 molecules in the (a, c) (c) and (b, c) (d) planes.

References
[1] K. Kjaer, J. Als-Nielsen, C.A. Helm, L.A. Laxhuber, H. Möhwald, *Phys. Rev. Lett.* **58**, 2224-2228 (1987); P. Dutta, J.B. Peng, B. Lin, J.B. Ketterson, M. Prakash, P. Georgopoulos, S. Ehrlich, *Phys. Rev. Lett.* **58**, 2228-2231 (1987); S. Grayer Wolf, L. Leiserowitz, M. Lahav, M. Deutsch, K. Kjaer, J. Als-Nielsen, *Nature* **328** 63-66 (1987).
[2] J. Pignat, J. Daillant, L. Leiserowitz, F. Perrot, *J. Phys. Chem. B* **110**, 22178-22184 (2006).

chain) at 0.2 mN/m and T=-2.5°C. **Figure 55** shows that an excellent agreement is obtained for the Bragg rod profiles. In **Figure 56**, the most interesting features are the co-planarity of chains and head-groups, an angle of 45° between the backbone planes, and, though the L2″ is a crystalline phase, the presence of many defects at the chain ends.

The method we have used is quite general, it uses data in the PDB format, and could be applied, for example to 2-dimensional peptide or protein crystals.

Principal publication and authors
P. Panine, E. Di Cola, M. Sztucki, and T. Narayanan, Polymer (2008), doi: 10.1016/j.polymer.2007.12.026.
ESRF

Early stages of polymer melt crystallisation

Unlike low molecular weight chemical compounds, polymeric materials do not transform to perfect crystals and usually turn into a metastable state that is partly crystalline and partly amorphous. This semi-crystalline structure, which develops during the solidification process, primarily controls the mechanical and physical properties of solid polymers. Polymer crystallisation has consequently been a topic of both fundamental and practical interest over the past half century [1]. It has been well established that the transformation of an entangled melt into a semi-crystalline state is a multi-step process. Despite enormous progress in understanding the mechanism of melt crystallisation, the initial step in the ordering process remains a subject of debate [2]. In recent years, there are somewhat contradictory reports on the early stage of crystallisation, deviating from the classical nucleation and growth mechanism. X-ray scattering techniques have been widely used in the investigation of different facets of polymer crystallisation but they suffer from the detection limits at such low crystalline fraction. This threshold of detection could introduce an apparent delay in the appearance of crystalline diffraction.

In order to unravel these scenarios of polymer crystallisation, we have reinvestigated the early stage of isotactic polypropylene (i-PP) crystallisation with unprecedented sensitivity and time resolution at the beamline **ID02** using combined small-angle and wide-angle X-ray scattering (SAXS/WAXS, respectively). We have followed identical crystallisation protocols as in the previous studies and in addition we precisely determined the isothermal condition (t_{Iso}=0) from the scattered intensity itself. **Figure 57** shows the onset of the

evolution of normalised SAXS and WAXS intensities as a function of isothermal time (t_{Iso}). The most striking feature of this plot is the clear evolution of WAXS signal prior to SAXS in contrast to previous experimental reports. The initial WAXS intensity appeared as a relatively broad peak and the SAXS signal started to evolve significantly after the emergence of nearly sharp diffraction peaks in WAXS.

Figure 58 presents the evolution of the scattering invariant (Q_I) and crystallinity (X_C) calculated from the normalised SAXS and WAXS intensities, respectively. Qualitatively, both quantities follow an exponential type growth, identical to the Avrami function conventionally used to describe crystallisation kinetics. However, an important feature in **Figure 58** is that the initial growths of X_C and Q_I significantly deviate from the Avrami behaviour as shown in the inset. The unprecedented sensitivity allowed us to detect the initial level of X_C, which appeared as broad peaks in the WAXS pattern prior to the onset of significant evolution of SAXS intensity. This plateau in crystallinity could be originating from the so-called baby nuclei observed in computer simulations [2]. In this metastable state, only the most favourable nuclei survive while nascent nuclei appear spontaneously resulting in a constant level of crystallinity (t_{Iso} < 30 s). The semi-crystalline lamellar morphology is destined at the following stage.
As depicted in the inset of **Figure 58**, X_C and Q_I follow power-law type growths, $t_{Iso}^{3/2}$ and t_{Iso}^{3}, respectively. For constant thickness of lamellae, $X_C \propto t_{Iso}^{3/2}$ corresponds to a lateral growth of lamellae by $t_{Iso}^{3/4}$ analogous to that seen in computer simulations [1]. The growth kinetics at subsequent stage is adequately described by the Avrami function with an exponent, $n \sim 1$ that implies high crystal nucleation rate and short induction period. The limit of detection usually reported in the literature is indicated by the green dotted line in **Figure 58**. This could explain why the SAXS intensity evolved prior to the onset of WAXS signal in previous experiments [2].

In conclusion, the unprecedented sensitivity realised in SAXS/WAXS experiments allowed us to detect the primary nucleation events in polymer crystallisation from melt. The crystalline lamellar long period is affixed at this early stage and the crystallisation kinetics follow the classical nucleation and growth behaviour. Furthermore, the growth exponent n depends on a whole host of parameters, in addition to the dimensionality of crystal growth as demonstrated by models involving cluster distribution rate equation.

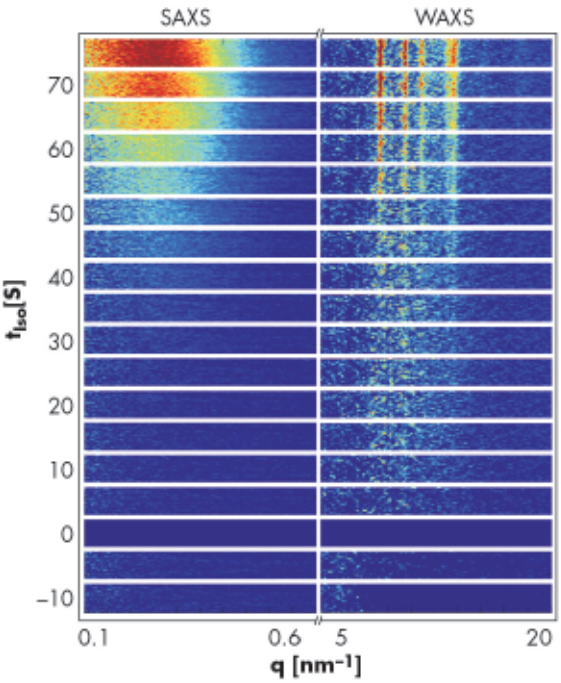

Fig. 57: Azimuthal sectors of SAXS and WAXS patterns recorded simultaneously following a rapid temperature quench to the crystallisation temperature of 145°C (t_{Iso} evolves after the sample reached the isothermal condition). The diffraction from crystalline (WAXS) nuclei is evident prior to significant evolution of SAXS. From each frame the melt background (t_{Iso}=0) has been subtracted.

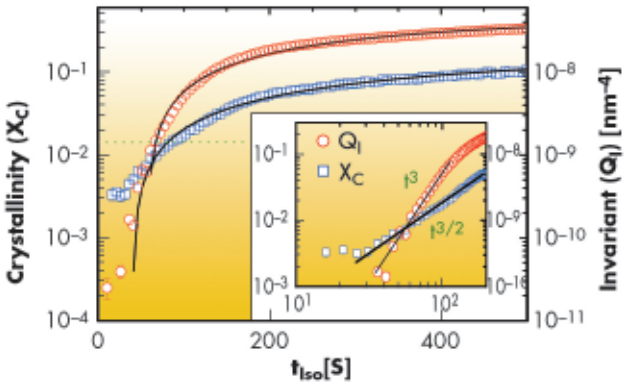

Fig. 58: Evolution of crystallinity and SAXS invariant during the early stages. The continuous lines show Avrami type growth kinetics with $n \sim 1$ and $\tau_C \sim 323$ s and 486 s for SAXS and WAXS, respectively. The inset depicts power-law growth of X_C and Q_I after 30 s of reaching the isothermal condition. The horizontal dotted green line depicts typical detection limit realised in previous experiments.

References
[1] A. Keller and S.Z.D. Cheng, *Polymer* **39**, 4461 (1998).
[2] M. Muthukumar, *Adv. Polym. Sci.* **191**, 241 (2005) and references therein.

Principal publication and authors
D. Sen (a,b), O. Spalla (a), O. Taché (a), P. Haltebourg (a), A. Thill (a) *Langmuir*, 23, 4296 (2007).
(a) LIONS, CEA Saclay (France)
(b) Bhabha Atomic Research Center, Mumbai (India)

Self-organisation during a drying process for porous grains

The synthesis of ordered, homogeneous porous grains is an expanding area of materials research. One strategy for their formation is to dry the spray of a complex mixture containing nanoparticles and templating agents [1]. In this process, a continuous flow of micrometric droplets, made from the initial dilute solution, is dried along a hot tube in order to evaporate the solvent. Self-organisation of the constituents takes place during the evaporation. Organic moieties can even be removed via further calcination. The local structure of the final grains strongly depends on the initial compositions.

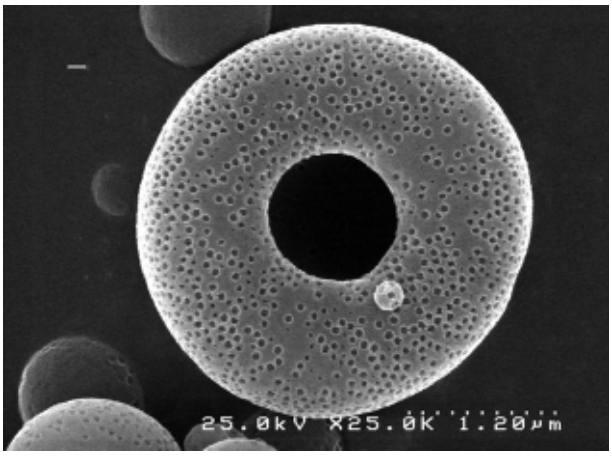

Fig. 59: Example of a doughnut-like grain obtained upon drying a solution containing a mixture of 5 nm silica nanoparticles with 50 nm polybromostyrene sulfonate. The grain was observed before complete calcination.

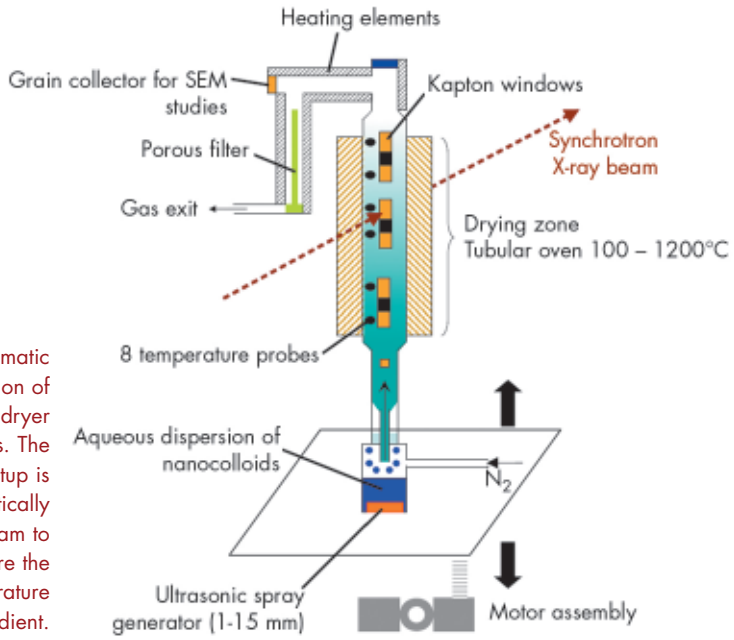

Fig. 60: Schematic representation of the spray dryer apparatus. The whole setup is displaced vertically through the beam to explore the temperature gradient.

Small-angle X-ray scattering can be used to investigate the ordered structural features of the final spray-dried grains at the nanometric scale [2]. However, the morphology of the grains at a larger scale depends critically on the kinetics of drying.

Two different regimes may be distinguished for the solvent evaporation from a complex nanoparticles solution confined in a droplet. Firstly, when the evaporation front moves faster than the time required for a particle to diffuse on the length scale of the drop, the grains may be heterogeneous. The final grains can be doughnut-like or even core-shell with an empty space inside, which has sometimes been observed by scanning electron microscopy (SEM). Secondly, when the drying is slower than the characteristic diffusion time of the nanoparticles, the evaporation occurs in a quasi equilibrium distribution of the nanoparticles inside the droplet and the formation of a dense spherical grain is anticipated.

For a solution containing a mixture of 5 nm silica nanoparticles with 50 nm polybromostyrene sulfonate we found that a large proportion of doughnuts were obtained, even when a slow evaporation rate was used (Peclet number $Pe = \tau_{dif}/\tau_{evap} = 0.01$). One of the doughnuts is shown **Figure 59**. Together with the sphere-doughnut transition, the inner homogeneity of this type of material remains a crucial question for their further applications.

A complete measure of the structure by SAXS at the absolute scale is one way to obtain a quantitative investigation of the homogeneity. Moreover, the evaporation and the related organisation of nanoparticles can be probed *in situ* thanks to the high brilliance of the light source. Therefore our aim was to investigate the organisation at different scales during the complete drying sequence. Experiments were performed at

beamline **ID02**, where a vertically mobile spray-drying system was set up (**Figure 60**). It allowed the whole process of grain drying and organisation to be traced directly inside the hot tube. A spray ($\Phi_{Droplets}$=0.07%) of very dilute (Φ_{SiO2}=2%) aqueous suspension of nanosilica (25 nm) was generated. After the evaporation profile reached equilibrium, the spray structure was scanned vertically along 50 cm of the tube (along which the temperature rose from 25°C to more than 100°C).

Figure 61 presents the evolution of I(q) when the system transforms from a dilute suspension of nanoparticles to densely-packed dried grains, the whole process occurring in 20 seconds.

From a quantitative model that takes into account the kinetics of evaporation inside the tube and the size distribution of the initial droplets in the spray, we are able to conclude that the compression is isotropic for the conditions (200-600°C) at which this spray system (and many others) usually work. Moreover, the occurrence of a layered morphology with a dense shell around a dilute core was invalidated since the quantitative variation of the scattering profile for such a case did not follow the experimental evolution of the scattering data (**Figure 61**) unlike the isotropic compression case as mentioned before. The source of the sphere-doughnut transition on a larger scale is yet to be found. However, slow drying does allow organised powders to be obtained, where pretty hexagonal organisation can be observed from the core to the surface of the grains [2].

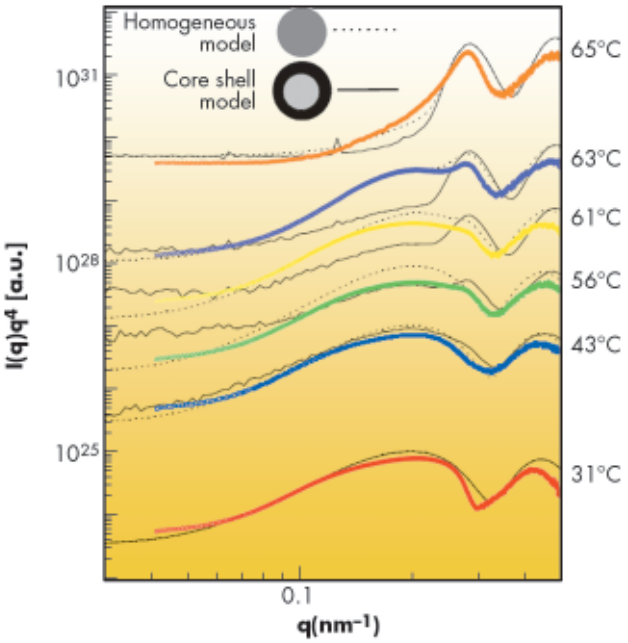

Fig. 61: Porod plots of the scattered intensity at different heights in the drying tube (corresponding to increasing temperatures). The doted lines represent the fit by a model taking into account the slow evaporation of water from the droplets, allowing a full reconformation of the nanoparticles inside the wet droplets until completion of the drying process.

References
[1] F. Iskandar, K. Mikrajuddin Okuyama, *Nano Lett.* **1**, 231 (2001).
[2] D. Sen, O. Spalla, L. Belloni, T. Charpentier, A. Thill, *Langmuir* **22**, 3798 (2006).

Intermediate steps in the mercerisation of a single cotton fibre

Principal publication and authors
J. Schoeck, R.J. Davies, A. Martel, and C. Riekel, *Biomacromolecules* **8**, 602-610 (2007).
ESRF

The transformation of cellulose I into cellulose II by aqueous NaOH is a commercial process known as "mercerisation". Mercerised cotton fibres exhibit a more appealing luster, greater tensile strength, and uptake dye more easily than their untreated counterparts. The conversion of cellulose during mercerisation involves at least one (possibly more) intermediate Na-cellulose crystalline phases. The study of these intermediate phases is of particular interest both from an academic and a commercial perspective. Current techniques to study these intermediate phases lack either spatial resolution (X-ray diffraction on fibre bundles) or have to be performed *ex situ* on ultrathin sections (electron diffraction). In contrast, X-ray microdiffraction at the **ID13** beamline provides the possibility of working *in situ* on single cotton fibres during the conversion process. The cotton fibre was kept under a slight tension during the conversion process and the formation of Na-cellulose was initiated locally by creating a NaOH-drop by using an inkjet system head. The high surface tension of the tiny NaOH-drop, about 300 micrometres diameter, keeps it attached to the cotton fibre (**Figure 62a**). Aqueous NaOH, diffusing from the drop into the fibre, becomes increasingly concentrated along its diffusion path as the fibre is

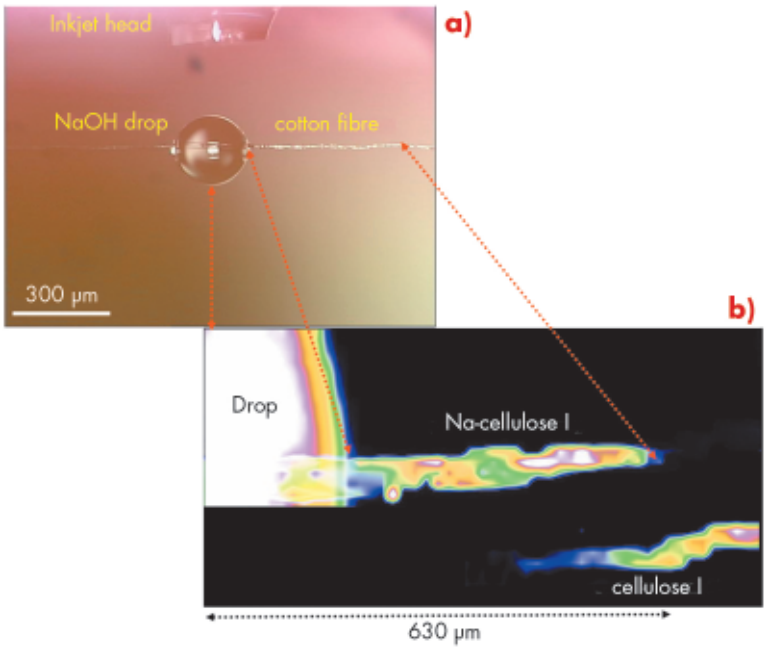

Fig. 62: a) Optical image of inkjet system head and NaOH-drop on single cotton fibre. b) composite image based on 002 intensities of Na-cellulose I and cellulose I. This allows a localisation of the cellulose I/Na-cellulose I conversion zone along the fibre. The cellulose I phase has been displaced vertically for better visibility.

permeable to water vapour. The extent of Na-cellulose I formation was studied by a mesh-scan along the reaction zone of the fibre with a submicrometre-sized beam. The extent of conversion of cellulose I into the crystalline Na-cellulose I phase could be easily determined from the intensities of the 002 Bragg reflections of both phases (**Figure 62b**). Future experiments will be performed at higher temperatures and will involve a washing step using a second inkjet system head, which would allow the study of the complete mercerisation process.

Structural Biology

Introduction

Macromolecular crystallography (MX) provides key information to advance basic research in biology and chemistry. MX drives forward biomedical research by informing on structure-function relationships of proteins and nucleic acids relevant to health, or pharmaceutical development. In the past year, the beamlines at ESRF have continued to support the pharmaceutical industry, helping them to carry out their research. The community sees little of this research but it remains nevertheless an important ESRF activity.

What the research community does see is the impressive output of publications, seminars or lectures founded on ESRF generated results. It is increasingly difficult to identify only a few highlights because of the high level of activity in structural biology in Europe for many important areas of biology. The increased efficiency and automation of synchrotron data collection at the ESRF are a major driving force in structural biology and certainly key in ensuring that European MX research remains internationally competitive. This is brought home in particular to the MX-Beamtime Allocation Panel (BTAP) review committee who see the results from the user community, and the publication lists including all of the top science journals, general and specialised. The success presents the MX-BTAP and the ESRF with a challenge. The continued growth of the structural biology community, oversubscription of beamlines and the need to continually update and improve facilities has placed a strain on the allocation of resources and it is a difficult juggling act to ensure researchers get beamtime sufficient for their needs. The user community has a duty here to help, and the efficiency of the BAG system might usefully be exploited by more laboratories.

That aside, now for some highlights. Success throughout Europe in the past year is impressive and we could fill this entire report solely with structural biology. Space restrictions mean we only present a subjective snapshot of ESRF research and we include examples from both the ESRF external and the in-house research programmes.

Irregularities in phosphotinositade 3-kinases occur frequently in many cancers, Miled *et al.* (p59) present a model for the structure of one such kinase - PI3Kα - in complex with a partner molecule. This complex reveals the location of the cancer inducing mutations and allows a description for the consequences of these mutations to be proposed. Niemann *et al.* (p60) have resolved the crystal structures of the bacterial surface protein InlB and the activating kinase Met, this complex initiates cell invasion in the human pathogen *Listeria monocytogenes*. The crystal structure reveals an unexpected region of contact between the partner proteins – an interaction which appears to be essential for activation of Met, presumably via a stable structural reorganisation upon complex formation. On a similar theme the entry of viruses into their hosts requires the virus to bind to one or more receptors on the host cell surface; fusion of the virus and host membrane follows. Vesticular stomatis virus (VSV) contains a single transmembrane glycoprotein that is responsible for both receptor recognition and membrane fusion. Roche *et al.* (p61) present the structure of this protein, VSV G, in different states. The ensemble of models reveals the spectacular structural rearrangements that the

protein undergoes in order to perform its functions.

The influenza virus remains a potent risk to human health. A search for an effective treatment has focussed on understanding the function of the polymerase responsible for transcription and replication of the viruses RNA genome. Using a novel technological approach Tarendeau *et al.* (p63) identified an unsuspected domain at the C-terminus, this domain plays a role in the localisation of the polymerase and offers some ideas for the mechanisms of transfer of influenza viruses to humans. Also using novel technology of a completely different form, Katona *et al.* (p64) deployed Raman spectroscopy to provide new data to elucidate the mechanism of Fe-superoxide reductase. The iron provides the oxidative centre in the enzyme and the Raman spectroscopy experiments allowed the reaction intermediates to be resolved and a reaction mechanism proposed.

Homologous recombination of DNA plays an important role in genetic diversification and the repair of DNA lesions. Bacteria employ a number of mechanisms to effect this action, and employ two major protein complexes: RecBCD (ESRF Highlights 2005) and RecFOR. Timmins *et al.* (p66) have determined the structure of the complex formed between RecR and RecO and proposed a model for the supercomplex that would be assembled as the RecRO complex binds to damaged DNA. Recombination and rearrangement of DNA is a ubiquitous biological activity and the key step is the formation of a four-way DNA junction – a Holliday junction. Hadden *et al.* (p69), determined the structure of a Holliday junction in complex with the protein partners necessary for resolving the junction. Their structure was the result of extensive screening for crystallisation and made significant use of the microfocus capabilities of the ESRF MX beamlines. The structure reveals a complex suggestive of extensive structural changes employed to ensure successful organisation of the DNA.

The cellular response to stress is a vital component of adaptation to environmental change for prokaryotic and eukaryotic cells. The signalling pathways that have evolved are sophisticated and require precise temporal regulation to maintain cell viability. MAPK kinases are responsible for the transduction and amplification of signals via phosphorylation. The MKP family of proteins dephosphorylate and deactivate MAPK kinases. In an apparent contradiction MKPs contain a catalytic cysteine sulphydryl group that is sensitive to oxidation. Thus one may expect that, under conditions of oxidative stress, MKPs would become oxidised and loose the ability to regulate MAPKs. To investigate the way in which Nature has handled this dilemma, Fox *et al.* (p67) studied an MKP under both oxidising and reducing conditions revealing the mechanism by which this family maintains activity under conditions of oxidative stress.

Drugs targeting the integral membrane protein leukotriene C_4 synthase (LTC_4S) are important targets for treatment of asthma. The structure of LTC_4S was determined by Martinez Molina *et al.* (p70) and revealed a protein that despite its relatively small size is able to recognise substrates with widely different chemical properties and which plays a crucial role in delivering these substrates to a lipid for conjugation. Translocation of proteins across membranes is a cellular function that is conserved throughout the kingdoms of life. A variety of mechanisms to perform this function are employed in Nature, including the two partner secretion system (TPS), which secrete large proteins that may serve as virulence factors. The structure of the transporter that secretes the *Bordetella pertussis* adhesion filamentous hemaglutanin, reveals a dynamic pore protein and allowed Clantin *et al.* (p72) to propose a mechanism of action.

The highlights reveal a number of elements shared with other projects not included here. Many projects required extensive screening, often requiring many hundred of crystals to be analysed and efficient automation is essential for success. The relatively low resolution of diffraction in some projects requires optimisation of experiments and the use of microbeams is mandatory. Projects require access to multiple complementary beamlines so each aspect of the structure determination process and the biological interpretation can be optimised. These themes are addressed in the proposals for the upgraded ESRF and maintenance of the ESRF's successful user programme will require careful organisation and optimisation of MX resources.

W.N. Hunter *(University of Dundee, UK) and* ***S. McSweeney***

Molecular mechanisms of oncogenic mutations in the phosphoinositide 3-kinase catalytic subunit

Principle publication and authors
N. Miled (a,b), Y. Yan (c), W-C. Hon (a), O. Perisic (a), M. Zvelebil (d), Y. Inbar (e), D. Schneidman-Duhovny (e), H.J. Wolfson (e), J.M. Backer (c) and R.L. Williams (a), *Science* **317**, 239 (2007).
(a) MRC Laboratory of Molecular Biology, Cambridge (UK)
(b) Laboratoire de Biochimie et de Génie Enzymatique des Lipases, Ecole Nationale d'Ingenieurs Sfax (Tunisia)
(c) Albert Einstein College of Medicine, NY (USA)
(d) Ludwig Institute for Cancer Research, London (UK)
(e) School of Computer Science, Tel Aviv University (Israel)

Acknowlegements
We thank M. Waterfield and B. Vanhaesebroeck for the p110α plasmid, A. McCarthy for help at ESRF beamline ID14-4, and M. Girvin and G. Gerfen for helpful discussions. The work was supported by AstraZeneca (RLW), MRC (RLW) and NIH GM55692 (JMB).

Phosphoinositide 3-kinases (PI3Ks) and their lipid product, phosphatidylinositol-(3,4,5)-trisphosphate (PtdIns(3,4,5)P_3), play key roles in many cellular processes [1,2]. Aberrations in PtdIns(3,4,5)P_3 levels, either through activation of PI3Ks or through inactivation of the lipid phosphatase PTEN, occur frequently in numerous forms of cancers. For example, recent data suggest that at least 50% of human breast cancers involve mutations in either PI3Kα or PTEN [3,4]. Cancer-causing mutations increase the activity of PI3Kα. This enzyme is composed of a 110 kDa catalytic subunit (p110α) and a tightly-associated regulatory subunit (p85). The effect of the regulatory subunit binding to the catalytic subunit is to stabilise the latter and to decrease its basal activity. The catalytic and regulatory subunits interact via the N-terminal adaptor-binding domain (ABD) of the p110α subunit and the coiled-coil region between the two SH2 domains of the regulatory subunit, *i.e.*, the iSH2 domain. Our crystallographic work carried out at beamline **ID14-4** resulted in the structure of a complex of the ABD with the iSH2 domain (**Figure 63**). Based on this structure and a model of the catalytic core of p110α derived from our earlier work at the ESRF [5], we devised a model of the minimum regulated p110/p85 heterodimer. We find that cancer-causing mutations in the ABD are not at the interface of the ABD and the iSH2 domain, and our model of the intact heterodimer suggests that such mutations may affect how the ABD interacts with the remainder of the p110 catalytic subunit.

Our model also suggested a mechanism for the functioning of a second type of cancer-causing mutation in p110α. Hot-spot cancer-causing mutations in the helical domain of the p110 catalytic subunit eliminate negative charge in a small region on the surface of the helical domain. Based on our model of the heterodimer, we proposed that in the wild type enzyme this negative patch interacts with positive charges on the surface of the N-terminal of the two SH2 domains (nSH2) in the regulatory subunit and this results in inhibition of the basal activity of the catalytic subunit (**Figure 64**). Eliminating negative charges in this area of the helical domain would lessen the interactions between the two domains and result in a loss of inhibition of the catalytic subunit by the regulating subunit. We tested this hypothesis by constructing a regulatory subunit in which we swapped key positive charges for negative ones. We found that this mutant

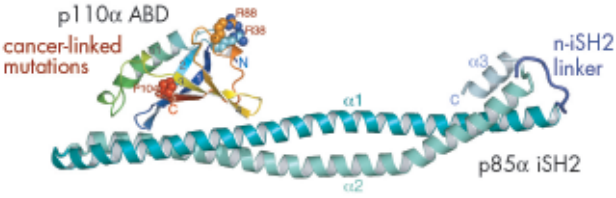

Fig. 63: A Ribbon representation of ABD/iSH2 heterodimer. The three residues in the ubiquitin-like ABD that were identified as sites of somatic mutations in colon cancers (shown in spheres) are not at the interface of the ABD with the coiled-coil iSH2 domain.

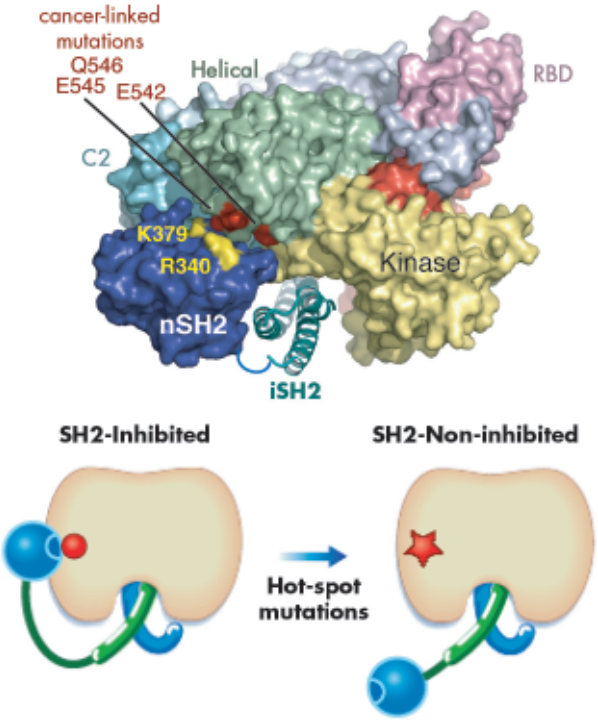

Fig. 64: A model illustrating the inhibitory contact between the nSH2 domain and the helical domain of p110α near the site of the helical domain hot-spot mutations (The p110α catalytic core was modelled on the p110γ catalytic core). R340 and K379 are part of a highly conserved phosphopeptide-binding surface on nSH2. Binding of nSH2 to the p110α helical domain and to phosphopeptide are mutually exclusive.

regulatory subunit inhibited the oncogenic form of the catalytic subunit, but not the wild type form of the catalytic subunit. These studies extend our understanding of the architecture of PI3Ks and provide insight into how two classes of mutations that cause a gain in function can lead to cancer.

References
[1] L.C. Cantley, *Science* **296**, 1655 (2002).
[2] M.P. Wymann, M. Zvelebil, M. Laffargue, *Trends Pharmacol Sci* **24**, 366 (2003).
[3] J. Luo, B.D. Manning, L.C. Cantley, *Cancer Cell* **4**, 257 (2003).
[4] L.H. Saal, K. Holm, M. Maurer, L. Memeo, T. Su, X. Wang, J.S. Yu, P-O. Malmström, M. Mansukhani, J. Enoksson, H. Hibshoosh, Å. Borg, R. Parsons, *Cancer Res.* **65**, 2554 (2005).
[5] E.H. Walker, O. Perisic, C. Ried, L. Stephens, R.L. Williams, *Nature* **402**, 313 (1999).

A bacterial key to host cell entry: Activation of the human receptor tyrosine kinase Met by a bacterial ligand

Principal publication and authors
H.H. Niemann (a), V. Jäger (a), P.J.G. Butler (b), J. van den Heuvel (a), S. Schmidt (a), D. Ferraris (a), E. Gherardi (b) and D.W. Heinz (a), *Cell* **130**, 235-246 (2007).
(a) Division of Structural Biology, Helmholtz-Centre for Infection Research, Braunschweig (Germany)
(b) MRC Centre and Laboratory of Molecular Biology, Cambridge (UK)

Listeria monocytogenes, a gram-positive, facultative intracellular human pathogen, employs the invasion protein InlB to enter normally non-phagocytic cells. This bacterial surface protein InlB binds to and activates the receptor tyrosine kinase Met on host cells [1]. Met activation leads to rearrangements of the actin cytoskeleton and ultimately causes uptake of *L. monocytogenes*. InlB is a multi-domain protein, but only its N-terminal half is essential for Met binding and activation. A capped leucine-rich repeat (Cap-LRR) domain of InlB harbours the high affinity Met-binding site and amino acids involved in InlB-Met interactions have been mapped to the concave face of the curved Cap-LRR [2]. Despite this high-affinity binding site, the Cap-LRR fragment of InlB alone cannot activate Met. Instead, activation additionally requires the so-called inter-repeat (IR) region, an immunoglobulin (Ig) like moiety that follows the Cap-LRR domain.

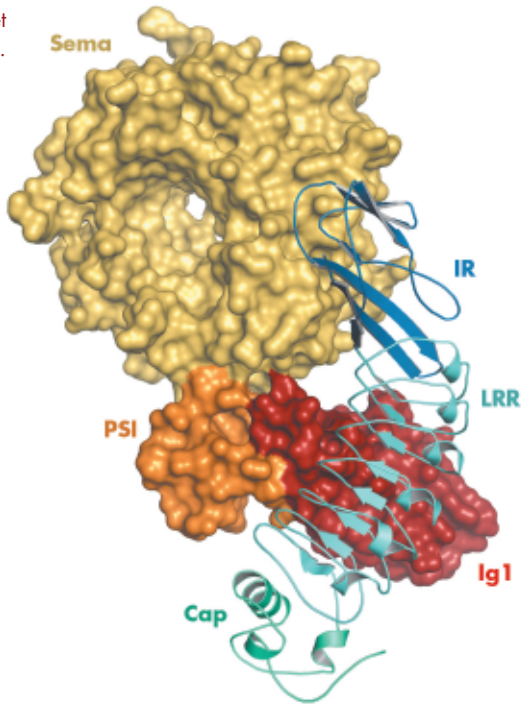

Fig. 65: Structure of the InlB/Met complex.

The extracellular domain of Met comprises a large seven-bladed β-propeller (Sema domain), a small cysteine rich domain (PSI) and four immunoglobulin-like domains (Ig1 – Ig4). Of these six domains the Sema domain exclusively binds the physiological Met ligand hepatocyte growth factor (HGF). Although a crystal structure of the Met Sema and PSI domains in complex with one domain of HGF has been solved [3], the mechanism of Met activation by HGF remains elusive. HGF and InlB can bind Met simultaneously [1], but the InlB-binding site on the ectodomain of Met was unknown. Likewise the structural basis of InlB mediated Met activation and the function of the IR region of InlB were unclear.

We determined the crystal structure of a complex between the Met-binding domain of InlB and a large fragment of the Met

ectodomain using data collected on beamline **ID23-2** (**Figure 65**). The kidney shaped InlB binds via the concave face of its Cap-LRR domain to the first immunoglobulin-like (Ig1) domain of Met. An unusual beta-hairpin extending from the core of Ig1 is pivotal for the interaction with InlB. This interface represents the primary contact between InlB and Met and involves five aromatic amino acid side chains that are exposed on the surface of InlB. The observed mode of binding is consistent with all biochemical data for InlB [1,2], but strikingly different from that of the physiological Met ligand HGF (**Figure 66**).

The structure additionally reveals an unexpected second region of contact between InlB and Met. This less prominent interface is formed between the InlB IR region and the Sema domain of Met (**Figure 65**). Binding studies had not predicted this contact, as it does not contribute measurably to binding affinity. However, it is essential for receptor activation. Comparison of our structure with that of HGF in complex with the Sema and PSI domains of Met reveals a dramatic conformational change in the Met ectodomain. The Met Sema domain undergoes a rigid body rotation of some 60° relative to its neighbouring PSI domain (**Figure 66**).

The arrangement of the Met domains in the complex with InlB is governed by the two-site interaction between both proteins and, therefore, represents a uniquely defined conformation. This assumption is confirmed by a second structure of the complex that we obtained in a different crystal form (data also collected on beamline **ID23-2**). The overall domain arrangement is very similar in both structures of the InlB/Met complex and the second interface between the InlB IR and the Met Sema domain is preserved. We, thus, propose that the rigid InlB acts as a "molecular clamp" and locks the otherwise flexible Met receptor into a defined, signalling competent conformation. Whether and how this InlB induced conformation results in the expected dimerisation of the Met ectodomain needs to be addressed by future investigations.

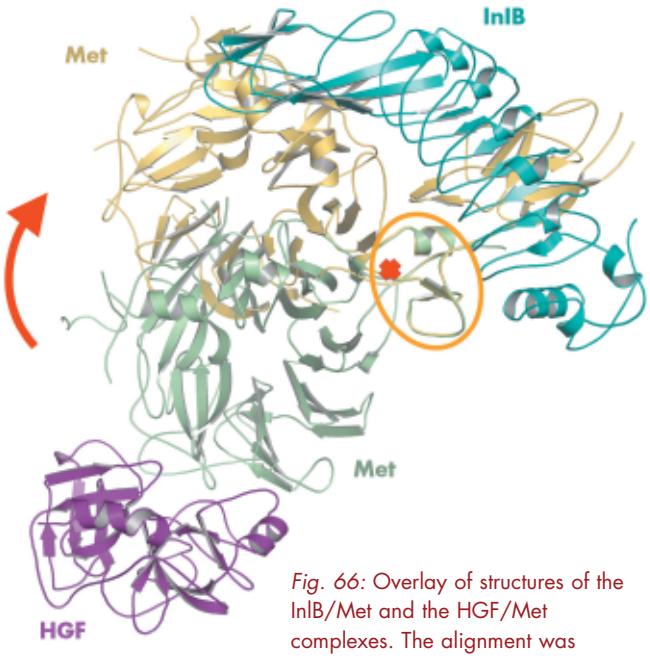

Fig. 66: Overlay of structures of the InlB/Met and the HGF/Met complexes. The alignment was performed on the PSI domain (marked by the orange oval).

References

[1] Y. Shen, M. Naujokas, M. Park, and K. Ireton, *Cell* **103**, 501–510 (2000).

[2] M.P. Machner, S. Frese, W.D. Schubert, V. Orian-Rousseau, E. Gherardi, J. Wehland, H.H. Niemann, and D.W. Heinz, *Mol. Microbiol.* **48**, 1525–1536 (2003).

[3] J. Stamos, R.A. Lazarus, X. Yao, D. Kirchhofer, C. and Wiesmann, *EMBO J.* **23**, 2325–2335 (2004).

Structure of the prefusion form of the vesicular stomatitis virus glycoprotein G

Entry of enveloped viruses into host cells requires binding of the virus to one or more receptors present at the host cell surface followed by fusion of the viral envelope with a cellular membrane. Activation of the fusion capacity involves large structural rearrangements of fusogenic glycoproteins upon interaction with specific triggers (*e.g.* low pH or cellular receptors). These conformational changes result in the exposure of a fusion peptide or fusion loops, which then interact with one or both of the participating membranes resulting in their destabilisation and merging [1].

Rhabdoviruses are enveloped viruses with a single-stranded non-segmented RNA genome of negative polarity. Vesicular stomatitis virus (VSV) is the prototype of the family. Its membrane contains a single transmembrane glycoprotein (G) that is involved in both receptor recognition and membrane fusion. Fusion is triggered by low pH-induced structural rearrangements during which G shifts from a prefusion native state to a postfusion conformation. In sharp contrast to fusogenic glycoproteins from other viral families, this low-pH induced conformational change is reversible: there is a pH

Principal publication and authors

S. Roche, F.A. Rey, Y. Gaudin, S. Bressanelli, *Science* **315**, 843 (2007).

UMR-CNRS 2472, UMR-INRA 1157, Laboratoire de Virologie Moléculaire et structurale, Gif sur Yvette (France)

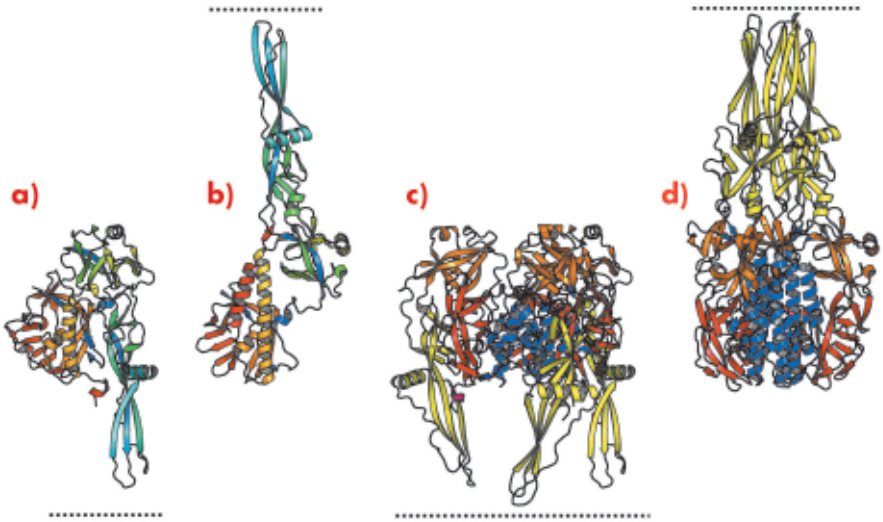

Fig. 67: Ribbon representation of the G protomer (a, b) and trimer (c, d) in both prefusion (a, c) and postfusion (b, d) conformations. Protomers are coloured by residue number in a gradient from blue (N terminus) to red (C terminus). Trimers are coloured by domain (lateral domain: red, trimerisation domain: blue, pleckstrin homology domain: orange, fusion domain: yellow) with the C-terminus in magenta. Pre- and post-fusion forms are superimposed on the rigid blocks made of the lateral domain and the invariant part of the trimerisation domain. The lipid bilayer, in which the transmembrane domains are anchored, is indicated by the dotted line.

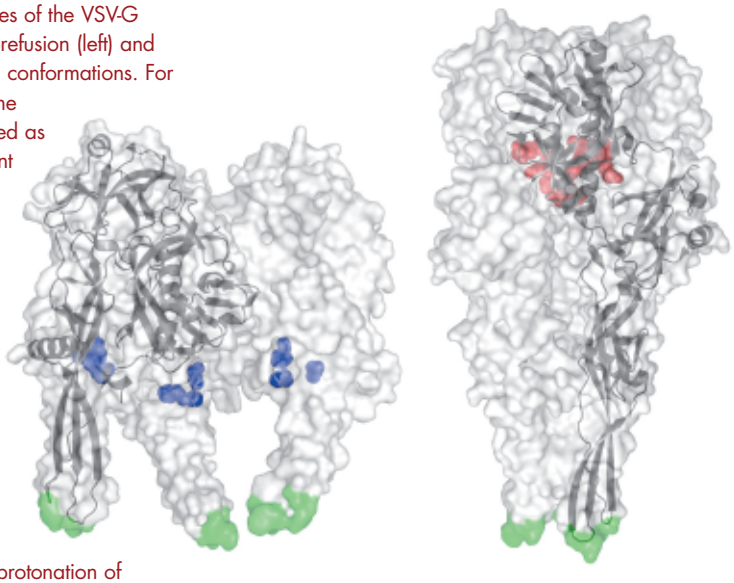

Fig. 68: Structures of the VSV-G ectodomain in prefusion (left) and postfusion (right) conformations. For each structure, the trimer is displayed as a semitransparent white surface with the fusion loops in green and a protomer is also drawn in black in ribbon represention. Despite its magnitude, the pH-triggered conformational change is fully reversible, with protonation of the histidine side chains (shown in blue) starting the forward transition and deprotonation of the aspartates and glutamates (red) driving the backward transition.

dependent equilibrium between the different conformations of G that is shifted toward the postfusion state at low pH [2].

We have previously determined the low pH, post-fusion, 3D structure of the VSV G ectodomain generated by limited proteolysis of the virions. It remained unclear to what extent the pre- and post-fusion conformations differ and thus we have also determined the structure of the prefusion form of VSV G. Comparison of the pre- and postfusion structures of VSV G reveals a dramatic reorganisation of the molecule that probably constitutes the largest reversible conformational change ever described for a protein (**Figure 67**). During the conformational change, three domains of G (out of four) retain their tertiary structure. Nevertheless, they undergo large rearrangements in their relative orientation due to secondary structure changes in hinge regions. The fourth domain, that is involved in the trimerisation of both the pre- and the post-fusion conformation, undergoes a major refolding event that includes large changes in its secondary structure (**Figure 67c** and **67d**).

Furthermore, we have previously identified acidic amino acid residues that are brought together in the central six helix bundle in the post-fusion (low pH) state [3]. In this conformation, they are protonated and participate in hydrogen bonds. The deprotonation of these residues at higher pH will induce strong repulsive forces that destabilise the trimer and initiate the conformational change back to the prefusion state (in which these residues are solvent exposed). Conversely, the prefusion structure revealed a conserved cluster of three histidines that could play the role of a pH sensitive molecular switch. Indeed, low pH–induced protonation of these residues leads to a cluster of positive charges that might trigger the movement of the fusion domain toward the target membrane (**Figure 68**).

Finally, it is noteworthy that in the case of rhabdoviruses, the pH dependent equilibrium between pre and post-fusion conformations of G indicates that the energy released during the structural transition of one trimer cannot be sufficient to overcome the energetic barrier and drive the fusion reaction. Indeed, the minimal number of spikes involved in the formation of a RV fusion complex has been estimated to be about 15 [2]. Interestingly, the crystalline form (P622) of the prefusion form reveals the ability of G to adopt a planar p6 lattice. We propose that such a local hexagonal lattice at the viral surface might organise the glycoproteins in an optimal manner for a concerted conformational change that can be used to overcome the high energy barrier encountered during fusion.

References
[1] W. Weissenhorn, A. Hinz, Y. Gaudin, *FEBS Lett.* **581**, 2150 (2007).
[2] S. Roche, Y. Gaudin, *Virology* **297**, 128 (2002).
[3] S. Roche, S. Bressanelli, F.A. Rey, Y. Gaudin, *Science* **313**, 187 (2006).

Structure and nuclear import function of the C-terminal domain of influenza virus polymerase PB2 subunit

Principal publication and authors
F. Tarendeau (a), J. Boudet (b), D. Guilligay (a), P. Mas (a), C. Bougault (b), S. Boulo (c), F. Baudin (c), R.W.H. Ruigrok (c), N. Daigle (d), J. Ellenberg (d), S. Cusack (a), J.-P. Simorre (b) and D.J. Hart (a) *Nat Struct Mol Biol.* **14** 229-33 (2007).
(a) EMBL, Grenoble (France)
(b) IBS, Grenoble (France)
(c) UVHCI, Grenoble (France)
(d) EMBL, Heidelberg (Germany)

The trimeric influenza virus polymerase, comprising subunits PA, PB1 and PB2, is responsible for transcription and replication of the segmented viral RNA genome [1]. It is of significant interest because structural characterisation may permit design of a new class of anti influenza drugs, and because mutations of the subunits can lead to avian-to-human infection. Despite intensive work, structural studies have been prevented by an inability to express the proteins, either individually or as a complex.

Using a novel random library screening technique for "difficult-to-express" proteins called ESPRIT (Expression of Soluble Proteins by Random Incremental Truncation), developed at the EMBL, we screened 27,000 genetic constructs to identify an independently folded C-terminal PB2 domain (**Figure 69**). The structure was initially solved by NMR at the IBS (**Figure 70**) revealing a well-packed domain containing three surface residues implicated in adaptation from avian to mammalian hosts. Analysis of the sequence of the flexible C-terminus suggested the presence of a previously overlooked bipartite nuclear localisation sequence (NLS). This putative function was confirmed using GFP (green fluorescent protein) fusions; we showed that both the domain and full-length PB2 subunit are efficiently imported into the nucleus dependent on the NLS (not shown). The 2.2 Å crystal structure of the domain complexed with human nuclear import factor importin α5 (data collected on beamline **ID23-1**) revealed how the last twenty residues of the domain unfold to permit binding within the superhelical groove of the importin in a classical manner (**Figure 71a**). A comparison of the two structures (**Figure 71b**) shows that one of the cross-species mutation residues (D701) tethers the NLS-containing peptide to the core of the domain in the unbound state via a salt bridge with Arg753. This interaction is broken when the NLS is unfurled during importin binding and suggests that the mutation D701N, observed in some pathogenic strains of influenza including H5N1 infecting humans in Vietnam [2], may alter the energetics of this interaction.

In conclusion, by exhaustive random construct screening, we identified an unsuspected domain at the C-terminus of

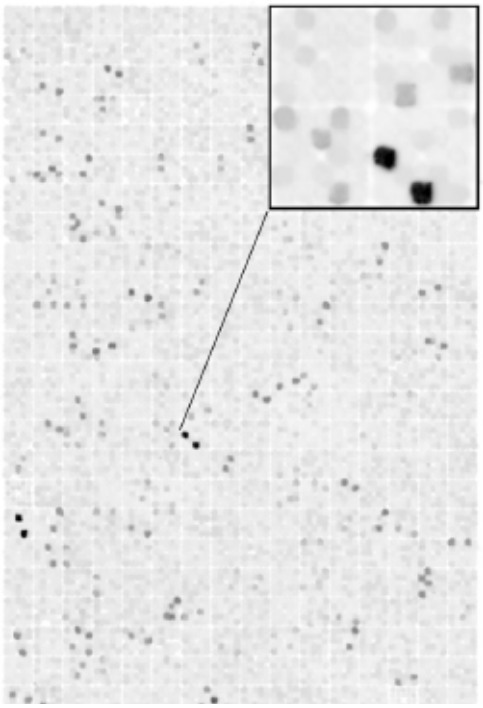

Fig. 69: Identification of PB2 C-terminal domain via a colony-based expression screen of 26,880 random deletion constructs of the *pb2* gene. Stable expression of soluble protein results in efficient *in vivo* labelling of a C-terminal biotin acceptor peptide. Detection is by fluorescent streptavidin and fluorimager.

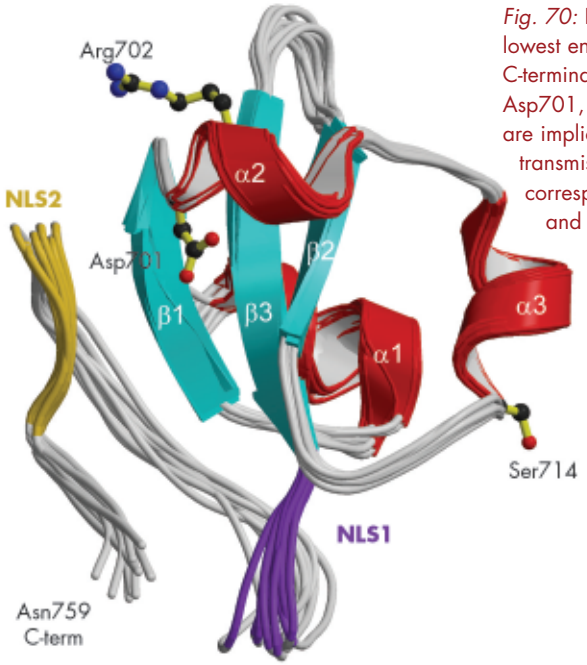

Fig. 70: Ribbon diagram of the 10 lowest energy NMR structures of the C-terminal PB2 domain showing Asp701, Arg702 and Ser714, which are implicated in cross-species transmission, and basic regions corresponding to the minor (purple) and major (gold) sites of the bipartite NLS.

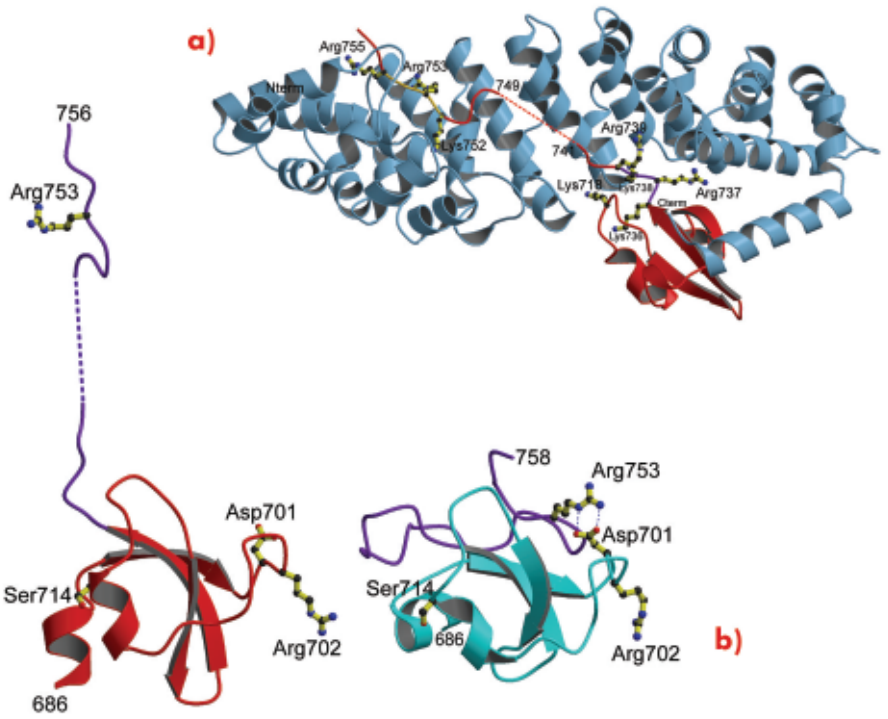

Fig. 71: X-ray structure of the PB2 C-terminal domain complexed with importin α5. (a) Ribbon diagram showing DPDE (red) bound to human importin α5 (slate blue) comprising 10 armadillo repeats. (b) Comparison of the PB2 domain structure in complexed (red) and free solution state (cyan) demonstrates unfolding of residues 736-759 (purple) upon binding to importin α5.

References
[1] D.L. Noah and R.M. Krug, *Adv. Virus Res.* **65** 121-45 (2005).
[2] M.D. de Jong, *et al. Nat Med* **12**, 1203-7 (2006).

the PB2 subunit and determined both the NMR solution structure of the isolated domain and the X-ray structure of a complex with the nuclear import receptor importin α5. Cell biology studies confirmed the role of the domain in nuclear localisation of the polymerase subunit. A comparison of the two structures sheds light on a new mechanism of avian-to-human transfer of influenza viruses, including some current H5N1 strains.

Principal publication and authors
G. Katona (a), P. Carpentier (a), V. Niviere (b), P. Amara (a), V. Adam (c), J. Ohana (a), N. Tsanov (a) and D. Bourgeois (a, c), *Science* **316**, 449-53 (2007).
(a) Institut de Biologie Structurale, Grenoble (France)
(b) iRTSV, CEA (France)
(c) ESRF

Raman-assisted crystallography provides insight into the mechanism of superoxide reductase

The "superoxide radical" ($O_2^{\bullet-}$) is a cytotoxic by-product of oxygen metabolism. In humans, about 2% of the oxygen taken in during breathing is transformed into $O_2^{\bullet-}$ instead of water. The amount of $O_2^{\bullet-}$ produced is increased in patients affected by neurodegenerative diseases such as Alzheimer's, resulting in a worsening of these illnesses. Scientists are therefore looking for drugs to eliminate the superoxide radical.

Superoxide reductase (SOR) is an iron containing metalloenzyme that eliminates the superoxide radical in some

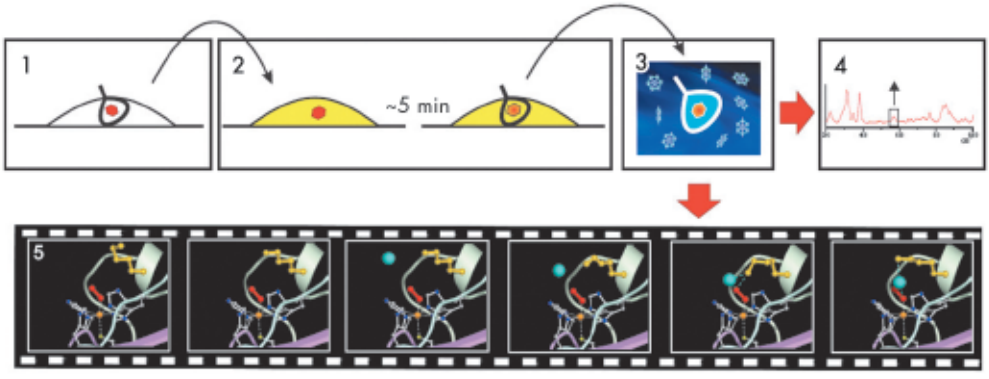

Fig. 72: Kinetic crystallography of superoxide reductase allowed a tentative film of the reaction pathway to be produced.

microaerophilic bacteria and archaea. Although it differs from its counterpart in humans, superoxide dismutase (SOD), SOR carries out a simpler reaction than SOD. Understanding the chemical tricks used by this enzyme is not only of fundamental interest in the field of iron biochemistry, but could also open new avenues for developing drugs.

Kinetic crystallography [1] was used to study the catalytic cycle of SOR, in collaboration with the team of V. Nivière (CEA/iRTSV, Grenoble, France). A stroke of luck allowed us to produce a movie of SOR in action (**Figure 72**). In a single crystal of a SOR mutant that specifically slows down catalysis, three intermediate states were trapped by freezing the sample at a certain time delay after the reaction was triggered. The existence of the three states in one crystal can be explained by the presence of nominally identical active sites in the crystal asymmetric unit that are surrounded by different packing environments, creating slight differences between them.

Before attempting a mechanistic interpretation of the trapped states, it was necessary to evaluate their biological relevance. With this in mind, we developed the technique of *in crystallo* Raman spectroscopy at the Cryobench laboratory [2,3]. This laboratory, developed in a close collaboration between the ESRF and the Institut de Biologie Structurale, is dedicated to complementing X-ray crystallography with *in crystallo* UV-visible spectroscopy [4]. Applying complementary techniques to the same sample appears increasingly important in understanding the relationship between structure, dynamics and function in biological macromolecules [5]. The central instrument of the Cryobench is a microspectrophotometer that allows the analysis of nano-volume samples (in the liquid or crystalline state) in conditions identical to those used on X-ray crystallography beamlines (**Figure 73**). In addition to absorption and fluorescence, we implemented Raman spectroscopy to identify specific chemical bonds in protein crystals. Raman spectra collected *in crystallo* are often instrumental in identifying intermediate states building up in the crystal, and in making sure that these states are not altered by X-rays during collection of diffraction data.

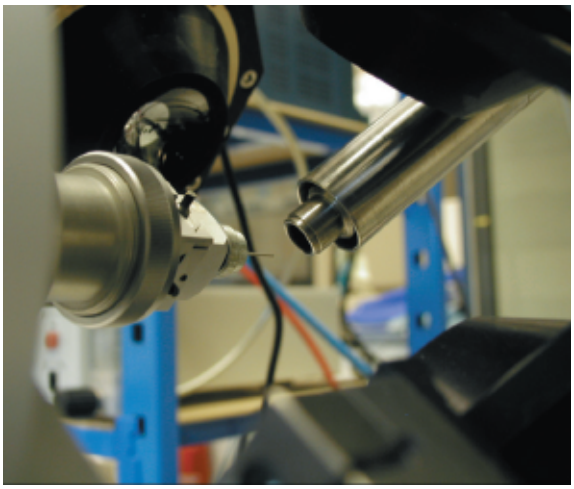

Fig. 73: Intermediate states can be trapped in protein crystals using spectroscopic monitoring at the Cryobench.

In the case of SOR, the Raman spectra collected on crystals provided evidence that the trapped states corresponded to iron-peroxide species also seen in solution, and were not altered by a moderate exposure to synchrotron X-rays. Thus we could confidently use the ~2.0 Å structures of the three intermediates to propose a mechanism for SOR function.

Several hypotheses to explain SOR activity have been previously inferred from biochemical studies. The binding mode of $O_2^{\bullet-}$, the role of key amino-acid residues, and the direct participation of a water molecule in catalysis were anticipated. The direct visualisation of these events now allows an understanding of how they fit together. We found that a key lysine residue moves around on the surface of the enzyme in order to grab a water molecule from the solvent. It then brings the water molecule into the enzyme active site, where it can donate a proton to the substrate bound in an "end-on" fashion (**Figure 72**). Puzzling questions remain, however, which will be addressed in future experiments. For example, when this lysine is mutated, the enzyme still functions, although at a slower rate: thus the mechanism suggested here might correspond to only one of several possible reaction pathways.

In conclusion, *in crystallo* Raman spectroscopy provides a complementary tool to X-ray crystallography, especially useful for researchers pursuing structural studies with mechanistic perspectives. The technique was used successfully to identify key iron-peroxide intermediates in the catalytic cycle of the non-heme enzyme superoxide reductase.

References

[1] D. Bourgeois and A. Royant, *Curr. Opin. Struc. Biol.* **15**, 1 (2005).

[2] P.R Carey and J. Dong, *Biochemistry* **43**, 8885 (2004).

[3] P. Carpentier, A. Royant, J. Ohana and D. Bourgeois, *J Appl Cryst* **40,** 1113 (2007).

[4] www.esrf.eu/UsersAndScience/Experiments/MX/Cryobench/

[5] T. De la Mora-Rey and C. Wilmot, *Curr. Opin. Struc. Biol.* **17,** 580 (2007).

Principal publication and authors
J. Timmins (a), I. Leiros (b) and S. McSweeney (a). *EMBO J.*, **26**, 3260-3271 (2007).
(a) ESRF
(b) The Norwegian Structural Biology Centre (NorStruct), University of Tromsø (Norway)

Structural insights into the early steps of homologous recombination in bacteria

DNA damage is a common occurrence that compromises the functional integrity of our genome. Well over 10,000 instances of DNA damage are estimated to occur daily in every human cell. The causative agents of the damage are mainly free radicals that are produced as natural by-products of food metabolism. If damaged DNA is left unrepaired, it generates mutations, replication errors, persistent DNA damage and genomic instability, which are ultimately associated with cancer and ageing. The mechanisms of DNA repair at a molecular level are largely unknown and a better understanding of the detailed mechanisms and principles underlying damage recognition in prokaryotes is an essential step towards obtaining a complete overview of the more complex human DNA repair systems. In prokaryotes, four repair pathways exist (homologous recombination, base-excision repair, nucleotide-excision repair and mismatch repair), all of which are essential for viability.

Homologous recombination, in addition to its fundamental role in genetic diversification of bacterial genomes, plays a key role in the repair of a variety of DNA lesions, including the lethal double-strand breaks. Initiation of homologous recombination can be carried out by either the RecBCD or the RecFOR proteins; in both cases these proteins act as mediators for RecA binding to single-stranded DNA in order to allow for homologous strand invasion. Genome sequence analysis of *Deinococcus radiodurans,* an outstanding bacterium capable of repairing and recovering from several hundred DNA double-strand breaks in its genome, has revealed that the genes encoding RecB and RecC proteins are missing, while all the genes encoding members of the RecFOR pathway (RecQ, RecJ, RecO, RecF and RecR) are present [1]. Inhibition of the RecFOR pathway in *D. radiodurans* increases the sensitivity of *D. radiodurans* cells to gamma-radiation, suggesting that RecFOR is essential for the repair of double-strand breaks.

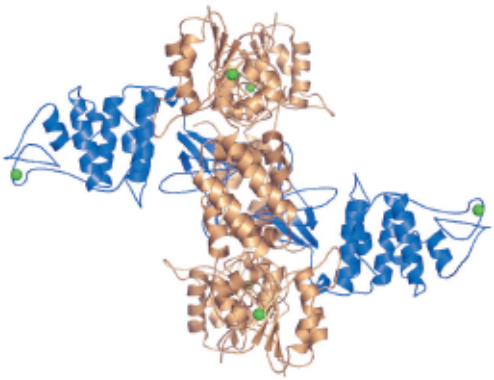

Fig. 74: Crystal structure of the hetero-hexameric complex formed between RecO (blue) and RecR (bronze). Zn^{2+} ions are illustrated as green spheres.

An increasing amount of structural information is becoming available for these proteins, which together with the biochemical and genetic data will no doubt improve our current understanding of the initial steps in homologous recombination. The individual crystal structures of RecF, RecO [2] and RecR from *D. radiodurans* have been solved over the past three years allowing the mapping of regions involved in protein-protein and protein-DNA interactions. To gain a better understanding of the detailed mechanisms involved in RecFOR-mediated recombination events, we have determined the crystal structure of the RecOR complex from *D. radiodurans* at 3.8 Å resolution using data collected at beamline **ID14-2**. The complex is a hetero-hexamer comprising two RecO molecules and four RecR molecules in which the RecO molecules are positioned on either side of the tetrameric ring of RecR, obstructing access to the interior of the ring (**Figure 74**). The interactions between RecO and RecR observed in our low resolution crystal structure were confirmed by mutagenesis and binding studies. This work identified a key ionic interaction between RecO and RecR as being essential for the stability of the complex. Furthermore, the structural data served as a framework for designing

mutants to investigate the ability of RecOR to bind DNA. Similar studies had previously been carried out using only the individual RecO and RecR proteins. This study revealed that two regions of the complex, one on RecO and another on RecR are critical for DNA binding. Both of these regions are located in the centre of the complex and would not be accessible for DNA binding in the configuration of RecOR observed in our crystal structure. Our mutagenesis and biochemical analyses taken together with the three-dimensional arrangement of the RecOR hetero-hexameric complex thus strongly indicate that a rearrangement of the complex needs to take place in order to allow DNA binding to occur. Chemical cross-linking studies indicate that RecOR most likely undergoes both local conformational changes and a larger architectural reorganisation upon binding to sites of double-strand break repair (**Figure 75**). Displacement of one of the two RecO molecules seems to be a prerequisite for DNA binding, but disruption of the tetrameric ring of RecR may also be needed.

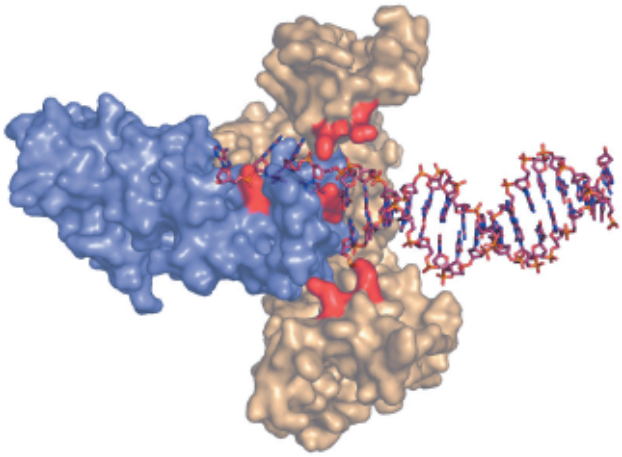

Fig. 75: Hypothesis of the binding of a structurally-rearranged hetero-trimeric complex of RecOR to double-stranded DNA with an extended single-stranded 3'overhang. Residues identified as being critical for DNA binding are coloured in red.

This study has shed light on the importance of studying protein complexes in addition to the individual proteins. Many of the features described for the single proteins were no longer observed within the context of the complex. Protein-protein and protein-DNA interactions are key to regulating many cellular processes. A better understanding of the processes regulating complex formation between the various Rec partners will certainly help in establishing the detailed sequence of events leading to RecA-dependent homologous recombination.

References
[1] O. White, *et al.*, *Science*, **286**, 1571-1577(1999).
[2] I. Leiros, J. Timmins, D.R. Hall, S. McSweeney, *EMBO J.*, **24**, 906-918 (2005).

Redox-mediated substrate recognition by Sdp1 defines a new group of tyrosine phosphatases

Eukaryotic organisms have evolved sophisticated cellular machinery that allows individual cells to respond to challenges, or stresses, coming from their environment. These stress-response systems work through a network of signal transduction pathways, which alert the cell to the presence of stress factors, and coordinate an appropriate response. Stress-response pathways can be triggered by a diverse range of stimuli that are potentially harmful to the cell, including UV radiation, oxidative and osmotic stress, heat shock and exposure to certain genotoxic substances. The physiological outcome can vary from a transient up-regulation of mechanisms to combat the immediate challenge, to growth arrest and programmed cell death – which prevents damaged cells from reproducing further. The fine control of this balance between cell survival and cell death has potential implications in the treatment of human cancers, as the cellular response to chemotherapeutic agents or radiotherapy may be partly orchestrated by stress-response mechanisms. This, together with studies that have linked components of mammalian stress-response pathways to tumorigenesis, has sparked interest in stress-response mechanisms in recent years.

At the heart of the signalling networks that sense cellular exposure to environmental stress is a highly conserved module known as the mitogen-activated

Principle publication and authors
G.C. Fox (a), M. Shafiq (b), D.C. Briggs (b), P.P. Knowles (b), M. Collister (b), M.J. Didmon (b), V. Makrantoni (b), R.J. Dickinson (b), S. Hanrahan (b), N. Totty (b), M.J.R. Stark (b), S. Keyse (b), N.Q. McDonald (b), *Nature* **447,** 487–492 (2007).
(a) BM16, ESRF
(b) Cancer Research UK

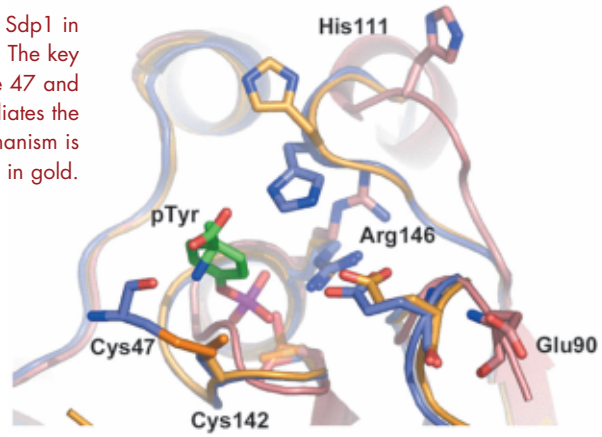

Fig. 76: The active site of Sdp1 in low and high activity states. The key disulphide between cysteine 47 and cysteine 142 that mediates the oxidative activation mechanism is shown in gold.

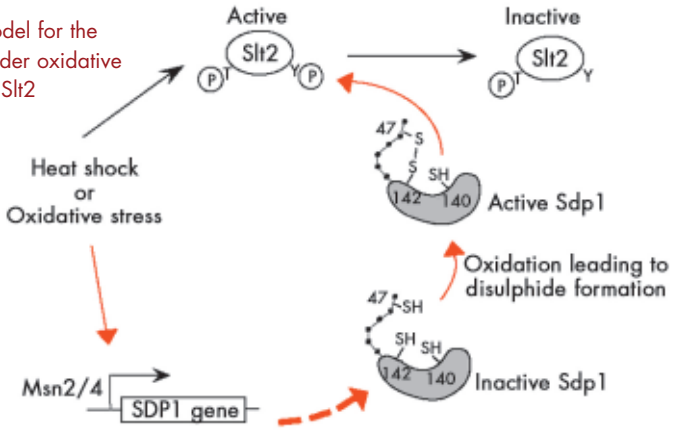

Fig. 77: Proposed model for the activation of Sdp1 under oxidative conditions leading to Slt2 dephosphorylation.

protein kinase (MAPK) cascade. The components of this cascade are enzymes that transduce and amplify signals using a phosphorylation mechanism involving the sequential activation of each protein in the pathway by the addition of phosphate. The magnitude and duration of signalling through the cascade depends on the nature of the incoming signal and the type of cell, and is a key factor in determining the cellular response. The cell has to be able to switch-off or regulate signalling through the cascade, once the initial sensing and signalling event has passed. A family of proteins known as the MAPK phosphatases (MKPs) carry out this function by dephosphorylating and thus inactivating specific MAPKs.

MKPs are cysteine-based phosphatases (CBPs) and possess a cysteine sulphydryl group that plays a central role in catalysis. Sulphydryl groups are sensitive to oxidation, which poses a conundrum for MKPs when the activating stimulus for their target MAPK involves reactive oxygen species (ROS). Under cellular stress induced by oxidative conditions the activity of CBPs would be expected to be temporarily lost; potentially leading to sustained or uncontrolled stress-induced MAPK signalling. We hypothesised that MKPs acting on stress-response pathways stimulated by ROS would present novel solutions to this apparent paradox.

To test this theory we targeted an MKP from yeast called Sdp1, which acts on a MAPK pathway activated by oxidative stress. Surprisingly, we found that this phosphatase exhibits increased activity under oxidative conditions. In stark contrast to other CBPs, the Michaelis constant of Sdp1 increased markedly in the absence of reducing agents, indicating that oxidation actually boosts the activity. Mutational and mass spectrometric analysis pinpointed a potential disulfide-bridge between two cysteines residues (Cys47 and Cys142) as the principle mediator of this effect.

To unravel the molecular basis of the mechanism, we crystallised Sdp1 in oxidising and reducing conditions and in the presence of a phosphotyrosine substrate. Data collected at the ESRF revealed that the proposed disulphide-bridge between Cys47 and Cys142 did occur under oxidising conditions (**Figure 76**). Moreover, this disulfide and a near-by histidine residue (His111) form a deep cleft that controls access to the active site of the enzyme, thus providing substrate selectivity. In oxidised crystals both the Cys47-Cys142 disulphide and His111 were in direct contact with the phosphotyrosine substrate. This interaction suggests that the boost in activity under oxidising conditions results from the formation of the intramolecular disulphide-bridge, which increases the enzyme's substrate affinity. The disulphide was not observed in crystals grown in reducing conditions indicating that Sdp1 switches from a high-activity to a low-activity form, when the cell returns to normoxic conditions.

This redox-mediated activation mechanism was unprecedented for a protein tyrosine phosphatase and immediately raised the question as to whether the mechanism was unique to Sdp1. Using sequence

homology searches we identified a family of proteins in yeast and filamentous fungi taxa with similar sequence motifs around the substrate access cleft. We have suggested the term "WH-phosphatases" to classify this previously unrecognised group and have shown that one of the paralogues – Msg5 – is also redox-activated. We have also proposed a model for the mechanism of WH-phosphatases from budding yeast (**Figure 77**). Here the formation of a disulphide-bond between a cysteine in the amino-terminal domain of the protein with a conserved cysteine in the active site acts as a switch to activate these enzymes in oxidising conditions, when the activities of other MKPs may be compromised.

In recent years, redox-mediated reactions that influence and regulate signalling pathways within the cell have become increasing recognised as key events in many cellular processes. The discovery of this novel mechanism for attenuating MAPK signalling in yeast raises the exciting prospect that analogous mechanisms remain to be uncovered in higher eukaryotes.

Acknowledgements
This work was funded by GlaxoSmithKline and Cancer Research UK.

The crystal structure of bacteriophage T7 endonuclease I resolving a Holliday junction

Principal publication and authors
J.M. Hadden (a), A.-C. Déclais (b), S.B. Carr (a), D.M.J. Lilley (b) and S.E.V. Phillips (a), *Nature*, **449**, 621-624 (2007).
(a) Astbury Centre for Structural Molecular Biology, University of Leeds (UK)
(b) CRC Nucleic Acid Structure Research Group, University of Dundee (UK)

The rearrangement, or recombination, of DNA is an ancient and ubiquitous biological process. Recombination is central to many biological processes such as the generation of genetic variation (and therefore evolution) and the incorporation of viral DNA into host DNA, resulting in successful infection.

The process of DNA recombination occurs in distinct stages (**Figure 78**) with the formation of a four-way (Holliday) junction being a central step. For the reaction to proceed the Holliday junction must be cleaved to yield 2 linear duplexes. This process is regulated by a junction-resolving enzyme that cleaves the Holliday junction resulting in rearranged DNA strands. Bacteriophage T7 encodes a protein, endonuclease I, which has been shown to act as a Holliday junction resolving enzyme.

To understand the mechanism by which endonuclease I binds and cleaves Holliday junctions, we have solved the structure of a complex of endonuclease I and a synthetic 4-way DNA junction using X-ray crystallography. To obtain high quality X-ray diffraction data we had to purify 17 different Holliday junction complexes, set up 25,000 crystallisation trials and collect data from approximately 200 crystals at beamline **ID23-2**. Our best data extended to 3.1 Å resolution and the structure of the complex was solved by molecular replacement using the structure of DNA-free endonuclease I [1] as the search model.

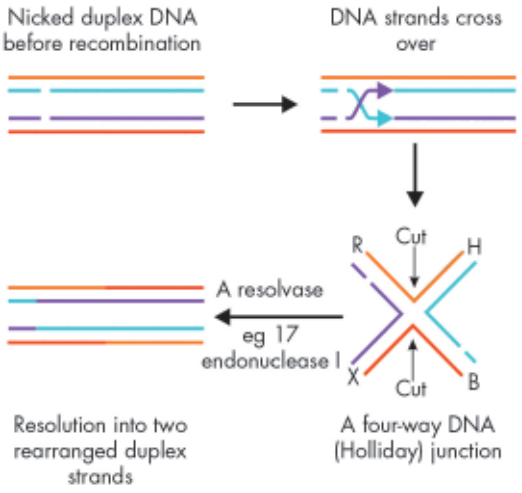

Fig. 78: The process of recombination.

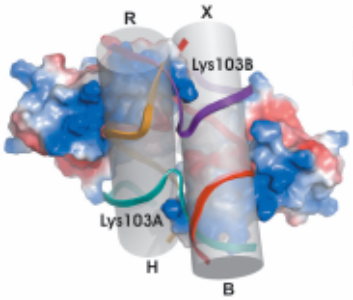

Fig. 79: Overall structure of the Holliday junction - Endonuclease I complex.

Acknowledgements
This work was supported by funds from the Wellcome Trust, BBSRC and Cancer Research UK.

In the complex (**Figure 79**), pairs of DNA helical arms are essentially stacked on top of one another (R stacked on H and X stacked on B) to form two pseudo-continuous duplexes with an angle between them of -80°. This represents an alteration of ~ 130°, from the right-handed stacked X-structure of the free Holliday junction in solution (interaxial angle ~ +50°) [2] and is consistent with studies of the structure of the endonuclease I - Holliday junction complex in solution. The observed conformation creates an almost continuous deep cleft across the major groove face of the junction which forms the principal binding site for the protein.

Significant induced fit occurs in the complex, with changes in the structure of both the protein and the junction. The enzyme is a dimer of identical subunits and presents two equivalent binding channels that contact the backbones of the junction's helical arms over 7 nucleotides. These interactions effectively measure the relative orientations and positions of the arms of the junction, thereby ensuring that binding is selective for branched DNA that can achieve this geometry.

Endonuclease I binding results in significant distortion of the structure of the junction, both globally (discussed above) and locally. The DNA backbones of the exchanging strands make tight turns at the centre of the junction, in order to pass from one duplex to the other. The adjacent phosphate groups around these turns come within ~ 6 Å of one another and the positively charged side chain of Lys103 is inserted between these two groups (**Figure 79**) to reduce the electrostatic repulsion.

The structure of the complex of endonuclease I bound to a Holliday junction shows how the geometry of this branched structure of the junction can be recognised, while at the same time being distorted by the enzyme. The recognition process exploits the dynamic character of the junction, allowing it to be 'moulded' onto the large binding surface of the protein.

References
[1] J.M. Hadden, A.-C. Déclais, S.E. Phillips, D.M. Lilley, *EMBO J.* 21, 3505-3515 (2002).
[2] M. Ortiz-Lombardia, A. Gonzalez, R. Eritja, J. Aymami, F. Azorin, M. Coll, *Nature Struct. Biol.* 6, 913–917 (1999).

Structural insights on synthesis of inflammatory mediators by human leukotriene C_4 synthase

Principal publication and authors
D. Martinez Molina (a,b), A. Wetterholm (a), A. Kohl (a), A.A. McCarthy (c), D. Niegowski (a,b), E. Ohlson (a), T. Hammarberg (a), S. Eshaghi (a), J.Z. Haeggstrom (a), P. Nordlund (a), *Nature* **448**, 613 - 616 (2007).
(a) Karolinska Institutet (Sweden)
(b) Stockholm University (Sweden)
(c) EMBL Grenoble Outstation (France)

Leukotriene C_4 synthase is an integral membrane protein that catalyses the conjugation between the reactive epoxide on the lipidic leukotriene A_4 (LTA_4) and the cysteinyl sulfur on glutathione (GSH). The product, LTC_4, together with its breakdown products (LTD_4 and LTE_4) are referred to as cysteinyl leukotrienes (Cys-LTs) or the "slow reacting substance of anaphylaxis". These molecules are powerful mediators of inflammation and cause constriction of smooth muscle cells in the airways as well as myocardial contractility. Drugs targeting the signalling pathways of Cys-LTs have offered therapeutic opportunities in the medical treatment of asthma.

The structure of human LTC_4S was solved using the MAD phasing technique using a Pt derivative, which, together with 2.0 Å data on the apo protein, was collected on **ID14-4**. We also solved a GSH complexed structure of LTC_4S to 2.2 Å using data from **ID23-2**. The use of the highly-automated stations with sample changers and a robust setup, allowed us to screen through more than 1000 crystals in the search for bound heavy atoms and ligands as well as well-diffracting crystals. The crystals grew in a cubic space group, assigned as the highly unusual F23, and contained only ~20% protein. The fact that the crystals diffract so well despite the high solvent content is interesting and is possibly due

to the high symmetry space group, as well as an intriguing 6-His polynuclear metal cluster that effectively ordered the crystals **(Figure 80a** and **80b)**.

LTC_4S is a compact homo-trimeric protein **(Figure 81a)** with a total of 12 membrane-spanning helices and three active sites buried in deep polar pockets at the interface of two monomers. A relatively long loop that connects helices 1 and 2 folds on top of the neighbouring monomer and contributes to subunit interactions. This loop also seals off the cytosolic entrance to the active site and is proposed to have some flexibility to allow GSH to enter. The active site needs to be accessible both to the lipidic substrate LTA_4, which may diffuse through the membrane layer, and to the highly water soluble co-substrate GSH, which can access from the cytosol. The active site forces the reactive cysteinyl thiolate on GSH towards the protein/membrane interface, where LTA_4 binds in a hydrophobic crevice formed between two monomers (**Figure 81b**). This open crevice stretches from the cytosolic face of the protein towards the peri-nuclear side where the most distal part is covered by a tryptophane side chain that serves as a lid on the crevice. In our electron-density maps we also see a number of extended features, likely to be due to lipids or detergents from the purification procedure that line the protein surface. Several of these can be found in, or near, the LTA_4 binding crevice and serve as a good substrate model because they have important structural similarities to LTA_4.

The different binding modes of aliphatic chains in the presence or absence of GSH give us a clue as to how recognition of LTA_4 and the positioning of the reactive epoxide is achieved. We propose that GSH binding precedes that of LTA_4 and assists in the formation of an appropriate lipid-binding crevice for LTA_4.

In conclusion, our structure shows how a fairly small protein can accommodate and recognise substrates with widely different chemical properties; the enzyme buries a highly-soluble substrate and presents it to a lipid for conjugation, a reaction that would never occur unless aided. These structural insights into the mechanism of LTC_4 formation could lead the way for development of new drugs in the treatment of asthma and chronic inflammation.

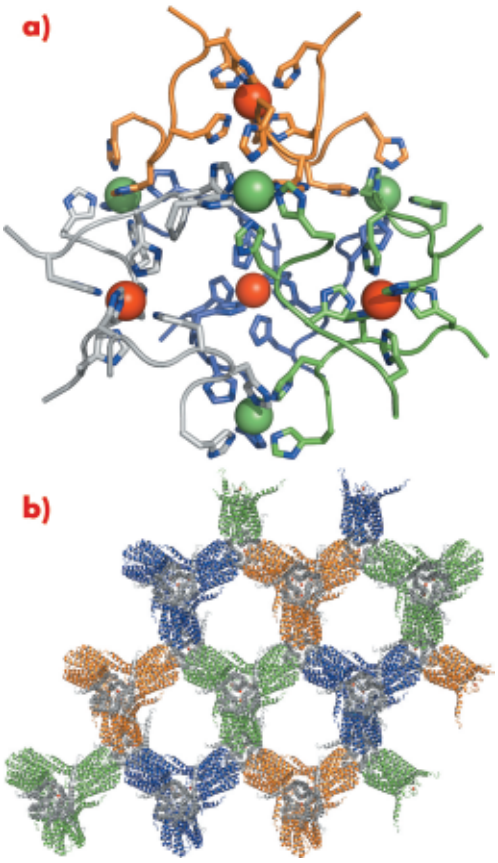

Fig. 80: (a) Metal cluster composed of 12 crystallographically related hexa-histidine tags from four trimers (colored respectively in green, orange, blue and light grey). Each trimer coordinates one metal internally (shown as a red sphere) and one monomer from three different trimers coordinates another metal (shown as a green sphere). In total, 48 histidine residues coordinate 8 metals. (b) Crystal packing, trimers are coloured green, orange, grey or blue.

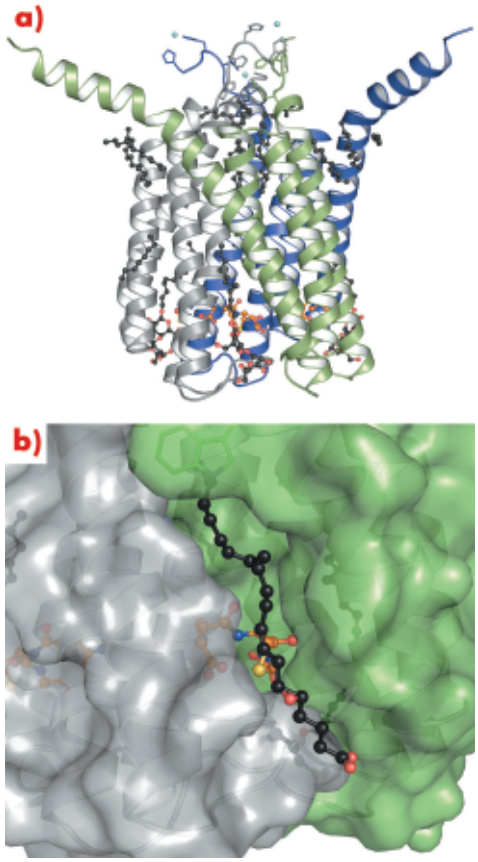

Fig. 81: (a) Side view of a trimer, monomers coloured grey, blue and green. Lipid and detergent molecules are visualised as black balls and sticks, the GSH backbone as orange balls and sticks. Metal ions are shown as cyan spheres. (b) Close-up, transparent surface view of (a) showing the binding crevice for docked LTA_4. The GSH that contains the thiolate is shown in yellow.

Principal publication and authors
B. Clantin (a), A.-S. Delattre (b), P. Rucktooa (a), N. Saint (c), A. Méli (c), C. Locht (b), F. Jacob-Dubuisson (b), V. Villeret (a), *Science* **317**, 957-961 (2007).
(a) IBL UMR8161 CNRS, Lille (France)
(b) U629, Lille (France)
(c) U554, Montpellier (France)

Crystal structure of FhaC: molecular insights into how proteins get across the outer membrane

Targeting of proteins to their dedicated subcellular compartments is essential for cell function and organelle biogenesis. Translocation of proteins across, or insertion into membranes is mediated by protein machines, some of which have been conserved throughout evolution, such as the transporters of the Omp85/TpsB superfamily. TpsB transporters are components of "Two-Partner Secretion" (TPS) systems in Gram negative bacteria [1]. They secrete large, mostly β-helical proteins called "TpsA" proteins that generally serve as virulence factors. TpsB transporters function as monomers and without accessory factors. The superfamily also includes the Toc75, Sam50/Tob55 and Omp85/YaeT homologs, which are the cores of large hetero-oligomeric complexes involved in protein transport across, and insertion of β-barrel proteins into, the outer membranes of chloroplasts, mitochondria and Gram-negative bacteria. In recent years, researchers have begun to make progress in understanding how these transporters work. The structure of FhaC, the outer-membrane transporter that secretes the *Bordetella pertussis* adhesin filamentous haemagglutinin (FHA) now provides structural insights into this process.

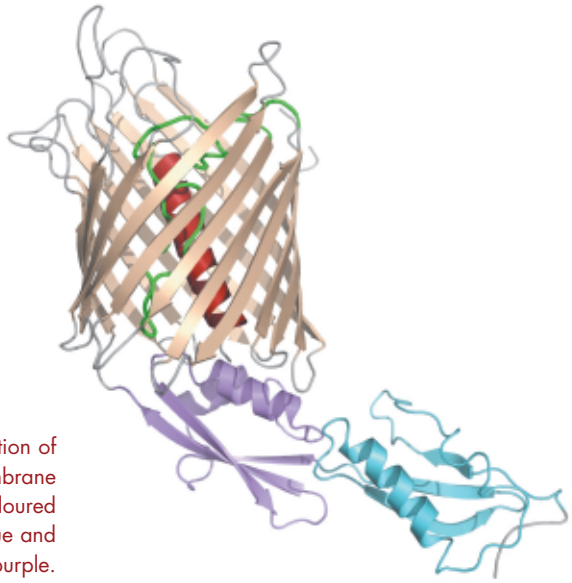

Fig. 82: Ribbon representation of FhaC viewed from the membrane plane. The α helix H1 is coloured red, POTRA 1 light blue and POTRA 2 purple.

The FhaC structure was solved by the single-wavelength anomalous diffusion (SAD) method with diffraction data measured to 3.5 Å resolution on **BM14**, and subsequently refined to 3.15 Å resolution using data measured on **ID14-4**. The structure shows a β barrel with an N-terminal extension consisting of an α helix and two periplasmic POTRA domains, which are organised around a three-stranded β sheet and one α helix (**Figure 82**). The β barrel consists of 16 antiparallel β strands connected by short turns at the periplasmic side and long loops at the cell surface. The channel within the barrel is occluded by loop L6, which folds into the barrel, and by the N-terminal α helix, which spans the channel interior. The observed residual opening is too narrow to allow for transport of a protein, even in an extended conformation. However, upon reconstitution of FhaC into planar lipid bilayers and application of a transmembrane potential, much wider channels were revealed, corresponding to channel widths of 8 to 10 Å. Thus, the channel appears to be dynamic: Upon binding of FHA to POTRA-1, the channel may open by extrusion of the α helix and/or loop L6, thus creating a protein translocation pathway. Previous work indeed showed a topological rearrangement in L6 upon coexpression of FHA.

Collectively, the data allowed us to propose the following model for transport of FHA across the outer membrane (**Figure 83**). The N-terminal TPS domain of FHA, which folds as a β helix after translocation [2], initially interacts in an extended conformation with the POTRA 1 domain in the periplasm. These interactions bring regions of FHA in proximity to the tip of loop L6 (**Figure 83a**). Conformational changes in FhaC then expel loop L6 out of the β barrel, opening the channel for FHA translocation. FHA may form a hairpin

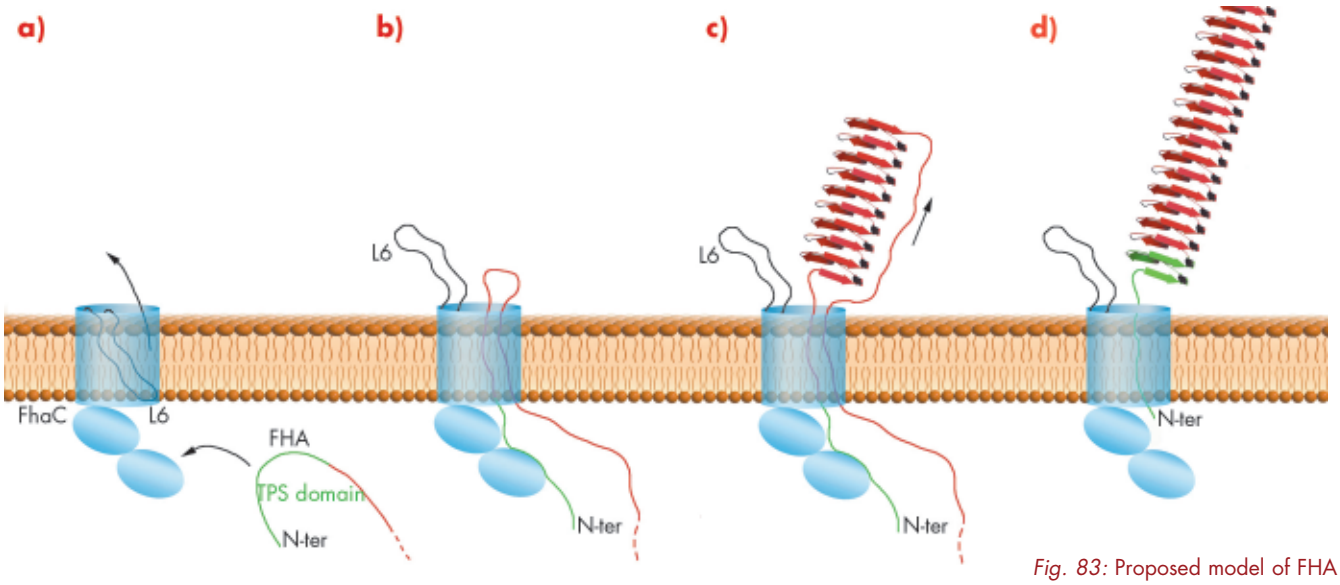

Fig. 83: Proposed model of FHA transport across the outer membrane.

made up of two extended polypeptide chains in the channel, with its TPS domain anchored in the periplasm (**Figure 83b**). The first repeats of the adhesin then reach the cell surface, where they progressively fold into β-helical coils. The formation of the FHA rigid β helix may provide the energy to drive its translocation through FhaC (**Figure 83c**). After the C-terminus of FHA has reached the surface, the TPS domain dissociates from the POTRA domains and is translocated, capping the N-terminus of the FHA β helix. Finally, loop L6 can move back into the barrel (**Figure 83d**).

The transport mechanism proposed here may apply more generally to the secretion of TpsA proteins by their dedicated TpsB transporters. All members of the Omp85/TpsB superfamily harbour one to several POTRA domains followed by a β barrel, as well as conserved motifs corresponding to the L6 loop within the barrel, and they mostly handle substrate proteins rich in β structure. Therefore, the major features described here are likely to remain valid throughout the family, although more complex molecular events are expected for some of these transporters given that they are part of macromolecular assemblies.

In conclusion, we have determined the first crystal structure of a member of the Omp85-TpsB transporter superfamily. It offers molecular insights into how proteins get into and across cellular membranes.

References

[1] J. Mazar, P.A. Cotter, *Trends Microbiol* **15**, 508-15 (2007).

[2] B. Clantin, H. Hodak, E. Willery, C. Locht, F. Jacob-Dubuisson, V. Villeret. *PNAS* **101**, 6194-9 (2004).

Surface and Interface Science

Introduction

With the additional preparations for the ESRF upgrade, which was entering a critical phase in 2007, the last year has been very busy for surface and interface science (SIS) at the ESRF. Two novel SIS beamlines are foreseen in stage one of the upgrade and a third one most likely in the second phase. This will result in a complete renewal of the existing portfolio of the ESRF SIS beamlines, presently comprising ID01, ID03, and ID32.

Major improvements were carried out at the three "core" SIS beamlines in 2007. The ID01 team commissioned a new high stability white beam monochromator, which is now suitable for sub-micrometre focusing. At ID03 the speed of the two diffractometers has been greatly increased with the help of the new ESRF "ICEPAP" stepper motor drives. Small-angle scattering, to study shape transitions in growth studies, is now routinely possible at ID03. Furthermore, a new UHV compatible high pressure chamber for GIXRD catalysis studies is presently being commissioned. At ID32 work has continued in preparation for the installation of a new ultra high vacuum system for photoelectron spectroscopy in 2008, which will allow the analysis of electron kinetic energies up to 15 keV with a resolution down to 20 meV. Furthermore, a new, fully equipped electrochemistry laboratory is now available for users close to the ID32 beamline.

Surface and interface science at the ESRF has always had a rather different bias to conventional laboratory-based UHV surface science. In the mainstream area, one exploits methods that specifically probe only the outermost few atomic layers of a solid. By contrast, X-rays allow one to probe beneath the surface, yet by suitable choice of experimental measurement conditions, X-ray scattering can also be surface specific. A major component of SIS at the ESRF has thus been to explore the properties of ultra-thin layers imposed by a surface or interface, such as in epitaxial growth of thin films, multilayers, quantum dots and, of course, buried interfaces *per se*. This remains a major strength of the facility. What is also true, however, is that mainstream surface science is shifting its centre of gravity as it aims to tackle problems of increasing complexity, and many of the resulting challenges can be addressed with great effect by X-ray scattering. For example, while UHV surface science studies are commonly undertaken with the aim of identifying basic mechanisms in heterogeneous catalysis, it is now recognised that in many such problems the mechanisms differ under UHV and 'high' pressure conditions, so the surface needs to be investigated under reaction conditions at pressures of the reactant and product gases up to 1 bar or more. Several specific examples of this type concern oxidation reactions (such as the CO oxidation reaction conducted in automobile catalytic converters) in which it appears that ultrathin oxide layers on the metal surface, only stable at elevated pressures, play a key role in the reaction. Optical methods such as X-ray scattering (and infrared spectroscopy) are almost the only methods available for *in situ* surface

studies under these conditions, and such experiments, particularly in the special chamber at ID03, are exploiting the special capabilities of the ESRF to the full. One such example is described by Over *et al.*, while Stierle *et al.* report the results of *in situ* studies of elevated pressure surface oxidation in a rather different system has been conducted on a special chamber at ID32.

A rather different case of surface complexity that retains the UHV environment is that of surface structures with a very large surface mesh. Tackling problems of this type was one of the earliest goals of surface X-ray diffraction at synchrotron radiation facilities, because the traditional method of low energy electron diffraction becomes intractable due to the computational complexity of multiple scattering calculations for such systems. While relatively few studies of this type are now conducted at the ESRF a recent investigation of the surface reconstruction of Sm(0001) at ID03, reported by Lundgren *et al.*, is a particularly elegant example. The modified electronic environment of the reconstructed surface layer of Sm atoms leads to a shift of some 7 eV in the L-edge, allowing anomalous scattering to be used to provide chemical as well as structural information on this complex surface phase.

While also reflecting the trend to increasing complexity, a rather distinct and clearly identifiable trend in the surface science community is an increasing emphasis on nanoscience. Of course, investigations focussed on just the outermost few atomic layers of a solid have always been concerned with scientific phenomena arising from localisation (perpendicular to the surface) on the nanometre scale, as have investigations of ultrathin single and multiple layer structures. Pursuing the growing interest in the science resulting from nanometre localisation in two and three dimensions, however, is thus a natural development within this community, the traditional techniques of surface science providing many of the necessary tools, although with an increasing need for lateral resolution. Scanning probe microscopies have had a huge impact in this area and offer attractive real-space imaging, yet they are limited in their ability to be applied at high resolution to dynamic studies at elevated temperatures and pressures. In such cases, X-ray scattering provides crucial complementary information. One classic example of nanostructuring of a single crystal surface is adsorbate-induced faceting, in which an initially flat surface breaks into a 'hill-and-valley' morphology due to a change in the relative surface free energies of different surface orientations due to the adsorbed layer. In such phenomena the adsorbate may be a result of a simple gas-phase reaction, such as atomic oxygen from dissociation of the molecular species, but may also involve an ultra-thin film of metal atoms. The results of an investigation of this type of nanoscale faceting on W(111) induced by Pt deposition is reported by Revenant *et al.*

The more detailed short reports that follow include six contributions from the core ESRF SIS beamlines, and also two articles from the French CRG beamline BM32, which is almost entirely dedicated to SIS studies. Specifically, in addition the article by Revenant *et al.*, there is a report on a novel technique using monochromatic and "white" X-radiation to obtain structure and strain of polycrystalline grains from Sicardy *et al.* Two studies are reported from experiments performed at ID01: Richard *et al.* have used a new way to study defects in crystals non-destructively, and Mocuta *et al.* describe experiments that employ a new technique, for which the ID01 staff have coined the name 'X-ray diffraction microscopy'. The two contributions from ID03 deal with catalysis (Over *et al.*) and the determination of the Sm(0001) surface structure using anomalous diffraction (Lundgren *et al.*). The formation of an ultra-thin oxide film was studied in real time by Stierle *et al.* at ID32 and van Bokhoven *et al.* show how to identify the location of aluminium in the unit cell of zeolite crystals, which largely defines their functionality, with the help of the X-ray standing wave method.

D.P. Woodruff *(University of Warwick) and* ***J. Zegenhagen***

From strain to defects

Principal publication and authors
M.-I. Richard (a, b), T.H. Metzger (a), V. Holý (c), K. Nordlund (d), *Phys. Rev. Lett.* **99**, 225504 (2007).
(a) ESRF
(b) Département de Recherche Fondamentale sur la Matière Condensée/SP2M/NRS, CEA Grenoble (France)
(c) Faculty of Mathematics and Physics, Charles University, Prague (Czech Republic)
(d) Accelerator Laboratory, University of Helsinki (Finland)

Revealing the core structure of defects

Nanostructures must be kept free of defects during device fabrication in order to obtain the desired electronic properties. The structure, nature, and location of defects can be determined by transmission electron microscopy (TEM), but it remains a destructive method. Diffuse X-ray scattering on the other hand is a well-established non destructive method for the investigation of defects in crystals [1]. Usually, the scattering from the deformed lattice around the defects is measured close to allowed Bragg peaks (the Huang scattering) and is used for the defect investigation. However, here the contribution of the defect cores is weak due to the rather small volumes of the defect cores and to the strong contribution of the Huang scattering, so that the investigation of the structure of the defect core is difficult. As a consequence, not only traditional X-ray diffuse scattering but also high-resolution TEM (HRTEM) measurements often fail to observe the atomic displacement field of the atoms in the core of defects.

We have developed a novel X-ray method to study the defect cores directly. A forbidden reflection is used for the suppression of the displacement-field scattering so that the scattered intensity consists mainly of the scattering from the core. Employing this method, we investigated the structure of the cores of extrinsic stacking faults created in Si crystal after amorphising ion implantation and subsequent annealing. The diffuse X-ray scattering has been measured on beamline **ID01**. A three-dimensional intensity distribution was collected by a linear detector perpendicular to the sample surface around the (200) forbidden reflection. The diffuse scattering was concentrated in intensity streaks along <111> directions visible in **Figure 84**.

The diffuse part of the scattered intensity from small defects in non-correlated random positions is a coherent superposition of two contributions $I(Q) \sim |E_1(Q)+E_2(Q)|^2$, where E_1 describes the scattering from the displacement field around a single defect and $E_2 = f(Q)\Sigma_c\ \Omega(R_c)\exp(-iQ.R_c)$ is the scattering from the defect core, $\Omega(R_c)$ is the shape function of a single defect core, $f(Q)$ is the atomic scattering factor and R_c is the position of the atoms of the defect cores. If $F_0(h) = 0$ as for the Si (200), the displacement-scattering term (E_1) is weak or can be neglected. Thus, the diffuse scattering results mainly from the defect cores.

The Si crystal contains randomly-distributed extrinsic stacking faults which lie in {111} planes having the Burgers vector b=1/3<111> perpendicular to the planes. The core of such faults consists of two extra {111} planes, having the nominal distance $\Delta_0=a\sqrt{3}/4$. From symmetry considerations it follows that the reciprocal-space distribution of the scattered intensity *I(Q)* is concentrated along <111> lines, perpendicular to the loop planes. Thus, the intensity observed in **Figure 84** stems from the diffuse scattering of the cores of stacking faults in Si. From the fit of the streak cross-section (see black dashed line in **Figure 84**), the mean radius R_0 = (30±2) nm of the faults follows.

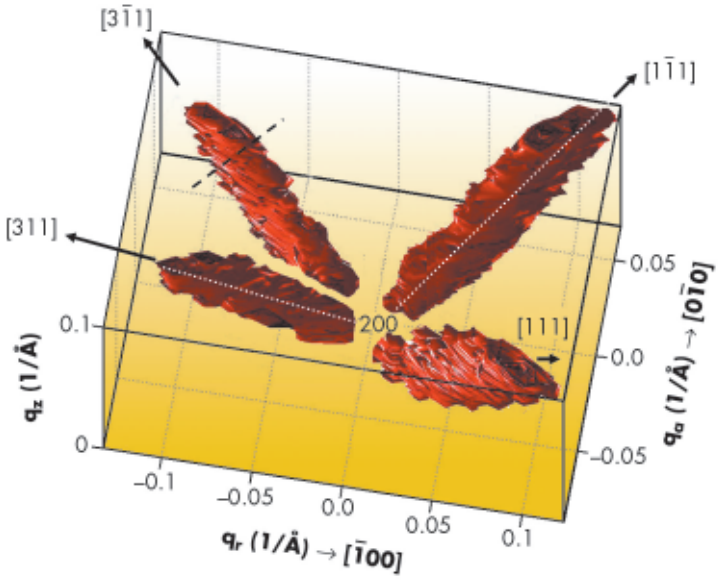

Fig. 84: Three dimensional reciprocal-space distribution around h (200). The scattered intensity is concentrated in streaks along <111> perpendicular to the stacking fault planes. The white dashed line denotes the trajectory along which the line scan in Figure 85 was extracted.

The intensity distribution along the streaks $I(q_{111})$ is plotted in **Figure 85**. Here q_{111} is the coordinate of q along the [111] direction depicted in **Figure 84** (see white dashed lines); q_{111}= 0 corresponds to the reciprocal lattice point h (200), forbidden for Si. We have fitted this distribution to the theory described above; the fit depends on only one free parameter Δ, which is the distance between the two extra planes forming the core of the extrinsic stacking-fault. After taking into account the scattering around several allowed reciprocal-space points, the fit reveals a core displacement of Δ=(2.1±0.2) Å. The correspondence of the measured and fitted intensity distribution is good (see **Figure 85**, full line), revealing the compression of the {111} planes in the defect cores ($\Delta < \Delta_0$). These results are well supported by atomistic simulations (see **Figure 85**, dashed line).

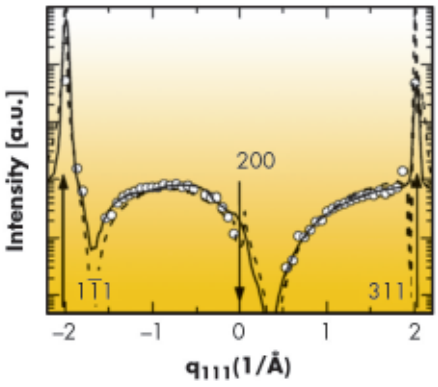

Fig. 85: Distribution of the measured intensity (points) along the trajectory denoted in Figure 84, along with its theoretical fit using the continuum approach (full line) and atomistic simulations (dashed).

To conclude, diffuse X-ray scattering around a forbidden reciprocal lattice point is well suited for the study of the cores of extrinsic stacking faults in Si. This novel, highly sensitive and destruction-free technique allows detection of stacking faults and characterisation of the small compression in their core. This unique method can also be extended to other kind of defects.

References
[1] M.A. Krivoglaz, X-ray and Neutron Diffraction in Non-ideal Crystals (Springer 1996).

Determination of the complete stress state of sub-micrometric Cu grains by microdiffraction

Authors
O. Sicardy (a), X. Biquard (b), J.S. Micha (c), F. Rieutord (b), O. Robach (b), O. Ulrich (b), O. Geaymond (d), V. Carreau (a).
(a) Direction de la Recherche Technologique, CEA-Grenoble (France)
(b) Département de Recherche Fondamentale sur la Matière Condensée, CEA-Grenoble (France)
(c) UMR Structures et Propriétés d'Architectures Moléculaires, CNRS-Grenoble (France)
(d) Institut Néel, CNRS-Grenoble (France)

Copper has become the material of choice for metallisation of microelectronics devices thanks to its high thermal and electrical conductivities. Typically, Cu lines within dielectric trenches are created by electrochemical deposition. Since the thermal expansion coefficient of Cu is higher than for the surrounding materials, thermal cycles during subsequent processing steps often induce high residual stress. Thus, the mechanical integrity of the Cu interconnect remains a major concern. For process optimisation it is necessary to exactly quantify stress in the Cu lines.

X-ray diffraction is a convenient technique for stress measurements in polycrystalline materials. It is non-destructive and it allows one to determine all components of the stress tensor. Measurements are specific for a certain crystalline phase (fcc copper in our case), which is very useful in the case of multi-component samples and complex geometry. However, the major limitation of this technique with laboratory X-ray sources is the spatial resolution, which hardly reaches below a few hundreds micrometres. This is insufficient for stress measurements of today's devices.

Sub-micrometre measurements have now become possible at the French CRG beamline **BM32**. A novel setup, utilising the X-rays from a bending magnet, allows investigation of the crystallographic orientations and strain/stress states of heterogeneous crystalline materials below the micrometre scale. Unique in Europe, it combines white and monochromatic beam micro-diffraction, following the method of MacDowell and co-workers [1] at ALS. The white beam from the bending magnet is focussed by mirrors onto an adjustable slit of typically 20 x 20 μm^2.

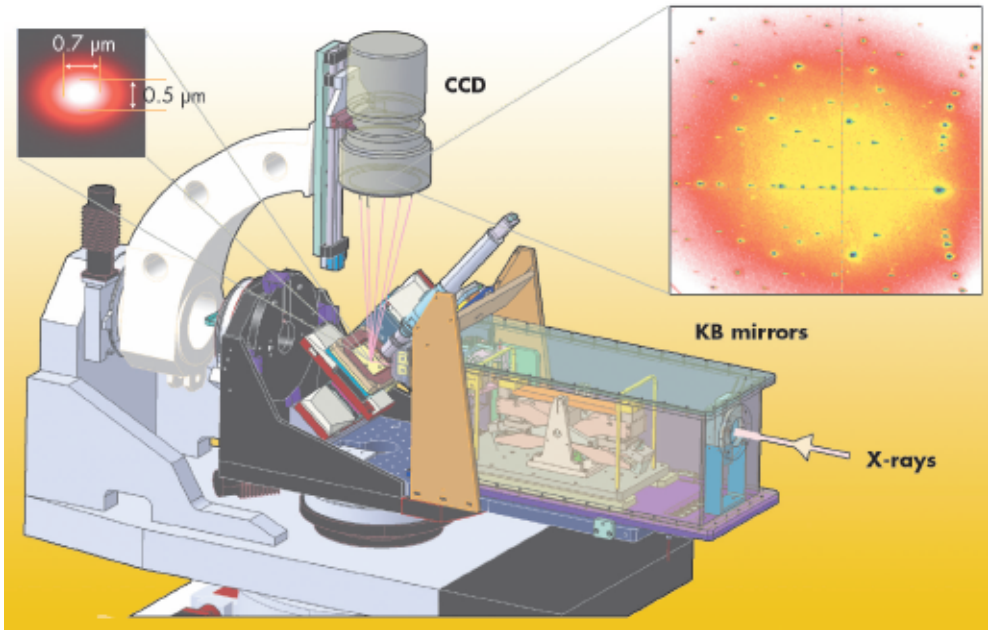

Fig. 86: Microdiffraction setup on the CRG beamline BM32.

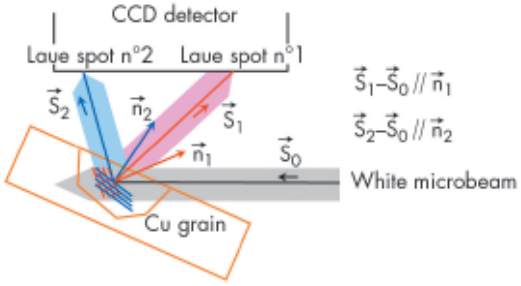

Fig. 87: Collection of a Laue diagram from a single grain.

This secondary source is further reduced to sub-micrometric dimensions using a pair of Kirkpatrick-Baez mirrors situated just before the sample (**Figure 86**).

This technique allowed the determination of all the components of the strain/stress tensors for a copper grain within a 260 nm wide and 250 nm thick interconnection line. It was scanned with a white (5-25 keV) microbeam and Laue diagrams of individual copper grains, smaller than 1 µm^3, have been collected by a CCD camera (**Figure 87**). Each Laue spot can be associated with a specific grain and lattice plane. As a result, both the orientation and lattice distortion of the copper grains can be deduced, allowing the full strain tensor for each grain to be obtained. However, this requires the "hydrostatic part" of the tensor to be determined by accurately measuring at least one lattice plane spacing of the grain. This is accomplished by switching the beamline optics into monochromatic mode and determining the X-ray energy corresponding to a Laue spot originating from a specific lattice plane.

Once the full strain tensor has been determined, the complete stress tensor is deduced using the known elastic constants of copper. As an example, a triaxial tensile state of stress has been measured on one grain of the interconnect line:

$$\left|\begin{array}{ccc} 594 & -135 & -27 \\ -135 & 277 & -249 \\ -27 & -249 & 383 \end{array}\right| \text{ MPa}$$

Principal stresses reach values of few hundreds MPa and the hydrostatic part is 418 MPa. The results are consistent with previous measurements performed at a macroscopic scale on the same kind of device [2].

References
[1] A.A. MacDowell, R.S. Celestre, N. Tamura, R. Spolenak, B. Valek, W.L. Brown, J.C. Bravman, H.A. Padmore, B.W. Batterman, J.R. Patel, *Nuclear Instruments and Methods in Physics Research A*, **467-468**, 936-943 (2001).
[2] A. Baldacci, C. Rivero, P. Gergaud, M. Grégoire, O. Sicardy, O. Bostrom, P. Boivin, J.S. Micha, O. Thomas, *34th European Solid State Device Research Conference ESSDERC*, 20-24 September 2004, Louvain.

From now to then: real-time studies

Nanoscale surface faceting

Principal publication and authors
C. Revenant (a), F. Leroy (a,b), G. Renaud (a), R. Lazzari (c), A. Létoublon (a,d), T. Madey (e), *Surf. Sci.* **601**, 3431-3449 (2007).
(a) DRFMC, CEA, Grenoble (France)
(b) CRMCN-CNRS, Marseille (France)
(c) Institut des Nanosciences de Paris (France)
(d) INSA, Rennes (France)
(e) State University of New Jersey (USA)

Adsorbed adatoms can influence surface structure and chemistry, including faceting of metallic and model bimetallic catalyst surfaces. The importance of bimetallic catalysts based on Pt-group metals has been increasingly recognised in recent decades, as they display important advantages over classical reforming catalysts. In particular, refractory metals (W, Mo, Re ...) alloyed with Pt-group metals are active catalysts for hydrogenation and hydrogenolysis reactions. The tungsten (111) surface covered with monolayer-thick films of some metals (Pt, Pd, Rh, Ir, Au) and annealed at temperatures higher than 700 K undergoes a massive reconstruction to form three-sided pyramids of nanometre-scale dimensions with mainly {211} facets (**Figure 88a**). A minimum coverage of the metal (1.7×10^{15} atoms/cm^2 in case of Pt) is necessary for the surface to become completely faceted. The pyramids are composed of tungsten, completely covered with the thin metal film. The driving force for faceting is attributed to the difference in surface energy of the different facets, but thermal annealing is needed to achieve sufficient surface atom mobility for mass transport [1].

This nanopatterned surface is of interest because it could be used as a template to grow ordered nanostructures, for instance with specific magnetic properties. This prompted us to undertake an X-ray study of the Pt/W(111) surface as a function of temperature to determine the appropriate conditions for ordering of small nanoparticles, and then to monitor the deposition of cobalt on this nanostructured surface. The experiments were carried out on the **BM32** beamline, using a newly-developed setup allowing both grazing-incidence small-angle X-ray scattering (GISAXS) and grazing-incidence X-ray diffraction (GIXD) on the same sample, *in situ*, in ultra high vacuum (UHV), at different growth stages (here of Pt and Co) [2]. Morphological and structural features are derived in a combined way from grazing-incidence X-ray scattering at small and large emergence angles.

First, a 1.1 monolayer of Pt was deposited on the W(111) surface. The GIXD measurements indicated that the Pt was fully lattice-strained to the substrate parallel to the surface and that the deposit was two-dimensional. The GISAXS patterns (**Figure 88b**) were quantitatively analysed, which yielded the morphological parameters [3]. Then, the first onset of nanofaceting was achieved by thermal annealing at ~715 K with pyramids of approximately 5 nm in size and 6 nm in separation. Annealing above 715 K resulted in a continuous increase of all the characteristic sizes of

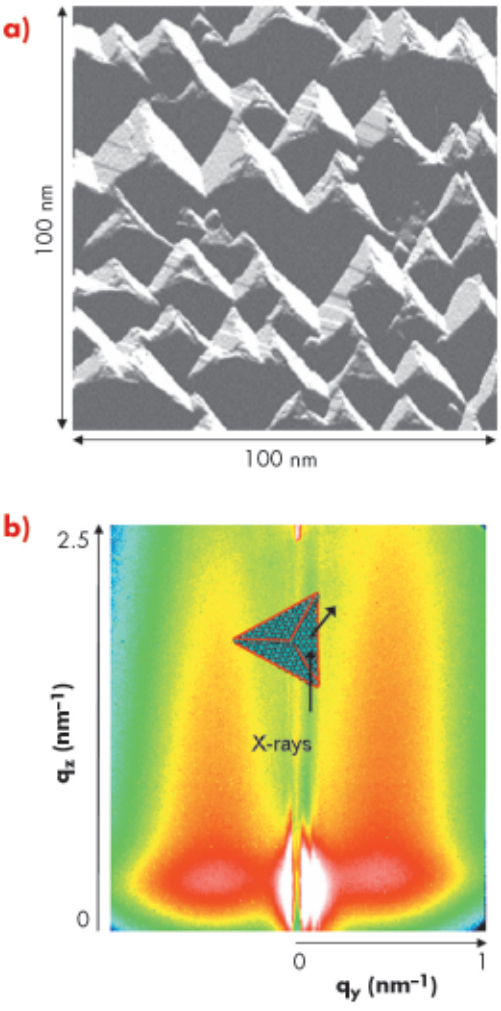

Fig. 88: (a) Scanning-tunnelling microscopy of 1 monolayer Pt/W(111) annealed at 1100 K. (b) Experimental GISAXS pattern for 1.1 monolayer of Pt/W(111) annealed at 800 K with the scattering geometry (inset).

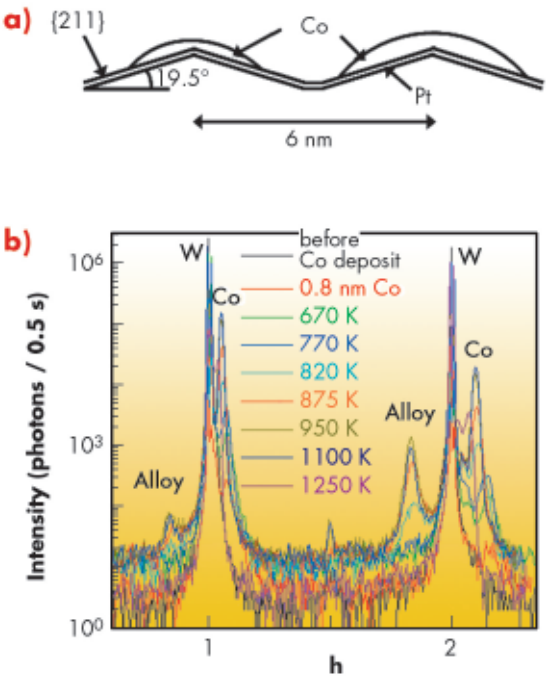

Fig. 89: (a) Schematic representation of Pt/W pyramids covered with Co islands. (b) Measured intensity during radial scans along the (*h h* 0.0325) direction on the facetted Pt/W(111) surface before the Co deposit, after the 0.8 nm of Co at ambient temperature, and after successive thermal annealing.

References
[1] K. Pelhos, T.E. Madey, J.B. Hannon, G.L. Kellogg, *Surf. Rev. Lett.*, **5**, 767-774(1999).
[2] G. Renaud, R. Lazzari, C. Revenant , A. Barbier, M. Noblet, O. Ulrich, F. Leroy, J. Jupille, Y. Borensztein, C.R. Henry, J-P. Deville, F. Scheurer, J. Mane-Mane, O. Fruchart., *Science* **300**, 1416-1419 (2003).
[3] C. Revenant, F. Leroy, R. Lazzari, G. Renaud, C.R. Henry, *Phys. Rev. B* **69**, 035411-035428 (2004).

the pyramids, while keeping a dense triangular packing.

The nanopatterned surface with the smallest pyramids has been used as a template for the growth of ordered nanostructures. A 0.8 nm-thick cobalt layer was deposited at room temperature. The three-dimensional Co islands obtained were correlated with the Pt/W nanopyramids (**Figure 89a**) and Co was in a relaxed state on Pt/W (**Figure 89b**). At approximately 800 K, a CoPt alloy was formed and became more ordered as the annealing temperature increased. At 1100 K, both defaceting and phase separation began; the CoPt alloy segregated on the W(111) flat surface, while Co formed an epitaxial layer on the {211} facets. In addition, in the temperature range of 1100-1200 K, the great majority of {211} large facets coexisted with some {110} small facets. Finally, the surface became flat again at 1250 K.

To conclude, the nanofaceting of the W(111) surface into {211} three-sided Pt/W pyramids upon thermal annealing of a 1.1 monolayer Pt deposit was investigated *in situ* by a combination of GISAXS and GIXD. Co deposited at ambient temperature on the facetted surface formed three-dimensional islands correlated with the W nanopyramids.

Authors
H. Over (a), O. Balmes (b), N. Bovet (c), E. Lundgren (c).
(a) Physikalisch-Chemisches Institut, Justus Liebig University Giessen (Germany)
(b) ESRF
(c) Dept. of Synchrotron Radiation Research, University of Lund (Sweden)

Direct detection of the structure-activity correlation in heterogeneous catalysis

A major challenge in (heterogeneous) catalysis research is the identification of the catalytically-active phase under practical reaction conditions. Frequently, the active phase is only stable under reaction conditions and may even change when the reactant mixture or the reaction temperature is varied. All these complications call for *in situ* characterisation of the catalytic system. To have full access to the atomic-scale structure of the catalyst one has to study model catalysts with low structural complexity such as single crystalline films. One has to pay for this simplification by the introduction of the so-called materials gap that has to be bridged in order to transfer atomic-scale information of the model catalyst to the practical catalyst consisting of metal nanoparticles dispersed on a support material.

With the CO oxidation reaction over RuO_2(110)/Ru(0001), we are in the fortunate situation that both the pressure and the materials gaps have been successfully bridged [1]. With the unique high-pressure chamber of beamline **ID03** [2], we were able to follow the surface structure of the Ru(0001)-based model catalyst by SXRD and the reaction rate of the product formation (CO_2) by mass spectrometry simultaneously during the catalysed CO oxidation reaction over RuO_2(110)/Ru(0001) under practical reaction conditions. In these experiments the high-pressure cell was used as a batch reactor.

In **Figure 90** we present a specific set of experiments aimed at elucidating the structure-activity relationship for the CO oxidation over the RuO_2(110)/Ru(0001) model catalyst. The 1.6 nm thick RuO_2(110) film on Ru(0001) was produced prior to the reaction experiments by exposing the Ru(0001) surface to 1000 Pa of O_2 at 640 K. The sample was then cooled to 350 K and 1800 Pa of CO was admitted to the reaction cell. Subsequently the reaction temperature was increased stepwise up to 720 K over a time period of 2800 s (**Figure 90a**, brown trace). At temperatures up to 500 K, the oxide film does not change as indicated by the repetitive h-scans (**Figure 90a**, black traces); the maximum intensity is found at h = 0.73 characteristic for the RuO_2(110) oxide surface [3]. For T = 350 K, almost no CO_2 is formed (**Figure 90b**, green trace) as indicated by a small value (< 5 Hz) of the turn over frequency (TOF). Above 400 K the CO_2 production is accelerated, revealing a constant TOF of 95 Hz (at 400 K) which increases to 190 Hz by raising the temperature to 450 K. Both CO and O_2 are consumed during the CO oxidation, but the stoichiometry of the reaction feed is nearly preserved during the first 2200 s as indicated in **Figure 90c** (red trace). In region C, the CO_2 production stops, although the temperature is increased to 500 K. Presumably, a deactivation of the catalyst occurs whose origin is not understood. At the end of region C (reaction time about 1600 s), the oxide film disappeared. Obviously, below 500 K the catalyst was stabilised in a metastable phase (oxide) in a reducing reactant mixture. Upon reduction of RuO_2(110) the activity increased substantially: TOF = 260 Hz. When the temperature was further increased to 640 K, the oxide reappeared (with higher diffraction intensity at h = 0.73). From corresponding l-scans we derive a thickness of the RuO_2(110) film of 2.3 nm. The oxidation process of Ru(0001) is accompanied by a sudden rise of the TOF value to 850 Hz. With this increase of the TOF the stoichiometry of the reactant feed drops significantly from 1.9 to 1.15, *i.e.* the reaction mixture is now much more oxidising than during the first 2000 s (**Figure 90c**, red trace). This change in the stoichiometry of the reactant feed may cause the rapid TOF decline to very small values <1 Hz. Practically the CO oxidation reaction stops although both CO (210 Pa) and O_2 (170 Pa) are still present in the gas mixture. A further increase of the temperature to 720 K did not restore the activity of the RuO_2(110) catalyst. The catalyst is deactivated either structurally or by the product CO_2 in the gas atmosphere.

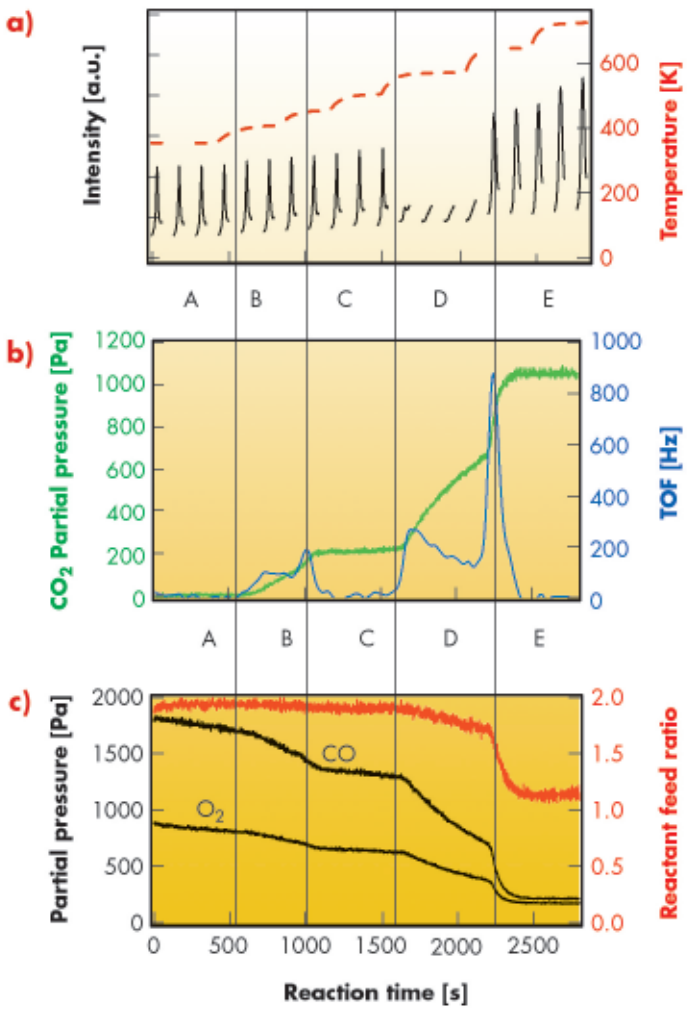

Fig. 90: The reaction cell is run as a batch reactor and both structural (a) and reactive properties (b, c) are monitored *in situ* by SXRD and mass spectrometry, respectively, during the CO oxidation reaction over RuO_2(110)/Ru(0001). Details are given in the text.

These particular experiments already demonstrate a complex structure-activity relationship even in the seemingly simple CO oxidation over RuO_2(110)/Ru(0001). The activity of the catalyst increases substantially in a transient way whenever the catalyst undergoes structural changes either by reducing RuO_2(110) or by forming RuO_2(110). At a temperature of 400 K, the (metastable) oxide catalyst works stably with a medium high activity. Deactivation of the catalyst appears in the temperature region of 450 K to 500 K. Complete deactivation is observed above 650 K and under strongly oxidising reaction conditions ($P(CO)/P(O_2)$ = 1.15).

References
[1] H. Over and M. Muhler, *Prog. Surf. Sci.* **72**, 3 (2003).
[2] P. Bernhard *et al.*, *Rev. Sci. Instrumen.* **70**, 1478 (1999).
[3] Y.B. He, M. Knapp, E. Lundgren, H. Over, *J. Phys. Chem. B* **109,** 21825 (2005).

Principal publication and authors
A. Stierle (a), R. Streitel (a), P. Nolte (a), A. Vlad (a), I. Costina (a), M. Marsman (b), G. Kresse (b), E. Lundgren (c), J.N. Andersen (c), R. Franchy (d) and H. Dosch (a), *New Journal of Physics* **9**, 331 (2007).
(a) Max-Planck-Institut für Metallforschung, Stuttgart (Germany)
(b) Computational Materials Physics and Centre for Computational Materials Science, Universität Wien (Austria)
(c) Department of Synchrotron Radiation Research, Lund University (Sweden)
(d) Institut für Grenzflächenforschung und Vakuumphysik, FZ Jülich (Germany)

Real-time observation of ultrathin oxide growth during alloy oxidation

Atomically-flat oxide films with homogeneous chemical composition are usually required for optimum performance of tunnelling magneto-resistance (TMR) devices which depends critically on the tunnelling barrier thickness and the interface roughness. One way of preparing thin epitaxial oxide layers with a thickness in the sub-nanometre regime and a well-defined interface to the substrate is the selective oxidation of alloys under controlled conditions. Therefore, a precise structural and chemical analysis of the oxide films is mandatory, as well as *in situ* characterisation of the oxide growth process, which is still poorly understood.

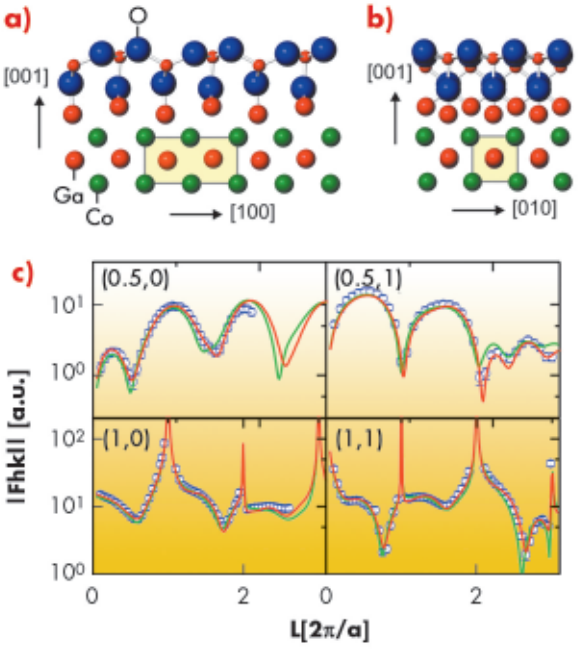

Fig. 91: View of the refined structure of the Ga_4O_4 layer on CoGa(100) along: a) the (010) axis; (b) the (100) axis. (c) Experimental X-ray diffraction structure factors (open circles). The best fit and the most stable DFT model structure factors are indicated by the red and green curves, respectively.

To unravel the atomistic structure of the well-ordered ultrathin epitaxial gallium oxide layer grown on the (100) surface of the inter-metallic B2-ordered alloy CoGa [1], we have adopted a multi-method approach where the results of high-resolution surface X-ray diffraction (SXRD) have been complemented by density functional theory (DFT) and core level spectroscopy (CLS) investigations. In addition, the initial stages of the atomic-scale oxide growth have been systematically studied using *in situ* SXRD. The X-ray experiment was conducted in an *in situ* chamber at the beamline **ID32** using an incident photon energy of 20 keV. For the surface structure determination, an oxide layer was prepared by oxidation at 750 K and 5 x 10^{-7} mbar O_2. A complete structural analysis was performed by measuring 16 symmetry non-equivalent surface rods and four independent crystal truncation rods.

The best fit and lowest DFT energy structural model (**Figures 91a** and **91b**) was found to consist of an fcc-like oxygen ion double layer with gallium ions located in truncated octahedral and tetrahedral sites. At the interface, two more Ga ions occupy sites of the corresponding stacking sequence of bulk β-Ga_2O_3. **Figure 91c** shows the experimental X-ray structure factors (open circles) together with those for the best fit (red curves) and the most stable DFT model (green curves). A remarkably good agreement between theory and experiment was observed, the average deviation between the X-ray and DFT positions within the oxide film being of 0.04 Å.

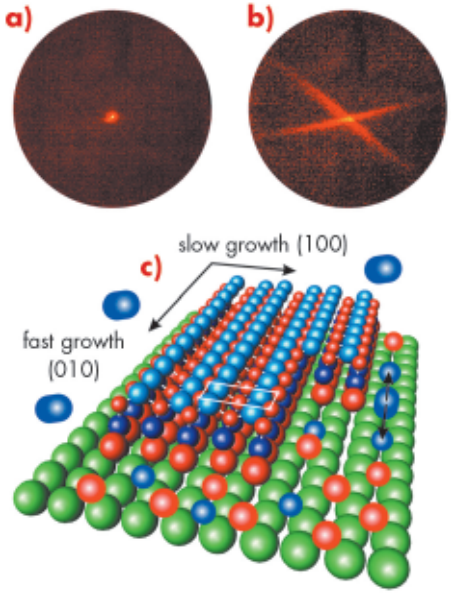

Fig. 92: 2D diffraction pattern at (1,1,1.2): a) for the clean surface and b) after oxidation at 600 K and 10^{-6} mbar oxygen; (c) Scenario for anisotropic gallium oxide growth for one domain.

The onset of oxide formation was investigated in real time on the atomic length scale following the line profile and intensity on an oxide-sensitive reciprocal space position *in situ*, during oxidation. **Figures 92a** and **92b** show the 2D

diffraction pattern obtained from the reciprocal lattice intersection with the Ewald sphere at (1,1,1.2) for the surface firstly in its initial clean state and then after oxidation at 600 K and 10^{-6} mbar oxygen. The formation of two streaks during oxidation gives evidence for the growth of oxide islands with anisotropic shape in two domains. From the time-dependent diffraction signal, the average oxide island width and the time for the completion of one full layer was found to depend strongly on the oxygen partial pressure. This is interpreted as evidence for a transition from a predominantly on terrace nucleation of oxide islands at elevated pressures to a nucleation of oxide islands at step edges for pressures in the 10^{-8} mbar regime.

An atomistic view of the scenario of the strongly anisotropic oxide growth was proposed, where oxygen is very likely supplied by dissociative chemisorption on the metal surface. The oxide grows much faster along the oxide (010) direction probably via the formation of parallel Ga-O-Ga chains, shifted relative to each other by half a substrate unit cell along the (010) direction (**Figure 92c**).

In conclusion, the surface gallium oxide film consists of an oxygen ion double layer which bears similarities with the bulk β-Ga_2O_3 structure. An oxygen pressure dependent transition in the growth behaviour was observed, thus allowing the structural perfection of the oxide layer to be tailored by the appropriate choice of oxidation conditions.

Reference

[1] R. Franchy, *Surf. Sci. Rep.* **38**, 195 (2000).

From atomic to mesoscopic structure

Identifying active sites in zeolites

Zeolites are widely used materials with a very wide range of applications. They are employed in almost every household in laundry detergents and as catalysts in industry such as petrochemical refining; they are also used as air and water purifiers, and as specific absorbents in agriculture. With natural zeolites being discovered more than 200 years ago, intensive research is nowadays aimed at developing new, artificial zeolites with tailored properties for specific tasks.

Active sites are created in the zeolite unit cell when tetrahedrally-coordinated silicon atoms, which are located on the so-called crystallographic T sites, are replaced by trivalent aluminium atoms. Besides the size of its pores, the performance of zeolites is determined by the occupation of specific T sites by aluminium. A zeolite structure database was created [1] by combining the results of many different experimental methods. However, the distribution of Al over the crystallographic T sites has remained unknown for many zeolites. This is seriously hampering the understanding of the function of some

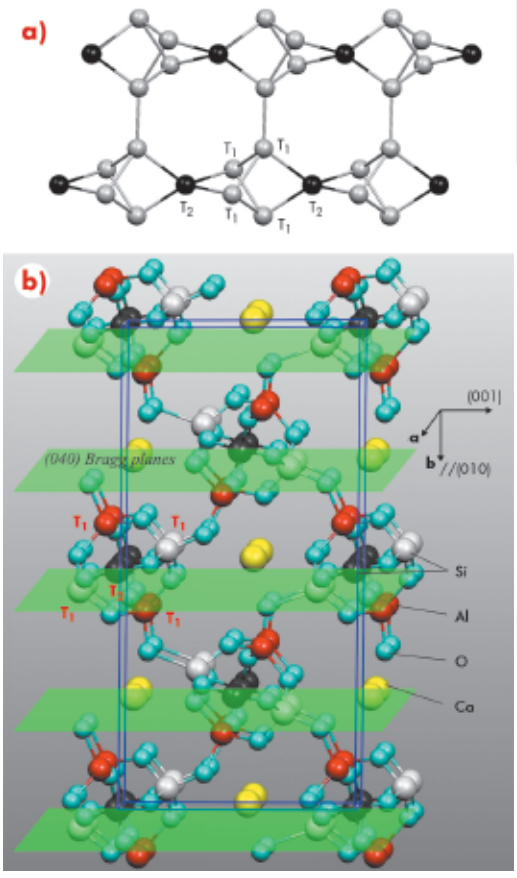

Fig. 93: a) Six of the building units of scolecite, which form a natrolite chain. The spheres represent the five T sites, four T_1 atoms and one T_2, that are occupied by aluminium or silicon. Sticks represent the oxygen atoms that bridge the T sites. The pores of the zeolite are formed by oxygen atoms connecting T_1 atoms of neighbouring chains. b) The atomic structure of the scolecite unit cell is marked by the blue rectangles with lattice parameters of a = 0.6522 nm, b = 1.8968 nm, c = 0.9840 nm, $\alpha = \gamma = 90°$, and $\beta = 109.97°$. The four T_1 sites associated with each T_2 site are indicated. The Bragg planes for the scolecite (040) reflection are indicated.

Principal publication and authors

J.A. van Bokhaven (a) , T.-L. Lee (b) , M. Drakopoulos (c) , C. Lamberti (d), S. Thiess (b,e), J. Zegenhagen (b).
(a) ETH Zurich (Switzerland)
(b) ESRF
(c) Diamond Light Source (UK)
(d) University Torino (Italy)
(e) University Hamburg (Germany)

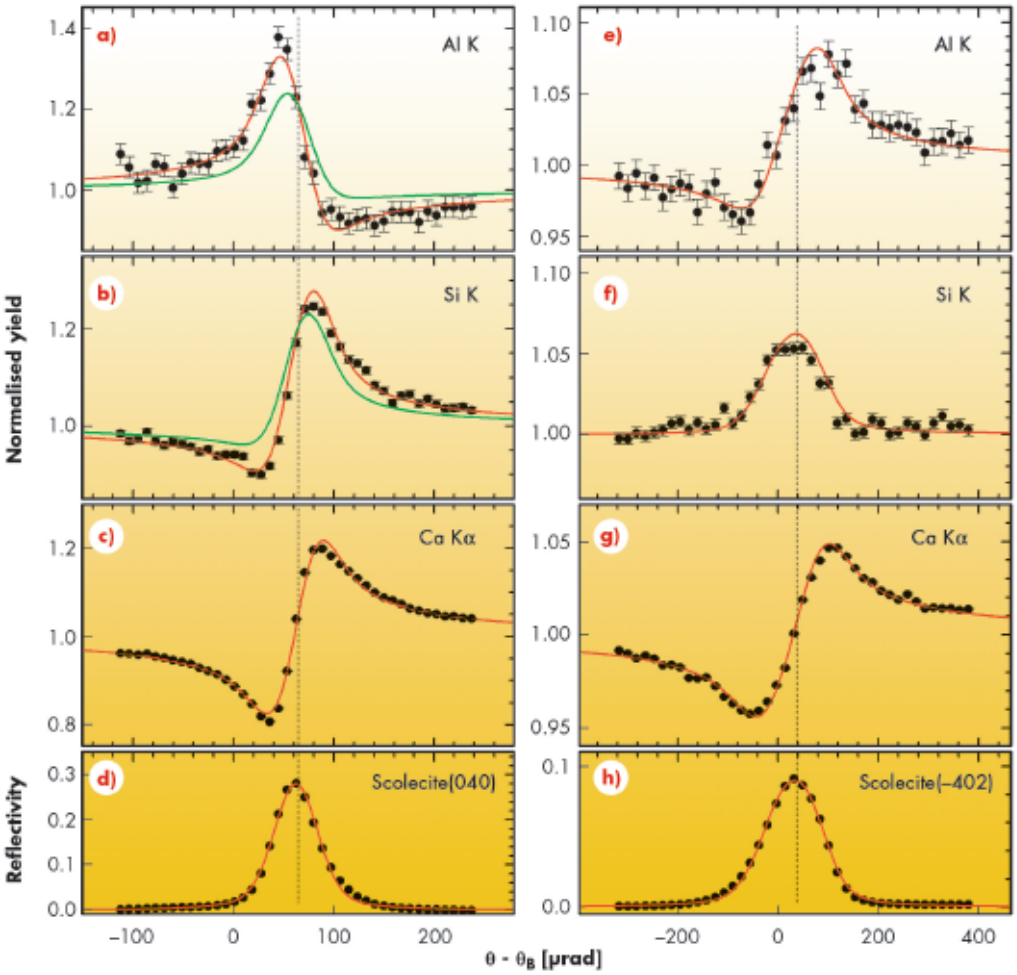

Fig. 94: The XSW-induced Al K, Si K, and Ca Kα fluorescence yields (filled circles in a - c and e - g) and the measured reflectivity (filled circles in d and h) obtained from Θ scans of the (040) and (-402) reflections. The red curves are the best fits to the data, with Al occupying two of the T_1 sites (a and b) exclusively. Green curves, calculated for aluminium occupancy of a,b sites: 0.7, of c,d sites: 0.15, and T_2: 0.3, demonstrate the sensitivity of the XSW measurement. In all cases, the remaining T sites are assigned to silicon, respecting the measured Si:Al ratio of 3:2.

technologically important zeolites and hindering the development of further zeolites with new functionalities.

To determine the aluminium occupation of T sites in zeolites directly, we used the X-ray standing wave (XSW) technique. The well-known zeolite, scolecite, was chosen as an example. Scolecite exhibits the natrolite structure (**Figure 93a**) with the composition $|Ca_4(H_2O)_{12}|[Si_{12}Al_8O_{40}]$. The calcium cation, which is compensating the charge produced by the trivalent Al, is loosely bound and can be exchanged easily. **Figure 93b** depicts the atomic structure of scolecite based on a previous refinement using neutron and X-ray diffraction data [2]. The sample used in the present experiment was a natural crystal and originated from Pune, India. The Si/Al atomic ratio was determined by energy dispersive X-ray spectroscopy as 3:2.

To determine the occupancy of the five T sites in question, we used the X-ray standing wave (XSW) technique at beamline **ID32**. The highly-collimated, focused 6.00 keV X-ray beam selected a small grain of sufficient crystalline quality from the mm-sized mosaic crystal. Three virtually orthogonal reflections, (-402), (002), and (040) (**Figure 93b**), with a lattice spacing of 0.163, 0.462 and 0.474 nm, respectively, were employed for the XSW measurements.

Using the atomic coordinates in Ref. [2] we calculated the Al, Si, and Ca yield for the selected reflections for different combinations of the occupation of the five crystallographic T sites by Al and Si. The resultant curves were compared with the experimental data, this is shown for two reflections in **Figure 94**.
All measured fluorescence yield curves are well reproduced by the calculated ones based on the best fit for the placement of Al and Si (and the known atomic coordinates). The result reveals unambiguously that aluminium is positioned only on half of the T_1 sites. If Al had occupied other positions, this would have been detected by a significant change in the yield curves shown in **Figure 94**.

References
[1] C. Baerlocher, W.M. Meier, D.H. Olson, *Atlas of Zeolite Framework Types*. Fifth Revised Edition, Elsevier, Amsterdam, 2001; http://topaz.ethz.ch/IZA-SC/StdAtlas.htm.
[2] J.V. Smith, J.J. Pluth, G. Artioli, F.K. Ross, Neutron and X-ray refinements of scolecite, *Proc. 6th Int. Zeolite Conf.* 842-850 (1984).

X-ray diffraction microscopy towards nanostructure visualisation

Authors
C. Mocuta (a), J. Stangl (b), K. Mundboth (a,b), T.H. Metzger (a), G. Bauer (b), I. Vartanyants (c), M. Schmidbauer (d), T. Boeck (d).
(a) ESRF
(b) Institut fuer Halbleiter- und Festkoerperphysik, Johannes Kepler Universitaet Linz (Austria)
(c) Hasylab at DESY, Hamburg (Germany)
(d) Institute for Crystal Growth, Berlin (Germany)

X-ray diffraction is a powerful non-destructive tool that can be used to analyse strain fields and composition profiles in condensed matter. With the development of small structures for micro- and nanoelectronics, local probes are gaining popularity for the understanding of novel properties related to the small size. We present here a scanning X-ray diffraction microscope (SXDM) for local probe X-ray diffraction experiments. The approach combines X-ray diffraction with strong focused X-ray beams to localise the micro/nanostructure(s) and analyse their strain and composition. The volume probed has to be adapted to the typical feature size, in many cases in the range of micrometres or smaller. Using epitaxial semiconductor islands grown on Si(001) [1] as a model system, we were able to identify and probe individual objects one by one. The results below were obtained for SiGe islands of 2-3 μm lateral size. The resolution is determined by the focus size. The ongoing refurbishment of the **ID01** beamline has permitted us to reach a submicrometre focus size thus making the technique applicable to individual nanostructures.

The principle of SXDM is shown in **Figure 95**: the X-ray beam is focused by X-ray lenses [2] onto a small spot (3 x 5 μm^2) on the sample, from where it is elastically scattered into the detector (a). The intensity distribution at different positions in reciprocal space is probed (b, c). If the focused beam is scattered at the bare sample surface (b), the intensity distribution shows a sharp Si substrate peak and a streak perpendicular to the sample surface, the crystal truncation rod (CTR). If the X-ray beam hits an island, additional scattering occurs (c). While measuring at this island-sensitive position in reciprocal space, the sample's lateral position is scanned, and the intensity is recorded as a function of the real space position in the fashion of a scanning probe microscope (d). By scanning the sample in the two lateral directions, an image of the island distribution on the sample is recorded (e), with the local strain being responsible for the observed contrast in the image. Any signal characteristic of the object (fluorescence, different lattice parameter, size broadening or coherent interference, etc.) could be used to produce this contrast: the setup works like a scanning probe microscope with tuneable probe signal.

Overlaid to the SXDM color map (panel e) are the island positions (squares) extracted from an optical microscopy image, showing a perfect agreement and proving the capabilities to distinguish and identify single micrometre-sized objects. Once the individual islands are identified, entire reciprocal space maps (RSM, see **Figure 96**) were measured for the particular islands marked by arrows. The red arrows mark islands identified as having a different structure than the majority (~97-98%) of the islands. Comparing the recorded signals, major differences concerning the distribution of the scattered intensity is found. On the (004) RSM (a,c), the position of the

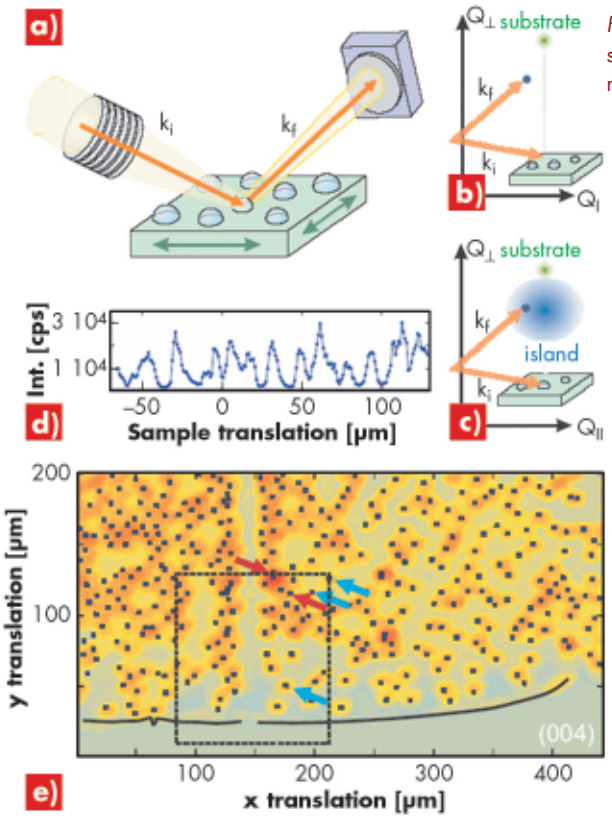

Fig. 95: Scheme of the scanning X-ray diffraction microscope (details in text).

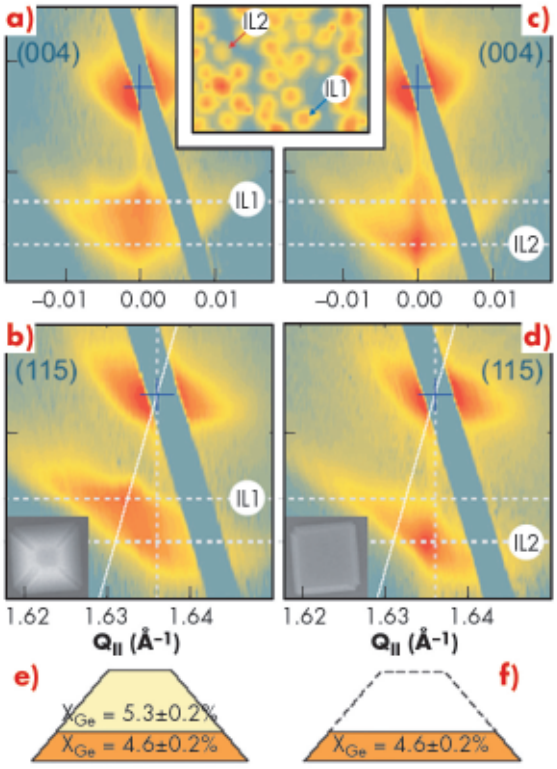

Fig. 96: RSM of SiGe islands around (004) and (115) reciprocal lattice points (top and bottom rows respectively) on particular single islands: (a,b) truncated pyramid-shaped islands and (c,d) flat islands respectively. The position of the substrate peak (cross) and the maximum scattered signal (IL1, IL2) are marked. The inset shows a SXDM map with the particular measured single islands pointed at by arrows. On panels (b,d), the vertical dotted line is the CTR, the continuous lines represent the relaxation lines. The insets show SEM images of the very same islands. (e,f) Ge concentration distribution in the islands (from FEM simulations).

maximum intensity changes, pointing to a different relaxation (average lattice parameter) in the direction perpendicular to the surface. Even more information can be accessed from the non-symmetric (115) reflections (b,d): the scattered intensity close to the relaxation line is a signature of relaxation in the epitaxial islands (IL1), while intensity along the CTR represents pseudomorphically strained material (IL2). The Ge concentration distribution is then obtained from fitting the experimental data and displayed in panels (e,f). The detailed analysis (finite element method (FEM) simulation, not shown here) also gives access to the strain field in the islands. The flat islands are found to represent the bottom part of the truncated pyramids; this morphology is confirmed by Scanning Electron Microscopy (SEM), imaging of the very same objects.

The approach presented here combines local resolution with strain and composition sensitivity. The method is non-destructive, depth-sensitive (works both for free surfaces and buried structures) and requires no particular sample preparation. It also opens the possibility of combining X-ray diffraction and complementary microprobe techniques (atomic-force microscopy, SEM, micro-photo-luminescence, near-field microscopies) on exactly the same micro- or nanostructure. In this example, differences between the morphology, strain and chemical composition of individual objects (truncated and flat pyramids) are clearly correlated and resolved, reaching sensitivities hardly achievable by other techniques, and particularly not by ensemble averaging measurements.

References
[1] M. Schmidbauer, *X-ray Diffuse Scattering from Self-organized Mesoscopic Semiconductor Structures*, Springer Tracts in Modern Physics 199, Springer Berlin Heidelberg (2004).
[2] C.G. Schroer *et al.*, *Phys. Rev. Lett.* **94**, 054802 (2005); *Appl. Phys. Lett.* **87,** 124103 (2005).

Probing a surface reconstruction with anomalous X-ray diffraction

Principal publication and authors
E. Lundgren (a), R. Westerström (a), J.N. Andersen (a), X. Torrelles (b), C. Quiros (c), S. Ferrer (d), I. Popa (e), D. Wermeille (e), R. Felici (e), to be published.
(a) Department of Synchrotron Radiation Research, Lund University (Sweden)
(b) Institut the Ciencia de Materials de Barcelona (Spain)
(c) Departamento de Física, Universidad de Oviedo (Spain)
(d) ALBA, Barcelona (Spain)
(e) ESRF

Surface X-ray diffraction (SXRD) is a powerful technique for the determination of surface structures. Whereas most traditional electron or ion based surface science techniques are limited to the vacuum environment, SXRD is able to determine structural parameters of surfaces under a gas pressure of several bar, or from a surface immersed in a liquid because of the negligible attenuation of hard X-rays. One drawback with SXRD is the often limited data set that can be collected during an experiment when compared to a more traditional technique such as low energy electron diffraction (LEED). This limits the uniqueness of the resulting structure determined on trial and error basis. This limitation can be reduced by the use of a two-dimensional detector, allowing a greater number of data points to be extracted in a shorter time span. Furthermore, SXRD can be combined with other experimental techniques, or with theoretical *ab initio* calculations based on DFT (density functional theory). The data set can also be extended by using anomalous diffraction [1].

In the present study we have investigated the surface reconstruction of Sm [2]. In this system, the bulk Sm atoms are trivalent ($4f^5(6s6p5d)^3$) and the surface atoms are divalent ($4f^6(6s6p5d)^2$). This valence transition, which is unique among the pure elements, leads to some very unusual surface properties, the most prominent being an expansion of the divalent surface Sm atoms by 22%, leading to a coincidence lattice. We have previously studied the resulting surface reconstruction in great detail, as summarised in **Figure 97a**. The correct identification of the structure was supported by *ab-initio* theoretical calculations.

In this structure, the different in-plane nearest-neighbour distance in the top-most layer with respect to the bulk layers can easily be detected using SXRD, **Figure 97b**. We have an extremely clear signal for differentiating between the single divalent surface layer and the deeper trivalent bulk layers. The window free design of the refurbished **ID03** beamline permitted us to reach the quadrupole (2p – 4f) resonance at 6.716 keV for trivalent Sm and perform surface resonant scattering from this single, well-defined surface layer.
In a first experiment we detected the diffracted intensities from the bulk signal at H = 0 and K = 1 (L = 0.2), and scanned across the L-edge, as shown by the black dotted line in **Figure 97c**.
A clear dip is seen at a photon energy of 6715 eV. If instead we detect the diffracted photons from the surface signal at H = 0.82 and K = 0, a clear shift of the dip to 6708 eV can be observed in the red dotted line in **Figure 97c**. Thus we find a shift between the bulk and the surface anomalous diffraction of approximately 7 eV. This value is very close to the shift in the 3d level between divalent and trivalent Sm atoms [3], directly showing that the surface signal stems from divalent Sm atoms while the bulk signal is from trivalent Sm atoms. The experiment thus confirms previous surface models for the valence induced surface reconstruction of Sm. It also demonstrates the ability of the ID03 beamline to scan the photon energy in a controlled manner, and the ability to reach the lower-lying (2p-4f) resonances in the important rare earth materials.

Anomalous SXRD can be used at ID03 in a simple way to gain additional, and sometimes essential chemical information on an unknown surface structure.
A detailed structural evaluation based on surface anomalous diffraction must include the photon energy dependence of the transmission function and the form factors involved. In addition, the sensitivity to anomalous scattering of the topmost reconstructed surface layer may be used to perform resonant magnetic diffraction measurements, allowing an accurate isolation and quantification of the magnetisation of the topmost atomic plane.

References
[1] B.E. Warren, *X-ray Diffraction*, Dover Publications Inc. (1990).
[2] E. Lundgren, J.N. Andersen, R. Nyholm, X. Torrelles, J. Rius, A. Delin, A. Grechnev, O. Eriksson, C. Konvicka, M. Schmid, P. Varga, *Phys. Rev. Lett.* **88** 136102 (2002).
[3] Å. Fäldt and H. Myers, *Phys. Rev. B* **33,** 1424 (1986).

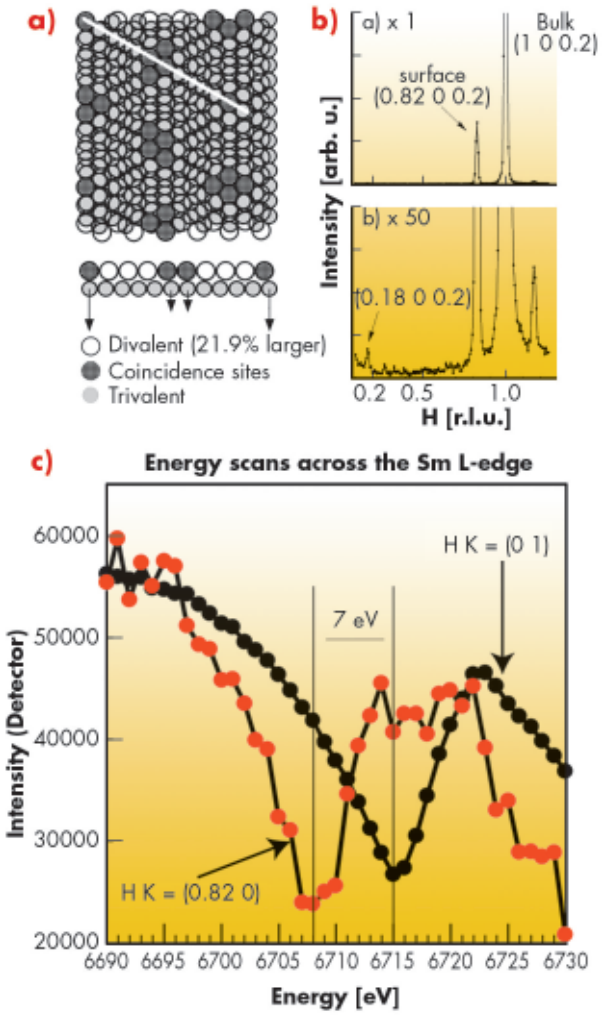

Fig. 97: (a) Top and side views of the surface reconstruction of Sm(0001). (b) In-plane H-scan (K=0) clearly showing the incommensurate surface layer. (c) Photon energy scans across the Sm L-edge at (H K L) = (0.82 0 0.2) (red-dotted line) and at (H K L) = (0 1 0.2) (black-dotted line) corresponding to diffraction from the surface and the bulk, respectively. The shift between the dips at resonance corresponds to the core level binding energy shift between divalent and trivalent Sm atoms as found by xps [3].

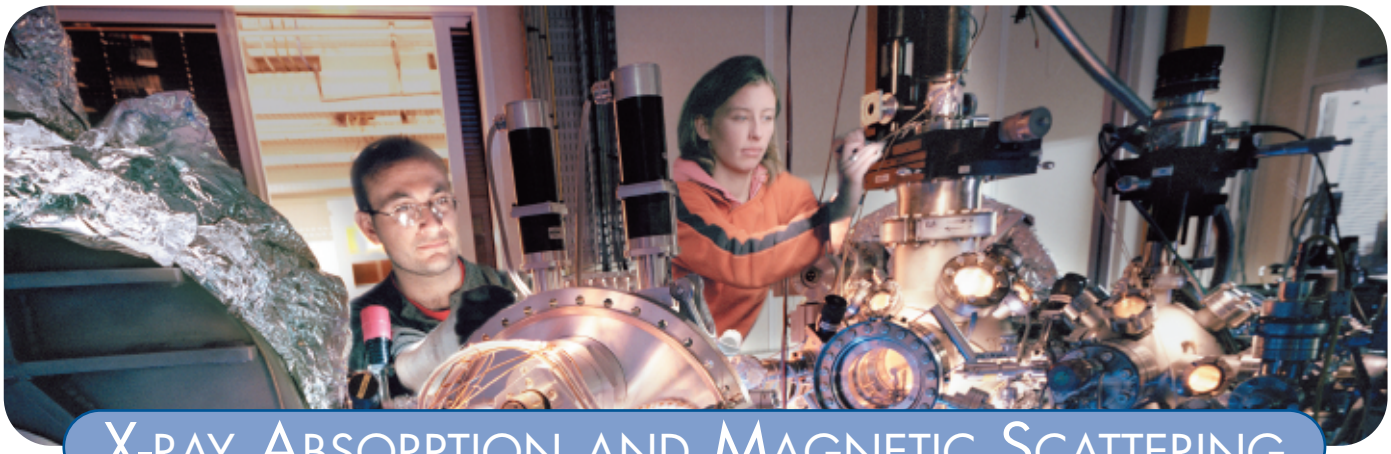

X-RAY ABSORPTION AND MAGNETIC SCATTERING

Introduction

Information on local crystal and electronic structure with elemental specificity is of paramount importance to understand many scientific problems. X-ray absorption techniques are particularly suitable for this. X-ray scattering methods can also give input on long range properties such as magnetic structures. Consequently, the topics of research studied at the X-ray absorption and magnetic scattering group of beamlines are wide ranging and cover both applied and basic research. Clearly, the research falling within these domains goes much further than can be covered in the Highlights. Nevertheless, in the following articles several typical examples of research carried out at ESRF and CRG beamlines using the unique properties of X-ray absorption and magnetic scattering methods are presented.

The current topical areas are extreme conditions, nanoscience and spintronics, and there are many experiments on oxide materials including high temperature superconductors. The growing number of studies involving sophisticated simulation or theoretical calculations points to the importance of a theoretical and experimental synergy to fully exploit experimental work.

It should also be noted that there is a continuing trend to combine experimental methods *in situ e.g.* in studies of catalysts. This is becoming particularly prevalent in

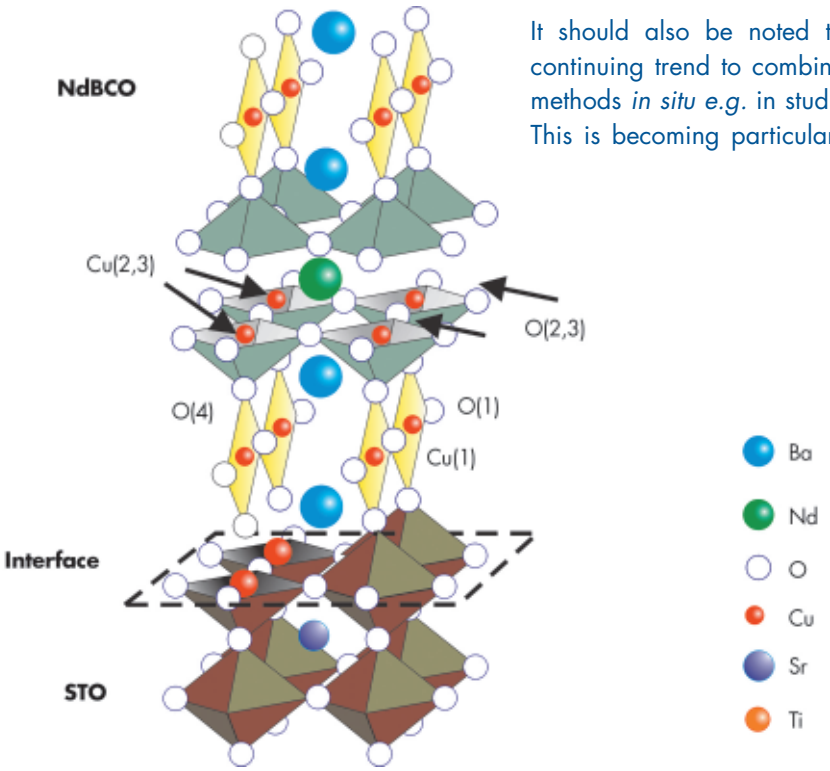

Fig. 98: Sketch of a $NdBa_2Cu_3O_7$ (001) (NdBCO) ultrathin film / $SrTiO_3$ (STO) interface engineered to investigate field effect doping in high temperature superconductors (see article Salluzzo *et al.* p 97).

the exploitation of sample environments involving high pressure, low sample temperatures, high magnetic and electric fields with the push to combine them together in the same experiment.

In addition, there is a growing importance in sample preparation and optimisation for specific X-ray experiments (for example, **Figure 98**). This requires a strong collaboration between X-ray scientists and specialists in the materials to be studied and sufficient infrastructure at or near the X-ray experimental facility to handle these special samples. This is one of the important aims of the current ESRF Upgrade programme.

N.B. Brookes

A structural-reactive rollercoaster: palladium nanoparticles during redox cycling

Principal publication and authors
M.A. Newton (a), C. Belver (b), A. Martínez-Arias (b), M. Fernández-García (b), *Nature Mat.* **6**, 528-532 (2007); *Angew. Chem Int. Ed.* **45**, 8629-8631 (2007).
(a) ESRF
(b) Instituto de Catalisis y Petroleoquímica, Madrid (Spain)

Supported noble metals, such as Pd, are widely used as heterogeneous catalysts; indeed most of us use such catalysts everyday within the exhaust system of our cars. These catalysts are designed to ensure that any toxic by products of the internal combustion engine (unburnt hydrocarbons, nitrogen oxides, and CO) do not reach the atmosphere at large and are instead converted efficiently to N_2, CO_2, and water. To achieve this, the catalysts have to be able to work within a rapidly changing "redox" (reduction/oxidation) environment; the changes being controlled to maximise efficiency by the car's engine management system.

Whilst this technological approach has existed for sometime, exactly what happens to the catalysts from a structural-reactive point of view within this cycling is far from being understood. Furthermore these catalysts, and similar ones used in a variety of industries, are still plagued with problems such as particle sintering, which limit their useful lifetime. Sintering causes initially small and well-separated metallic catalyst particles to agglomerate and form larger species. This has two effects: firstly the active surface area of the metal component is massively reduced; and secondly the very chemistry displayed by the much bigger particles may be radically different (and often unwanted) relative to the much smaller starting particles.

Recently we have carried out an experiment designed to permit the internal working of catalysts during redox cycling to be studied with accurate time-resolution, and from three synchronous approaches: structural (in this case dispersive EXAFS, **ID24**); the global measurement of performance (mass spectrometry); and a time-resolving probe of the species that exist transiently on the surface of the catalyst during the cycling (infrared spectroscopy).

Our findings are that the structure (size/shape) of the supported Pd nanoparticles appears to be very fluid

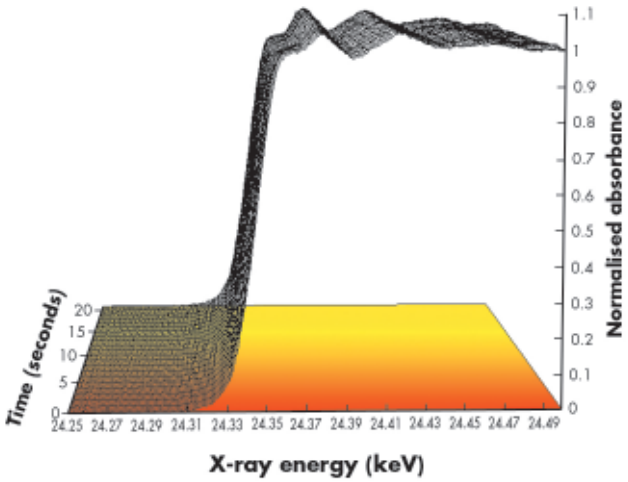

Fig. 99: Normalised Pd K edge energy dispersive EXAFS spectra derived during a switch from a 5%NO/He feed to a 5%CO/He feed (both 75mlmin^{-1} flow) at 673 K over a 1wt%Pd/10ZCA sample. Each spectrum was acquired in ca. 250 msecs. For clarity only 1 spectrum/second is plotted. The red to yellow shading is indicative of the switch from the NO to CO feed.

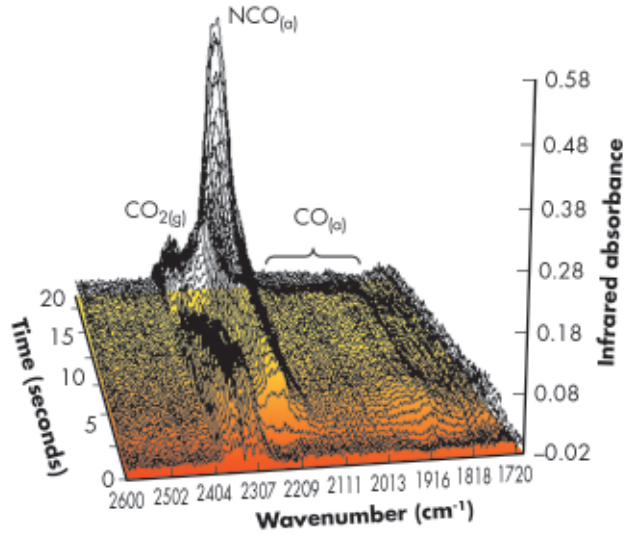

Fig. 100: Infrared spectra (averaged over 9 reversible NO/CO switches) taken at the same time as the EXAFS spectra shown in Figure 99, collected with a 3 Hz spectral acquistion speed. The major gas phase and surface functionalities observed during the experiment are indicated. Again the shading of the flow of the graph indicates the change of reactive feedstock.

indeed, changing very rapidly in response to the changes in composition of the reactive feedstock. There were indications that oxidation of the Pd nanoparticles was relatively slow compared to their structural rearrangement and this even in the presence of relatively large amount of O_2.

Figures 99 and **100** shows results typical of the observed behaviour from both XAFS and infrared perspectives for a 1wt%Pd/10ZCA sample (10ZCA = 10% zirconia/ceria/alumina). The dynamic behaviour of the surface functionality is clearly delineated by the infrared component of the experiment allowing us to follow the formation and removal of a number of different species with, in the current case, a temporal resolution of 300 milliseconds. From this we can identify a number of carbonyl species forming and reacting; isocyanate (NCO) species forming on the Pd but migrating to the oxide where they decompose; the formation of CO_2 in the gas phase; and a number of other species such as adsorbed NO on Pd and carbonate species associated with the support material.

At the same time the dispersive XAFS lets us see how the Pd responds to the dynamism exhibited by its feedstock. Both the near edge (XANES) and extended XAFS (EXAFS) spectra indicate that the size and the shape of the Pd particles varies rapidly and reversibly with the changes in environment: the Pd agglomerates under a reducing (CO) environment and disperses to smaller/flatter particles under oxidising (NO) conditions, moreover, these techniques also allowed us to determine that oxidation of the Pd component (to for instance PdO) is much slower than the aforementioned structural rearrangements. Under these circumstances therefore, it is these more subtle, and apparently more facile, size and shape changes that have the potential to play a significant role in the catalytic chemistry being displayed by the operating catalyst rather than the other, more well-known processes, such as oxidation.

Quantification of the precise nature of the structure reactivity by means of a variety of types of measurement paints a picture of a massively responsive and dynamic nano-world. Therein the variables of starting metal particle size, temperature and the redox potential of the gas phase are braided together in complex and sensitively interdependent ways that can have a massive bearing on their cumulative performance as functional materials.

Long-lasting controversies on properties of matter at high pressure: the role of XAS

Principal publications and authors
G. Aquilanti (a), A. Trapananti (a), M. Minicucci (b), F. Liscio (c), A. Twaróg (d), E. Principi (b), S. Pascarelli (a), *Phys. Rev. B*, **76**, 144102(6) (2007); G. Aquilanti (a), H. Libotte (e), W.A. Crichton (a), S. Pascarelli (a), A. Trapananti (a), J.-P. Itié (f), *Phys. Rev. B*, **76**, 64103(7) (2007).
(a) ESRF
(b) CNISM, CNR-INFM, Università degli Studi di Camerino (Italy)
(c) Laboratoire de Thermodynamique et Physico-Chimie Métallurgiques, ENSEEG, Saint Martin d'Hères (France)
(d) Faculty of Physics, Warsaw University of Technology (Poland)
(e) Département de Physique, Université de Liège (Belgium)
(f) Synchrotron Soleil, Gif-sur-Yvette (France)

The thermodynamic variable pressure is being increasingly employed to study the behaviour of matter when atoms are brought closer together. This allows experimental verification of the different models used to describe the structural and the electronic properties of matter. If diffraction methods are still the predominant high pressure techniques for structural studies involving synchrotron radiation, X-ray absorption spectroscopy (XAS) offers a complementary description of matter under pressure: it gives a local picture since it probes the local environment around the photoabsorber atom with chemical selectivity. It is also sensitive to pressure-induced electronic transitions since it probes the electronic density of states above the Fermi level. Here we show two examples that highlight the complementarity of XAS with respect to other more conventional techniques in the understanding of fundamental issues in condensed matter physics.

Metallic zinc, together with its electronic counterpart metallic cadmium, are intriguing systems among divalent hexagonal close-packed structured metals as the *c/a* axial ratio exceeds about 14-15% the ideal value for *hcp* structures. This anomaly makes many of its solid state properties highly anisotropic and, at high pressure, Zn is believed to undergo a Lifshitz or electronic topological transition (ETT) near 10 GPa. This type of phase transition arises when distortion of the electronic band structure due to an external agent such as doping, hydrostatic pressure or anisotropic strain modifies the topology of the Fermi surface. For this reason, compressed zinc has been extensively studied both theoretically and experimentally with a disconcerting plethora of different results. In particular X-ray diffraction on Zn under pressure has proven to be particularly sensitive to hydrostatic conditions [1]. We have studied compressed metallic zinc using energy dispersive XAS at **ID24** in different hydrostatic conditions. The aim of this study was to gain direct evidence for the ETT in solid Zn under pressure by probing the variation of the X-ray absorption near-edge structure (XANES). In fact, according to the electric dipole selection rules, Zn K-edge XANES directly probes the density of unoccupied states with *p* symmetry. Therefore, the variations as a function of pressure of the near-edge structure of the spectra are a probe for pressure-induced changes in the electronic density of states above the Fermi level and may give direct evidence of the ETT. **Figure 101** shows the near-edge part of the spectra acquired using various pressure transmitting media, 4:1 methanol:ethanol and neon, to provide different hydrostatic conditions.

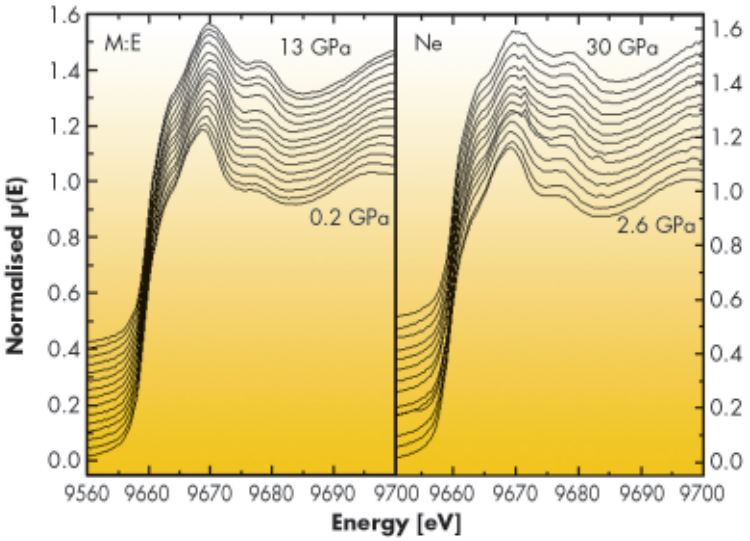

Fig. 101: XANES spectra for metallic Zn measured using 4:1 methanol:ethanol (left panel) and Ne (right panel) as pressure transmitting media.

Methanol:ethanol is known to yield quasihydrostatic conditions only up to 10 GPa, whereas previous experiments suggest that the strength of solid Ne above 100 GPa is sufficiently low that the material can be used as a quasihydrostatic medium over this pressure range. The gradual evolution of the XANES features with pressure for the two experiments carried out in different hydrostatic conditions not only show no evidence of an electronic transition in Zn under pressure, but also demonstrate that

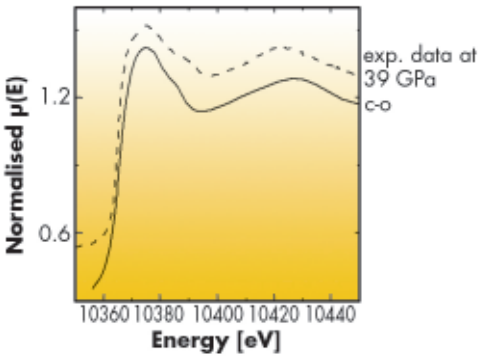

Fig. 102: From bottom to top: Simulated Ga K-edge spectrum of GaP in a chemically ordered *Cmcm* structure (*c-o*) and experimental data at 39 GPa (dashed line).

XAS is much less sensitive to nonhydrostaticity.

Besides the sensitivity to changes in electronic structure, the chemical selectivity of XAS can be used to give an insight complementary to diffraction in the determination of chemical order in high pressure structures. Knowledge of local chemical order is of capital importance because with increasing density, the relative weight of different energetic terms in play are modified, and it is often difficult to foresee how and to what extent this occurs. Therefore, being able to tell for example whether or not atoms A are predominantly surrounded by atoms B in an AB alloy, allows one to test thermodynamical and structural models derived using theoretical methods. The octect compounds $A^{(n)}B^{(n-1)}$ are a class of compounds extensively studied at high pressure using X-ray diffraction. In particular the increased popularity of angle dispersive X-ray diffraction has led to a re-evaluation of the high pressure phase diagram of this class of materials and to the identification of *Cmcm* as a common structure at high pressure [2]. Using XAS we have been able to verify that the high pressure *Cmcm* phase of gallium phosphide is locally chemically ordered, when X-ray diffraction could only conclude on the presence of long-range disorder. Ga K-edge XANES spectra measured on beamline **ID24** were compared to state-of-the-art full multiple scattering calculations (**Figure 102**) and confirm unequivocally the occurrence of a *Cmcm* symmetry with a high degree of local chemical ordering. This means that, notwithstanding the low ionicity of this compound, this parameter still dictates short range interactions even at very high densities.

References
[1] K. Takemura, *Phys.Rev. B*, **60**, 6171-6174 (1999).
[2] R. J. Nelmes, M.I. McMahon, S.A. Belmonte, *Phys. Rev. Lett.* **79**, 3668-3671 (1997)

On the occurrence of polymorphism in liquid Sn at high-pressure

Principal publication and authors
A. Di Cicco (a), A. Trapananti (b), E. Principi (a), S. De Panfilis (b) and A. Filipponi (c), *Appl. Phys. Letters* **89**, 221912 (2006).
(a) Università Di Camerino (Italy)
(b) ESRF
(b) Università dell'Aquila (Italy)

Solids are known to transform between polymorphs having different structure and physical properties in response to pressure and temperature. The occurrence of analogous density driven phase transitions between two liquids, characterised by different local structures and thermodynamic properties has been the subject of intense interest since a liquid-liquid transition has been discovered in phosphorus (see [1] for a review).

Theoretical models and simulations have shown that liquid-liquid (L-L) phase transitions are possible and most likely to occur as metastable transitions in the undercooled liquid regime. From the experimental side, however, support for the existence of these transformations is still rare, mainly as a consequence of the technical difficulties in probing liquids under metastable and extreme conditions.

In various pure metals, the existence of liquid polyamorphism was inferred by rather sharp changes in the electrical conductivity, specific heat and sample volume. Theoretical studies indicate liquids described by soft-core interatomic potentials (like Ge, Sn, Ga, or Bi), among the possible candidates for exhibiting structural changes in their liquid stable or metastable state.

We further studied the interesting case of liquid Sn, with the aim of clarifying whether the reported anomalies are associated with changes of the local structure and/or nucleation properties.

Using X-ray absorption spectroscopy in combination with complementary techniques, like fixed energy X-ray absorption temperature scans and X-ray diffraction also available at beamline **BM29**, we have investigated solid and liquid Sn in the 0-4 GPa and 300-850 K pressure and temperature range using a large-volume Paris-Edinburgh apparatus.

From the X-ray absorption temperature scans recorded at different pressures (**Figure 103**, upper panel) we discovered that above a critical pressure (~ 2 GPa), the undercooling of liquid Sn is drastically reduced by preferential nucleation of the liquid into a solid phase (Sn-III) expected to be stable at higher pressure (~ 3 GPa). This can be observed in **Figure 103**, where the transition to the Sn-III phase is associated with a sudden increase of the absorption level and the occurrence of diffraction peaks identified as reflections of the body centred tetragonal Sn-III phase.

In the lower panel of **Figure 103**, the XAS signals collected at 2.5 GPa, at four different temperatures (marked in the X-ray absorption temperature scan, lower inset) show the close similarity between the local structure of liquid Sn and solid Sn-III.

In order to maximise the structural information that could be extracted from the experimental data, the XAS signals were analysed by Reverse Monte Carlo (RMC) modelling [2]. This approach provides three dimensional models of a disordered system compatible with XAS and diffraction data. These models can be analysed in terms of pair distribution functions, coordination numbers and bond angle distributions, to obtain a complete insight into the atomic correlations on the microscopic level.

From such analysis, the local structure of liquid Sn is clearly different from that of simple close-packed liquids, such as Cu. In molten Sn, where the bond angle distributions, *f(θ)* in **Figure 104**, are characterised by a broad hump in the region between 90° and 110°, which includes the tetrahedral angle. A more detailed analysis in terms of local coordination numbers also demonstrates that the total *f(θ)* includes contributions from low-coordinated structural units having some degree of tetrahedral ordering, plus close-packed configurations of higher coordination number. Pressure induces a gradual modification of the local structure: tetrahedral-like structural units are progressively reduced upon compression.

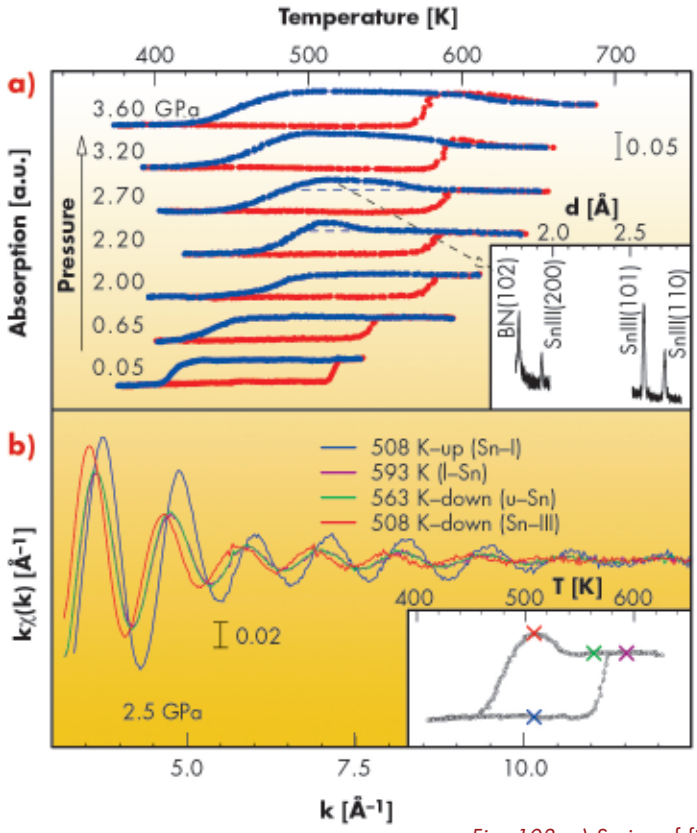

Fig. 103: a) Series of fixed-energy X-ray absorption temperature scans at different pressures. The drastic changes of the absorption during heating (red) and cooling (blue) ramps correspond to phase transitions. Above 2 GPa, undercooled Sn nucleates in a metastable phase, identified as solid Sn-III by X-ray diffraction (inset). b) XAS kχ(k) signals measured at 2.5 GPa at four different temperatures (marked in the X-ray absorption temperature scan, lower inset).

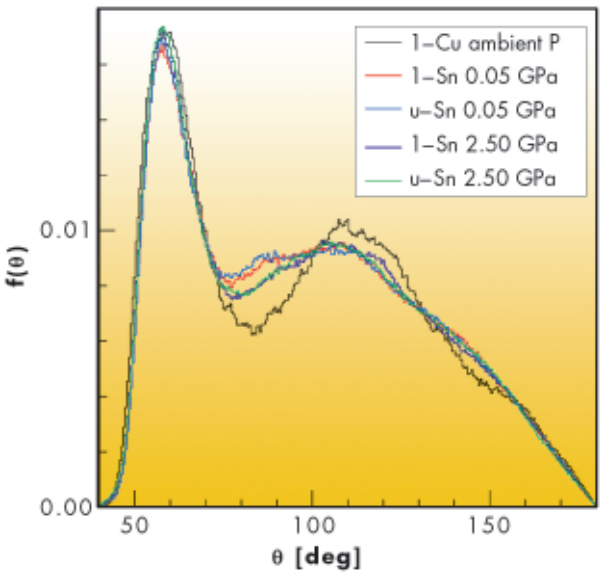

Fig. 104: Angular distributions of liquid and undercooled Sn at 0.05 and 2.5 GPa, compared with liquid copper at ambient pressure.

References
[1] P.F. McMillan, *J. Mater. Chem.* **14**, 1506 (2004).
[2] A. Di Cicco and A. Trapananti, *J. Phys. Cond. Matter* **17**, S135 (2005).

In conclusion, we observed the occurrence of an anomalous phase selection above 2 GPa in liquid Sn. This was found to be accompanied by tiny and gradual changes of the local ordering: upon pressurisation, the local structure evolves toward an arrangement having a closer affinity with a close-packed liquid, but without any sharp modification corresponding to a liquid-liquid phase transition.

Principal publications and authors
M. Vračar (a), A. Kuzmin (b), R. Merkle (a) J. Purans (b), E.A. Kotomin (a), J. Maier (a), O. Mathon (c), *Phys. Rev. B* **76**, 174107 (2007).
(a) Max Planck Institute for Solid State Research, Stuttgart (Germany)
(b) Institute of Solid State Physics, Riga (Latvia)
(c) ESRF

Structural studies of $Sr(Fe_xTi_{1-x})O_{3-\delta}$ solid solutions by XAS and Raman spectroscopy

The perovskite solid solution series $Sr(Fe_xTi_{1-x})O_{3-\delta}$, $0 \le x \le 1$, is an interesting system spanning the range from slightly iron-doped $SrTiO_3$ as a model representative of acceptor-doped large band gap electroceramics, to iron-rich $Sr(Fe_xTi_{1-x})O_{3-\delta}$ materials, which are good electronic and ionic conductors. Such materials can serve as key functional materials in fuel cells, electrochemical sensors and permeation membranes. In $Sr(Fe_xTi_{1-x})O_{3-\delta}$, the iron substitutes for Ti^{4+} partly in the oxidation state of Fe^{3+} and partly as Fe^{4+}, the actual Fe^{3+}/Fe^{4+} fraction depending on total iron concentration, oxygen partial pressure, and temperature. The charge compensation for Fe^{3+} occurs predominantly by the formation of mobile oxygen vacancies. For dilute Fe^{4+} centres (high spin d^4 configuration) a Jahn-Teller distortion is predicted by quantum chemical calculations [1]. The formation of an iron impurity band occurs for iron concentrations higher than about 3-10% and represents a drastic change of the electronic structure [1]. The iron in metallic conducting $SrFeO_3$ is known to have an undistorted octahedral coordination. The transition between these limiting cases is addressed in this study.

For each Fe concentration an oxidised (almost all Fe^{4+}) and reduced (Fe^{3+}) sample was investigated. Fe and Ti K-edge XAS spectra were recorded at beamline **BM29**. EXAFS show different local inter-atomic distances, for oxidised samples, Fe^{4+}–O^{2-} distances are smaller than half-lattice constants obtained by XRD. Splitting of the first Fe^{4+}–O^{2-} coordination shell was not observed directly. However, for oxidised samples, we observe an increase of the mean square radial distribution (MSRD) with decreasing x (**Figure 105**). For low x, MSRD of Fe^{4+} is even larger than that of Fe^{3+} for which oxygen vacancies are present. These findings also remained in low temperature measurements proving a strong static disorder. All these observations can be explained plausibly by a local Jahn-Teller distortion around dilute Fe^{4+} centres.

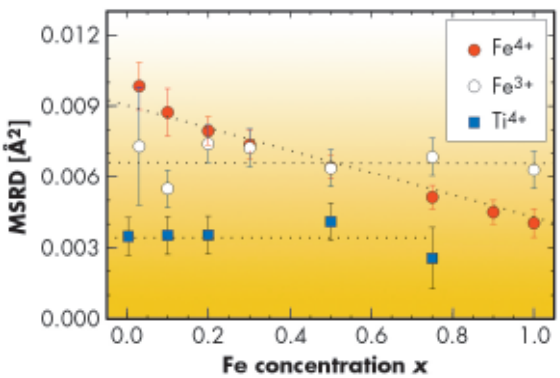

Fig. 105: Concentration dependence of the MSRD for Fe^{4+}–O^{2-} and Ti^{4+}–O^{2-} bonds (oxidised samples) and Fe^{3+}–O^{2-} (reduced samples) in the first coordination shell, all at room temperature. Dotted lines are guides for the eye.

Raman spectra of oxidised samples show a new peak in the otherwise Raman-inactive cubic perovskite structure, **Figure 106**. This indicates a local symmetry breaking which is inseparably related to the presence of Fe^{4+}, and thus strongly suggests a Jahn-Teller distortion (Note that the reduced samples, in spite of oxygen vacancies present, exhibit no Raman peak). The Raman peak decreases with increasing iron concentration at

similar x where the iron impurity band starts to form, which is consistent with the absence of the Jahn-Teller distortion for $SrFeO_3$.

Although none of the individual observations alone gives the final proof of a Jahn-Teller distortion around Fe^{4+} ions, the combination of results obtained by XAS, especially the iron concentration dependence of the Fe^{4+}–O^{2-} MSRD, and Raman spectroscopy strongly supports its presence, most pronounced for $x \sim 0.03$ and decreasing for higher iron concentrations. The decrease of the Jahn-Teller effect with increasing x can be understood qualitatively by the change in the electronic structure of the materials from insulator to metal. A quantitative modelling of the variation of the Fe^{4+}–O^{2-} MSRD and the intensities of the Raman lines remains a challenging theoretical problem.

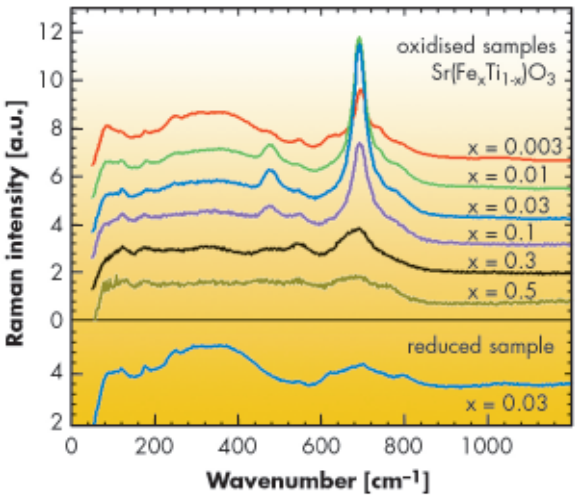

Fig. 106: Raman spectra for oxidised $Sr(Fe_xTi_{1-x})O_3$. The spectra are scaled to comparable intensity in the 200-400 cm^{-1} range and shifted upward for clarity. Bottom panel: reduced $Sr(Fe_{0.03}Ti_{0.97})O_{2.985}$ sample.

References

[1] R.A. Evarestov, S. Piskunov, E.A. Kotomin, G. Borstel, *Phys. Rev. B* **67**, 064101 (2003).

Depth-resolved study of impurity sites in low-energy ion-implanted As in Si

Principal publication and authors

F. d'Acapito (a), S. Milita (b), A. Satta (c), L. Colombo (c,d) , *J. Appl. Phys.* **102**, 043524 (2007).

(a) CNR-INFM-OGG, GILDA CRG Grenoble (France)

(b) CNR-IMM, Bologna (Italy)

(c) CNR-INFM SLACS Cagliari (Italy)

(d) Dept. of Physics University of Cagliari (Italy)

The electrical and diffusion properties of dopant atoms in silicon are of primary importance for the realisation of ultra-shallow junctions for transistors in the semiconductor industry. In arsenic-doped Si:As, important phenomena appear when the doping level reaches volumes as high as 10^{21} cm^{-3}, namely: (i) the concentration of free carriers does not increase linearly with the doping level; (ii) rapid thermal annealing (RTA) enhances the concentration of active carriers, while further annealing decreases the number of electrically-active impurities to saturation levels; (iii) the As diffusion coefficient starts to increase rapidly. Furthermore, upon RTA the original implant profile is modified significantly by the transient enhanced diffusion effect, generating long tails of dopants into the substrate and their accumulation near the surface. To explain the electrical As deactivation and its enhanced diffusion one can use X-ray measurements and computer simulation techniques. The extended X-ray absorption fine structure (EXAFS) technique has been widely used since it characterises the local atomic structure around the dopant atom. The efficacy of *ab initio* calculations to reproduce the local structure of point defects has also been demonstrated.

In this work we combine EXAFS measurements and *ab initio* total energy calculations to investigate these phenomena. In particular, we investigated four crystalline Si:As samples, obtained by implanting Si (001) substrates with As^+ ions at an energy of 5 keV and a fluence of $1x10^{15}cm^{-2}$ and treated by different thermal budgets.

The EXAFS measurements were carried out at the arsenic K edge (E = 11867 eV) in glancing angle geometry, at **BM08**, the GILDA CRG beamline. For each sample, spectra were collected in *total reflection* (TR), and *high angle* (HA) modes. TR uses an incident beam below the critical angle for the total reflection, and the latter above, so that the As site in surface part (about 6 nm in TR mode) or in the bulk (300 nm in HA mode) of the sample are probed.

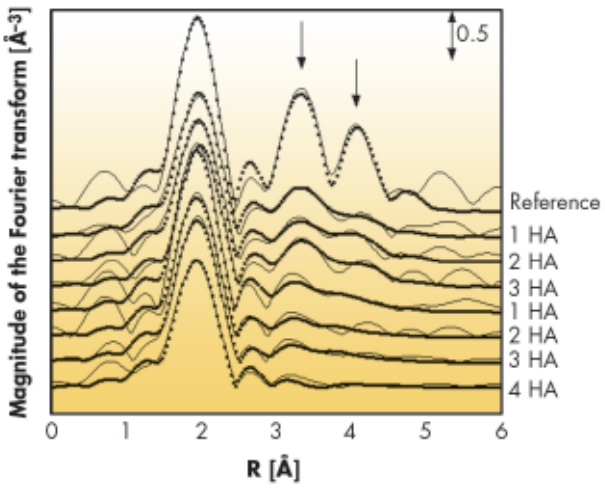

Fig. 107: Fourier transform patterns of the raw EXAFS spectra (lines) compared with the best fit curves (dots). The spectra numbers identify the sample treatment: 1 corresponds to RTA at 900°C, 2 to RTA at 1050°C, 3 to spike annealing at 1050°C, 4 to the as implanted. The reference sample is described in the text.

The experimental findings were supported by our theoretical study based on the density functional theory (DFT). **Figure 107** shows the Fourier Transform pattern of the EXAFS spectra of the samples measured both in TR and HA. The *reference* used for As in a substitutional position is the spectrum of an Si (001) wafer implanted with As^+ ions at an energy of 70 keV and a fluence of $3x10^{15}$ cm^{-2} and annealed at 1100°C in N_2 for 100 s.

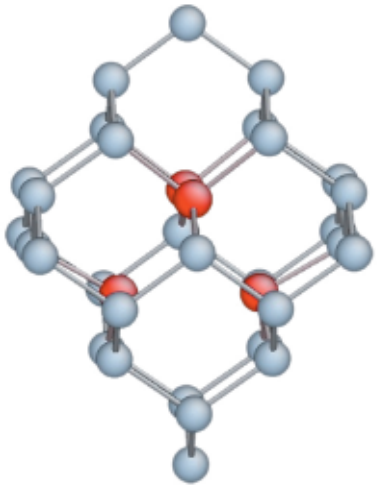

Fig. 108: Balls and sticks representation of the V-As_4 complex.

Arrows indicate the peaks that exhibit the more marked change when passing from HA to TR series. In our case, the peaks located in the region from 3.0 to 4.5 Å correspond to the second and third coordination shells. They are weaker in the HA spectra than those in the reference spectrum and they disappear in the TR spectra. This indicates an increase of the disorder in all the samples, which is more evident in the shallow region.

The HA data, relative to all the As content, also in the deeper part of the implant, reveal the presence of As in the Si matrix linked to a vacancy. Only by comparing the value of the distance for Si second neighbours resulting from the fit of the experimental data and those obtained by DFT calculations for various complexes V-As_n (n=1 to 4) we could identify V-As_3 and V-As_4 as those present in the material. **Figure 108** represents a model of the V-As_4 complex.

In the TR case we found a very disordered environment with possible presence of As precipitates. This is due to the crystallisation front that, initiating from the amorphous/crystalline interface during the annealing, transports dopants towards the Si/SiO_2 interface (snowplough effect) creating in this zone an increased concentration of As impurities and defects.

In this work we have carried out a depth-selective EXAFS investigation in grazing incidence geometry on arsenic doped silicon samples. Evidence of different environments of the impurity along the concentration profile has been found and the experimental findings have been compared with an *ab initio* study. In summary, As occupies predominantly substitutional positions and it is linked to vacancies forming As_3V and/or As_4V complexes. Conversely, near the surface, the local structure appears to be extremely disordered, plausibly as a consequence of the As accumulation at the surface due to the thermal annealing treatment.

References
[1] A. Lietoila, J.F. Gibbons and T. W. Sigmon, *Appl. Phys. Lett.* **36** (9), 765 (1980).
[2] M. Ramamoorthy and S. T. Pantelides, *Phys. Rev. Lett.* **76** (25), 4753 (1996).
[3] A. Satta, E. Albertazzi, G. Lulli and L. Colombo, *Phys. Rev. B* **72** (23), 235206 (2005).

Carrier doping by electric field effect in high critical temperature superconductors

Principal publication and authors
M. Salluzzo (a), G. Ghiringhelli (b), J.C. Cezar (c), N.B. Brookes (c), G.M. De Luca (a), F. Fracassi (b) and R. Vaglio (a), *Phys. Rev. Lett.* (2008), *accepted.*
(a) CNR-INFM COHERENTIA and Dipartimento di Fisica Università di Napoli (Italy)
(b) CNR-INFM COHERENTIA and Dipartimento di Fisica, Politecnico di Milano (Italy)
(c) ESRF

High critical temperature superconductor (HTS) physics is a subject of great interest that has led to much theoretical and experimental efforts. An intriguing point yet to be explained is the phenomenological T (temperature) vs doping phase-diagram (**Figure 109a**). Carriers are usually added to the 2D-CuO_2 planes by chemical substitution in the adjacent charge-reservoir layers. For example, in the "123" family (*e.g.* $Y_1Ba_2Cu_3O_{7-\delta}$ and $Nd_1Ba_2Cu_3O_{7-\delta}$ (NdBCO)), the oxygen content of the Cu(1)O chains in the charge-reservoir layer (see inset of **Figure 109a**) determines how many holes are transferred to the CuO_2 sheets by a charge-transfer mechanism. Besides chemical doping, an elegant way to modify the number of carriers per CuO_2 plane is to create a field effect device in which the channel is made of a very thin HTS film. The electric field creates charges (and therefore carriers) in the thin channel, and can modify the doping. Since HTSs are extremely sensitive to the number of holes present in the CuO_2 planes, the electric field effect provides a very interesting reversible method to investigate the phase diagram. However, a direct doping of the CuO_2 planes has not yet been demonstrated. A simple interpretation of the field effect mechanism, taken from the classical picture valid in Si/SiO_2 MOSFET, fails in the case of the strongly electron-correlated HTS materials.

We studied the changes in the electronic states of $Nd_{1.2}Ba_{1.8}Cu_3O_7$ thin films under application of an electric field using X-ray absorption spectroscopy (XAS) at beamline **ID08**. The experiment was designed to measure the changes in both the XAS spectra and the conductivity of the device. A typical measurement of the change in the resistance as a function of the induced carrier density is shown in **Figure 109b** for an insulating 2 unit cell NdBCO film. As expected the channel resistance decreases from the hole depletion (negative gate voltage) to the hole accumulation (positive gate voltage) modes. A simple calculation of the expected change of carriers, based on the assumption that all the measured charges become carriers in the CuO_2 planes, shows that a transition to the superconducting phase is expected. However, this does not occur.

The reasons for this apparent discrepancy come from the XAS results. The effect of the electric field doping on the density of unoccupied states around the Cu L_3 edge of a 3 unit cell is shown in **Figure 110**. Similar results were obtained on 2 unit cell (Mott insulating) and 4 unit cell (superconducting) samples. The Cu L_3 spectra, measured on the NdBCO films at 10 K, present the typical features of all cuprates, *i.e.*, a main peak at 932.0 eV

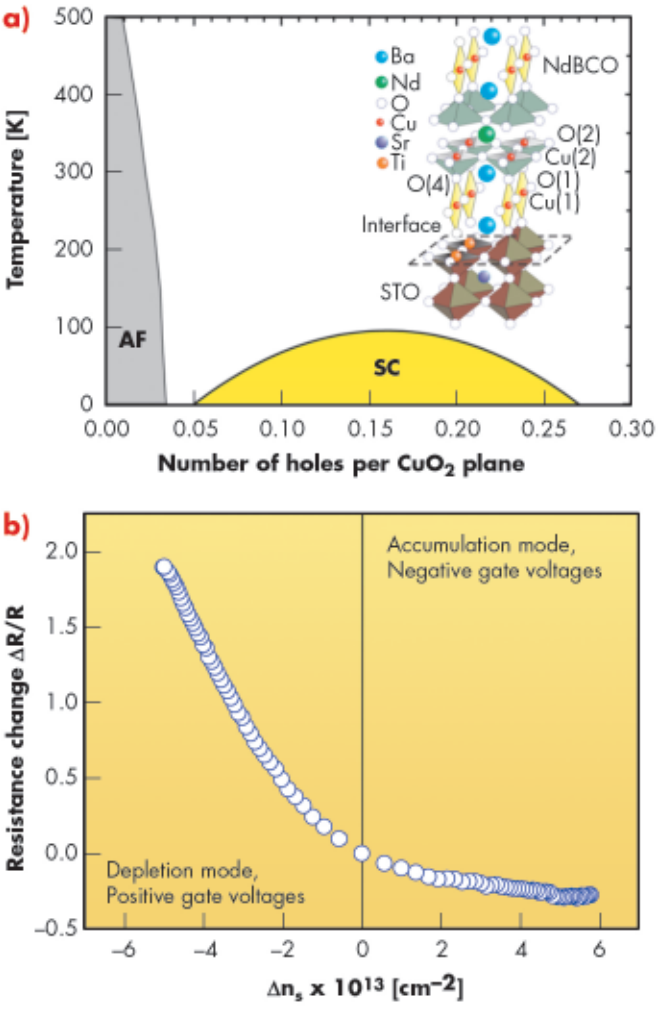

Fig. 109:
a) Phenomenological phase diagram of the cuprates and the structure of the NdBCO/STO interface studied in this work (inset).
b) The change in the resistance of a 2 unit cell NdBCO film as a function of the injected holes by field effect.

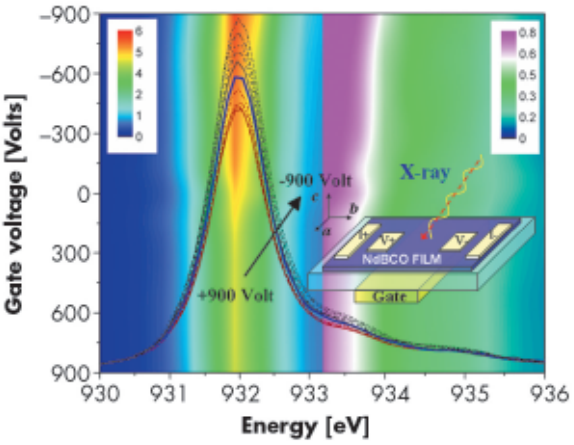

Fig. 110: Cu L_3 edge total electron yield XAS spectra as a function of the gate voltage shown as colour maps around (a) the main $3d^9$ peak at 932 eV and (b) the Zhang Rice ($3d^9L$ ligand state) at 933.5 eV. Each XAS spectra measured at different gate voltages between +900 volt and –900 volt are overlapped to the colour map. A sketch of the experimental configuration used is shown in the inset.

and a shoulder at 933.5 eV due to the Zhang-Rice singlet [1]. The main changes occur around the main absorption peak at 932 eV, and are related to a doping of the Cu(1) ions in the chains of the charge reservoir [2]. The effect is strongly anisotropic, since the holes can be accommodated mainly in the *ab* plane, *i.e.* along the Cu(1)O chains. The increase of the Zhang-Rice satellite, reveals that a fraction of the holes is transferred to the conducting CuO_2 planes. It is also worth noting that simultaneously the weight of the charge transfer peak (the satellite in the spectra) increases by the same amount, revealing that these carriers are transferred from the chains to the planes, doped by the field effect. This charge redistribution is necessary to reduce the build up of electrostatic energy.

Our experiment demonstrates that the Zhang-Rice band occupancy, in turn related to the superconductivity, is changed by a field effect because of the charge redistribution between the CuO_2 planes and the charge reservoir, and not by direct band-filling as in conventional band semiconductors and usually assumed to apply for HTS. This mechanism is the same governing the charge transfer from the chains to the CuO_2 planes by chemical doping in the whole HTS family.

References
[1] M. Salluzzo, G. Ghiringhelli, N.B. Brookes, G.M. De Luca, F. Fracassi and R. Vaglio, *Phys. Rev. B* **75**, 054519 (2007).
[2] G. Ghiringhelli, N.B. Brookes, C. Dallera, A. Tagliaferri, and L. Braicovich, *Phys. Rev. B* **76**, 085116 (2007).

Vector part of optical activity probed with X-rays in hexagonal ZnO

Principal publication and authors
J. Goulon (a), N. Jaouen (a), A. Rogalev (a), F. Wilhelm (a), C. Goulon-Ginet (a), C. Brouder (b), Y. Joly (c), E.N. Ovchinnikova (d) and V.E. Dmitrienko (e), *J. Phys.: Condens. Matter* **19**, 156201 (2007).
(a) ESRF
(b) Institut de Minéralogie et de Physique des Milieux Condensés, Universités Paris-VI et VII (France)
(c) Institut Néel, CNRS, Associé à l'Université J Fourier, Grenoble (France)
(d) Physics Department of Moscow State University (Russia)
(e) Institute of Crystallography, Moscow (Russia)

Optical Activity (OA) which is a consequence of spatial dispersion is to be commonly described with a third rank tensor. Decomposing the latter tensor into irreducible representations invariant under the symmetry operations of the rotation group *O(3)* yields a pseudo-scalar, a polar vector and a pseudo-deviator. The pseudo-scalar term exists only for enantiomorphous systems that exhibit OA at optical wavelength. Unfortunately, OA associated with the pseudo-scalar term becomes vanishingly small in the X-ray range. Crystals which admit a pseudo-deviator as rotational invariant were shown to be those which exhibit X-ray natural circular dichroism (XNCD) [1].

Surprisingly, crystals in which the OA tensor has only an irreducible part that transforms as a *polar vector* in *O(3)* will exhibit neither enantiomorphism nor natural circular dichroism.

In 1905, Voigt was the first to try to detect the vector part of OA: his idea was that, in crystals of suitable symmetry, a linearly-polarised incident light could be *reflected* as an elliptically polarised light [2]. The first successful experiment was reported only in 1978, by Ivchenko *et al.* [3], who looked for OA at the exciton resonances in a hexagonal CdS crystal. In 1990, Graham and Raab [4] suggested that the most appropriate experiment to measure the vector part of OA in *6mm* crystals is circular dichroism in reflectivity when the optical c axis is perpendicular to the reflection plane and when the angle of incidence Θ is close to 45°. Unfortunately, specular reflectivity of X-rays cannot be used for such measurements because the off-diagonal terms responsible for OA vanish at glancing angles. However, we suggested that the vector part of OA could still be measured in the X-ray

resonant diffraction regime using circularly-polarised X-rays at Bragg angles near 45° for which the crystal will act as a linear polarimeter.

Our first experiment has been performed at beamline **ID12** using a UHV compatible reflectometer/diffractometer featuring excellent mechanical reliability and a high reproducibility. For this challenging experiment we selected a high-quality ZnO single crystal with hexagonal symmetry (Würtzite structure). This crystal exhibits a strong (300) reflection characterised by a Bragg angle varying from 43.13° to 42.69° over the whole Zn K-edge XANES range (9655-9735 eV). A major experimental difficulty arose from the imperfect polarisation transfer function of the double crystal monochromator that resulted in the existence of an unwanted Stokes-Poincare component P_2 (even though very small: 1.95% at 9.7 keV) which also changes the sign when the helicity of the incident photons is reversed.

The results of this delicate experiment are displayed in **Figure 111**. A typical Zn K-edge DANES (diffraction anomalous near edge structures) spectrum of our ZnO single crystal (c axis perpendicular to the scattering plane) is reproduced in **Figure 111a**. in which we plotted the integrated area below the (300) diffraction peak as a function of the incident photon energy. The circular dichroism spectra shown in **Figure 111b**. were obtained as a direct difference of the DANES spectra for left- and right-circularly polarised incident X-ray photons. Graham and Raab [4] pointed out that the sign of the circular dichroism should be reversed if the crystal were rotated by 180°, *i.e.* when the angle between the c axis of the crystal and reflection plane changed from +90° to –90°. This is precisely what we have observed, as illustrated by **Figure 111b**. Note that such a 180° rotation should leave the unwanted linear dichroism unchanged provided that the diffraction planes are perpendicular to the rotation axis. The sum of two circular dichroism spectra should reproduce the X-ray linear dichroism (XLD) due to the small P_2 polarisation component in the monochromatic beam. As shown in **Figure 111c**. the spectral shape of this residual signal perfectly reproduces the XLD spectrum measured simultaneously in the total fluorescence yield detection mode.

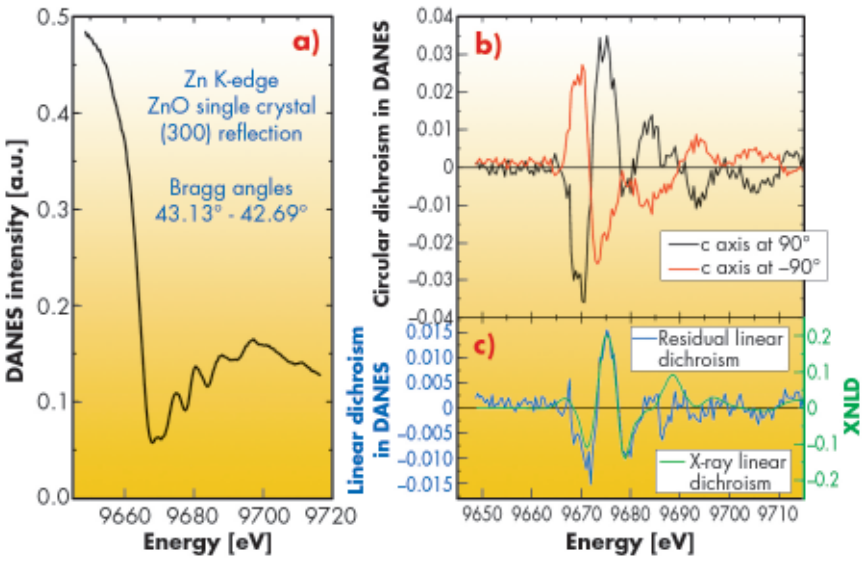

Fig. 111: XNCD in the Zn K-edge DANES spectra of ZnO (300) single crystal: a) A polarisation averaged DANES spectrum. b) circular dichroism DANES spectra for two orientations of the crystal. c) Comparison of the residual signal with XLD spectrum.

This is the first example of X-ray circular dichroism measured in the DANES regime using a non-centrosymmetric single crystal. This experiment clearly establishes the possibility to unravel the vector part of optical activity in the X-ray range. We have also shown that the effective operator responsible for the vector part of OA can be assigned to the vector product $\mathbf{L} \times \boldsymbol{\Omega}_L - \boldsymbol{\Omega}_L \times \mathbf{L} \propto \mathbf{n}$, in which $\mathbf{L}$ and $\boldsymbol{\Omega}_L$ are time-reversal odd operators associated with the orbital angular momentum and the orbital anapole respectively, whereas $\mathbf{n}$ is a true time-reversal even electric dipole. This observation is consistent with the pyroelectric properties of zincite crystals. Given that ZnO belongs to a very important class of semiconducting materials, we expect this pioneering experiment to open a completely new field of applications for X-ray optical activity.

References
[1] J. Goulon *et al.*, *J. Exp.Theor. Phys.* **97**, 402 (2003).
[2] W. Voigt, *Ann. Phys.(Leipzig)* **18**, 651 (1905).
[3] E.L. Ivchenko *et al.*, *Sol. State Comm.* **28**, 345 (1978).
[4] E.B. Graham and R.E. Raab, *Proc. R. Soc. A* **430,** 593 (1990).

Principal publication and authors
Y. Krockenberger (a,b), K. Mogare (b), M. Reehuis (b,c), M. Tovar (c), M. Jansen (b), G. Vaitheeswaran (b,d), V. Kanchana (b,d), F. Bultmark (e), A. Delin (d), F. Wilhelm (f), A. Rogalev (f), A. Winkler (a), L. Alff (a), *Phys. Rev. B* **75**, 020404(R) (2007).
(a) Institut für Materialwissenschaft, TU Darmstadt (Germany)
(b) Max-Planck-Institut für Festkörperforschung, Stuttgart (Germany)
(c) HMI, Berlin (Germany)
(d) Department of Materials Science and Engineering, KTH Stockholm (Sweden)
(e) Department of Physics, University of Uppsala (Sweden)
(f) ESRF

Novel half-metallic double perovskites for spintronics with tunable conductivity

Materials with a high spin-polarisation of the conducting charge carriers are of great interest for spintronics. In particular, an ideal material with 100% spin-polarisation is called a half-metal. Such materials can be found in several materials classes: In classic oxides such as magnetite or CrO_2, in manganites and intermetallic Heusler alloys, but also in the group of double perovskites. Double perovskites are of special interest, since within this group half-metals with above room-temperature transition temperatures are found. At the same time, within the vast perovskite family, heteroepitaxial multilayers of different functional materials such as insulators, magnetic metals, and even superconductors, can be grown for future spintronic devices.

We have rediscovered [1] a double perovskite that has the highest Curie-temperature known so far within this group (725 K or 450°C): Sr_2CrOsO_6.

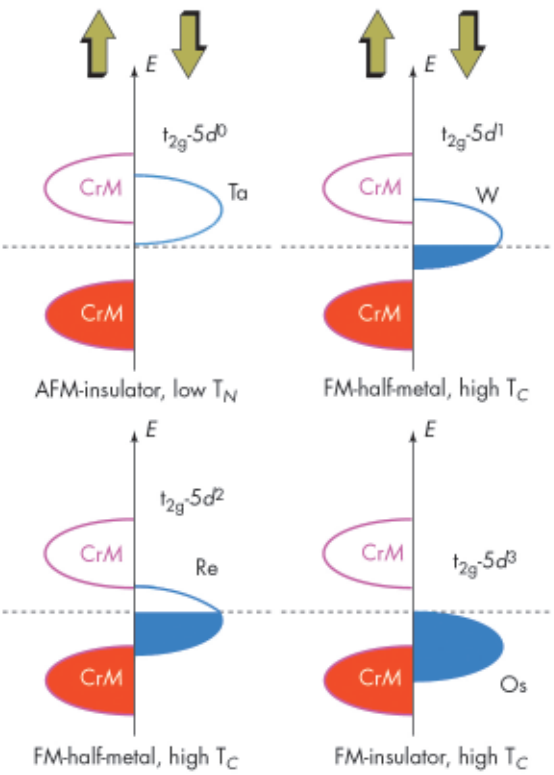

Fig. 112: Simple model of the effect of 5*d* doping in Sr_2CrMO_6 with *M* = Ta, W, Re, and Os.

It was erroneously considered to be non-magnetic at room-temperature. Osmium is certainly an odd element with difficult metallurgy, however, one may remember that filaments in light bulbs are being made from osmium and tungsten. The role of Os in the compound Sr_2CrOsO_6 is to supply spin-polarised charge carriers. As in the light bulb filament, one can also have tantalum, tungsten, and rhenium at the crystal site of osmium. Since these ions are in the 5+ state, they supply a number of spin-polarised electrons per unit cell, 0, 1, 2 and 3 electrons for Ta, W, Re, and Os, respectively. These spin-polarised electrons are also the glue and origin of ferrimagnetism of these compounds. In the case of Sr_2CrTaO_6 with no doped electrons, correspondingly, no ferrimagnetism is observed. With increasing number of doped electrons, the Curie-temperature of the compounds also increases: 450 K for Sr_2CrWO_6, 635 K for Sr_2CrReO_6, and finally 725 K for Sr_2CrOsO_6. With the changing number of electrons, the conductivity also changes. In Sr_2CrOsO_6 the metallic band ($5d_{t2g}$) is completely filled. Therefore, Sr_2CrOsO_6 is an insulator and at the same time it still has the highest Curie-temperature. The band scheme is illustrated in **Figure 112** [1]. This result is remarkable because it brings to light the possibility to tune a material in order to obtain fully spin-polarised conductivity in a desired range between a good metal and an insulator. In the future, an elegant way to tune the spin-polarised carrier density in a spintronics device would be to use the field effect.

In order to elucidate the mechanism of ferrimagnetism in the described double perovskites, it is of utmost importance to measure (separately) the spin and orbital magnetic moments at the Os (or W or Re) site. The magnetic moments of these ions are induced in the specific double perovskite structure from the magnetic Cr^{3+} ions. Within a model of kinetic energy driven exchange it is expected

that the induced spin magnetic moment scales with the Curie-tempereature of the compound [2]. It is the merit of beamline **ID12** that such measurements can be made with very high quality. In excellent agreement with neutron scattering experiments, the existence and scaling of the induced magnetic moments has been confirmed unambiguously by X-ray magnetic circular dichroism (XMCD) experiments (**Figure 113**). At the Os site, a spin-magnetic moment of -0.17 μ_B/formula unit (the minus sign indicates the anti-parallel orientation with respect to the Cr magnetisation) and an orbital magnetic moment of 0.015 μ_B/formula unit has been measured. In addition, it could be shown that spin-orbit coupling has to be taken into account due to the heavy ionic mass of Os.

In conclusion, we have shown that the mechanism of magnetic coupling in the ferrimagnetic double perovskites also applies to insulating compounds with filled bands, where even the highest Curie-temperature is observed for this class of materials. This finding may contribute to the development of thin-film based field-effect transistors with the ability of switching between high and low conductivity that is in both cases fully spin-polarised and therefore desirable for spintronics.

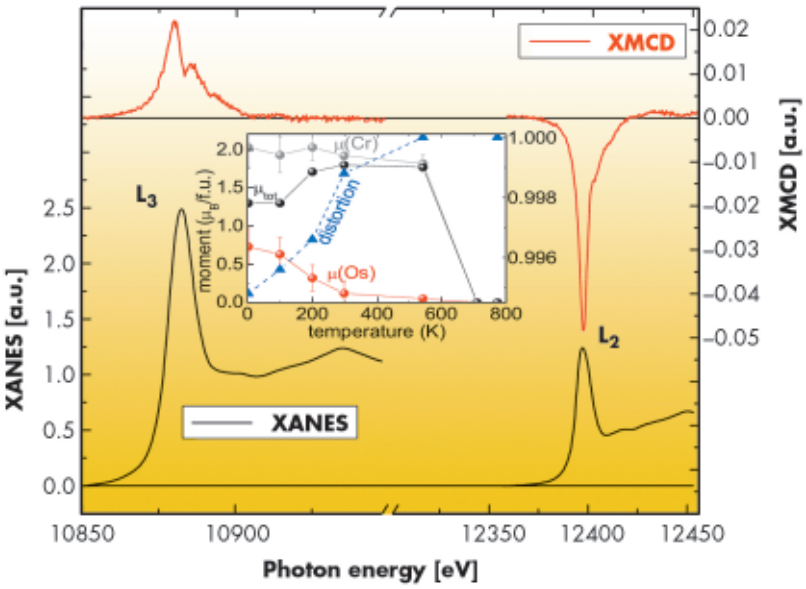

Fig. 113: X-ray absorption near-edge structure (XANES, left axis) and XMCD signal (right axis) at the Os L_2 and L_3 edges in Sr_2CrOsO_6. The inset shows the element-resolved magnetic moments of Cr (μ_{Cr}) and Os (μ_{Os}), the total magnetic moment (μ_{tot}), and the lattice distortion as determined from neutron scattering.

References

[1] L. Alff, in *Electron Correlation in New Materials and Nanosystems*, K. Scharnberg, S. Kruchinin (Eds.), *NATO Science Series II* **241**, 393-400 (2007).

[2] P. Majewski, S. Geprägs, O. Sanganas, M. Opel, R. Gross, F. Wilhelm, A. Rogalev, L. Alff, *Appl. Phys. Lett.* **87**, 202503 (2005).

Incipient orbital order in double perovskite Ba_2FeReO_6

Double perovskites are materials of the form $A_2BB'O_6$, where the transition metal atoms B and B' alternate between neighbouring oxygen octahedra, as depicted in **Figure 114**. Some double perovskites have their conduction band fully spin polarised [1]. The Re-based double perovskites in particular have attracted attention due to their fairly high transition temperature from a paramagnetic to ferrimagnetic state (513 K for Ca_2FeReO_6), which makes this family of materials candidates for future spintronics applications. We studied the compound Ba_2FeReO_6 using X-ray magnetic circular dichroism (XMCD) at the $L_{2,3}$ edges of both Re and Fe, associated with synchrotron and neutron X-ray powder diffraction. The neutron diffraction was performed on the BT-1 diffractometer at the NIST Center for Neutron Research and the X-ray diffraction data was taken at the XPD beamline of the Laboratório Nacional de Luz Síncrontron (LNLS). The XMCD data at Re and Fe $L_{2,3}$ edges was measured at the DXAS beamline at LNLS and beamline **ID08** at the ESRF, respectively.

A clear transition from the cubic to a tetragonal structure was evident in the diffraction data when we decreased the temperature below 309 K, which is also the paramagnetic to ferrimagnetic transition temperature. Magnetic field dependent X-ray powder diffraction proved that both transitions are related, and also that a quite strong

Principal publication and authors

C. Azimonte (a,b), J.C. Cezar (c), E. Granado (a,b), Q. Huang (d), J.W. Lynn (d,e), J.C.P. Campoy (a), J. Gopalakrishnan (e,f), and K. Ramesha (f), *Phys. Rev. Lett.* **98**, 017204 (2007).

(a) Instituto de Física "Gleb Wataghin", UNICAMP, Campinas (Brazil)

(b) Laboratório Nacional de Luz Síncrotron, Campinas (Brazil)

(c) ESRF

(d) NIST Center for Neutron Research, Gaithersburg (USA)

(e) Center for Superconductivity Research, University of Maryland (USA)

(f) Solid State and Structural Chemistry Unit, Indian Institute of Science, Bangalore (India)

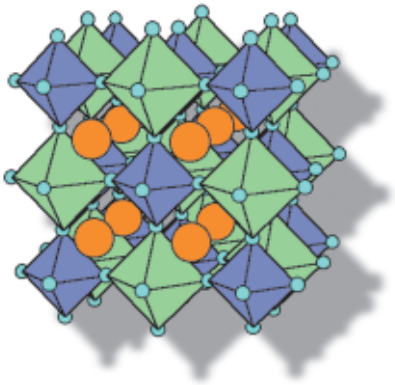

Fig. 114: Crystalline structure of a double perovskite $A_2BB'O_6$. The transition metal atoms B and B′ are in the centre of alternating oxygen octahedras. The cation A occupies the interstices between the octahedras.

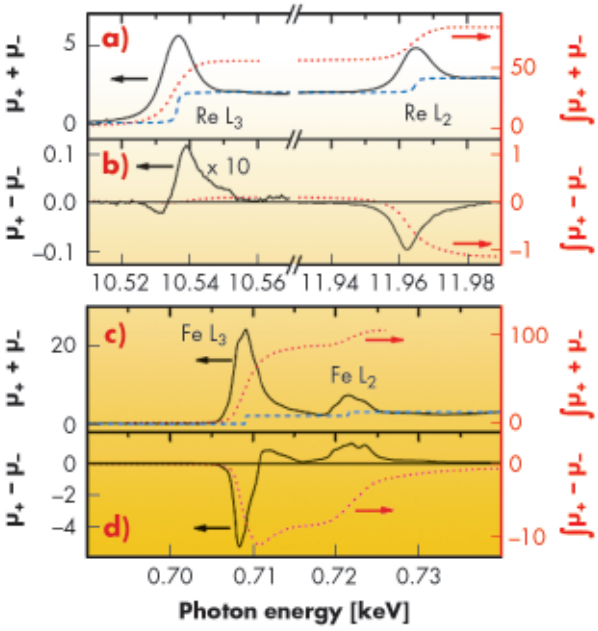

Fig. 115: X-ray absorption and X-ray magnetic circular dichroism at Re (top) and Fe (bottom). The red dotted lines indicate the integrals used in the sum rules calculations.

magnetoelastic effect develops below the transition temperature. Also from these diffraction measurements, we obtained a linear magnetoelastic constant $\lambda_{100} = 1.1 \times 10^3$, which is a giant value for transition metal based metallic systems.

Usually magnetoelastic effects are associated with strong spin-lattice interactions, which take place through the spin-orbit coupling. Therefore, we anticipated the presence of non-negligible orbital moments in the system. To investigate such spin-lattice interactions we measured the XMCD at both Re and Fe $L_{2,3}$ edges. XMCD allowed us to discriminate the contribution of each element in the material to the total magnetisation. By applying well-established sum rules, we evaluated separately the spin and orbital contribution of Fe and Re.

Figure 115 shows the isotropic X-ray absorption spectra of Re and Fe measured at 10 K and the corresponding XMCD signals, which are shown as continuous lines. The integrals used to calculate the sum rules are shown as dotted red lines in these figures. It is very interesting to note that the orbital moment of the probed atom is directly proportional to the integral of the XMCD signal. From the red dotted lines in **Figures 115b** and **115d** one can see that this integral has a non negligible value in the case of Re, whereas it is almost zero for Fe. This direct result let us conclude that the Re orbital moment is responsible for the unusual magnetoelastic behaviour in this sample. To obtain quantitative results for the spin and orbital moments we employed sum rules based on the integral values shown in **Figure 115**. For Fe we found spin and orbital moments of $m_{spin} = 2.8(2)\ \mu_B$ and $m_{orb} = 0.04(2)\ \mu_B$. In the case of Re, $m_{spin} = -0.64(4)\ \mu_B$ and $m_{orb} = 0.19(1)\ \mu_B$. The negative value for the spin moment of Re simply reflects the ferrimagnetic alignment between Fe and Re atoms in the sample. It is also worth noting the size of the Re orbital moment. Indeed, the ratio m_{orb}/m_{spin} is -0.293 for Re and 0.013 in the case of Fe. Thus the orbital moment is quite large for Re, whereas it is almost quenched for Fe. One must remember that the 5d transition metals are on the verge of becoming magnetic. Nonetheless, even in the case of Re impurities in Fe, the m_{orb}/m_{spin} ratio is calculated to be about ten times smaller than what was found in our measurements [2].

Based on the information obtained from XMCD and diffraction we can draw two important conclusions: i) calculations show that the conduction band in Ba_2FeReO_6 has an Re 5d character, which means that in this material the conduction electrons carry an appreciable orbital momentum; ii) in analogy to the manganites, which also present a huge magnetoelestic effect, we can suggest that Ba_2FeReO_6 is on the verge of developing an orbital ordering state.

References
[1] K.-I. Kobayashi, T. Kimura, H. Sawada, K. Terakura and Y. Tokura, *Nature* **395**, 677 (1998).
[2] H. Ebert, R. Zeller, B. Drittler and P.H. Dederichs, *J. Phys.* **67**, 4576 (1990).

Probing 4f magnetism of intermetallic compounds by resonant magnetic scattering

Principal publication and authors
C. Giles (a), C. Adriano (a), R. Lora-Serrano (a), F. de Bergevin (b,c), J.C. Lang (d), G. Srajer (d), C. Mazzoli (c), L. Paolasini (c), P.G. Pagliuso (a), *Phys. Rev. B* **76**, 104515 (2007).
(a) Universidade Estadual de Campinas, São Paulo (Brazil)
(b) CNRS
(c) ESRF
(d) Advanced Photon Source, ANL, Chicago (USA)

Recently, a new series of tetragonal compounds, R_mMIn_{3m+2} (R= light rare-earth; M=Rh or Ir; m=1,2), have become an interesting area of research since the discovery of new heavy fermion superconductors (HFS) for some of the Ce-based compounds [1]. Extensive investigation on these materials has revealed fascinating physical properties such as quantum criticality, non-Fermi-liquid behaviour, and interplay between magnetism and superconductivity, as the Ce-based compounds in these series are presumably magnetic-mediated HFS.

The existence of structurally-related families of rare-earth-based compounds provides a great opportunity to explore the involvement of the 4f-electron magnetism in HFS. From earlier studies, the role was established for the tetragonal crystalline electrical field (CEF) in determining the spatial direction of the ordered R moments with respect to the lattice and the evolution of the Néel temperature T_N in the series. The compounds of this family containing Sm ions remain untested and may be particularly important because of the presence of excited J-multiplet states in Sm^{3+} and quadrupolar interactions. Sm_2IrIn_8 in particular is the only compound with a clear first order antiferromagnetic transition at T_N = 14.2 K. This value is slightly smaller than the T_N~16 K of the cubic $SmIn_3$ which according to the CEF trends observed in other members of this family suggest that the ordered Sm moments should lie in the *ab* plane.

We report the solution of the magnetic structure of the intermetallic antiferromagnet Sm_2IrIn_8 by means of X-ray resonant magnetic scattering (XRMS) which is the only technique available for the investigation of microscopic magnetism for highly neutron absorber ions such as Sm, where the often preferred technique of neutron scattering becomes nearly prohibitive.

XRMS studies were performed at beamline 4-ID-D at the Advanced Photon Source (APS) in the vertical scattering geometry and at beamline **ID20** at the ESRF in the horizontal configuration. This allowed us to access all four polarisation channels of the 2x2 matrix of the electric dipole transition form factor and to determine the magnetic moment orientations through their polarisation dependence at the dipolar (E1) resonance by comparing the relative intensities of experimental (1/2,0,*l*) magnetic peaks with the calculated ones.

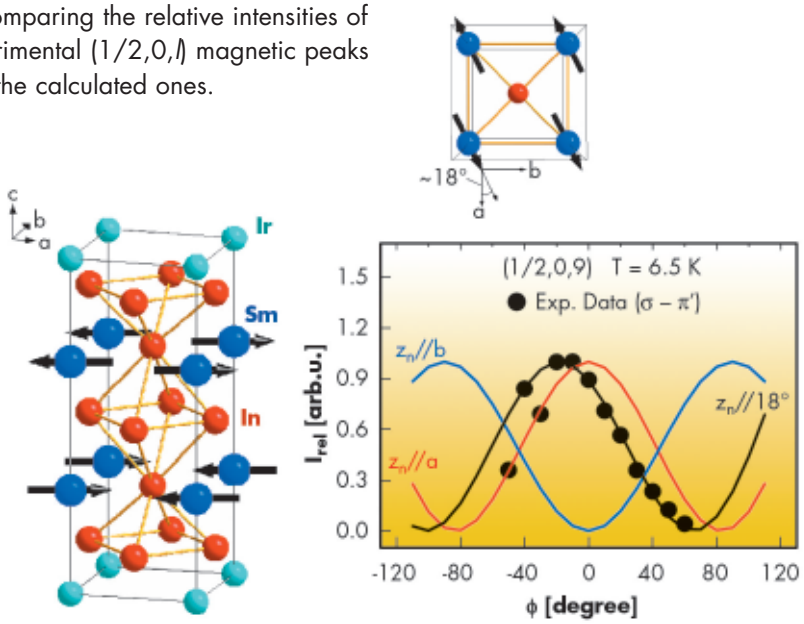

Fig. 116: Magnetic structure of Sm_2IrIn_8 below T_N=14.2 K (left) and a Sm-In plane top view (top right) showing the in-plane arrangement of Sm moments. The graphic (bottom right) shows the relative intensities as a function of the azimuthal angle to the (1/2 0 9) magnetic reflection. The other curves represent the variation expected for the magnetic moments along the *a* (red line), *b* (blue line), and 18° away from *a* (black line), directions.

To determine the exact orientation of the magnetic moments within the *ab* plane, we have performed azimuthal scans (ϕ scan) through the (1/2,0,9) reflection (**Figure 116**) at the E1 resonance. At the σ-π′ polarisation channel, this procedure allows the determination of moment directions with no ambiguity because the magnetic cross section is strongly dependent on the magnetic moment direction and the polarisation of the incoming and scattered radiation. **Figure 116** shows a model of the magnetic unit cell of Sm_2IrIn_8 can be constructed using these results.

The energy line shape curves for the polarisation channels σ-π′ and σ-σ′ of the (1/2,0,9) diffraction peak at (a) the L_2 and (b) the L_3 absorption edges of Sm^{3+} ion at T=5.9 K are shown in **Figure 117**.

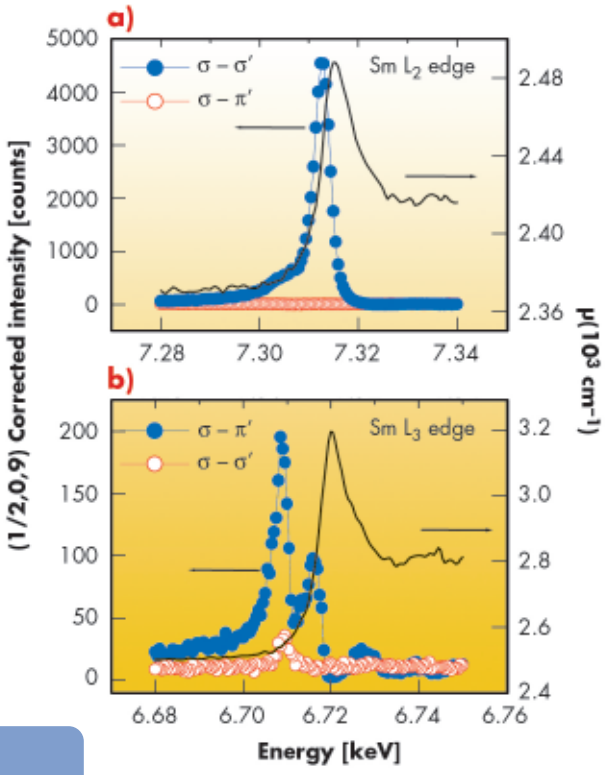

Fig. 117: Energy scan of the (1/2,0,9) magnetic peak at T = 5.9 K for σ-π′ (closed blue circles) and σ-σ′ (open red circles) polarisation channels at the L_2 (top) and L_3 (bottom) absorption edges. The data have been corrected for absorption, μ(E), using the measured fluorescence yield. Arrows indicate the scales for the fluorescence yield (right) and the observed data (left).

References
[1] J.D. Thompson *et al.*, *J. Magn. Magn. Mater.* **226-230**, 5 (2001).
[2] P.G. Pagliuso *et al.*, *J. Appl. Phys.* **99**, 08P703 (2006).

The solid lines in both panels represent the absorption spectrum, μ(E), extracted from fluorescence yield. Our data in **Figure 117a** reveal a strong enhancement of the scattered intensities at the σ-π′ channel (closed circles) and no enhancement at the σ-σ′channel for the same energy range. The energy line shape around the Sm L_3 edge is presented in **Figure 117b**. A high energy peak appears at 6.716 keV, while a low energy and more intense enhancement can be observed at 6.708 keV. The presence of this pre-edge enhancement in the energy curves of **Figure 117** confirms an expected quadrupole (E2) contribution to the resonant X-ray scattering in Sm_2IrIn_8.

Following the investigation of the isostructural magnetic non-Kondo compounds from the R_mMIn_{3m+2} family, we have studied the magnetic structure of Sm_2IrIn_8. The magnetic order is commensurate with propagation vector η = (1/2,0,0) and the Sm moments oriented in the *ab* plane, 18° away from the *a* axis. Based on this result we conclude that the general CEF trend of the R_mMIn_{3m+2} is also qualitatively present in Sm_2IrIn_8.

Authors
V. Scagnoli (a), L. Paolasini (a), M. Kohgi (b), K. Kuwahara (c), K. Iwasa (d).
(a) ESRF
(b) Tokyo University of Fisheries (Japan)
(c) Tokyo Metropolitan University (Japan)
(d) University of Tohoku, Sendai (Japan)

Magnetic phase diagram determination of CeP by resonant X-ray diffraction

Cerium containing rare-earth compounds are especially interesting because of their variable electronic structure, due to the ground state of Ce^{3+}, which is a Kramers doublet. The energy of the inner 4*f* level is nearly the same as that of the outer (valence) electrons, and only small amounts of energy are required to change the relative occupancy of these electronic levels. This gives rise to "dual valency states", which can be apparent when a volume change of about 10 percent occurs upon the application of high pressures or low temperatures. It is not surprising, therefore, that CeP, a monopnictide compound (CeX, where X=P, As, Sb, Bi) with the NaCl-type structure, exhibits unusual transport and magnetic properties. When cooled to temperatures below 10K in a magnetic field lower than 0.5 Tesla, CeP shows a simple anti-ferromagnetic phase (AFM), with ferromagnetic planes coupled antiferromagnetically along the cubic axis (see **Figure 118a**). At higher magnetic fields the ordering of the Ce magnetic moments changes dramatically, with a long period magnetic structure in which ferromagnetically coupled Ce-ion double layers with a large magnetic moment of about 2 μ_B co-exist with weakly coupled magnetic Ce layers, as shown in **Figure 118a**.

These magnetic modulations, coupled with interlayer distance variations, are strongly sensitive to the magnetic field and high pressure conditions. This has been determined in numerous neutron and X-ray scattering experiments, carried

out to find the magnetic and structural modulations as a function of the magnetic field and high pressure [1-2]. The unusual magnetic properties have been ascribed to the strong magnetic polaron effect, produced by the combination of localisation of the low-density carriers and mixing effects between Ce ions and the *p* state of the neighbouring pnictogens (*p-f* mixing).

High magnetic field resonant magnetic X-ray diffraction experiments were performed at **ID20** using the new superconducting magnet station to investigate the CeP low temperature magnetic phase diagram up to 10 Tesla.

Using the Ce L_3 edge resonance, the magnetic interlayer ordering of the Ce can be studied in great detail, as illustrated in **Figure 118b**. Different phases are represented in different colours. Phase I (yellow) and phase II (green) are characterised by two-sublattice magnetisations, where two adjacent Ce ferromagnetic (F) layers carry the largest magnetic moment (Γ8 ground state). The (F) layers are separated by a sequence of weak antiferromagnetic (AF) Ce planes (Γ7 ground state) with propagation vector 2/11 and 2/9, respectively. The sample can therefore be regarded as an exchange bias system, but at the nanoscale. The odd number of weak AF layers is due to the interlayer coupling between F and weak-AF planes. At higher temperatures and higher magnetic field these weak-AF planes became paramagnetic, and the so-called ferro-paramagnetic phase (FP) occurs. The FP phase consists of a stacking of F planes aligned along the magnetic field and paramagnetic layers (phase III).

Direct microscopic proof of the existence of these different FP phases was needed above 5T. New phase boundaries (full squares) were found by scanning the reciprocal space as a function of both temperature and magnetic field. They correspond to the magnetic phase transition determined previously by magnetoresistance measurements [3], and they appear in quite a systematic way as a function of applied magnetic field (2/10, 2/9, 2/8, ...). In other words, the F and P atomic planes distances can be continuously modulated by a magnetic field.

Figure 119 illustrates the smooth change in the modulation of the Ce planes as a function of applied magnetic field, which reduces the number of planes separating the ferromagnetic ones. It would be interesting to follow this progressive reduction up to the full ferromagnetic ordering of the Ce moments. To achieve this, high fields up to 60 Tesla will be needed.

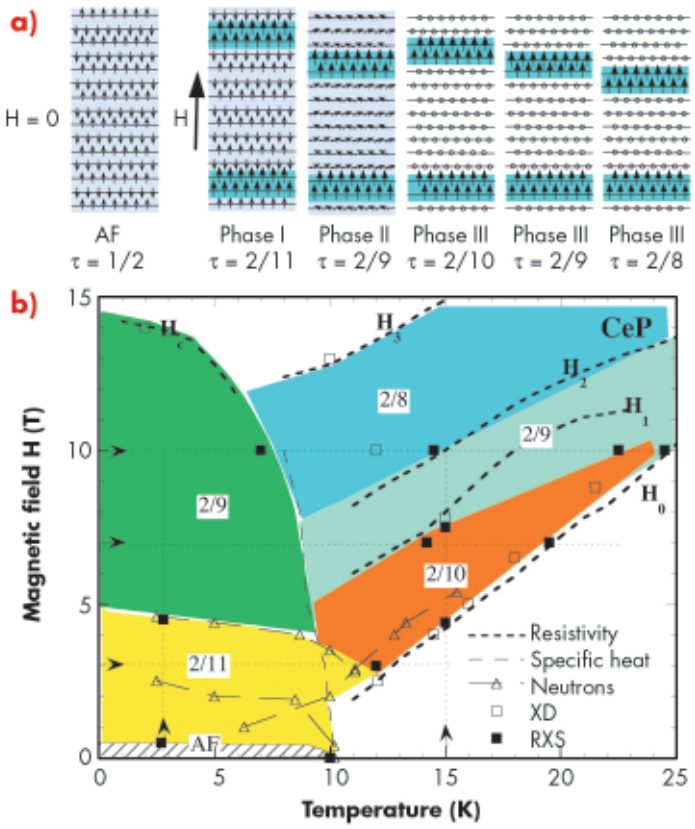

Fig. 118: a) Proposed magnetic ordering as function of temperature and magnetic field. b) Magnetic phase diagram of CeP determined by resonant X-ray diffraction (square dots).

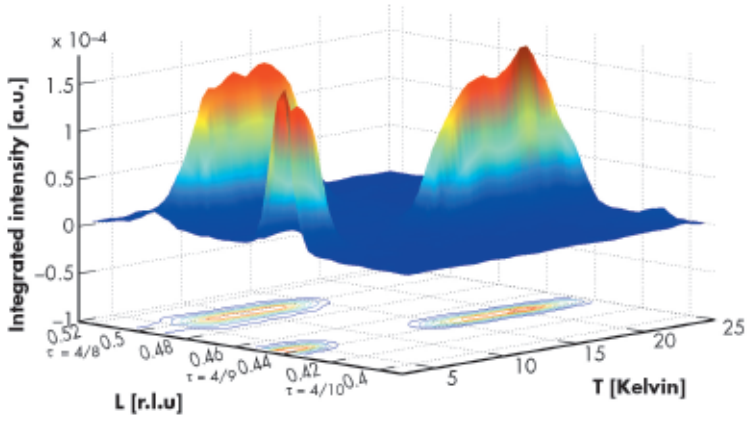

Fig. 119: Observation of phase boundary crossings. The phase II (τ=4/9) present at low temperature disappears after a short coexistence with the phase III (τ=4/8). Further increasing of the temperature makes more favourable a modulation τ=4/9 (T~15K) and finally of (τ=4/10) around 25K.

References

[1] M. Kohgi, K. Iwasa, K. Kuwahara, A. Hannan, D. Kawana, Y. Noda, T. Shobu, K. Katsumata, Y. Narumi and Y. Tabata, *Physica B* **345**, 55 (2004).

[2] A. Hannan, D. Kawana, K. Kuwahara, M. Kohgi, Y. Narumi, Y. Tabata, S. Shimomura, Y. Tanaka and K. Katsumata, *J. Phys. Soc. Jpn.* **74**, 2301 (2005).

[3]T. Terashima, S. Uji, H. Aoki, J.A.A.J. Perenboom, Y. Haga, A. Uesawa, T. Suzuki, S. Hill and J.S. Brooks, *Phys. Rev. B* **58**, 309 (1998).

X-ray Imaging and Optics

Introduction

X-ray imaging techniques are being used more and more frequently in modern synchrotron radiation facilities. The feature common to all of these techniques is that they apply to inhomogeneous samples, where it is important to measure "locally" a given property such as density, composition, chemical state or distortion. These techniques take advantage of most of the photon-matter interactions: absorption, wavefront modification, diffraction, scattering, photoemission, etc. An increasing part of the experimental results obtained at the ESRF can now be considered as "X-ray images", *i.e.* maps over the sample of the "local" value of a physical quantity. In this case "local" does not mean atomic level (whereas in some cases atomic information can be extracted from the images) but corresponds to the very important 10^{-3}-10^{-8} m range, where many biological and materials science phenomena occur.

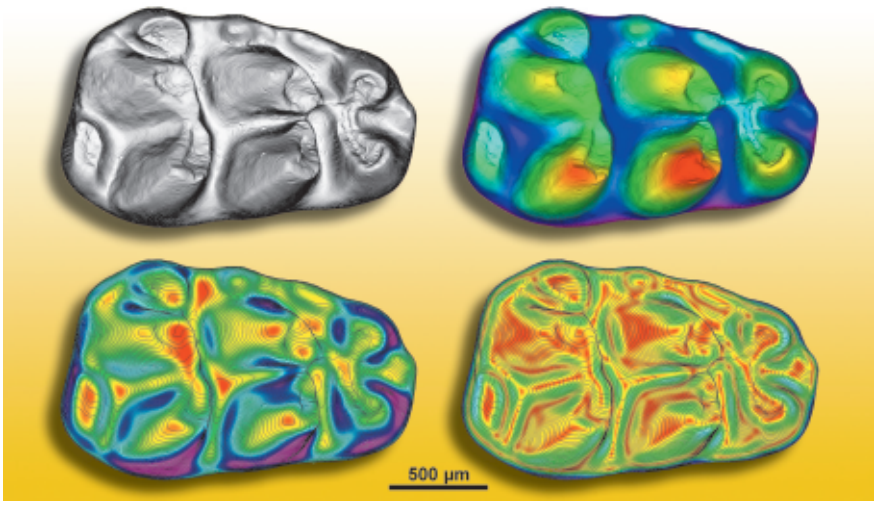

Fig. 120: Synchrotron radiation microtomographic maps of the external morphology of the first lower molar of *Progonomys cathalai* (late Miocene, from Montredon, South of France). Top left corner: 3D rendering colour topographic map. Top right corner: colour topographic map with contour lines. Bottom left corner: colour slope map with contour lines. Bottom right corner: colour angularity map with contour lines. Depth between two consecutive contour lines: 12.5 µm (From Lazzari, Tafforeau, Aguilar and Michaux, Paleobiology, 2008).

These microscopy techniques apply to a wide variety of topics. Indeed, this chapter shows contributions in biological and biomedical applications (iron storage within dopamine neurovesicles, the microvascular network in brain, improved three dimensional imaging of breast tissues), materials science (3D real-time observation of solidification in binary alloys, optical luminescence microscopy in GaN), and also applications to Cultural Heritage (study of micrometric pigment in Grunewald's paintings, occurrence in early homo sapiens of modern human development). Paleontology is an emerging scientific area at the ESRF and other synchrotron radiation facilities: the number of paleontological proposals has increased from zero to 20% of the proposals for microtomography over the last five years. As an example, **Figure 120** shows various quantitative maps computed from X-ray synchrotron microtomographic data, of the external morphology of a molar of an ancestor of rats and mice, which allow a good comparison of the morphological details of several similar fossils, and an identification of the mastication directions of this animal.

The importance of synchrotron radiation-based X-ray imaging techniques is reflected by the considerable effort of ESRF users and staff in pushing the limits of the techniques in terms of resolution and domains of applications, and in starting new techniques. This effort is exemplified in the present chapter by contributions on scanning X-ray microscopy to study microbes involvement in geochemical cycles and near field X-ray speckles.

A substantial part of the ESRF Science and Technology Programme 2008-2017 relies on improved imaging techniques. The spatial resolution is heading towards the nanometre scale, and high temporal resolution will increasingly allow chemical and industrial processes to be followed *in situ*. Developments exploiting the partial coherence of synchrotron X-ray beams for phase contrast imaging or coherent diffraction imaging will continue. This requires a combined effort, high throughput imaging being strongly dependent on detector improvements and computing for the reconstruction of holographic images from a set of radiographs, and the iterative determination of the phase of the scattering amplitude in coherent diffraction imaging. Developments in all of these areas are going to occur in the very near future.

J. Baruchel

Biological and biomedical applications

Iron storage within dopamine neurovesicles revealed by X-ray fluorescence nano-imaging

Principal publication and authors

R. Ortega (a), P. Cloetens (b), G. Devès (a), A. Carmona (a,c), S. Bohic (b,d), *PLoS ONE* **2**, e925 (2007).

(a) CNRS-Universités de Bordeaux 1 et 2, Chimie Nucléaire Analytique Bioenvironnementale, Gradignan (France)

(b) ESRF

(c) Universidad de Sevilla, Centro Nacional de Aceleradores, Sevilla (Spain)

(d) INSERM, Institut des Neurosciences, Equipe 6, Grenoble (France)

Parkinson's disease results from a shortage of dopamine in the brain induced by the selective death of dopamine producing neurons in the substantia nigra. Dopaminergic neurons die in a slow but progressive manner leading to a depletion of dopamine in the striatum compromising the capacity of the brain to orchestrate voluntary movement. The causes of the selective death of dopaminergic neurons are still largely unknown. Increasing evidence suggests that abnormal iron handling in the brain may be involved in the etiology of Parkinson's disease [1]. Indeed, iron specific accumulation in the substantia nigra is associated with Parkinson's disease [2]. It has been suggested that dopamine may exert a protective effect by chelating iron in dopaminergic neurons and that this system might be at fault in Parkinson's disease. It is therefore theoretically possible that dopamine-iron complexes may exist in dopaminergic neurons but they have not yet been evidenced experimentally.

Up to now the lack of analytical techniques with sufficient spatial resolution and detection sensitivity prevented the study of iron distribution in neurons at the subcelullar level. An original setup for high spatial resolution chemical imaging has been developed on **ID22** beamline with a 88 nm X-ray beam (**Figure 121**) of very high flux, up to 10^{12} photons/s. The characteristics of this X-ray nanoprobe fulfil the requirements for mapping biological trace element distributions at a size compatible with the analysis of most cellular compartments such as mitochondria, lysozomes, or

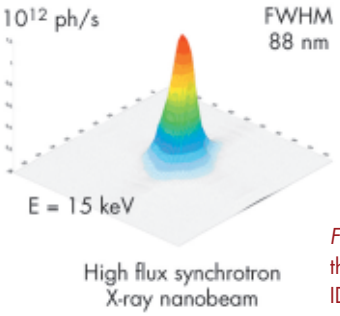

Fig. 121: The intensity distribution in the focal plane of the X-ray fluorescence nanoprobe end-station installed on ID22 beamline.

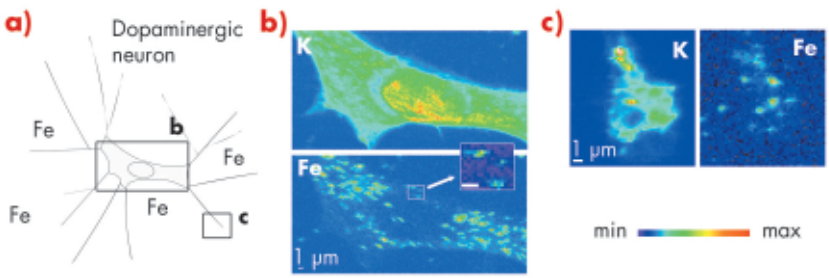

Fig. 122: Synchrotron X-ray fluorescence nano-imaging reveals iron sub-cellular distribution. a) dopamine producing cells were exposed *in vitro* to iron. Chemical element distributions, here potassium and iron, were recorded on distinct cellular areas such as b) cell bodies, and c) neurite outgrowths, and distal ends. Iron was found in 200 nm structures in the cytosol, neurite outgrowths, and distal ends, but not in the nucleus. Min-max range bar units are arbitrary. Scale bars = 1 µm.

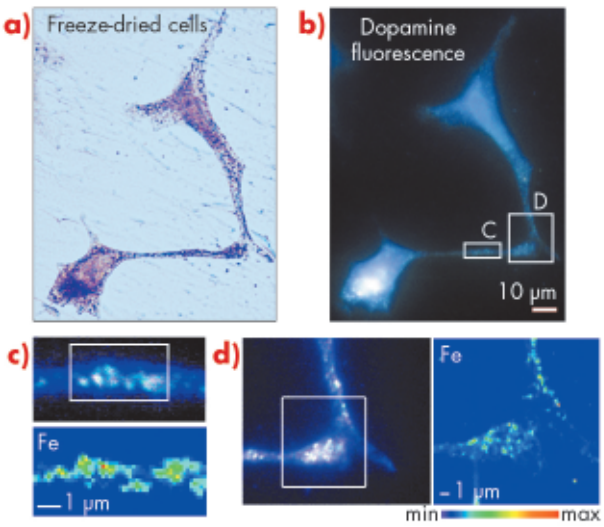

Fig. 123: Iron is localised within dopamine neurovesicles. a) Visible light microscopy of freeze-dried cells. b) Epifluorescence microscopy of the same freeze-dried cells enables the identification of dopamine distribution. c, d) Synchrotron X-ray fluorescence nano-imaging reveals the distribution of iron. Dopamine and iron are co-located within 200 nm structures characteristic of dopamine neurovesicles as identified by epifluorescence microscopy. A large number of iron and dopamine neurovesicles are found in c) neurite outgrowths and d) distal ends. Min-max range bar units are arbitrary. Scale bars = 1 µm.

References
[1] E. Bossy-Wetzel, R. Schwarzenbacher, S.A. Lipton, *Nature Med.* **10**, S2 (2004).
[2] D.T. Dexter, F.R. Wells, F. Agid, Y. Agid, A.J. Lees, *et al.*, *Lancet* **2**, 1219 (1987).
[3] H.A. Lashuel, H. Hirling, *ACS Chem. Biol.* **1**, 420 (2006).

neurosecretory vesicles. As exemplified in **Figure 122**, this newly developed synchrotron X-ray fluorescence nanoprobe is able to detect down to 10^{-18} g of Fe within a cellular structure as small as 100 nm diameter.

Using this X-ray fluorescence nano-imaging system we investigated the subcellular distribution of iron in dopamine producing neurons. PC12 rat pheocromocytoma cell line was used as an *in vitro* model of dopamine producing cells. The study shows that iron accumulates into dopamine neurovesicles (**Figure 123**). In addition, the inhibition of dopamine synthesis results in decreased vesicular storage of iron. These results indicate a new physiological role for dopamine in iron buffering within normal dopamine producing cells. They also suggest that the elevation of iron concentration in the substantia nigra of Parkinson's disease patients may lead to a lack of iron-dopamine binding capability rendering the dopaminergic neurons more prone to iron toxicity. It has been suggested that mutations in α-synuclein, a protein mutated in some familial forms of Parkinson's disease, could result in a reduced number of vesicles being available for dopamine storage, leading to an accumulation of dopamine in the cytoplasm and increased levels of oxidative stress [3]. In this context, a mechanism involving iron in Parkinson's disease progression could result from the redistribution of highly oxidant iron-dopamine compounds in dopaminergic neurons. Using synchrotron X-ray fluorescence nano-imaging it is now possible to investigate the subcellular distribution of metal ions involved either in pathological or physiological functions.

Principal publication and authors
L. Risser (a), F. Plouraboué (a), A. Steyer (b), P. Cloetens (c), G. Le Duc (c), C. Fonta (d), *J. Cereb. Blood flow and Metabolism* **27**, 293–303 (2007).
(a) IMFT UMR5502 CNRS-INPT/UPS, Toulouse (France)
(b) OSES Université de Paris I (France)
(c) ESRF
(d) CERCO UMR5549 CNRS-Université Paul Sabatier Toulouse 3 (France)

From homogeneous to fractal micro-vascular networks in the brain

Knowledge of cortical micro-vascular organisation is important for a broad range of fundamental biological and clinical subjects. Methods for quantifying micro-vascular structures inside tissues are usually two-dimensional and restricted to small volumes. Synchrotron tomography offers a great improvement in the analysis of vascular network because it permits analysis in three dimensions with micrometre resolution and a very large accessible volume. This technique is aided by a recently developed tissue preparation whereby the micro-vascular networks are injected with a contrast agent [1].

As micro-vascular networks are extremely complicated structures, some relevant structural parameters are needed to describe angiogenesis or to define malignancy criteria. Previous studies have used simple parameters such as vascular density in normal cortical tissues and fractal dimension in tumour vascular networks [2]. The quality of multi-scaled analysis can nevertheless suffer from restriction on the investigation methods: lack of spatial resolution, insufficient penetration depth inside the tissue or restriction to two-dimensional analysis, as in most previous analyses. For this reason we analysed the 3D multi-scale properties

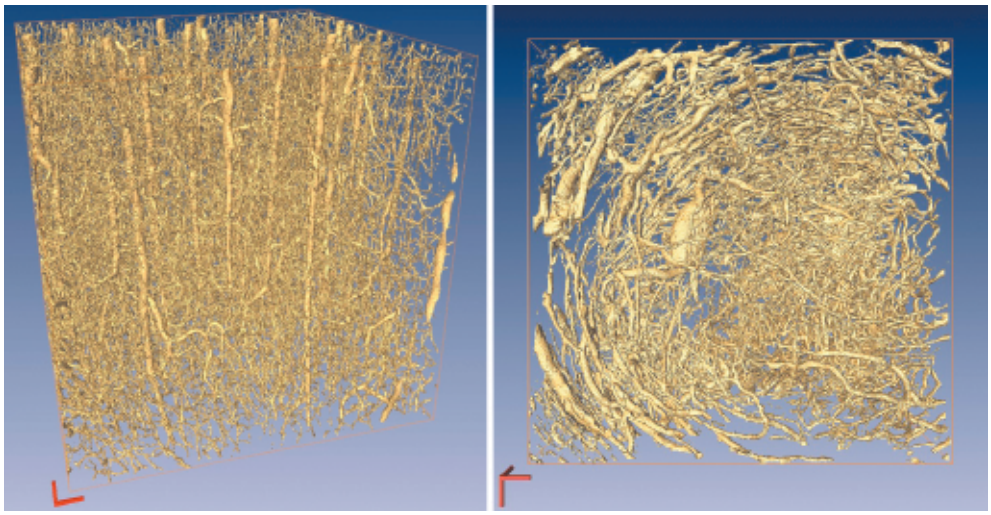

Fig. 124: Volume rendering of cortical vascular network in (a) healthy marmoset monkey, and (b) implanted tumour in a rat. 3D scale-bar (in red) is 100 micrometres in each direction.

of the spatial distribution of vascular networks in detail, both in normal cortical tissues and in implanted tumours. As a reference we chose either normal marmoset monkey cortex or healthy rat cortex to be compared with implanted 9L gliosarcoma in rats, as illustrated in **Figure 124**.

The implantation of 9L gliosarcoma in rat brain was carried out at the BioMedical facility, while the absorption tomography experiments took place at beamline **ID19**. The vascular component of the images is extracted from usual hysteresis thresholding. Digitised images are then submitted to two complementary multi-scale analysis methods. First, we used standard box-counting in order to investigate the possible fractal distribution of vessel density. An illustrative result is plotted in **Figure 125a**, within which one clearly distinguishes two distinct linear regimes. The first regime associated with small length-scales is the fractal regime for which the vessel density is non-trivially scale-dependent, whilst the second one is just the cubic variation of density with length-scale expected with homogeneous objects. The transition value between fractal to non-fractal regimes defines the representative elementary volume (REV) of the vascular structure.

We found both fractal dimension and REV scale to be statistically larger in tumours than in normal tissues.

Secondly, from the vessel digitisation we compute the distance map to any vessel. This map is a scalar field associated with each point of the image for which the Euclidian shorter distance to any vessel is computed. By computing how "far" any point is located in the neural tissue from the vascular network, one can obtain insights into the spatial distribution of oxygen by the vascular network and how the network drains metabolic products. These statistical properties of the aperture map can be further quantified by computing its power spectrum. This is illustrated in **Figure 125b** where, again, one can clearly distinguish two regimes. At large wavelength, *i.e.* short distances, the power spectrum displays a clear linear trend associated with a self-affine distribution of distance map which is the

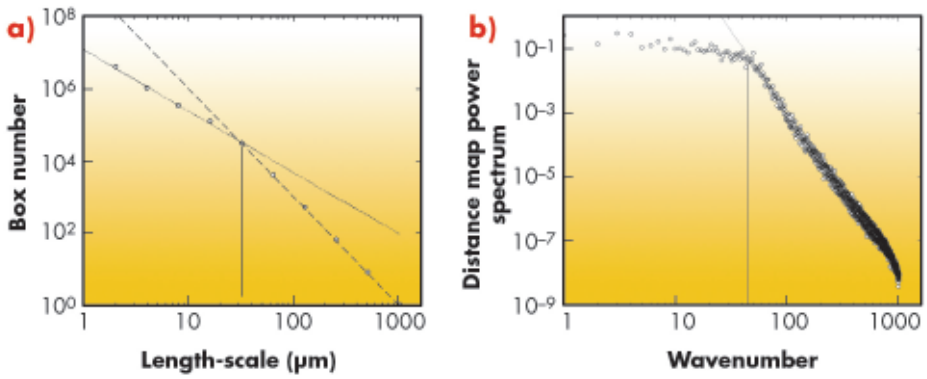

Fig. 125: (a) Fractal analysis of the marmoset vascular network with a box-counting method plotted on bi-logarithmic coordinates: box number versus their size in micrometres. The fractal regime is represented by a dotted line, the slope of which leads to a fractal dimension equal to 1.7, whilst the homogeneous regime associated with a slope equal to -3 is plotted with long dashes. (b) Averaged power spectrum of the distance map computed from a vascular network in bi-logarithmic coordinates. The vertical line indicates the wavelength cut-off associated with the power law behaviour.

References
[1] F. Plouraboué, P. Cloetens, C. Fonta, A. Steyer, F. Lauwers, and J-P. Marc-Vergnes , *J. Microscopy* **215**,139-148 (2004).
[2] J. Gazit, D. Berk, M. Leunig, L. Baxter, and R.K. Jain , *Phys. Rev. Lett.* **75**, 2428-2431 (1995).

signature of the fractal distribution of vessel density observed in **Figure 125a**. For short wavelengths, the power spectrum saturates, indicating a white-noise de-correlated field at large distances associated with a homogenised distance map structure.

This investigation has resolved the apparent contradiction of previous studies for which normal vascular networks have been found to be either fractal or not. We also provide new analysis tools and parameters for the quantification and differentiation of normal and tumoural angiogenesis.

Principal publication and authors
A. Bravin (a), J. Keyriläinen (a, b), M. Fernández (a, c), S. Fiedler (a, d), C. Nemoz (a), M-L. Karjalainen-Lindsberg (a), M. Tenhunen (b), P. Virkkunen (a), M. Leidenius (a), K. von Smitten (a), P. Sipilä (h) and P. Suortti (a, c) *Phys. Med. Biol.* **52,** 2197–2211 (2007).
(a) ESRF
(b) Helsinki University Central Hospital (Finland)
(c) Department of Physical Sciences, University of Helsinki (Finland)
(d) European Molecular Biology Laboratory, Hamburg (Germany)
(h) Radiation Metrology Laboratory, Radiation and Nuclear Safety Authority (Finland)

High-resolution mapping of human breast tissue samples and comparison with their histopathology

Computed tomography (CT) could be extremely important in breast cancer diagnosis, for localising a tumour and revealing its size and inner structure. Conventional whole-body CT scanners do not have sufficient spatial resolution, and the radiation dose is excessive. High-resolution scanners, with an instrumental resolution of about 0.4 mm, are changing this situation, although their accessible domain of spatial resolution and image contrast remains limited by the allowed dose. The attainable resolution is at the limit of revealing essential morphological features of a small-size tumour.

Refraction and scattering contrast are utilised in analyser-based X-ray imaging (ABI), where perfect crystal X-ray optics is used for conversion of small changes in the propagation direction to intensity changes [1]. The contours of the areas where the tissue density changes are emphasised, revealing the morphology of the object. Here we report on the investigation of human breast samples (tumorous and non-tumorous) with the purpose of demonstrating the clinical importance of ABI-CT in mammography.

Figure 126 shows a series of images of a surgically-removed breast sample, which was affected by a bifocal ductal carcinoma. In **Figure 126a** there is a histological section, which was used as a standard for interpretation of findings. A planar screen-film mammogram taken at the hospital is shown in **Figure 126b**. The CT image acquired with a clinical scanner (**Figure 126c**) had a spatial resolution of about 0.7 mm. The synchrotron radiation ABI-CT image (TOP) shown in **Figure 126d** was acquired at **ID17** using a taper optics Frelon camera [2] with a spatial resolution of more than one order of magnitude better (0.047 mm) and using the same dose as for the clinical scanner. This image shows a stronger contrast and has a much higher spatial resolution than **Figure 126b**; the collagen-rich areas are identified by rapid variations of intensity, which correspond to the orientation of the collagen fibres.

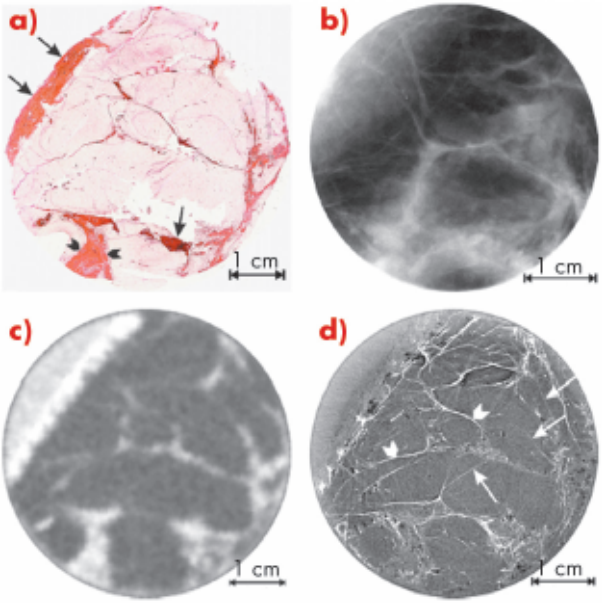

Fig. 126: (a) Scanner image of the histologic whole-mount slide from the centre plane of 24 mm thick sample with ductal carcinoma. The nuclei are shown in brown or black, young collagen and reticulin in bluish, mature collagen in red, adipocytes in white and both red blood cells and muscle in a yellow colour; (b) clinical screen-film mammogram of the same sample (26 kV, 5.0 mAs); (c) clinical CT image of the same sample (80 kVp, 50 mAs); (d) ABI-CT TOP image of the same sample (33 keV).

The results of this study show that ABI-CT images acquired with a high-resolution detector permit a significant improvement in the visualisation of the morphology and of the overall architecture of the breast tissues. All ABI-CT images show an enhanced contrast [1] and many details become visible that would otherwise be radiotransparent with both planar and CT imaging with conventional sources. The one-to-one correspondence of the ABI-CT image with the corresponding optical image of the stained histology section is evident. The independent observations by the pathologist and the radiologist involved in this study identified the same features in the histological sections and in the ABI-CT images, and they arrive at very similar conclusions.
Earlier studies highlighted that small-angle X-ray scattering (SAXS) from collagen, which is rejected by the analyser at the TOP position, is much stronger than scattering from the adipose tissue [3].
In the areas where cancer has invaded, the molecular structure of collagen differs from the structure of normal 'healthy' collagen [3,4]. SAXS from collagen in these areas is stronger than scattering from normal collagen. Further studies are needed to show whether this difference is sufficiently large to be observed in the TOP images.

The next step in ABI-CT is the reconstruction of volume images from the two-dimensional images. The goal is to produce a high-resolution 3D image of the tumour that can be arbitrarily rotated on the computer screen and inspected visually. In principle, the ABI method can be imported to the clinical environment because the refraction and scattering contrast in analyser-based imaging do not require the full coherence of the synchrotron beam. On the other hand, compact SR sources that operate in the hard X-ray regime are being developed, and these will be ideally suited to many medical applications including ABI.

References
[1] A. Bravin, *J. Phys. D: Appl. Phys.* **36**, A-24-29 (2003).
[2] P. Coan, A. Peterzol, S. Fiedler, C. Ponchut, J.C. Labiche and A. Bravin *J. Synch. Rad* **13**, 260-270 (2006).
[3] M. Fernández, J. Keyriläinen, R. Serimaa, M. Torkkeli, M-L. Karjalainen-Lindsberg, M. Tenhunen, W. Thomlinson, V. Urban and P. Suortti *Phys. Med. Biol.* **47,** 577–92 (2002).
[4] M. Fernández, J. Keyriläinen, R. Serimaa, M. Torkkeli, M.-L. Karjalainen-Lindsberg, M. Leidenius, K. von Smitten, M. Tenhunen, S. Fiedler, A. Bravin, T.M. Weiss and P. Suortti *Phys. Med. Biol.* **50,** 2991–3006 (2005).

Materials science applications

In situ imaging of microstructural changes at solidification and partial remelting of Al-Cu alloys

The solidification process of alloys involves the continuous transition from the liquid to the solid state and the final properties of the solidified alloys strongly depend on the resulting microstructure. This microstructure is usually characterised on 2D sections by optical or scanning electron microscopy. Solidification models, developed on the basis of the physical mechanisms that are possibly occurring when solid and liquid are coexisting, are validated by these post-solidification observations. Direct characterisation of the dynamical phenomena occurring during solidification would greatly improve these models and our knowledge of the solidification process. This requires *in situ* 3D observations which are now possible by fast X-ray tomography experiments carried out at high resolution on both the ID15 and ID19 beamlines. Limitations, however, exist in terms of size of the specimens and in the kinetics of the evolution of the microstructure. Another limitation is that the liquid and the solid phases must exhibit sufficiently different absorption coefficients to be clearly distinguished when they are coexisting. Al-Cu based alloys are therefore good candidates for these experiments.

The solidification experiment was carried out with an Al-7%Si-10%Cu alloy using a cylindrical specimen of 1.5 mm in diameter and 3 mm in height which was

Principal publications and authors
N. Limodin (a), E. Boller (b), L. Salvo (a), M. Suéry (a), M. DiMichiel (b), Proc. 5th Decennial Inter. Conf. on Solidification Processing, Sheffield, 23-25 June 2007, Ed. Howard Jones, The University of Sheffield, 316-320; N. Limodin (a), L. Salvo (a), M. Suéry (a), M. DiMichiel (b), *Acta Materialia* **55**, 3177-3191 (2007).
(a) SIMaP, INP Grenoble, Saint-Martin d'Hères (France)
(b) ESRF

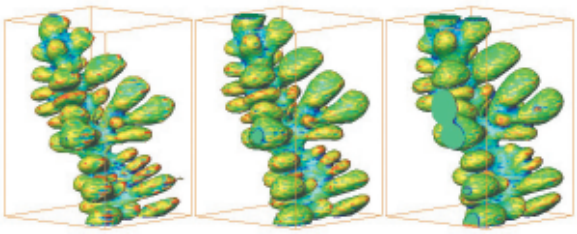

Fig. 127: Evolution of an individual dendrite in an Al-Si-Cu alloy with increasing solid fraction.

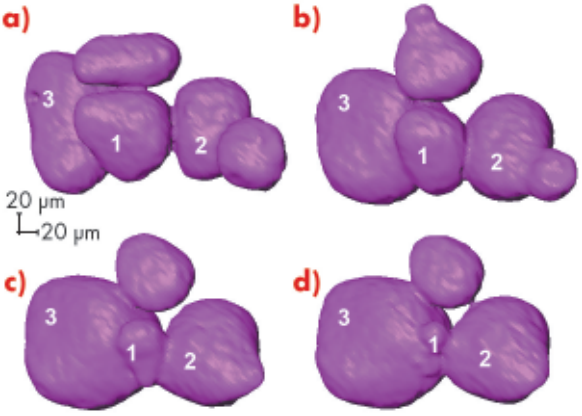

Fig. 128: Morphological changes occurring while maintaining a constant temperature for a group of solid grains in an Al-Cu alloy: (a) 1560 s; (b) 3360 s; (c) 4260 s; and (d) 4560 s.

glued with zirconia paste on the top of an alumina rod placed on the rotating stage. It was heated until it became completely liquid and then slowly solidified while being supported by its own oxide skin. The solidification experiment was carried out at the **ID19** beamline and a gas blower was used to heat up and cool down the specimen at a controlled cooling rate. The scan time to take 400 projections over a 180° rotation of the specimen was 20.7 s and the cooling rate was 3°C per min. Radiographs were recorded using the FReLoN 2k14 CCD-camera developed at the ESRF.

This experiment allows the *in situ* observation of the continuous growth of the dendrites as shown in **Figure 127**. Several mechanisms occur concurrently, *i.e.* dissolution of small secondary arms, filling of the gap between two arms. These mechanisms have been proposed in the literature [1] but this is the first time that they have been observed directly during solidification. These morphological changes can be quantified in terms of variation of the solid-liquid interface area or local curvatures of the solid phase and compared with predictions of the models.

In situ tomography can also be carried out while maintaining an alloy isothermally in the semi-solid region to study the evolution of the microstructure when the solid fraction remains constant. Such experiments were carried out on the **ID15** beamline for an Al-15.8%Cu alloy processed to produce globular solid particles rather than dendritic structures. For this experiment, a similar type of specimen was used with the same holding procedure but in this case a resistance furnace developed at ESRF was used. The maintain temperature was 555°C which leads to a solid fraction of 0.68 after a period of 1500 s required to reach thermodynamic equilibrium. In a similar way as for solidification, 400 projections were taken over a 180° rotation of the specimen using a DALSA CCD-camera. The scan time for this total rotation is smaller than 15 s. Again during these experiments local changes at the scale of the individual solid particles were observed *in situ*. **Figure 128** shows these changes where coalescence of particles of similar size (1 and 2) occurs initially followed by dissolution of the smaller particle (1) for the benefit of the bigger ones (2 and 3).

These experiments clearly demonstrate that fast X-ray tomography is a very powerful technique to characterise *in situ* and in real-time the microstructural evolution of a solid-liquid mixture during solidification and partial remelting. The basic mechanisms that are occurring at the scale of the solid grains or dendrites can be observed and the morphological changes can be quantified. There are still some limitations in the observations but it is anticipated that these limitations will be overcome in the next few years thanks to the continuous improvement in the available equipments and techniques.

References
[1] M. Chen and T.Z. Kattamis, *Mater. Sci. Eng.* **A247**, 239 (1998).

Scanning X-ray excited optical luminescence microscopy in GaN

Principal publication and authors
G. Martinez-Criado (a), B. Alen (b), A. Homs (a), A. Somogyi (a), C. Miskys (c), J. Susini (a), J. Pereira-Lachataignerais (d), J. Martinez-Pastor (e), *Appl. Phys. Lett.*, **89**, 221913 (2006).
(a) ESRF
(b) Microelectronics Institute, Madrid (Spain)
(c) Walter Schottky Institute, Garching (Germany)
(d) Chemical and Environmental Research Institute, Barcelona (Spain)
(e) Materials Science Institute, Valencia (Spain)

The enormous demand for superior optoelectronic devices has systematically stimulated the application of new optical characterisation techniques. Here, we propose a photoluminescence approach based on X-ray core-level excitation using a hard X-ray microbeam. So far, a typical X-ray microscope provides significant information in terms of elemental specificity, chemical mapping, coordination chemistry, and site symmetry. If a photoluminescence spectrum is also recorded at each point, patterns of electron-hole recombinations may be produced simultaneously that show complementary properties in a spatially-resolved manner. Usually, the effect of doping, strain, and disorder are studied with high sensitivity by radiative transitions. The experimental layout of the optical-sensitive scheme at **ID22** is shown in **Figure 129a**. To study the recombination channels in highly-demanded wide-band-gap materials, UV-visible wavelength detection was prioritised. Thus, aspheric collection optics and fibre optic accessories have been incorporated to bring the UV-visible light into an optical spectrometer coupled to a linear Si CCD. Based on freestanding GaN and epitaxially-grown GaN:Mn on a-Al_2O_3, the applications of the scanning X-ray excited luminescence technique will be described.

Figure 129b displays a red-green-blue (RGB) map of the intensities associated to the transitions located at 3.0, 2.6, and 1.9 eV from the GaN:Mn/Al_2O_3. The X-ray excited luminescence signal was recorded with an excitation energy of 13 keV over a 100x65 mm^2 scanned area. The detailed spectral analysis suggested the presence of different peaks, where both Al_2O_3 and GaN:Mn-related transitions are overlapped. The emission at 1.9 eV has been assigned to the trace impurity Fe^{3+} in Al_2O_3, while a luminescence band around 3.0 eV accompanied with another transition at 2.5 eV was tentatively attributed to Mn-related recombinations in GaN. The typical donor-acceptor pair recombinations, attributed to oxygen related complexes and vacancy defects in nitrides, are superimposed at 2.8 and 3.2 eV, respectively. Although the common yellow band associated with intrinsic defects (V_{Ga}) is a competitive GaN recombination channel, the luminescence does not exhibit any transition at 2.2 eV. Therefore, within the experimental accuracy, a visible nonuniformity characterises the Mn centres in good correlation with a former X-ray fluorescence map [1].

Expanding the microprobe versatility, XANES data in both photon collection modes (X-ray excited luminescence and X-ray fluorescence) are also recorded. To avoid the overlapping of both GaN and substrate-related emissions, in **Figure 130**, the Ga *K* edge XANES have

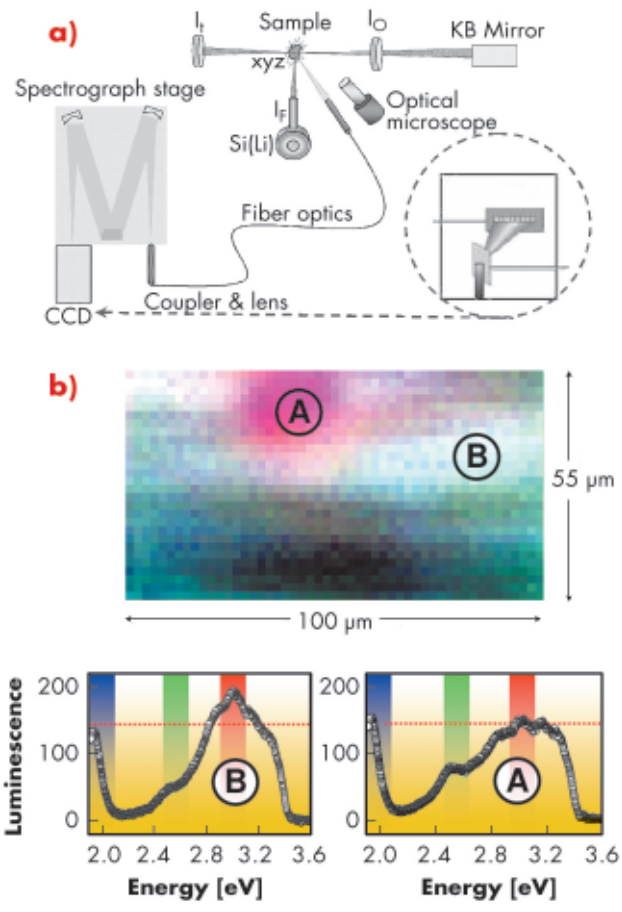

Fig. 129: a) Schematic layout of the scanning X-ray excited optical luminescence arrangement. b) Spatial variation of the different transition intensities (defined in the plots) recorded on GaN:Mn/Al_2O_3. The corresponding colour scales are included in the graphs (light represents low counts, dark high counts).

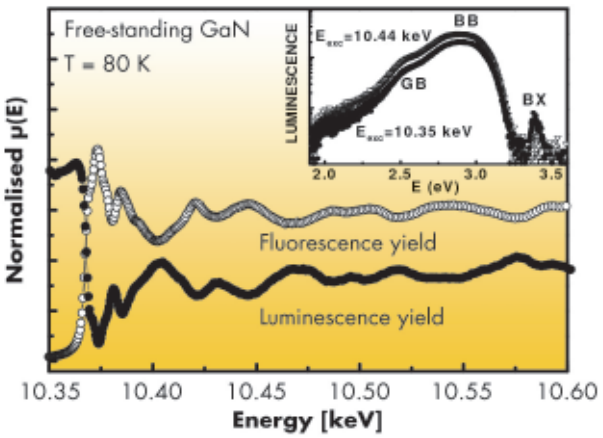

Fig. 130: Normalised XANES spectra around the Ga K edge taken in both X-ray excited optical luminescence and X-ray fluorescence modes from a freestanding GaN layer. The inset shows the luminescence spectra excited with X-ray energies below and above the Ga K edge.

References
[1] G. Martinez-Criado, A. Somogyi, S. Ramos, J. Campo, R. Tucoulou, M. Salome, J. Susini, M. Hermann, M. Eickhoff, M. Stutzmann, *Appl. Phys. Lett.*, **86**, 131927 (2005).
[2] C. Gauthier, H. Emerich, and J. Goulon, *Jpn. J. Appl. Phys., Part 1*, **32**, 226 (1992).

been plotted for a freestanding GaN layer. The inset displays the luminescence excited with X-ray energies above and below the Ga *K*-edge. The spectra consist of two broad bands with insensitive shapes to the excitation energy. The blue emission band (BB) dominates at 2.8 eV, whereas the green band (GB) at 2.5 eV commonly attributed to defects is observed as a shoulder. The bound exciton (BX) lines appear at higher energies with very low intensity. As expected for a thick and totally absorbing sample (~100 mm thick) under the used experimental geometry, the luminescence shows a negative edge jump with inverted oscillations, suggesting that the high-energy electrons excited from outer core states contribute more to the optical luminescence than those from inner core states [2].

In summary, despite the energy relaxation and transfer processes involved, relevant optical transitions have been examined spatially and spectrally resolved in GaN:Mn/a-Al_2O_3. The luminescence scanning probe illustrated the nonuniform distribution of the Fe^{3+} ions and defect-related centres in sapphire, also showing a good agreement between the Mn related luminescence map and formerly reported Mn pattern by X-ray fluorescence [1]. Furthermore, the luminescence from a freestanding GaN film was monitored around the Ga *K* edge, demonstrating that no additional radiative channels are created above the Ga *K* shell.

Cultural heritage applications

Micrometric atypical pigment identified in Grünewald Isenheim Altarpiece

Principal publication and authors
M. Cotte (a,b), E. Welcomme (a), V.A. Solé (b), M. Salomé (b), M. Menu (a), P. Walter (a), J. Susini (b), *Anal. Chem.* **79**, 6988-6994 (2007).
(a) Centre of Research and Restoration of the French Museums, CNRS-UMR171, Paris (France)
(b) ESRF

Mathias Grünewald is an important German Renaissance painter. He created his magnum opus, the *Isenheim Altarpiece*, during ~1512–1516. His renown is mainly based on his unique skill in handling colours. In preparation for an exhibition held at Colmar (France) and Karlsruhe (Germany) late 2007, chemical analyses were conducted to establish the list of painting pigments used by the artist. In a first approach, non-invasive analytical portable instruments, allowing *in situ* screening, were favoured. Interestingly, antimony was detected in several parts of the artwork, in particular for the rendering of metallic reflects, as shown in **Figure 131** (sleeping guard in the *Resurrection* scene). Although sulphur seemed to be associated with antimony, this correlation was questionable due to the high concentration of lead that strongly overlaps with sulphur emission lines. Antimony is not commonly found in paintings. It is usually associated with Naples yellow, a lead antimony oxide, used in paintings in a much later period.

To further the identification of Grünewald's antimony pigment, micro-sampling was performed, guided by portable XRF measurements. When such micro-sampling are allowed on ancient paintings, fragments are usually tiny, precious, heterogeneous and complex, which makes their chemical analysis arduous. As illustrated here, micro-imaging techniques are particularly relevant as they can simultaneously provide identification and

localisation of the various ingredients, even in intricate mixtures. Transversal cross-sections were prepared to reveal the whole stratigraphy of the painting fragments. Micro X-ray fluorescence was carried out at the **ID21** beamline, first at the antimony L-edges and then at the sulphur K-edge. Fitting of fluorescence data was arduous due to interferences of K-lines of sulphur with M-lines of lead, and of K-lines of calcium with L-lines of antimony (**Figure 132a**). This data processing was performed using PyMCA software developed at the ESRF [1]. Elemental maps show that antimony distribution is limited to an intermediate layer, above a lead layer and below a varnish superficial layer (**Figure 132b**). They also reveal that antimony and sulphur distributions are similar and that these elements are present as few micrometres-sized grains, surrounded by a lead white matrix. These maps suggested the probable presence of stibnite (Sb_2S_3), a grey antimony sulfide. Additional μ-XANES was performed at the Sb L_{III}-edge and the S K-edge to confirm this assumption and to refute the presence of any other antimony pigments that can be used in painting (in particular Naples yellow ($Pb_2Sb_2O_7$) or Kermesite (Sb_2S_2O)). Special care was given to minimise the micro-probe drift while scanning the energy. Indeed, micro-probe stability was a critical issue to selectively analyse the antimony grains without shifting into the lead white matrix. Sulphur was found to be in a reduced state (sulphide), without chemical bonding to lead. Comparison with reference compounds gave clear support to the suggestion that the antimony-containing compound was stibnite. This pigment has been found in only about ten other paintings, all of them originating from Italy in the first half of the 16th century. Grünewald tailored the metallic aspects of the painting by mixing micrometric stibnite grains with a lead white matrix.

Fig. 131: Part of the *Resurrection*, from the *Isenheim Altarpiece*, by Grünewald (picture E. Lambert, © C2RMF). The white star indicates where the micro-sampling was done.

Lateral resolution, chemical sensitivity, and imaging are the key points that explain the advantage of synchrotron-based imaging techniques for the analysis of fragments of ancient paintings. The continuous development of software is very helpful for the processing of data obtained, not only on synchrotrons but also with laboratory as well as portable instruments. This study illustrates the complementarity between portable and synchrotron instruments in the discovery of the secrets of the ancient painters.

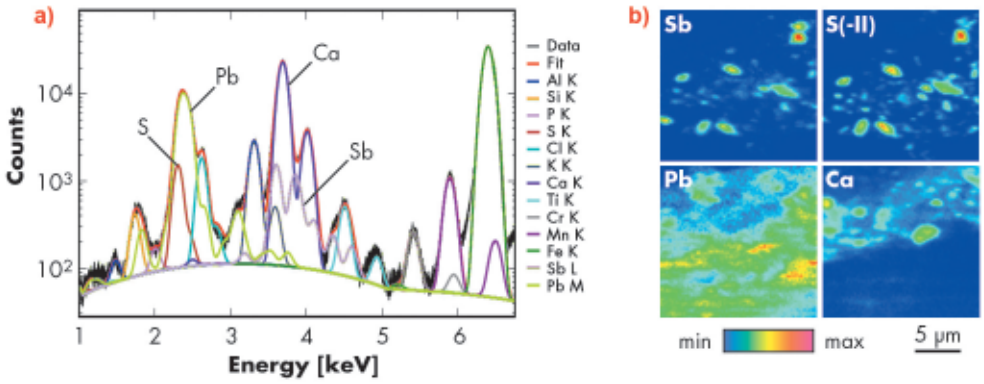

Fig. 132: Identification of stibnite micrometric grains by μ-XRF: a): fluorescence spectrum obtained at 7.2 keV, over the cross-section and fitted with PyMCA. b): fitted elemental mapping of antimony, sulfides, lead and calcium. Map size: 17 × 16 μm²; step size: 0.25 × 0.25 μm²; beam size: 1 × 0.4 μm² (hor. × ver.).

Reference

[1] V.A. Solé, E. Papillon, M. Cotte, P. Walter, J. Susini, *Spectrochim. Acta Part B* **62**(1), 63-68 (2007).

Phase-contrast imaging demonstrates earliest occurrence of human growth and development

Principal publications and authors
T.M. Smith (a), P.T. Tafforeau (b,c), D.J. Reid (d), R. Grün (e), S. Eggins (e), M. Boutakiout (f), J.-J. Hublin (a), *Proc. Natl. Acad. Sci. USA* **104**, 6128-6133 (2007); P. Tafforeau, T.M. Smith, *J. Hum. Evol.* **54** (in press).
(a) MPI for Evolutionary Anthropology, Leipzig (Germany)
(b) LGBPH, CNRS, Poitiers (France)
(c) ESRF
(d) Newcastle University (UK)
(e) RSES, Australian National University, Canberra (AZ)
(f) University Mohammed V-Agdal, Rabat (Morocco)

The subject of modern human origin is one of the most debated topics among anthropologists. There is little consensus about where and when the first members of our species, *Homo sapiens*, became fully modern. While fossil evidence tells a complex tale of mosaic change during the African Stone Age, almost nothing is known about changes in human 'life history', or the timing of development, reproductive scheduling, and lifespan. Tooth growth, and most importantly molar tooth eruption age, represents one of the most powerful clues to reconstruct growth processes in fossil humans [1]. Dental enamel is a unique hard tissue that begins growing early in an individual's life, and completes formation during adolescence. It permanently records daily accretional growth (including birth), and is not subject to modification (other than wear) during an individual's life. By using incremental growth lines in teeth, similar to annual rings in trees, developmental rate and time may be accurately established millions of years after death [2]. Recent research has shown that early fossil humans (australopithecines and early *Homo*) possessed short growth periods, which were more similar to chimpanzees than to living humans [3]. However, it is unclear when, and in which group of fossil humans, the modern condition of a relatively long childhood arose.

In this study, tooth growth and eruption were examined in one of the earliest representatives of *Homo sapiens*, found in Jebel Irhoud, Morocco and dated to approximately 160,000 years ago. With a combination of a novel application of synchrotron imaging [4-5], conventional microtomography, and developmental analysis, we reconstructed tooth formation time and determined the age at death of the fossil child (**Figure 133**). The results show that the Moroccan fossil, at almost 8 years of age, is currently the oldest member of the genus *Homo* to show a modern human life history profile. These findings and other evidence suggest that modern biological, behavioural, and cultural characteristics appeared relatively late in the past six million years of human evolution.

The new application of high-resolution propagation phase contrast X-ray synchrotron local microtomography, whose first results were obtained four years ago [4], permits previously inaccessible developmental features to be revealed non-destructively [4-5]. By imaging teeth prior to physical sectioning and comparing the same areas in our

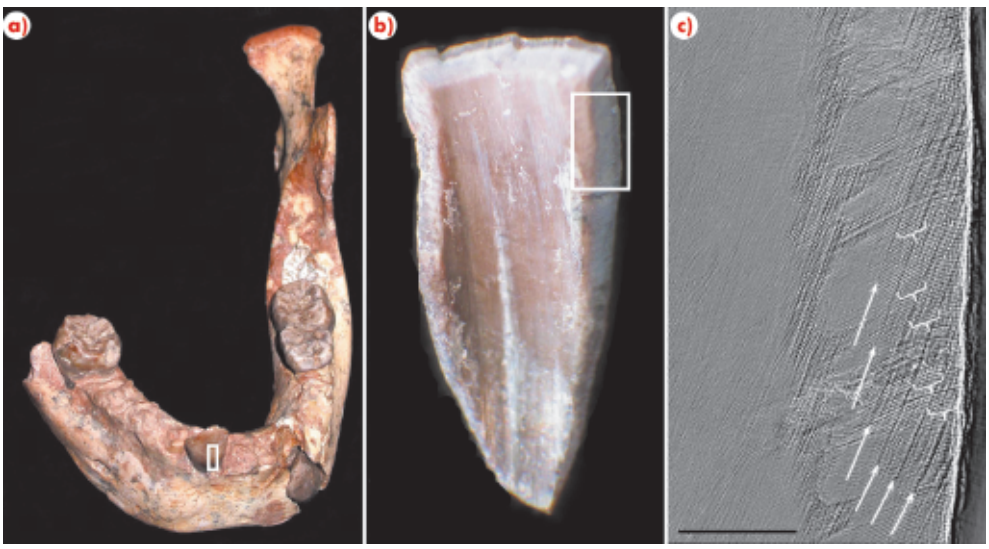

Fig. 133: a) The North African juvenile fossil mandible showing the location of the incisor tooth enamel (white box) sampled at the ESRF. b) Close up of enamel fragment, with the area of interest shown in the white box. c) Synchrotron image showing growth lines (white arrows) with 10 daily lines between them (white brackets). Scale bar = 200 micrometres.

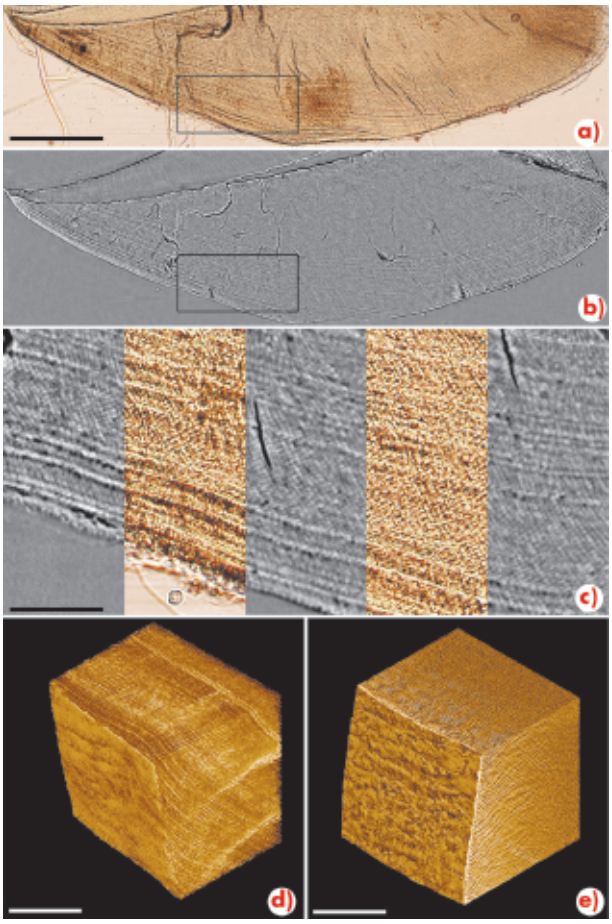

Fig. 134: Comparison of (A) physical and (B) virtual sections of a chimpanzee molar germ, illustrating (C) correspondence between incremental features. Application of the 3D technique on an intact germ (D) and a fossil oran-utang molar (E). Scale bar = 500 micrometres in A and B, 100 micrometres in C, and 250 micrometres in D and E.

second study, we demonstrated the accuracy of virtual histology (**Figure 134**). Ongoing applications of this technique will permit more precise assessments of mammalian evolutionary developmental biology, as well as greater understanding of the three-dimensional structure of dental tissues.

Recent studies performed on the ESRF beamline **ID19** have shown that microscopic incremental features in dental tissues can be imaged with high fidelity using phase contrast X-ray synchrotron microtomography. This technique has been applied for non-destructive and precise assessment of the age at death and length of the growth period in fossil teeth. Future non-destructive applications will reveal growth processes in additional rare human fossils, allowing finer resolution of the evolution of human life history.

References

[1] B.H. Smith, R.L. Tompkins, *Annu. Rev. Anthropol.* **24,** 257–279 (1995).

[2] T.M. Smith, D.J. Reid, J.E. Sirianni, *J. Anat.* **208**, 125-138 (2006).

[3] C. Dean *et al. Nature* **414**, 628-631 (2001).

[4] P. Tafforeau, Ph.D. Thesis, Université de Montpellier II, pp. 284 (2004).

[5] P. Tafforeau *et al., Applied Physics A* 83, 195-202 (2006).

Emerging techniques for biology, geoscience, nanomaterials

Revealing the presence and nature of living microorganisms in rocks

Microbial life colonised all lithospheric environments wherever carbon and energy sources, subsurface porosity, and temperature permit and it is now well recognised that the Earth subsurface is a major habitat for prokaryotes [1]. Moreover, the number of microbes that thrive deep below ground probably exceeds the number found in other components of the biosphere, thus contributing significantly to the overall biomass and biodiversity on Earth.

Therefore the study of this deep biosphere has important implications for our understanding of global biogeochemical cycles and interactions between the biosphere and the geosphere [2].

One of the key challenges in the understanding of the complexities of the subsurface and its microbial inhabitants is the exploration of the metabolic diversity of the prokaryotic populations, their energy sources, and biogeochemical

Principal publication and authors

B. Ménez (a,b), C. Rommevaux-Jestin (a,b), M. Salomé (c), Y. Wang (d), P. Philippot (a,b), A. Bonneville (a), E. Gérard (a,b,e), *Chem. Geol.*, **240**, 182-192 (2007); E. Gérard (a,b,e), F. Guyot (a,d), P. Philippot (a,b), P. Lopez-Garcia (e), *J. Microbiol. Methods*, **63**, 20-28 (2005).

(a) Centre de Recherches sur le Stockage Géologique du CO_2 (IPGP/TOTAL/SCHLUMBERGER), IPGP, CNRS UMR 7154, Paris (France)

(b) Géobiosphère Actuelle et Primitive, IPGP, CNRS UMR 7154 & Université Denis Diderot (Paris)

(c) ESRF

(d) IMPMC, Paris (France)

(e) ESE, CNRS UMR 8079, Université Paris-Sud, Orsay (France)

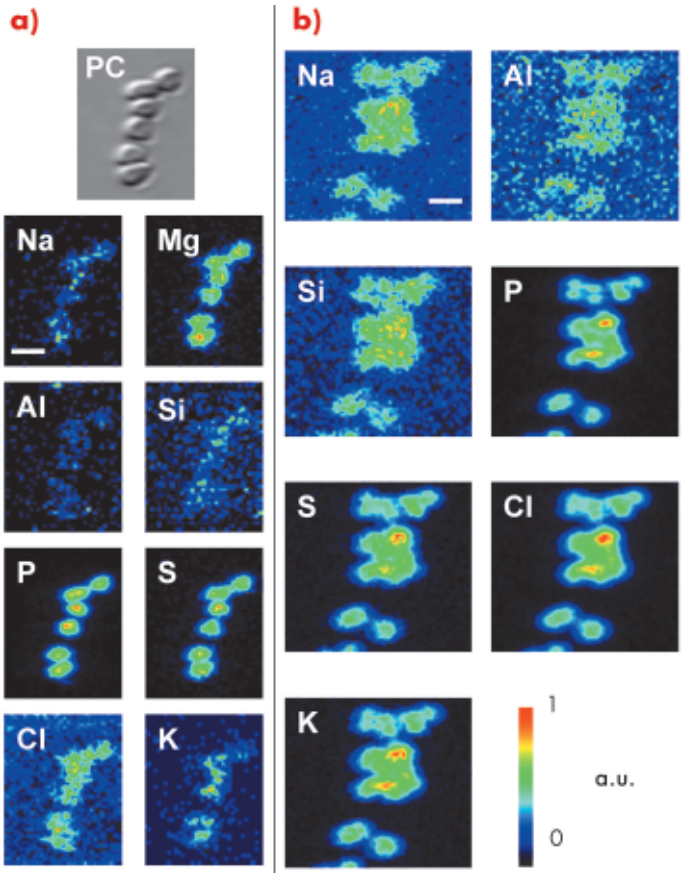

Fig. 135: Cultured *D. radiodurans* cells as shown by X-ray microscopy in transmission and fluorescence modes on (a) Ultralene® film and (b) carbonate. Phase-contrast X-ray image (PC) and two-dimensional elemental distributions, showing the same field of view, were obtained using 70 and 2000 ms/pixel integration time with an associated pixel size of 0.1 * 0.1 and 0.2 * 0.2 μm², respectively. The scale bar corresponds to 2 μm (a.u. is for arbitrary unit).

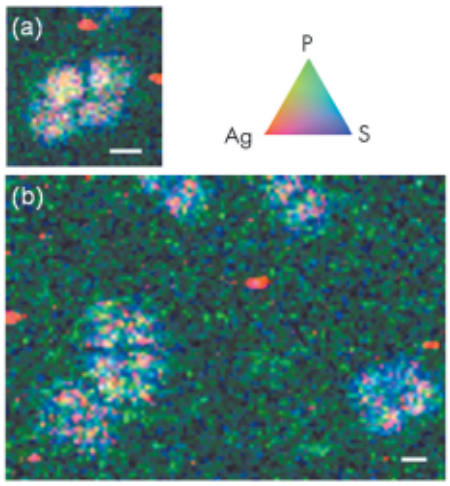

Fig. 136: Duplicates X-ray microscopy observations of silver-enhanced ultra small immunogold particles in single tetrads of *D. radiodurans* hybridised with fluorescein-labelled bacterial probe EUB338 on carbonates. Tricolor (RGB) synchrotron X-ray fluorescence elemental maps were obtained by scanning the surface at pixel size of 0.25 * 0.25 μm² and 0.33 * 0.33 μm² and with integration time of 3000 ms/pixel and 2000 ms/pixel for panels (a) and (b), respectively. The scale bars correspond to 2 μm for each. Red codes for Ag, green for P, and blue for S. Each pixel is coloured in proportion to their respective signal. This finally allows hybridised cells that display a good spatial correlation between S, P, and Ag to be distinguished from individual Ag grains (in red) belonging to the background signal.

transformations. Here we demonstrated the ability of scanning X-ray microscopy using synchrotron radiation to localise and investigate the phylogenetic affiliation of individual prokaryotic cells on various mineral surfaces (*e.g.* silicates, carbonates, basaltic glass). This was achieved by applying a newly developed protocol based on fluorescence *in situ* hybridisation coupled to ultra-small immunogold. For this purpose, universal and specific fluorescein-labelled oligonucleotide probes were hybridised to the ribosomal RNA of prokaryotic microorganisms in heterogeneous cell mixtures (*i.e.* a simple model composed of a 1:1 mix of cultivable bacteria from different taxonomic divisions, namely *Escherichia coli* and *Deinococcus radiodurans*). Antibodies against fluorescein coupled to subnanometre gold particles were then used to label the hybridised probes in the ribosome. After increasing the diameter of the metal particles by silver enhancement to optimise their detection, the specific gold-silver signal was visualised on various substrates by using the scanning X-ray microscope operating at beamline **ID21**. This method involves associating heavy metal fluorescence signals emerging specifically from the gold-silver nanoparticles to the location of microbes, highlighted by their light element fluorescence (**Figure 135**). These spatial distributions constitute the cell chemical fingerprint, firmly elaborated by taking advantage of the morphological and spatial information provided by the phase contrast X-ray imaging. **Figure 136** highlights the successful localisation of a specific gold-silver signal on carbonates at the single prokaryotic-cell level, with a satisfactory detection efficiency and spatial resolution. Overall, this potentially allows imaging the presence and nature of living microorganisms in rock samples. The possibility to simultaneously link the phylogenetic identification of microorganisms with the chemical and structural characterisation of associated mineral phases (*i.e.* inorganic substrate and biomineralisation that constitute metabolic reactants and byproducts) by using complementary synchrotron-based methods (*i.e.* X-ray microdiffraction and X-ray absorption microspectroscopy) offers great innovation for assessing the geochemical impact of subsurface microbial communities and unravelling microbe and mineral interactions in the deep biosphere.

References
[1] J.P. Amend, A. Teske, *Palaeogeogr., Palaeoclimatol., Palaeoecol.*, **219**, 131-155 (2005).
[2] J.K. Fredrickson, T.C. Onstott, In: J.K. Fredrickson and M. Fletcher (Eds), Subsurface Microbiology and Biogeochemistry, New York, pp. 3-37 (2001).

X-ray near-field speckles: a new approach to small-angle scattering

Principal publication and authors
R. Cerbino (a), L. Peverini (b), M.A.C. Potenza (a), A. Robert (c), P. Bösecke (b), M. Giglio (a), Nature Physics, *accepted*.
(a) Department of Physics, Università degli Studi di Milano (Italy)
(b) ESRF
(c) Stanford Linear Accelerator Center, CA (USA)

Speckles are generated whenever a scattering object is illuminated by electromagnetic radiation with a sufficient degree of coherence. In modern synchrotron beamlines the necessary spatial coherence is achieved by selecting a single coherence area of the beam. This is typically done by using a limiting aperture with size of the order of 10 μm and implies a considerable loss in terms of accessible area. For the first time, we have recently observed at **BM05** that the use of limiting apertures is not necessary if one operates in the deep Fresnel [1] region (near field) of the object. The radiation emitted by the bending magnet is mildly monochromatised by a multilayer monochromator and impinges directly on the sample. The proximity of the detector to the sample guarantees the coherent superposition of the stochastically-dephased scattered waves with the transmitted beam. From this originates a speckle field with the same properties of the recently-discovered optical near-field speckles [2]. Optical near-field speckle images can be numerically Fourier transformed by getting results fully equivalent to far-field scattering experiments, where the Fourier transform takes place due to free space propagation. We report in **Figure 137a** a typical speckle image obtained with an area detector at about 3 cm from a cellulose acetate membrane. The background has already been subtracted and only the fluctuating part of the signal is shown. The circular symmetry of the speckles in **Figure 137a** and of the Fourier power spectrum in **Figure 137b** indicates that spatial coherence effects are negligible. Even though the principle underlying near-field experiments is wavelength independent, some additional precautions must be taken into account in the X-ray case. This is due to the strongly-uneven frequency response of X-ray area detectors and to the presence of an oscillatory transfer function caused by the Talbot effect, clearly visible in **Figure 137b**. After correction for these effects and azimuthal average, one is left with the scattering intensity distribution in absolute units as a function of the scattering wavevector q, reported in **Figure 138**, in the range $[1\times10^{-4}, 4\times10^{-3}]$ nm^{-1}. In the same graph we report at higher q results on the same sample obtained with a state of the art ultra small-angle X-ray scattering (USAXS) instrument, like the Bonse-Hart (BH) camera installed at ID02. We find a peak at $q_p = 2.3 \times 10^{-3}$ nm^{-1} which can be associated to a characteristic size $d_p = 2\pi / q_p = 2.7$ μm, related to the alternating void structure in the sample.

Additional experiments have also shown that a temporal monitoring of the near field speckles allows small-angle dynamic scattering measurements to be performed. We have tested the method on a colloidal suspension of silica particles in water. The data are in very good agreement with higher wavevectors X-ray photon

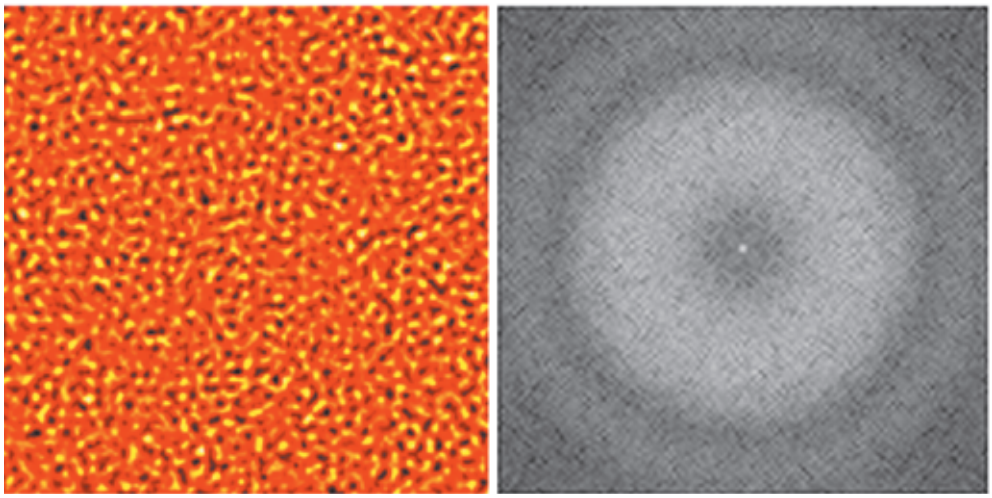

Fig. 137: a) Speckle image recorded at about 3 cm from a cellulose acetate membrane. The background has already been subtracted and only the fluctuating part of the signal is shown. b) Two dimensional Fourier power spectrum of the image (a).

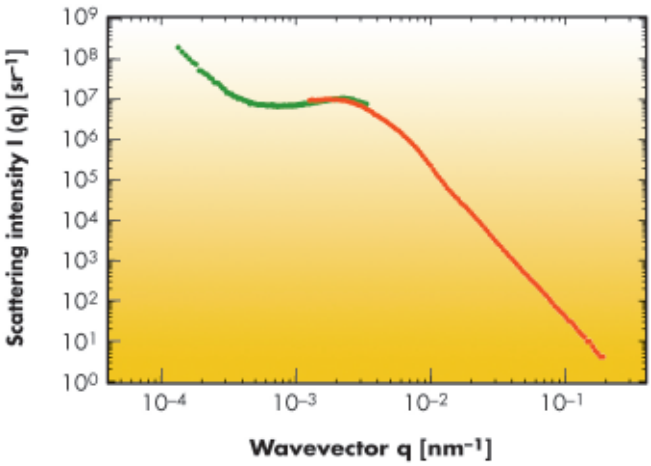

Fig. 138: Absolute scattering intensity I(q) for a microporous membrane with nominal pore size 0.45 μm. The red curve (high q) corresponds to data obtained with a Bonse-Hart camera. The green curve (low q) is obtained with the near field speckle method.

correlation spectroscopy (XPCS) data taken at ID10A on the same sample.

A near field speckle based scattering experiment is experimentally simple and shares the same instrumentation with phase-contrast imaging experiments. It offers access to a wavevector region not available to existing techniques, representing therefore a useful complementary technique. A relevant benefit is also represented by the possibility of using the full beam (in our measurements 1 mm^2) for dynamic measurements. This suggests the use of the method for the space-resolved investigation of the dynamics of complex fluids and other inhomogeneous systems.

References
[1] R. Cerbino, *Phys. Rev. A* **75**, 053815 (2007).
[2] D. Brogioli, A. Vailati, M. Giglio, *Appl. Phys. Lett.* **81**, 4109 (2002).

The Accelerator and X-ray Source

Introduction

Throughout 2007, the Accelerator and Source Division has continued its efforts to improve performances as well as preparing for the forthcoming upgrade. A number of exciting developments have been carried out, which are described hereafter.

Beam parameters of the storage ring

Table 1 presents a summary of the characteristics of the storage ring's electron beam.

Table 2 gives the main optic functions, electron beam sizes and divergences at various source points. For insertion device source points, the beta functions, dispersion, sizes and divergences are calculated in the middle of the straight section.

Two representative source points for each type of bending magnet (even or odd number) have been selected, corresponding to observation angles of 3 and 9 mrad from the exit.

The associated source point originates from a location in the bending magnet with a different magnetic field. Electron beam profiles are Gaussian and the size and divergence are presented in terms of rms quantities.

Energy	[GeV]	6.03
Maximum current	[mA]	200
Horizontal emittance	[nm]	4
Vertical emittance (minimum achieved)	[nm]	0.025
Revolution frequency	[kHz]	355
Number of bunches		1 to 992
Time between bunches	[ns]	2.82 to 2816

Table 1: Principal characteristics of the electron beam.

		Even ID (ID02, ID06...)	Odd ID (ID01, ID03...)	Even BM (BM02, 4,...) 3 mrad	Even BM (BM02, 4,...) 9 mrad	Odd BM (BM01, 3,...) 3 mrad	Odd BM (BM01, 3,...) 9 mrad
Magnetid Field	[T]	Variable	Variable	0.4	0.85	0.4	0.85
Horiz. beta functions	[m]	37.5	0.3	1.3	0.9	2.1	1.6
Horiz. dispersion	[m]	0.144	0.033	0.059	0.042	0.088	0.073
Horiz. rms e- beam size	[μm]	415	51	95	75	131	112
Horiz rms e- divergence	[μrad]	10.3	108	115	111	102	97.4
Vert. beta functions	[m]	3.0	3.0	41.2	41.7	31.6	31.7
Vert. rms e- beam size	[μm]	8.6	8.6	32	32	28	28
Vert. rms e- divergence	[μrad]	2.9	2.9	1.3	1.3	0.9	0.9

Table 2: Beta functions, dispersion, rms beam size and divergence for the various source points.

Table 3: Current, lifetime, bunch length and energy spread for a selection of filling modes.

Filling pattern		Uniform	7/8+1	Hybrid	16-bunch	4-bunch
Number of bunches		992	870	24x8+1	16	4
Maximum current	[mA]	200	200	200	90	40
Lifetime	[h]	75	65	30	16	6
Rms energy spread	[%]	0.11	0.11	0.11	0.12	0.16
Rms bunch length	[ps]	20	20	25	48	55

The associated full width half maximum sizes and divergences are 2.35 times higher. Horizontal electron beam sizes and divergences are given for the uniform filling modes and apply to almost all filling patterns except for the single bunch, for which a slightly larger size and divergence is attained due to the increased energy spread of the electron beam. Vertical electron beam sizes and divergences apply to the uniform, 2 x 1/3 and hybrid filling modes only. To increase the lifetime of the stored beam, the vertical beam sizes and divergences are increased by about 50% in the 16 and 4 bunch filling patterns.

The lifetime, bunch length and energy spread mainly depend on the filling pattern. These are given in **Table 3** for a few representative patterns. Note that in both the 16-bunch and 4-bunch filling patterns, the energy spread and bunch length decay with the current (the value indicated in the table corresponds to the maximum current). The bunch lengths are given for the usual radio frequency (RF) accelerating voltage of 9 MV (8 MV for 16-bunch and 4-bunch).

Summary of accelerator operation

In 2007, 682 shifts (5455 hours) of beam were initially scheduled. Of these 5455 hours, 5343 were effectively delivered (including 56 hours of refill). This represents a beam availability of 97.94%, which is slightly less compared to the previous year, mainly due to a single major failure of a stripline chamber (see below). Dead time due to failures accounts for the remaining 2.06% (**Table 4**). The number of failures is however comparable to the previous year, thus leading to a Mean Time Between Failures of 56.8 hours. In July 2007, a major vacuum leak developed in the feedthrough of a stripline vacuum chamber used for beam diagnostics. Consequently, two cells (~ 50 m) of the ring circumference reached atmospheric pressure requiring full vacuum processing with baking. Seventy-six hours of user time (user service mode, USM) were lost following this incident. The autumn operation schedule was subsequently revised and it was possible to gain two days within the user program to compensate for the lost beamtime. Thirteen long delivery periods (*i.e.* more than 100 hours) without a single interruption took place in 2007, two of those weeks even lasted 168 hours! **Figure 139** highlights the fifth week of run in 2007-02, when the beam was delivered in the new hybrid mode "7/8 + 1" for 144 hours without a single hitch.

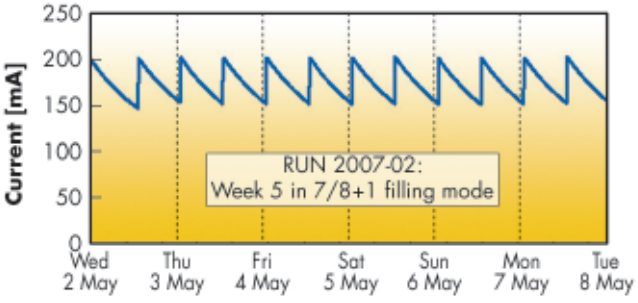

Fig. 139: An example of a full week of delivery without a single failure, in the new hybrid mode.

RUN NUMBER	TOTAL 2006	2007-01	2007-02	2007-03	2007-04	2007-05	TOTAL 2007
Start		19/1/07	30/3/07	8/6/07	17/8/07	26/10/07	
End		21/3/07	30/5/07	25/7/07	17/10/07	17/12/07	
Total number of shifts	**804**	182	183	141	183	156	**845**
Number of USM shifts	**653**	145.9	149.1	107	152	128	**681.96**
Beam available for users (h)	**5118.9**	1131	1169.2	805.4	1180.9	1004.9	**5291.4**
Availability	**98.66%**	**97.82%**	**99.12%**	**94.82%**	**98.17%**	**98.44%**	**97.94%**
Dead time for failures	**1.34%**	2.2%	0.9%	5.2%	1.8%	1.6%	**2.1%**
Dead time for refills	**0.70%**	0.9%	1.1%	0.7%	1.1%	0.3%	**1%**
Average intensity (mA)	**147**	114	130	134	136	182	**138.4**
Number of failures	**85**	24	11	8	31	22	**96**
Mean time between failures (h)	**61.5**	48.6	108.4	107	39.2	46.5	**56.8**
Mean duration of a failure (h)	**0.8**	1.1	1	5.5	0.7	0.7	**1.17**

Table 4: Overview of storage ring operation in 2007.

Filling patterns

No significant changes in the distribution of the modes are to be noted for 2007 compared to the previous years (**Figure 140**). The multibunch modes remain dominant, making up 71% of the shifts. However, in the multibunch type filling patterns, the so-called "7/8 + 1" was a newcomer during run 2007-01. It represents a good compromise for most users. It satisfies many users who need a single bunch with no bunches filled in the vicinity as well as those who want the maximum current with the longest lifetime. The presence of an unfilled gap in the time structure (1/8 of the circumference) stabilises the electron beam against ion instabilities. The filling pattern is delivered with a vertical emittance of 25 pm. A single bunch of 2 mA, placed in the middle of the gap, is delivered with a filling ratio of 10^{-9} between filled and unfilled bunches. One week of uniform and 2 weeks of 7/8 filling pattern were converted to 2/3 filling pattern due to an RF cavity failure in June and July 2007. In addition, one week of uniform delivery was converted to 2/3 filling mode in August due to insufficient vacuum conditioning following numerous interventions during the summer shutdown. During run 4, the 16 bunch filling mode was delivered with a maximum of 70 mA instead of 90 mA due to outgassing induced by a defective RF liner immediately upstream of a radio frequency cavity.

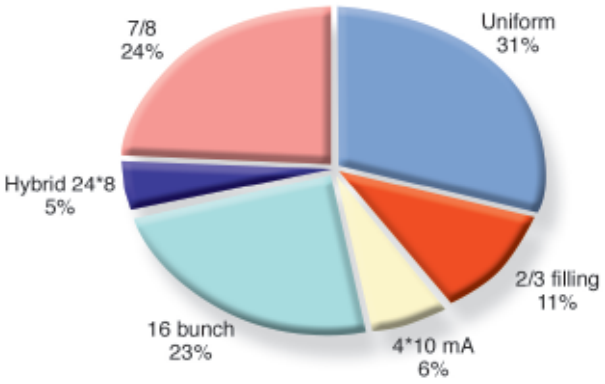

Fig. 140: Distribution of filling modes scheduled for 2007.

Lattice studies

The lattice of the ESRF storage ring was designed with 32 long straight sections of alternating high and low horizontal beta values. This currently provides 5 m of available space for insertion devices. The ESRF Upgrade Programme proposes to increase the length of selected insertion device straight sections from 5 to 7 m. This will provide a higher level of brilliance and increased insertion device (ID) flexibility. For example, longer insertion devices for a single beamline, sharing of the straight sections between two experimental stations using the canted undulator approach, reshuffling RF cavities layout and freeing straight section space for new beamlines are possible uses of the gained ID length.

The first step of this programme was achieved in 2006 with the implementation in USM of a new lattice in which the 2 quadrupoles (QD1 and QD8) located on both sides of the undulators were no longer powered (**Figure 141**). These quadrupoles can be removed and longer (6 m) insertion devices installed.

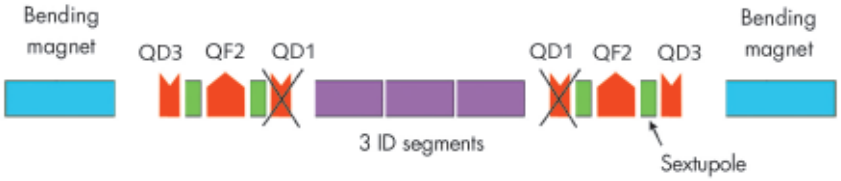

Fig. 141: Schematic lattice design of a long high beta straight section. Bending magnets, quadrupole and sextupoles are shown in blue, red and green respectively. The segments of the insertion devices are represented in purple. With the new lattice in use, the quadrupole family QD1 on both sides of the insertion devices is no longer powered and can be removed extending the total length of straight section available to insertion devices from 5 to 6 m. On the low beta straight sections, the quadrupole families QD1,QF2 and QD3 becomes QD8,QF7 and QD6. The last quadrupole QD8 adjacent to a low beta undulator have been switched off in the new lattice settings.

Fig. 142: Lifetime achieved with a ring current of 100 mA in 1/3, 2 x 1/3 and uniform filling mode with the previous lattice settings with all quadrupoles powered (in blue) and the new lattice (in red).

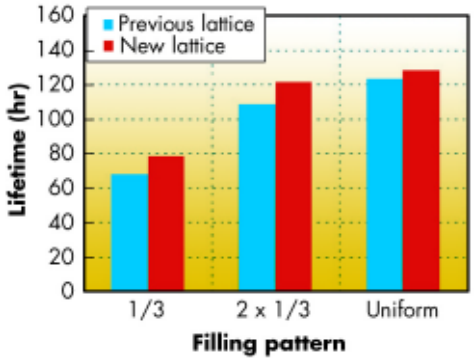

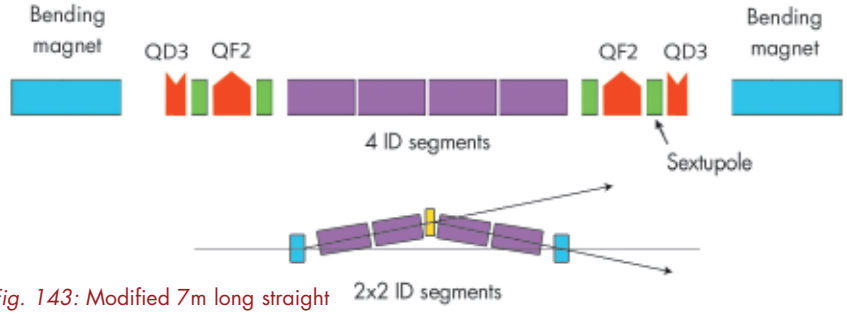

Fig. 143: Modified 7m long straight section with 4 insertion device segments or alternatively two longer undulator segments that are canted in order to generate two X-ray beams to independent beamports.

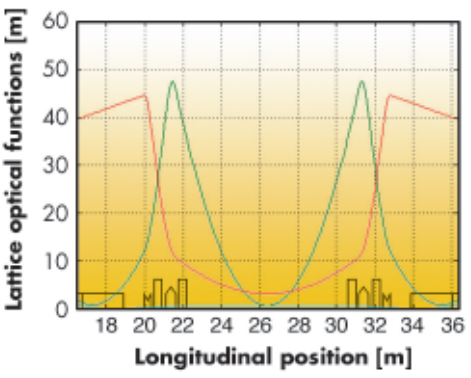

Fig. 144: Beta-functions in a 7 m long low beta straight section.

This new type of lattice with no current in QD1 and QD8 has been in use during USM since October 2006. The lifetime of the stored electron beam was lower than that achieved previously resulting in higher beam losses in the ring tunnel. Further lattice investigations were carried out in 2007. An improved lifetime was achieved by increasing the vertical tune by one integer, which necessitated the retuning of all quadrupole and sextupole currents. The electron beam sizes and divergences of the modified lattice present negligible change in the horizontal plane. The greatest change is in the vertical plane and corresponds to a 3 m vertical beta in the middle of the insertion device straight section as opposed to 3.5 m for the lattice that has been in use since October 2006. Measurements show that the lifetime of the beam in this new lattice is slightly longer than that achievedpreviously with the lattice where all quadrupoles were powered (in use between 1996 and 2006). This is illustrated in **Figure 142**.

A further increase of the length of insertion devices from 6 to 7 m is possible by redesigning the QF2 and QF7 quadrupole for a shorter length and by displacing the sextupoles adjacent to the undulator. This will require the manufacture of new quadruples with a field gradient of around 25 T/m. A schematic of such a 7 m straight section is shown in **Figure 143**. The horizontal and vertical beta functions in a low beta straight section are presented in **Figure 144**.

In order to minimise costs and shutdown time, the 7 m long straight sections will not be implemented on all straight sections in one go, rather one by one on a limited number of sectors. The drawback of such a strategy is that the symmetry of the lattice will be broken and consequently this may have a detrimental effect on the dynamic aperture resulting in a reduction of the injection efficiency and lifetime. Extensive calculations and experiments are being carried out to simulate the symmetry break produced by such 7 m straight sections. Obviously, the behaviour of a 7 m long straight section cannot be tested experimentally in

advance since magnets and vacuum chambers need to be manufactured and installed at the right location. However, on the existing lattice, it is possible to detune a single straight section and break the periodicity by individually powering the magnets of the straight section. Such detuned straight sections generate a modification of the beta function and the displaced magnets excite resonances in the lattice in a manner similar to those observed on a 7 m straight section. The experimental investigations of the lattice with one or several detuned straight sections constitutes therefore a very useful study.

Detuning requires the powering of the quadrupole and sextupole in the associated straight section independently of those of the same quadrupoles in the other straight sections. This capability was implemented several years ago on three high beta straight sections (ID04, ID06 and ID20) and one low beta straight section (ID11). Various combinations of detuning have been implemented during lattice tests with 1, 2 or 3 sections detuned. In each case, similar lifetime and on-momentum horizontal aperture could be observed once the current settings of the quadrupole and sextupole within the detuned straight section had been re-optimised.

Transverse bunch by bunch feedback

In 2006, bunch by bunch feedback systems were installed and commissioning was begun. These feedback systems operate in each of the three orthogonal directions (longitudinal, horizontal and vertical). The feedback loop monitors the position selectively bunch by bunch (from any one of the maximum 992 bunches present along the ring circumference), then computes and applies a kick to the corresponding bunch in order to stabilise its motion. The loop makes use of fast digital electronics based on field programmable gate arrays (FPGA).

The goal of the longitudinal feedback system is to dampen the instability driven by the beam in the higher order mode (HOM) of the radio frequency cavities, above 200 mA. The first successful test occurred in December 2006 and testing will continue during 2008. The horizontal and vertical feedback systems allow the damping of resistive wall as well as ion driven instabilities which are at their most severe in uniform filling mode at high current.

In the future, it is planned to raise the current from 200 to 300 mA in uniform or 7/8 +1 filling modes only. In such filling modes, the ion induced instability may severely increase the vertical emittance. The associated beam blow-up can be significantly reduced by an increase in the vertical chromaticity of the ring magnet lattice, however the latter has a detrimental effect on the lifetime. The vertical bunch by bunch feedback system is an alternative means to combat the ion induced instability.

The efficiency of both horizontal and vertical bunch by bunch feedback systems has been demonstrated through several experiments where the feedback systems were proven effective in combating various instabilities. It was first used to store a 200 mA ring current in uniform filling mode with zero horizontal and vertical chromaticities and unchanged horizontal and vertical emittances. Later, during tests at 300 mA there was evidence that the feedback systems efficiently damped the ion induced instability. In this test, the beam required the vertical feedback to keep a low vertical size to avoid triggering a vacuum chamber protection interlock.

In November and December 2007, the vertical feedback was operated regularly in user time (USM) in uniform filling mode. **Figure 145** presents the image of the beam as seen through a pinhole camera without (left hand-side) and with (right hand-side) feedback. The effect of the feedback systems is particularly

noticeable immediately after the shutdown during which the opening of a number of vacuum vessels to atmospheric pressure results in poor vacuum and a strong influence from ions.

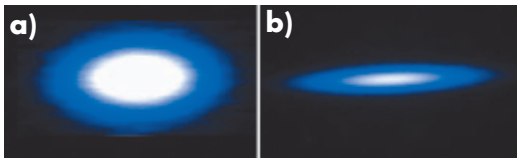

Fig. 145: The electron beam in a bending magnet afforded by a pinhole camera system. a) No vertical feedback; b) Vertical feedback system in use.

From these experiments, it appears that both the increase in chromaticity and the transverse feedback are complementary methods to ensure the stabilisation of the beam at high ring current. A precise study of the advantages and drawbacks of each technique will be undertaken in the year to come.

Charge, current and injection efficiency

Efficiency of the transfer of electron bunches between the various components of the acceleration system from the linac to their eventual capture in the storage ring needs to be optimised to maximise the rate of current storage during refill and to reduce losses that lead to environmental radiation and vacuum chamber activation. Efficiency is closely monitored during the preparation of each new beam delivery mode and then subsequently at each refill during operation. A system for monitoring the transfer efficiency has been in use since the start of operations at the ESRF using torroidal current transformers that monitor the passage of beam charge in the TL1 and TL2 transfer electron beamlines as well as in the booster and storage rings. The proximity of these charge measuring elements to transient noise sources (kicker magnets) and their broadband acceptance, makes them susceptible to error at low beam current. The current injection efficiency system is no longer capable of keeping up with the increasingly more stringent regulations on permitted radiation dose exposure. Furthermore, optimisation of the accelerator complex now needs to be done at even lower beam current.

A new system has been developed using narrow band high signal level detectors (striplines) placed in the vicinity of the electron beam passage at different locations in the ESRF accelerator complex. The induced RF signal at the ESRF characteristic frequency (352.2 MHz) is amplitude demodulated using digital processing techniques. The fast digitalisation of analog signals (analog to digital converters) coupled with very high speed digital circuits based on commercially produced FPGAs, have allowed a significant improvement in the precision of such RF measurements. A device developed by Instrumentation Technologies called 'Libera' incorporates these new developments. This device has been developed for high precision beam position monitoring for the latest generation of electron storage rings. Its embedded firmware has been optimised to perform relative and absolute measurements of beam charge at 4 locations at the ESRF: linac to booster transfer line TL1, booster, booster to storage ring transfer line TL2 and the storage ring (see **Figure 146**). Digital conversion and digital filtering is performed within the device, which then reports values of the beam charge and transfer efficiency between the various accelerator components to the control system.

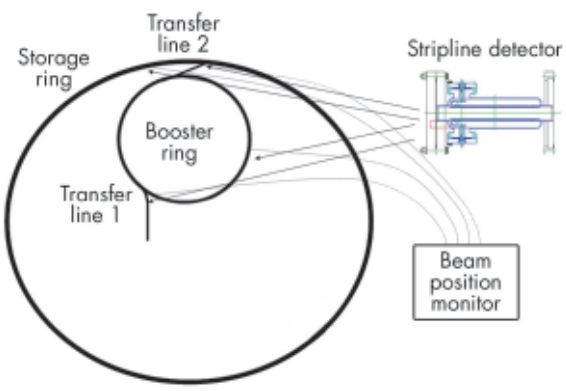

Fig. 146: Schematic diagram of the new injection efficiency measurement system. FPGA based electronics monitor the current in the various parts of the accelerator complex by means of high sensitivity stripline chambers. The signals are demodulated at 352 MHz and processed in real time to provide current, charge and transfer efficiency measurements to the operator in the control room.

Cryogenic in-vacuum undulator development

A cryogenic permanent magnet undulator (CPMU) has recently been developed. The advantage of the CPMU comes from the increased remanence and coercivity of NdFeB magnetic material at low temperature. The increased remanence results in a proportionally increased undulator magnetic field while the increased coercivity results in an improved resistance to demagnetisation following exposure to an electron beam [1]. As the temperature is reduced the remanence increases and reaches a maximum of around 140 K when a spin reorientation transition (SRT) takes place. Ultimately, a fully optimised CPMU should provide a field enhancement of around 30% over conventional room temperature in-vacuum undulators.

A full-scale prototype has been constructed. The device has a period of 18 mm and a magnetic length of 2 m. It corresponds to a modified version of a standard ESRF in-vacuum undulator. The grade of the magnet material was selected to allow full baking at 120°C, but has resulted in a limited field enhancement. The goal was to develop the technology and field measurement system while minimising the risks, making sure that the undulator can be safely operated on the ring. The high precision magnetic measurement system needs to be operated under vacuum with magnetic assemblies at cryogenic temperature. **Figure 147** shows the CPMU undergoing field measurement. The measuring bench includes a fast scanning Hall probe and a stretched wire system for the measurement of the field integral components. Both systems are implemented using a vacuum chamber specifically built for such a purpose.

The measuring bench has all the required motorisation outside the vacuum. The associated motions are transmitted either by magnetic coupling (Hall probe bench) or by mechanical connection through bellows (stretched wire bench). The local field measurements are performed at a constant speed (30 mm/s) while reading the three field components at 100 micrometre steps along 2.4 m long scans. The longitudinal positioning accuracy is based on laser interferometers tracking both the position and the pitch angle of the moving hall probe carriage. **Figure 148** shows the peak field of the undulator at different temperatures for a gap of 6 mm. It reveals the maximum connected to the SRT and compares favourably with the prediction of non linear models performed with RADIA. The RADIA model has been developed following the magnetic characterisation (B vs H) of the NdFeB samples as a function of temperature. The magnetic measurements confirm the predicted temperature for maximum field (around 150 K for the prototype). The 4% discrepancy between the measured and predicted peak field vs temperature can be explained by an offset in the magnetic gap measurement.

Fig. 147: The CPMU undergoing magnetic measurements.

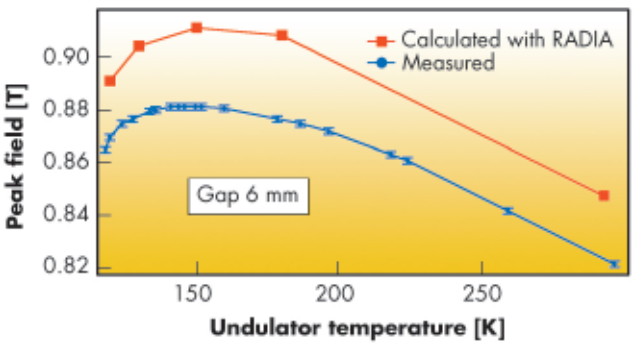

Fig. 148: Measured and predicted peak field versus temperature for the CPMU with a gap of 6 mm.

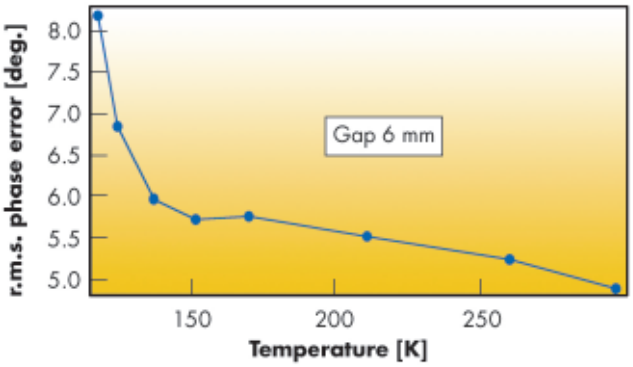

Fig. 149: Measured rms phase error versus temperature for the CPMU.

Figure 149 presents the rms value of the optical phase error computed at each pole of the undulator. The phase error is directly connected to the X-ray spectrum quality of the device. The observed change of phase error between room temperature and 150 K is due to a residual temperature gradient along the undulator assembly.

The cooling system is a liquid nitrogen closed loop which is identical to the system adopted at ESRF for the cooling of cryogenic monochromators.

To achieve the targeted temperature of 150 K at the magnetic assembly, the connection between the cooling channels and the magnetic assembly is done with distributed flexible copper spacers providing the necessary temperature drop. Such a cooling system is well adapted for this type of long device both in terms of cooling efficiency and running costs. The typical measured heat budget is 150 W when the undulator assembly is at 150 K. The prototype will be installed in the ID06 straight section during the Christmas 2007 shutdown.

Reference

[1] T. Hara *et al., Phys. Rev. Spec. Top. Accelerators, and beam*, Vol. 7 (2004).

Facts and Figures

Member and associate countries
(as of January 2008)

Members' share in contribution to the annual budget:

27.5%	France
25.5%	Germany
15%	Italy
14%	United Kingdom
4%	Spain
4%	Switzerland
6%	Benesync (Belgium, The Netherlands)
4%	Nordsync (Denmark, Finland, Norway, Sweden)

Additional contributions
(percentages refer to Members' total contribution):

1%	Portugal
1%	Israel
1%	Austria
1%	Poland
0.47%	Czech Republic
0.2%	Hungary

The beamlines

Details of the public ESRF beamlines as well as those operated by Collaborating Research Groups (CRG) are given in **Tables 5** and **6**. **Figure 150** shows the location of the beamlines in the experimental hall.

The Accelerator and Source Division beamline ID06 has been moved to ID30 and became operational in 2007. ID06 is being transformed into a multi purpose instrumentation development beamline and is presently under commissioning.

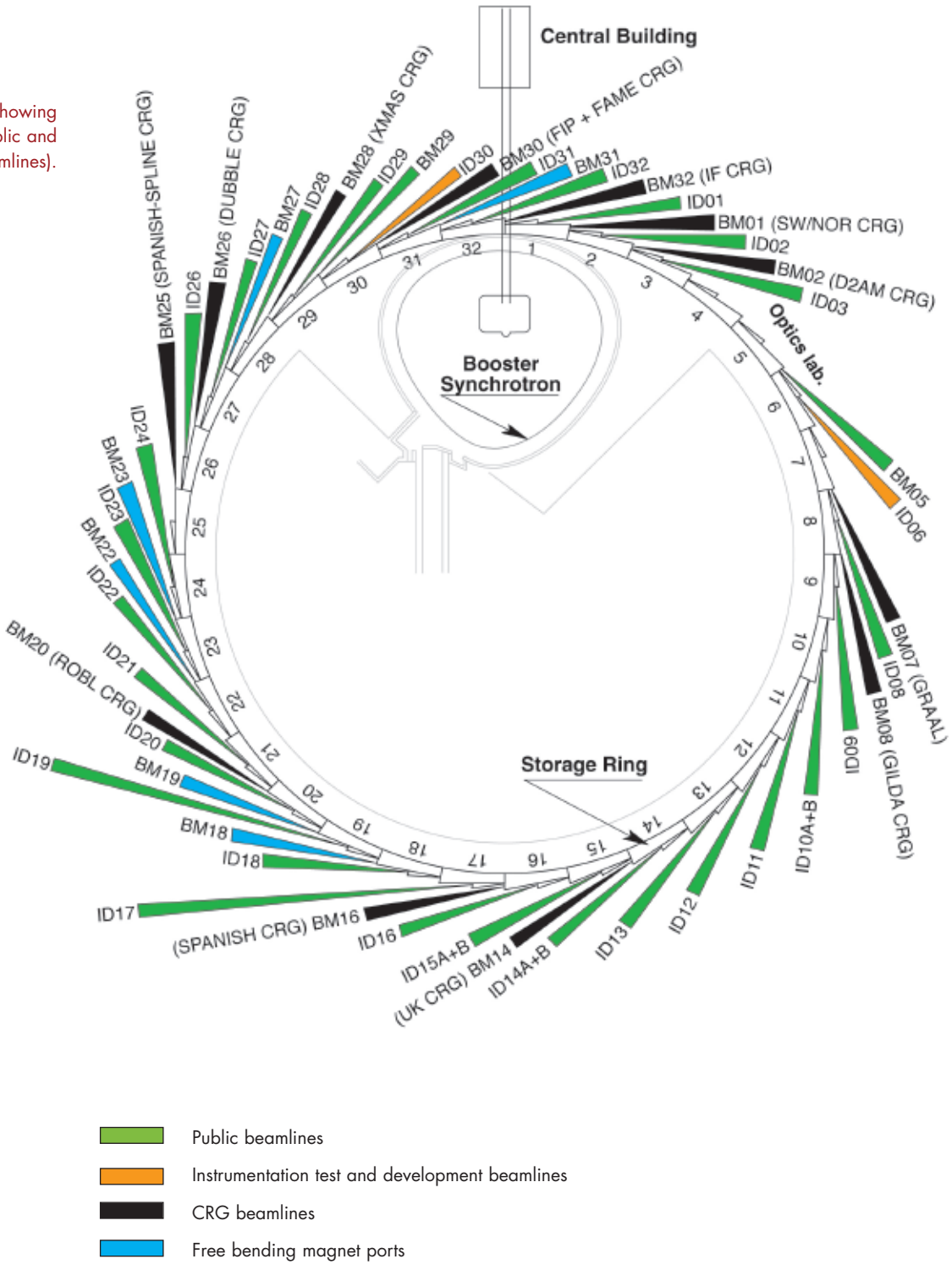

Fig. 150: Experimental hall showing location of the beamlines (public and CRG beamlines).

SOURCE POSITION	NUMBER OF INDEPENDENT END-STATIONS	BEAMLINE NAME	STATUS
ID01	1	Anomalous scattering	Operational since 07/97
ID02	1	High brilliance	Operational since 09/94
ID03	1	Surface diffraction	Operational since 09/94
ID06	1	ESRF instrumentation and techniques test beamline	Under commissioning
ID08	1	Dragon	Operational since 02/00
ID09	1	White beam	Operational since 09/94
ID10A	1	Troika I + III	Operational since 09/94
ID10B	1	Troika II	Operational since 04/98
ID11	1	Materials science	Operational since 09/94
ID12	1	Circular polarisation	Operational since 01/95
ID13	1	Microfocus	Operational since 09/94
ID14A	2	Protein crystallography EH 1	Operational since 07/99
		Protein crystallography EH 2	Operational since 12/97
ID14B	2	Protein crystallography EH 3	Operational since 12/98
		Protein crystallography EH 4	Operational since 07/99
ID15A	1	High energy diffraction	Operational since 09/94
ID15B	1	High energy inelastic scattering	Operational since 09/94
ID16	1	Inelastic scattering I	Operational since 09/95
ID17	1	Medical	Operational since 05/97
ID18	1	Nuclear scattering	Operational since 01/96
ID19	1	Topography and tomography	Operational since 06/96
ID20	1	Magnetic scattering	Operational since 05/96
ID21	1	X-ray microscopy	Operational since 12/97
ID22	1	Microfluorescence	Operational since 12/97
ID23	2	Macromolecular crystallography MAD	Operational since 06/04
		Macromolecular crystallography microfocus	Operational since 09/05
ID24	1	Dispersive EXAFS	Operational since 02/96
ID26	1	X-ray absorption and emission	Operational since 11/97
ID27	1	High pressure	Operational since 02/05
ID28	1	Inelastic scattering II	Operational since 12/98
ID29	1	Multiwavelength anomalous diffraction	Operational since 01/00
ID30	1	Machine division beamline	Operational since 09/07
ID31	1	Powder diffraction	Operational since 05/96
ID32	1	X-ray standing wave and surface diffraction	Operational since 11/95
BM05	1	Optics - Open Bending Magnet	Operational since 09/95
BM29	1	X-ray absorption spectroscopy	Operational since 12/95

Table 5: List of the ESRF public beamlines.

SOURCE POSITION	NUMBER OF INDEPENDENT END-STATIONS	BEAMLINE NAME	FIELD OF RESEARCH	STATUS
BM01	2	Swiss-Norwegian BL	X-ray absorption & diffraction	Operational since 01/95
BM02	1	D2AM (French)	Materials science	Operational since 09/94
BM07	1	GRAAL (Italian / French)	Gamma ray spectroscopy	Operational since 06/95
BM08	1	Gilda (Italian)	X-ray absorption & diffraction	Operational since 09/94
BM14	1	UK CRG	Macromolecular crystallography (MAD)	Operational since 01/01
BM16	1	SPANISH CRG	Structural biology (MAD, SAX)	Operational since 01/03
BM20	1	ROBL (German)	Radiochemistry & ion beam physics	Operational since 09/98
BM25	2	SPLINE (Spanish)	X-ray absorption & diffraction	Operational since 04/05
BM26	2	DUBBLE (Dutch/Belgian)	Small-angle scattering & interface diffraction Protein crystallography + EXAFS	Operational since 12/98 Operational since 06/01
BM28	1	XMAS (British)	Magnetic scattering	Operational since 04/98
BM30	2	FIP (French) FAME (French)	Protein crystallography EXAFS	Operational since 02/99 Operational since 08/02
BM32	1	IF (French)	Interfaces	Operational since 09/94

Table 6: List of the Collaborating Research Group beamlines.

User operation

After more than a decade of successful operation of the facility for scientific Users, the year 2007 saw the full complement of 31 public beamlines, together with 11 additional beamlines operated by Collaborating Research Groups (CRGs) available for experiments by visiting research teams.

Figure 151 shows the increase in the number of applications for beamtime since 2001, and confirms that although the main beamline construction effort was complete by 1999, the number of applications for beamtime continues to increase steadily.

Proposals for experiments are selected and beamtime allocations are made through peer review. Review committees of specialists, for the most part from European countries and Israel, have been set up in the following scientific areas:

- chemistry
- hard condensed matter: electronic and magnetic properties
- hard condensed matter: crystals and ordered systems
- hard condensed matter: disordered systems and liquids
- applied materials and engineering
- environmental and cultural heritage matters
- macromolecular crystallography
- medicine
- methods and instrumentation
- soft condensed matter
- surfaces and interfaces

The Review Committees met twice during the year, some six weeks after the deadlines for submission of proposals (1 March and 1 September). They reviewed a record number of 1907 applications for beamtime, and selected 888 (46.6%), which were then scheduled for experiments.

Features of this period:

- increasing numbers of proposals submitted for research into environmental issues, into palaeontology and artefacts relating to our cultural heritage.
- the continued successful operation of the Block Allocation Group (BAG) scheme for macromolecular crystallography users. This scheme, designed to encourage groups of users to block together their multiple requests for beamtime, and the scheduling of their experiments, encompassed 48 groups from Europe and Israel in 2007.

Requests for beamtime, which is scheduled in shifts of 8 hours, totalled 29 959 shifts or 239 672 hours in 2007, of which 13 681 shifts or 109 448 hours (45.7%) were allocated. The distribution of shifts requested and allocated, by scientific area, is shown in **Table 7**.

The breakdown of shifts scheduled for experiments by scientific area in the first half of 2007 is shown in **Figure 152**. This period saw 2799 visits by scientists to the ESRF under the user programme, to carry out 691 experiments. **Figure 151** shows the rapid rise in the number of user visits since 2001, the higher numbers in recent years reflecting in part the multiple visits made by macromolecular crystallography BAG teams.

Overall, the number of users in each experimental team averaged 4 persons, and they stayed for some 4 days. Users responding to questionnaires indicate that they particularly appreciate the assistance they receive from scientists and support

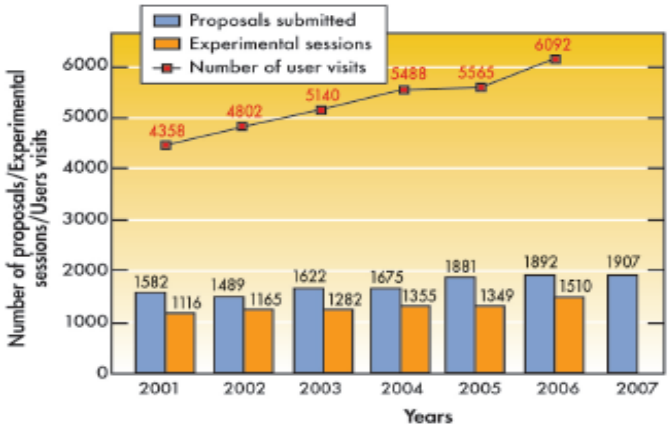

Fig. 151: Numbers of applications for beamtime, experimental sessions and user visits, 2001 to 2007. N.B. Final numbers of experiments and user visits for 2007 were not available at the time of going to press.

Table 7: Number of shifts of beamtime requested and allocated for user experiments, year 2007.

Scientific field	Total shifts requested	Total shifts allocated
Chemistry	2 918	981
Hard condensed matter:		
• Electronic and magnetic prop.	5 532	2 298
• Crystals and ordered structures	3 824	1 458
• Disordered systems	1 941	627
Applied materials and engineering	2 597	1 464
Environmental and cultural heritage matters	2 020	714
Macromolecular crystallography	3 038	2 415
Medicine	876	487
Methods and instrumentation	868	456
Soft condensed matter	2 889	1 203
Surfaces and interfaces	3 456	1 578
Totals	**29 959**	**13 681**

staff on beamlines, and travel and administrative arrangements, in addition to the quality both of the beam and of the experimental stations. Facilities on site, such as preparation laboratories, the Guesthouse and a canteen open 7 days a week, also make an important contribution to the quality of user support.

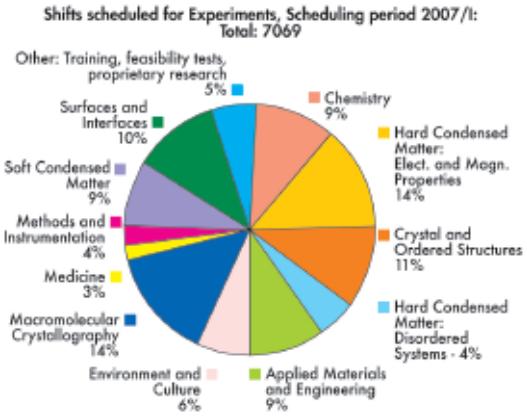

Fig. 152: Shifts scheduled for experiments, March to July 2007, by scientific area.

Administration and finance

Expenditure and income 2006

Expenditure	kEuro		Income	kEuro
Machine			2006 Members' contributions	68 448.7
Personnel		4 705.3	Funds carried forward from 2005	15.0
Recurrent		2 380.5		
Operating costs	*1 999.4*		Other income	
Other recurrent costs	*381.1*		Scientific Associates	4 005.1
Capital		3 145.4	Sale of beam time	2 422.1
Machine developments	*3 145.4*		Compensatory funds	68.0
			Scientific collaboration and Special projects	3 401.3
Beamlines, experiments and in-house research				
Personnel		22 960.4		
Recurrent		6 982.9		
Operating costs	*3 964.1*			
Other Recurrent costs	*3 018.1*			
Capital		7 474.0		
Beamline developments	*2 878.9*			
Beamline refurbishment	*4 595.1*			
Technical and administrative supports				
Personnel		16 542.1		
Recurrent		10 604.9		
Capital		3 551.7		
Unexpended committed funds				
Funds carried forward to 2007		13.0		
Total		**78 360.2**	**Total**	**78 360.2**

Revised expenditure and income budget for 2007

Expenditure	kEuro		Income	kEuro
Machine			2007 Members' contributions	69 743
Personnel		4 980	Funds carried forward from 2006	13
Recurrent		2 225		
Operating costs	*1 836*		Other income	
Other recurrent costs	*389*		Scientific Associates	4 275
Capital		3 877	Sale of beam time	2 400
Machine developments	*3 877*		Compensatory funds	210
			Scientific collaboration and Special projects	3 565
Beamlines, experiments and in-house research				
Personnel		24 530		
Recurrent		6 520		
Operating costs	*3 350*			
Other Recurrent costs	*3 170*			
Capital		7 057		
Beamline developments	*3 855*			
Beamline refurbishment	*3 202*			
Technical and administrative supports				
Personnel		16 620		
Recurrent		10 140		
Capital		3 627		
Industrial and commercial activity				
Personnel		460		
Recurrent		170		
Personnel costs provision				
Total		**80 206**	**Total**	**80 206**

Expenditure 2006 by nature of expenditure

	kEuro
PERSONNEL	
ESRF staff	42 409.3
External temporary staff	41.0
Other personnel costs	1 757.5
RECURRENT	
Consumables	7 774.1
Services	9 463.5
Other recurrent costs	2 730.8
CAPITAL	
Buildings, infrastructure	1 801.4
Lab. and Workshops	250.1
Machine incl. ID's and Fes	3 145.4
Beamlines, Experiments	7 474.0
Computing Infrastructure	928.7
Other Capital costs	571.4
Unexpended committed funds	
Funds carried forward to 2007	13.0
Total	**78 360.2**

Revised budget for 2007 by nature of expenditure

	kEuro
PERSONNEL	
ESRF staff	44 595
External temporary staff	85
Other personnel costs	1 910
RECURRENT	
Consumables	7 250
Services	9 445
Other recurrent costs	2 360
CAPITAL	
Buildings, infrastructure	1 817
Lab. and Workshops	400
Machine incl. ID's and Fes	3 877
Beamlines, Experiments	7 057
Computing Infrastructure	840
Other Capital costs	570
Total	**80 206**

2007 manpower
(posts filled on 31/12/2007)

	Scientists, Engineers, Senior Administrators	Technicians and Administrative Staff	PhD students	Total
Staff on regular positions				
Accelerator and Source	25	36		61
Beamlines, instruments and experiments*	210	68.2	26	304.2
General technical services	51.6	66.9		118.4
Directorate, administration and central services	30.3	50.6		80.9
Sub-total	*316.8*	*221.7*	*26*	*564.5*
Other positions				
Short term contracts	3	10.2		13.2
Staff under "contrats de qualification" (apprentices)		21		21
European Union grants	10		1	11
Temporary workers		1		1
Total	**339.8**	**253.9**	**27**	**610.7**
Absences of staff (equivalent full time posts)				20.7
Total with absences				*590*
Scientific collaborators and consultants	*10*			*10*
External funded research fellows	*6*		*11*	*17*

** Including scientific staff on time limited contract.*

Financial resources in 2005, 2006, 2007 and 2008, by major programme

(current prices in MEuro for the respective years)

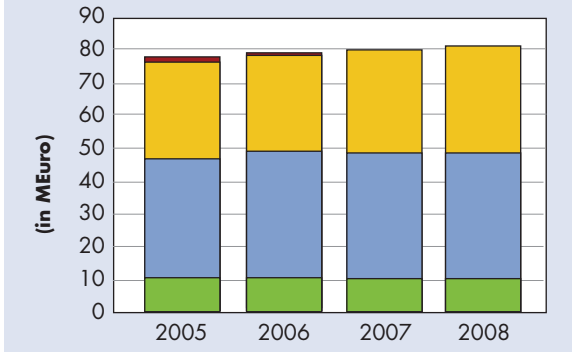

Financial resources in 2005, 2006, 2007 and 2008, by nature of expenditure

(current prices in MEuro for the respective years)

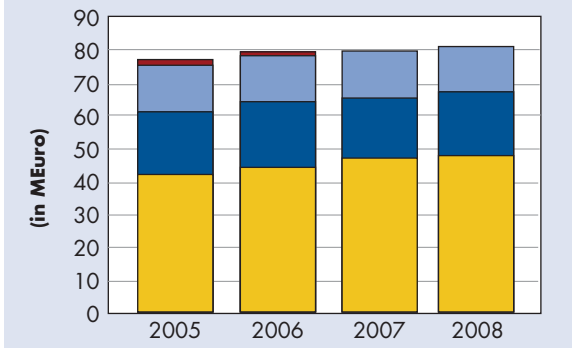

Organisation chart of the ESRF

(as of January 2008)

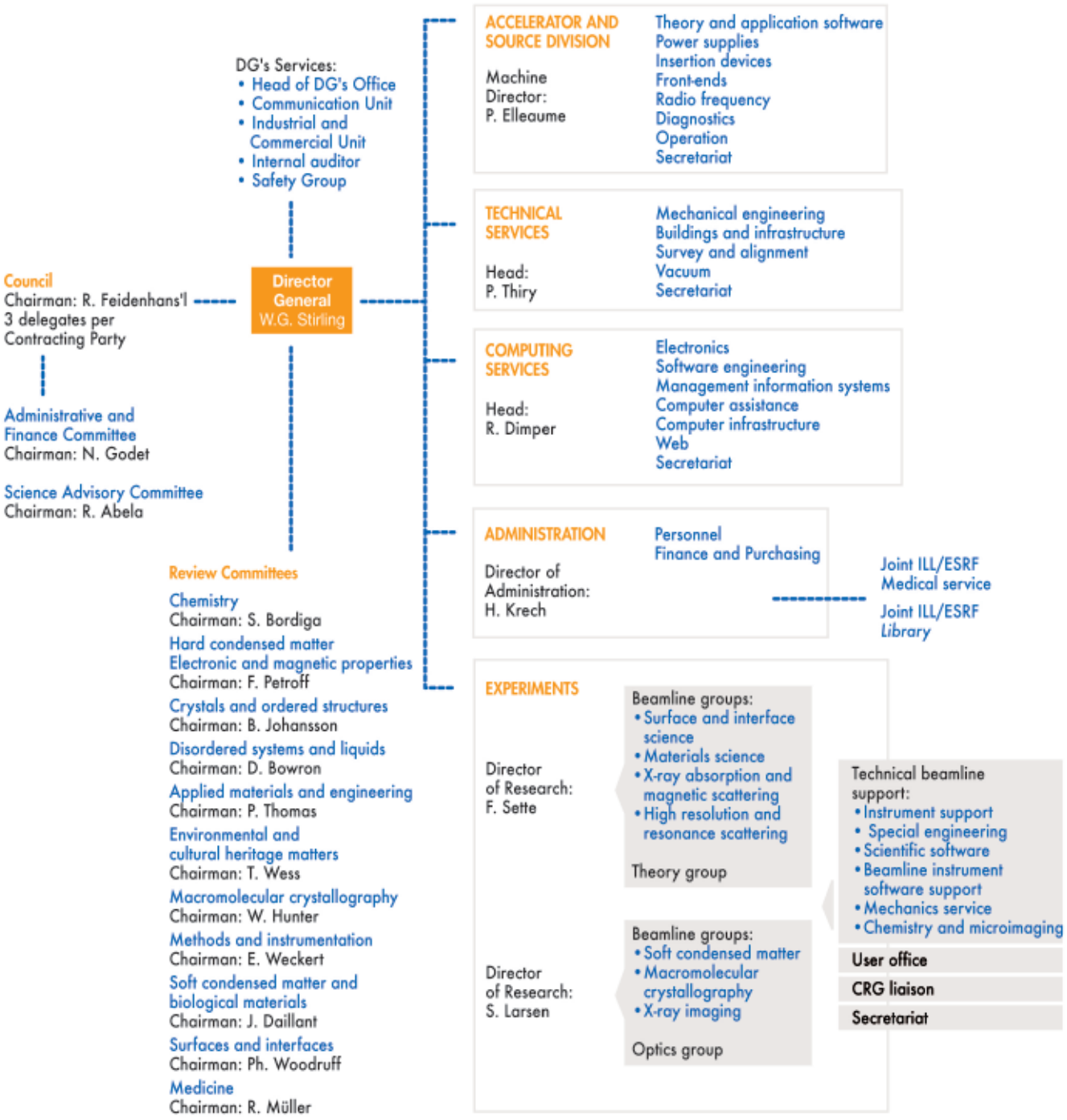

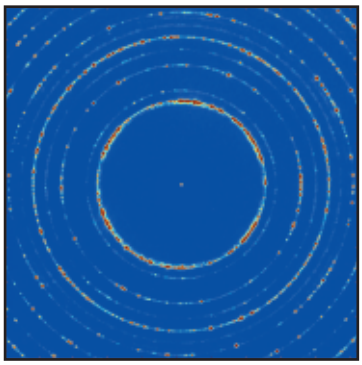

Cover image

X-ray diffraction pattern of TRIP steel taken with the high-energy (80keV) X-ray microbeam available at beamline ID11. Each diffraction spot contains information on an individual grain within the material (see p30, *Monitoring metastable grains in steel*). Image courtesy of E. Jimenez-Melero.

Photo credits

G. Admans (p5, p57, p89, p121), G. Garner (p5, p75), P. Ginter (cover photo, p24, p46, p57, p58, p74, p88, p106), D. Morel (p24, p107, p129).

We gratefully acknowledge the help of:

C. Argoud, J. Baruchel, B. Boulanger, N.B. Brookes, R. Davies, P. Elleaume, A. Fitch, F.M.F. de Groot, C. Habfast, W.N. Hunter, E. Jean-Baptiste, A. Kaprolat, G. Kotliar, M. Krisch, S. Larsen, G. Leonard, R. Mason, C. Riekel, M. Rodriguez Castellano, R. Rüffer, F. Sette, W.G. Stirling, S. McSweeney, D.P. Woodruff, J. Zegenhagen, and all the users and staff who have contributed to this edition of the Highlights.

Editor
G. Admans
Layout
Pixel Project
Printing
Imprimerie du Pont de Claix

Communication Unit
ESRF
BP220 • 38043 Grenoble • France
Tel. (33) 4 38 88 19 46 • Fax. (33) 4 76 88 25 42
http://www.esrf.eu